Novel interfaces in hybrid composite-metal struts

By

JORDAN JONES

Department of Aerospace Engineering
UNIVERSITY OF BRISTOL

A dissertation submitted to the University of Bristol in accordance with the requirements of the degree of DOCTOR OF PHILOSOPHY in the Faculty of Engineering.

JUNE 2019

Word count: 70,346

Abstract

This research aims to propose and examine a novel composite-metal joining solution, for applications to hybrid, tubular struts. The joint is initiated via the filament winding of carbon-fibre tows around features (pins) that are structured onto the surface of the metal. The interlocking between the fibre-tows and metal pins provides a joining mechanism that both, exploits the high tensile stiffness and strength of the fibre reinforcement, and results directly from composite manufacture.

Design parameters of the hybrid composite-metal joint and strut are considered. Unique winding patterns are required for joint and strut fabrication, without inducing manufacturing defects such as tow puncturing. The resulting tow trajectories contribute to non-uniform fibre volume content on the structure. The effect on the strut's elastic properties is assessed using numerical methods, in which the tow's volumetric contribution is considered at discrete sections of the strut. Joint efficiency is dependent upon design considerations, including the pin distribution, the tow path through the pin array and the manner in which the tow's direction is reversed around the pins, during a process referred to as "pull-back". A simple analytical framework is developed to study these effects, in which the interaction between the filament wound fibre-tows and the pins, is described using a belt-and-pulley analogy. These analyses allow for a preliminary performance ranking of joint and strut configurations.

A multi-scale modelling framework is developed to determine the mechanical properties of the hybrid strut, using a meso-scale approach. Firstly, the Single-Filament (SF) method is used to predict the as-manufactured path of the tows on the structure. The virtual tows are represented as a chain of truss elements, which allows for their kinematic behaviour to be simulated. The virtual tows are then meshed using 3D continuum (solid) elements for their cross-sections, prior to mechanical analyses using quasi-static virtual tests. Matrix material is included and linked with the virtual tows using a constraint-based coupling mechanism, so that strut properties can be assessed in its final, consolidated, operating form.

A higher fidelity modelling approach is then used to predict joint properties in further detail. The virtual tows are modelled using the Multi-Filament (MF) method, in which the tows are described as bundle of virtual fibres. Deformations induced in the fibre-tows, due to their interactions with the metallic pins during the filament winding process, are simulated. Information regarding the tows' non-uniform geometric shape and internal architecture, is then used to assess the joint's mechanical performance with improved realism.

Following assessment of the joint's theoretical capabilities, manufacturability is considered via the fabrication of a conceptual, prototype hybrid strut. Modifications are made to a commercial 4-axis filament winding machine to improve tow placement around the pins; with winding patterns constructed using the numerical programming language G-code. X-ray computed tomography scans are conducted to provide high resolution images for the joint, in order to visually appraise the novel interface initiated between the tows and the pins during the filament winding process.

Dedication and acknowledgements

I would like to thank my supervisor Stephen Hallett for his continued help and support throughout this project. I would also like to thank my industrial supervisors at Airbus UK; Alan Shepherd, Greg McCombe, Frazer Wilson, Billy Chan and Rob Main, for providing the initial research direction and industry perspective. Special thanks are also owed to fellow PhD students and research associates at the Bristol Composites Institute, within the University of Bristol, in particular, Adam Thompson, whose knowledge of composite fabric modelling has been invaluable.

PUBLICATIONS

- **Jordan Jones, Luiz F.Kawashita, Byung Chul Kim and Stephen R.Hallett. Modelling of Novel Hybrid Composite-Metal Joints, VI Conference of Mechanical Response of Composites (ECCOMAS) September 2017.**

- **Jordan Jones, Luiz F.Kawashita, Byung Chul Kim and Stephen R.Hallett. Analysis of Novel Hybrid Joints for Composite Struts, 18th European Conference on Composite Materials (ECCM18) June 2018.**

AUTHOR'S DECLARATION

I declare that the work in this dissertation was carried out in accordance with the requirements of the University's Regulations and Code of Practice for Research Degree Programmes and that it has not been submitted for any other academic award. Except where indicated by specific reference in the text, the work is the candidate's own work. Work done in collaboration with, or with the assistance of, others, is indicated as such. Any views expressed in the dissertation are those of the author.

SIGNED: ..... DATE: .....

TABLE OF CONTENTS

List of Tables

List of Figures

Figure **Page**

CHAPTER 1

INTRODUCTION

Fibre reinforced composite materials offer benefits in terms of high specific strength and stiffness, and improved fatigue and corrosion resistance. The associated weight-saving benefits and increased component life-cycle are of particular interest for the aviation industry. However, metals may still be preferred for certain applications. This necessitates the developed of hybrid composite-metal component alternatives. The mechanical properties of the hybrid structure may be determined by the efficiency of the interface between the two materials'.

Current, prevalent composite-metal joining methods such as mechanical fastening (bolting/riveting) and adhesive bonding have significant limitations. With mechanically fastened joints, bolt-hole drilling causes destruction of the fibre reinforcement, peeling of the surface plies and stress concentrations at the hole boundary. This damage can initiate fatigue cracks and reduce structural strength. Adhesively bonded joints exhibit sudden failure with high scatter, thus tending to unreliability. Additionally, failure modes which initiate at the bond-line, such as cohesive failure, are difficult to inspect visually.

However, primarily, both joining methods fail to account for the unique anisotropy inherent with composite materials. In order to improve load transfer capability, the joining mechanism should provide a direct coupling between the metallic component and the composite material's fibre reinforcement, which acts as the predominate load-carrying constituent. To accomplish this, joining should be considered as a primary process where composite manufacture and composite-metal integration are achieved simultaneously. This will allow for manipulation of the fibre reinforcement to initiate a direct mechanical interaction between the fibre tow and metallic part.

This research, conducted in partnership with Airbus UK, considers a novel hybrid composite-metal joining solution which achieves these objectives. To provide context for assessment of the novel joining mechanism, its application is examined for a particular landing gear component.

However, it should be noted that the composite-metal joint proposed in this work is not constrained to this particular component and may potentially be utilsed for the construction of a wide range hybrid composite-metal structures.

1.1 Hybrid composite-metal joint and strut

Landing gear strut components, such as the lower-side stay pictured in figure 1.1(a), commonly consist of a titanium alloy or high strength steel [19]. The strut can be simplified to a tubular structure with pin-lug joints located at its ends (figure 1.1(b)), which allow it to connect to other parts of the landing gear, and retract and extend into the main aircraft structure, during take-off and landing. Metal must be retained at the strut ends as bearing loads are transferred through the pin-lug connectors, but the central part of the strut predominately experiences axial loads (tension and compression). This offers the potential for the development of a weight optimised, hybrid composite-metal strut component, through substitution of the central part of the strut with carbon-fibre composite material.

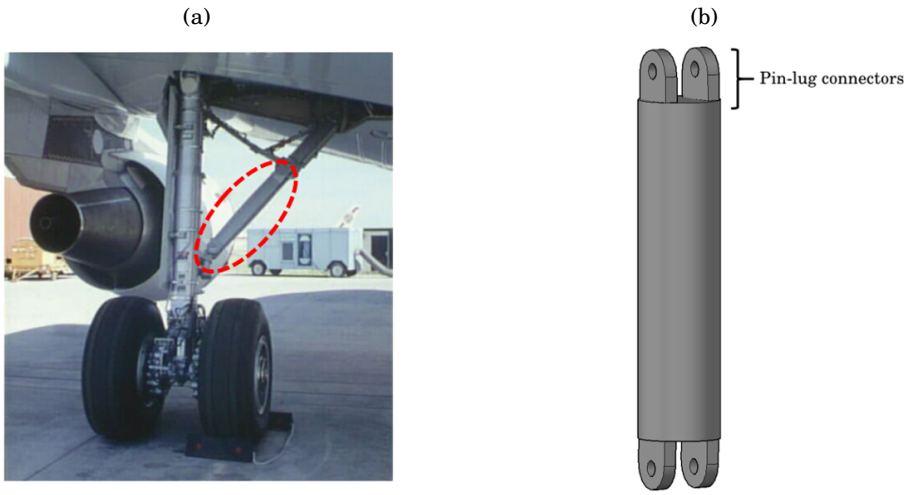

Figure 1.1: (a) Aircraft landing gear side-stay. (b)Simplification of the component to a metallic cylindrical tube with pin-lug joints situated at the ends (not to scale).

Metal must be retained at the strut ends as bearing loads are transferred through the pin-lug connectors, but the central part of the strut predominately experiences axial loads (tension and compression). This research, conducted in partnership with Airbus UK, considers the potential for a weight optimised, hybrid composite-metal strut component, through substitution of the central part of the strut with carbon-fibre composite material.

In order to be suitable for such high performance strut components, the composite-metal joint at the strut ends must provide improved efficiency and load-carrying capability than current, prevalent technologies. The joining mechanism should utilise the high stiffness and strength of

the composite material's fibre reinforcement, by establishing a direct, robust connection between the fibres and the metallic part. This can only be achieved through simultaneous consideration of composite manufacture, and composite-metal joining. The (dry) fibre reinforcement can then be manipulated prior to matrix infiltration and consolidation of the composite.

As reviewed in section 2.4, a mechanical interlocking and form-fit between the fibre reinforcement and the metal can be provided by structuring protrusions (or pins) to project from the metal's surface. Braiding technologies have been used to integrate the braid yarns to the surface-structured metal, in the manufacture similar tubular, hybrid composite-metal struts and drive-shafts for rail and automotive applications (section 2.4.1). However, such braided/surface-structured joints have two primary disadvantages. Firstly, the joining mechanism relies on the "shear-locking" of adjacent (non-axial) yarns around the pins and therefore does not take advantage of the high tensile strength of the fibres. Secondly, manufacturing defects, such as the yarn puncturing, have been found to occur frequently during the braiding process.

Consequently, this work considers filament winding for the fabrication of the hybrid composite-metal strut and initiation of the joint at the surface-structured metal interface. Direct reversal of the fibre-tows around the pins during the filament winding process, referred to as tow "pull-back", establishes a direct, robust connection between the fibre reinforcement and the metal immediately at the composite manufacture stage, and utilises the high tensile stiffness and strength of the fibres in the joint. Furthermore, filament winding may lead to improved precision of tow placement around the metallic pins, which should prevent defects such as tow-puncturing.

A brief overview of the filament winding fabrication technique is given in section 1.2 in order to provide a background. Similarly, braiding, which can be considered the nearest "competitor" technology, with respect to the manufacture of such high performance composite-metal joints for tubular struts, is also reviewed in section 1.3. The structure of the thesis is then outlined in sections 1.4 and 1.5.

1.2 Filament winding

In the filament winding of fibre-reinforced composites, fibre filaments, or tows, are fed through a delivery eye onto a rotating mandrel [4], [20]. A typical winding system consists of the machine to control the relative directions of motion and rotation; racks of fibre spools from which the tow is drawn, and tensioning devices to control the tension in the fibre-tows during layup [21].

Dry or pre-impregnated fibres can be drawn from the spools. For wet-winding, the fibre-tows are impregnated by drawing them through a resin bath, prior to passing through the delivery eye and placement on the mandrel. Following curing and consolidation of the composite, the mandrel may be removed, resulting in a hollow component, or left as a permanent part of the structure.

Winding machines can be categorised based on their relative motions of control (or degrees of freedom). The simplest is a two-axis filament winder, where the tow delivery system can traverse

along the length of the mandrel, which can also rotate about its longitudinal axis, as shown in figure 1.2(a). In a four-axis filament winding machine, the tow delivery system can move in the "cross-feed" direction perpendicular to the mandrel axis, allowing it to move towards and away from the mandrel's surface (figure 1.2(b)). Rotation of the delivery eye about the cross-feed axis is also possible, this is useful for preventing tow twisting during layup.

Movements about the winding machine's relative degrees of freedom are controlled so that the fibre tows/filaments are laid down according to the desired pattern or angle, which generally determine the mechanical properties of the part [3]. The winding angle is defined as the acute angle between the tow centreline trajectory and the longitudinal axis of the mandrel. Each fibre-tow is placed individually during the winding process, with the winding pattern repeated until the mandrel is covered to the required thickness.

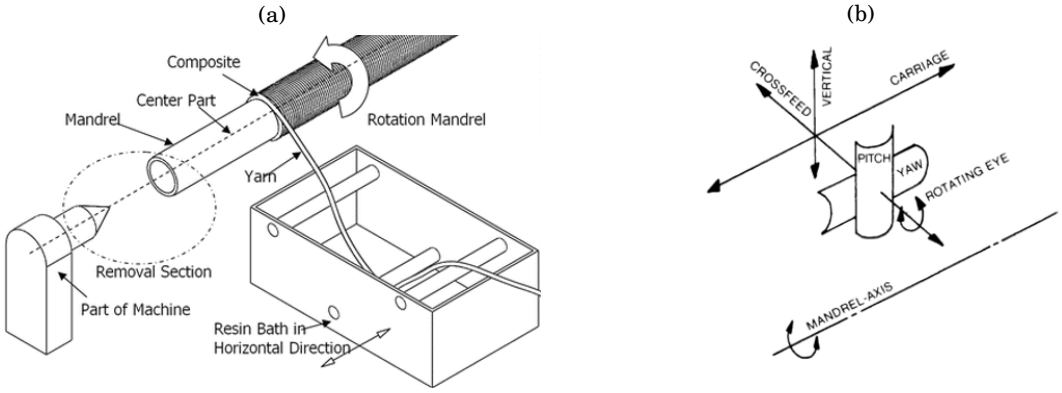

Figure 1.2: (a) Schematic of the filament winding process [3]. (b) Degrees of freedom of a filament winding machine [4].

Generally, there are 3 main filament winding patterns: helical, hoop and polar [5], [22]. In helical winding, the tow delivery system traverses up and down the mandrel's longitudinal axis at a speed, coordinated with the mandrel's rotational velocity, so as to layup the tow in accordance with the prescribed angle. Hoop (or circumferential) winding may be considered an example of helical winding in which the angle approaches 90°. The delivery eye moves along the mandrel axis by the width of the fibre-tow for each full rotation of the mandrel. High angle helical and hoop winding patterns are used to improve circumferential strength.

For polar winding, the tow pull-back occurs at the mandrel apex. Curved surfaces, such as demi-spherical or domed shaped end-caps, are typically used in the pull-back region [23]. For example, in the manufacture of high performance, composite pressure vessels [24], [25]. Polar patterns can produce near axial tow paths, which can improve axial (longitudinal) tensile and compressive strength.

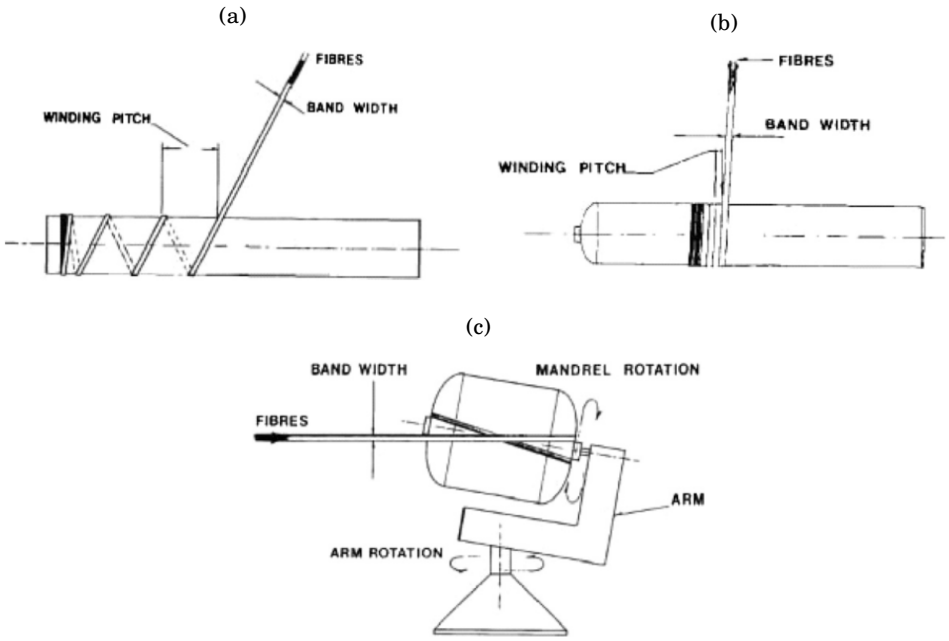

Figure 1.3: (a) Helical, (b) hoop and (c) polar winding patterns [5].

1.3 Braiding

In the braiding of three-dimensional composite preforms [26], [27], [6], warp and weft yarn carriers (bobbins) move both circumferentially around the braid wheel (figure 1.4), and radially to intertwine the yarns and form the braid pattern. Out-of-plane yarn movement (crimp) results from the interlacing of the braid yarns [28].

Bobbin and mandrel "take-up" speeds can be controlled to lay yarns at a prescribed braid angle [29]. Over-braids can be used to increase mandrel coverage and composite thickness. Axial yarn paths can be included for a tri-axial braid pattern, by adding additional stationary bobbins to the braid wheel.

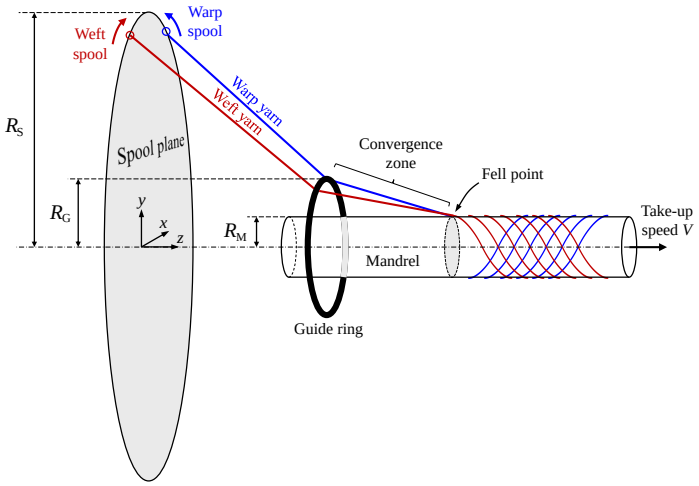

Figure 1.4: Schematic of the braiding process [6].

1.4 Thesis overview

This thesis aims to propose and examine a novel hybrid composite-metal joining solution, which uses filament winding to directly integrate carbon-fibre tows with pin structured metallic end-fittings in a tubular strut component; through use of analytical, numerical and experimental methods. The main objectives for this research are summarised below.

(1) Introduce the novel hybrid composite-metal strut and joining mechanism, and characterise the winding patterns necessary for its construction.

(2) Explore the theoretical range of strut and joint designs.

(3) Develop efficient modelling tools that allow the mechanical performance potential of the hybrid composite-metal strut and joint to be assessed.

(4) Utilise the modelling tools to predict joint properties, such stiffness, strength and load transfer behaviour, and evaluate how this may vary between joint designs, and against alternate composite-metal joining solutions.

(5) Examine the manufacturability of the proposed hybrid composite-metal joint and strut, and investigate limitations imposed by current technologies.

1.5 Thesis structure

From the overview and objectives outlined above, this thesis has been organised into the following chapters:

Chapter 2 - Literature Review
A review of literature covering the joining of composite materials and composite-metal joints for hybrid structures. Limitations of current joining technologies are discussed and a novel approach is proposed.

Chapter 3 - Strut and joint design
A novel composite-metal joining solution, for the manufacture of high performance, hybrid composite-metal strut components, is introduced. Design parameters of the composite-metal joint and strut are considered using analytical and numerical approaches, in order to explore the theoretical variability in strut and joint manufacture, and to determine a preliminary relative performance ranking of designs prior to assessment via Finite Element Methods (FEM) in chapters 4 and 5.

Chapter 4 - Meso-scale mechanical performance assessment of the hybrid composite-metal joint and strut
Modelling capabilities for the hybrid strut are first developed by using the Single Filament (SF) method to predict the as-manufactured path of the tows on the strut. This characterisation of the individual tow paths is then used to construct a meso-scale mechanical model, in which matrix material is included via a constraint-based coupling mechanism, in order for strut properties to be evaluated in its final consolidated, operating form.

Chapter 5 - Meso-scale mechanical performance assessment of the composite-metal joint using a higher fidelity approach.
A higher fidelity model is developed to assess the properties of the composite-metal joint with improved realism. The Multi-Filament (MF) method is used to predict realistic tow geometries and internal architectures for the joint region, with significant deformations induced in the fibre-tows due to their interactions with the pin-structured end-fittings. This information is then transferred to a joint mechanical model using a novel Single Filament Superposition (SFS) approach. Joint performance is compared against alternative joining methods.

Chapter 6 - A manufacturing concept for the novel hybrid composite-metal joint
An early stage, conceptual prototype of the hybrid strut is manufactured using a 4-axis filament winding machine. Unique winding patterns for the strut and joint, are constructed using the numerical programming language (G-code), in which tow pull-back occurs around the metallic

pins. Experimental procedure also allows for the verification of the tow geometries gained through use of the MF modelling method in chapter 5.

Chapter 7 - Conclusions

A summary of the work presented in this thesis is given. Conclusions regarding the feasibility and mechanical performance of the proposed hybrid composite metal joint are drawn. Possibilities for future development of the joining solution are also discussed.

CHAPTER 2

LITERATURE REVIEW

Current methods for joining composite materials are often limited to mechanical fastening (also referred to as bolting or riveting), adhesive bonding, or a combination of the two. These techniques have been the subject of extensive research, which has contributed to their prevalence across a number of industries, including automotive and aerospace. However, despite their established use, as reviewed here, the efficiency of such joints is typically limited when one of the joint substrates is a fibre-reinforced plastic (FRP) composite material. This is principally due to their high degree of anisotropy.

Several authors have proposed adapting both bolted, and adhesively bonded joints, to better account for composite material properties and behaviour. Such strategies, also reviewed here, typical involve improving stress distribution and out-of-plane properties in the region of the joint.

This thesis seeks to move beyond the consideration of joining as a secondary process. To realise the full potential for composite materials and composite-metal hybrid structures, joining should be considered in parallel with design and fabrication so that the fibre reinforcement can then be manipulated to initiate a direct mechanical interaction with the metal part. This offers potential to increase structural integration and improve load transfer capability.

Novel joining solutions that consider these objectives are consequently reviewed. In general, these joints firstly manufacture physical features to protrude from the surface of the metal. Fibre-tows are then placed, combined and inter-mingled with these metallic surface features during the layup of dry fabrics or pre-impregnated laminates, or using fabrication methods such as braiding. An interlocking and mechanical form-fit is then developed between the fibre-tows and the metal, with an adhesive bond being initiated by co-curing of the matrix during consolidation of the composite part. The advantages and limitations of these more innovative solutions are discussed. These analyses support the proposal of a composite-metal joining solution that is

examined in this thesis, and its application to the manufacture of the hybrid strut outlined in chapter 1.

2.1 Mechanical fastening

Mechanical fastening, or bolting, is a well-established joining method historically utilised in the construction of non-composite (metallic) structures. Mechanically fastened joints have obvious advantages in terms ease of production, replication and disassembly. Additionally, there is no pre-requisite for extensive surface preparation prior to coupling (unlike adhesive bonding, see section 2.2). However, the increased structural weight associated with the addition of the bolt (or rivet) may reduce the potential for a weight optimised joint.

Additionally, joint efficiency is typically significantly lower for composite materials. Stress concentrations develop in the proximity of the bolt-hole. Bolt-hole drilling is a damaging process [30], which causes discontinuities in the fibre reinforcement and resin degradation at the hole boundary. For composite laminates, delamination is induced [31] [32] leading to premature joint failure and reduction in fatigue life.

Literature to-date has focused on the development of analytical and numerical models to detail the complex stress distribution around the bolt hole, to allow for improved prediction of joint strength and failure behaviour. These are reviewed by Camanho and Matthews [33]. The complexity of the stress mechanics in the proximity of the bolt means that mechanically fastened joints for composite laminates can typically display several potential failure modes, as seen in figure 2.1.

Several authors have considered the influence of geometric parameters in determining joint strength and failure behaviour. Persson and Eriksson [34] conducted an experimental investigation into several factors affecting static and fatigue strength of multiple-row bolted composite laminates. A total of eight factors relating to hole quality, joint geometry (spacing, edge distances), material properties, laminate configuration, fastener type and environmental conditions, were studied and ranked in order of importance. In both static and fatigue testing, it was found that a high ratio of hole diameter to spacing width was the most significant positive factor. The fastener type, hole diameter to laminate thickness and clamp-up force were also important determinants of joint strength under static loading.

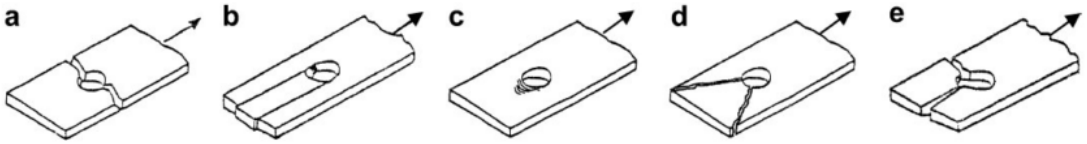

Figure 2.1: Typical modes of failure associated with bolted joints for FRP composite materials, (a) Net-tension (b) Shear-out (c) Bearing (d) Tear-out (e) cleavage [7].

In particular, bearing failure is a local compressive failure mode, occurring due to contact and frictional forces acting between the bolt-hole edge and the bolt, resulting in out-of-plane deformation. Composite materials typically display low bearing strength, damage is then observed as delamination, micro-buckling of the fibre reinforcement and matrix cracking [35].

As discussed in section 2.1.2, substituting plies for metal foils offers a technique for improving the bearing performance of bolted joints. Furthermore, as examined in section 2.1.1, the use of strain-relief inserts offers an effective method for re-distributing the stress concentrations in the region of the bolt.

2.1.1 Strain-Relief Inserts

Strain-relief inserts have been used to relieve stress concentrations in the region of the bolt-hole. A thin bushing of an isotropic material (usually metal) is bonded to the hole boundary. The localised reduction in anisotropy enables more effective redistribution of the stresses via the ductility and normal plasticity of the insert material.

Herrera-Franco and Cloud [36] conducted an experimental investigation into the use of inserts for bolted joints in cross-ply glass-epoxy composite laminates. An insert material was bonded to the bolt-hole boundary in double-shear lap joints. The use of aluminium inserts resulted in a 75% reduction of bearing stress in the bearing region and 90% decrease around the hole edge, against a reference case without inserts. Thereby reducing the possibility of shear-out failure.

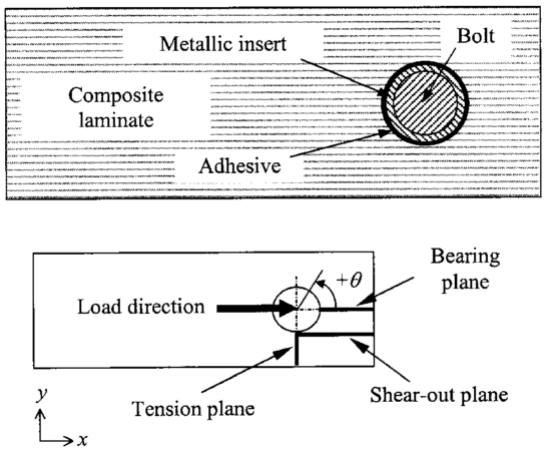

Figure 2.2: The use of strain relief inserts in a bolted joint for composite laminates [8], in order to reduce stress concentrations at the hold boundary.

Camanho and Matthews [8] used a combined numerical and experimental approach to study double shear-lap CFRP bolted joints in which different insert materials, of varying thickness's, were bonded to the bolt-hole boundary using an epoxy adhesive. It was concluded that thinner, more compliant insert materials produced the greatest improvements, with regards to reducing

stress concentration effects in the bearing and tension planes at the bolt-hole without developing higher tensile stresses in the adhesive.

2.1.2 Interleaving

Interleaving describes the process by which plies within composite laminates are substituted with metal sheets (or foils) in the bolt proximity. Local isotropy of the laminate is thereby increased, resulting in improved bearing resistance in the joint.

Kolesnikov *et al.* [9] used interleaving to locally reinforced carbon-fibre reinforced polymer (CFRP) plies with foils of the titanium alloy (Ti-6AL-4V), in single and 3-row bolted joint specimens. On-axis and 90° off-axis tensile loading was conducted up to the fracture point. Maximum joint strength improvements of 91%, at 23% titanium content, and 156%, for 54.5% titanium content, were achieved against the reference case of the unreinforced laminate; for the on-axis and off-axis loading respectively. Furthermore, the CFRP-titanium hybrid specimens achieved bearing capabilities similar to pure titanium alloy at a relatively low titanium content of 50%.

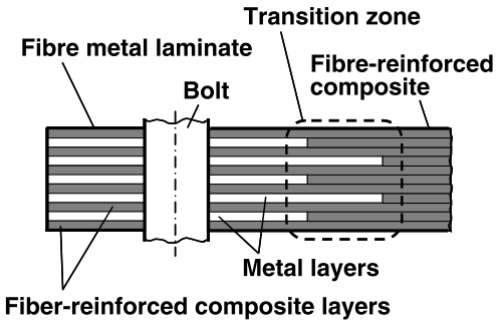

Figure 2.3: Schematic of bolted composite joint with interleaved metal layers [9], utilised to improve bearing properties.

Camanho *et al.* [37] conducted an experimental and numerical investigation into the mechanical response of bolted joints in hybridised titanium-CFRP laminates. It was concluded that significant improvements in bearing strength were experienced when plies were substituted for titanium sheets in the joint vicinity. Furthermore, the rate increase was found to be proportional to the level of titanium integration, with the specimen with the highest titanium content yielding a 158% increase in bearing strength, compared to an unaltered CFRP laminate.

2.2 Adhesive Bonding

As with mechanical fastening, adhesive bonding is also a well-established joining method. It describes the means by which separate components, or adherends, are joined by the addition of a substance (adhesive) that promotes surface attachment. An adhesively bonded joint typically

displays five possible modes of failure: adhesive, cohesive, interlaminar, tensile and transverse (figure 2.4). Cohesive failure results from delamination at the adhesive-adherend interface, where as adhesive failure is delamination of adhesive itself. The remaining three modes are failure in the adherends themselves.

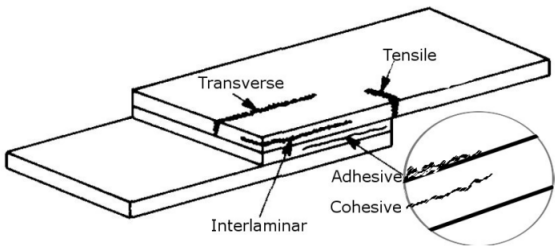

Figure 2.4: Failure modes of adhesively bonded joints [7].

In general, adhesive joints do not display the stress concentrations observed in mechanically fastened joints as load transfer between adherends is distributed over larger joining areas, reducing the negative influence of the composite material's low bearing properties. Furthermore, unlike bolted joints, the adherend is undamaged by the bonding process and negligible increase in structural weight occurs through addition of the adhesive.

Bond strength has been found to be dependant on several factors including the level of surface preparation [38], joint configuration, choice of adhesive and environmental conditions [39]. Adhesive lap-joints for composite materials have been extensively researched from an experimental perspective and in terms of both analytical and numerical models, a review of which can be found in [40] and [41].

Other disadvantages are apparent in the fact that failure modes that initiate at the bondline, such as cohesive and adhesive failure, are difficult to inspect visually. The lack of ability to inspect the integrity of a joint and ensure a good bond is one of the major reasons that adhesives are not more commonly used in aerospace structures.

Additionally, degradation of the adhesive surface due to oxidation/atmospheric pollution can significantly reduce bond strength, even for minimal exposure times (2/3 hours) [42]. Consequently, high scatter in joint strength is typically observed, reducing reliability. For composite laminates, adhesively bonded joints can introduce high out of shear and peel stresses [43], resulting in sudden, premature joint failure via cohesive and/or adhesive mechanisms. As examined in section 2.2.1, through-thickness reinforcement (TTR) techniques can be used to improve delamination resistance in adhesively bonded joints for composite materials.

2.2.1 Through-thickness reinforcement

Delamination resistance, impact tolerance and through-thickness stiffness of adhesively bonded composite joints may be improved through the use of through-thickness reinforcement (TTR)

techniques. These include stitching, tufting [44] and z-pinning [45]. These methods operate under the principle of shielding delamination crack propagation through a phenomenon known as the "bridging effect"; by which the crack driving force is reduced and delamination inhibited [46]. Ultimate joint failure load can consequently be increased with final failure typically being categorised into Mode-I, Mode-II or mixed-mode types. Mode-I occurs via sliding or tensile pull-out of the reinforcement perpendicular to the joint plane. Mode-II is caused by deflection or breakage of the reinforcement due to shear-forces in the joint plane.

TTR techniques require a needle to be driven into (or through) the joining laminates, as such, they would not be appropriate for use in hybrid composite-metal joints as the presence of the metal would prevent such a process occurring. However, as described in section 2.4, the mechanism by which delamination resistance and joint strength is increased is similar to that provided by surface-structured composite-metal joints.

2.3 Bolted-bonded

Bolted-bonded joints simultaneously utilise both mechanical fastening and adhesive bonding. Such joints may offer a fail-safe mechanism, whereby load transfer occurs via the bolt(s) following adhesive failure. Examples in literature may refer to bolted-bonded solutions as "hybrid" joints, in the respect that they use a combination of two joining techniques that can be employed independently. However, this work refrains from describing bolted/bonded joints as hybrids, in order to avoid confusion with the use of the term to characterise a joint between a composite and non-composite (metallic) component.

Early works by Hart-Smith [47] found that load transfer in bolted-bonded joints occurred mainly via the adhesive, with the passivity of the bolt offering no significant improvement to joint strength and efficiency over a simple bonded mechanism. Instead, it was found that the unloaded bolt contributed to arresting crack propagation caused by adhesive failure; thus improving fatigue life when compared to adhesively bonded joints.

However, Kelly [48], [49] conducted a combined numerical and experimental investigation into single-lap bolted-bonded joints, to determine the effects of geometrical and material properties on load distribution in the joint. In addition to increases in joint strength in the range of 11-22% against a reference case of a bonded-only joint, it was found that joint configurations could be designed in which bolt loading increased by 35%. Parameters such as adherend thickness and overlap length were determined to be critical in determining the degree of bolt loading.

2.3.1 Co-cured/bolted-bonded joints

Several authors have offered improvements to bolted-bonded joints by promoting adhesion between the components using the excess resin in the FRP composite, rather than through the application of a separate adhesive. This is referred to as "co-curing", and has immediate benefits

in terms of the reducing the time and manufacturing costs associated with the necessity of having separate cure cycles (for the resin and adhesive) and determining material-compatible adhesives.

This technique may also allow the bolts to be inserted into dry-fibre fabrics or weaves. The absence of the resin allows the fibres to move following bolt insertion, causing localised undulation of fibres around the bolt, as shown in figure 2.5. The requirement for bolt-hole drilling is removed, resulting in a more "fibre-friendly" joint in which damage to the fibre reinforcement is eliminated. Stress concentrations in the region of the bolt-hole are reduced and sealing performance is improved.

Unlike the previous joining solutions discussed, this method moves towards consideration of joining as a primary process, (in which composite fabrication and joining are achieved simultaneously), as the composite part is only consolidated after the joint has been established.

Matsuzaki *et al.* [10] conducted an experimental investigation into the static and fatigue strength of bolted/co-cured GFRP-Aluminium single lap joints. Two pairs of steel bolts were inserted into the nets of a glass fibre knit fabric, prior to impregnation with epoxy resin. Static and fatigue tensile lap-shear tests were conducted, with results being compared against bolted only and co-cured (adhesive) only specimens.

The static tests found the bolted/co-cured joint exhibited an improvement of 1.84 times greater maximum shear strength against the co-cured joint, with only a quarter of the scatter. In the bolted/co-cured joint, crack propagation was arrested by the bolts through a similar bridging mechanism to that provided by TTR techniques. Adhesive failure was observed prior to joint failure, after which point load transfer was maintained by the bolt and the bolted/co-cured joints behaved analogously to the bolted specimens, with similar maximum tensile shear strength. The bolted/co-cured joints also displayed significantly greater fatigue strength (increase by a factor of approximately 15) against the bolted-only joint. This was due to the absence of damages and reduced stress concentrations in the bolted/co-cured joint attributable to the lack of bolt-hole drilling.

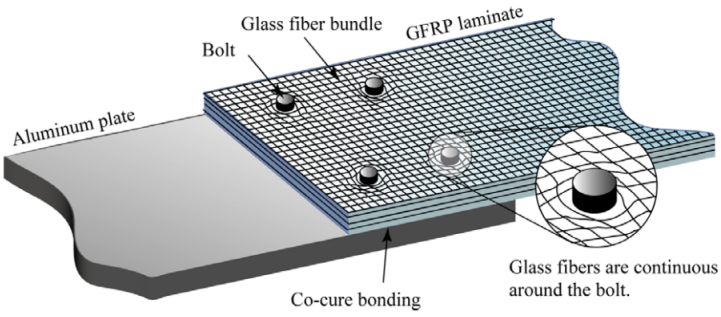

Figure 2.5: Illustration of the "fibre-friendly" bolted/co-cured approach utilised by Matsuzaki *et al.* [10], for the case of GFRP-Aluminium single lap joints. The localised undulation of the fibre reinforcement around the bolt is highlighted.

2.4 Surface-structured joints

Surface sculpting, or structuring, describes the process by which physical features are manufactured to project from the surface of the metal, in a composite-metal hybrid joint. Dry-fibre fabrics, or weaves, can then be pressed and integrated onto these features, prior to resin infiltration and consolidation. As with the "fibre-friendly" bolted/co-cured method discussed in section 2.3, the joining mechanism can be considered as a combination of mechanical fastening, via the form-fit and interlocking between the fibre-tows and the metallic surface features, and an adhesive bond provided by co-curing of the matrix.

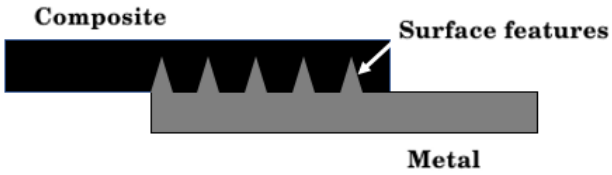

Figure 2.6: Illustration of a composite-metal surface structured (single-lap) joint.

A distinction lies in the fact that surface-structuring does not require the introduction of a separate joining structure, such as a bolt or rivet, which can add considerable parasitic weight. Instead joining material is manufactured directly from the metal's surface.

Additionally, as reviewed by Messler [50], surface-structuring is an example of composite-metal joint enacted via a micro-mechanical interlock. Here, the metallic features used to interact with the composite material's fibre reinforcement are of a smaller dimensional scale, when compared to macro-means such as bolts and rivets. As discussed here, this gives scope for structural adaptation via employment of a potentially large number of these features in complex arrays on the surface of the metal parent; in addition to the possibility of tailoring the geometric shape of the features themselves.

These metallic surface features are commonly referred to as "proggles" or "pins". Methods used for their manufacture include Additive Layer Manufacturing (ALM or 3D-Printing), Selective Laser Melting (SLM) [51] [52], The Welding Institute (TWI) developed Electron Beam Surfi-Sculpt^{TM} (EBS) technology [53] and Cold Metal Transfer (CMT) [54].

Nguyen *et al.* [55] used SLM to manufacture grooves or dimples onto the surface of a titanium substrate prior to integration with CFRP via co-cure adhesion, for Double Cantilever Beam (DCB) Mode-I crack-growth specimens. Inter-facial strength and fracture toughness was increased against bonded-only specimens (without surface structuring), as the roughness of the SLM surface provided increased contact area and an improved interlocking of the adhesive and adherend. No significant conclusions were made regarding the relative performance of the surface features based on their geometric shapes (i.e. dimples vs grooves).

Ucsnik *et al.* [11] conducted an experimental investigation into the effect of pin shape on joint strength, energy absorption capacity and failure behaviour for the case of surface-structured

CFRP-steel double lap shear joints. CMT was used to manufacture 7x5 pin arrays onto the top and bottom surfaces of the metallic substrate. Layers of biaxial non-crimp fabric (NCF) were then massaged and brushed onto and around the pins prior to infusion with RTM6 (Hexcel) resin and subsequent co-curing. Tensile-shear tests were then conducted for cylindrical and ball-head shaped pins, as seen in figure 2.7. A reference joint established only via co-cure adhesion, i.e. with no modification of the metal's surface, was also tested for comparison purposes.

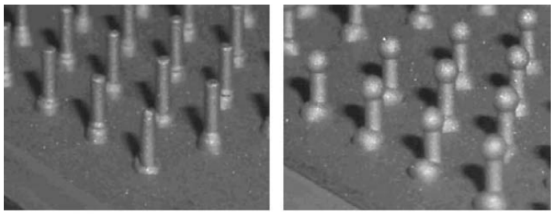

Figure 2.7: Cylindrical and ball-shaped pins manufactured using CMT by Ucsnik *et al.* [11].

Local strains at the maximum force were increased by factors of 4.7 (at 1.22%) and 10 (at 2.6%) for the cylindrical and ball-head shaped pin joints, respectively. A greater degree of elongation was observed against the reference joint as following adhesive failure load transfer was sustained by the pins with final failure occurring with bending and shear-off of the cylindrical and ball-head shaped pins, respectively, and local deflection and micro-cracking in the composite.

Furthermore, shear strength was increased by 11% and 52% for the structured joints using cylindrical and ball-head shaped pins, respectively, against the reference joint. Similarly, energy absorption increased by a factor of 28 and 30. The authors conjectured that superior performance of the ball-head shaped pins was attributable to the undercuts around the pin tip. These provide an improved form fit between the pins and the composite's fibre reinforcement, preventing deflection and delamination in the joint region via a similar bridging mechanism to that provide by TTR techniques.

Bianchi [7] conducted a detailed investigation into the bridging forces provided by metal pins in surface-structured/co-cured composite-metal joints. FE models were constructed to simulate Mode-I tensile-pullout and Mode-II shear loading of a single spike-shape metallic pin, as shown in figures 2.8(a) and 2.8(b), respectively. The metal pins were modelled similarly to carbon-fibre Z-pins [45] utilised in the TTR of joints between composite laminates, with appropriate adjustment of the pin's material properties. Model results were validated using experimental procedure.

Mode-I bridging performance was found to predominately depend on friction between the pin and the surrounding laminate, with frictional forces due the thermal compressive stress exerted by the neighbouring matrix material following laminate curing. Consequently, the author conjectured that this mechanism can thereby be improved by the manufacture stage, through optimisation of the co-cure process. Mode-II bridging capability was characterised by bending deformation in the pin, ploughing into the laminate and pin shear-off, as delamination was

inhibited. Pin strength and bridging performance was found to be highly influenced by pin aspect ratio and shape.

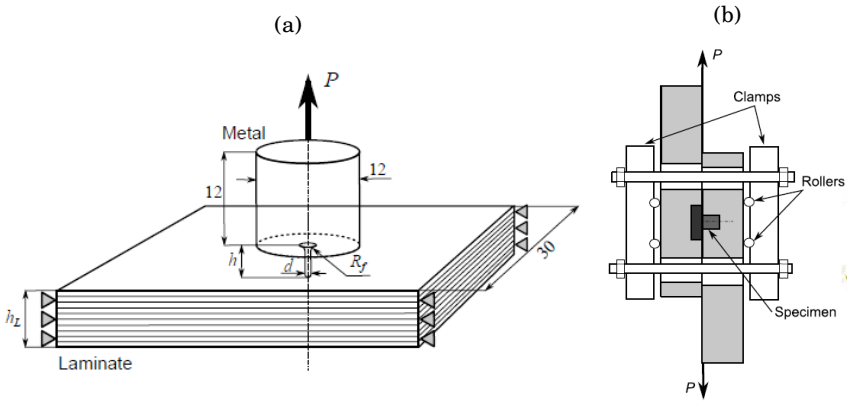

Figure 2.8: Schematics for the (a) Mode-I single-pin pull-out test and (b) Mode-II single-pin shear test, used in Bianchi [7].

FE methods were also developed to predict the performance and failure behaviour of full surface-structured/co-cured composite-metal double-lap joints using a 5 by 7 array of spiked-shaped pins. Experimental methods were utilised for model validation with the pins constructed using CMT technology. Pin bridging effect were found to initiate when the delamination crack reached the first pin row, after which point crack propagation was retarded, increasing joint failure load against an adhesive-only reference joint.

Geometric parameters such as pin density were also considered, with configurations consisting of 2, 4 and 7 pin rows (for a total of 10, 20 and 35 pins in each case), being examined. Joint strength was found to increase with number of pins, although pin rows further from the joint run-out were predicted to provide reduce bridging capability. Load recovery after adhesive failure was found to be solely dependant upon the load carrying capability offered by the pins. A higher number of pins was therefore predicted to be advantageous, although the author noted that increasing pin density may promote failure modes not included in the modelling framework, such as tensile failure of the laminate.

Xiong *et al.* [12] examined the effect of composite orientation in Surfi-Sculpt^{TM} single lap-shear joints between carbon-fibre woven prepreg and Ti-6Al-4V. Integration between the composite and metal was achieved by pressing the metallic pins into the prepreg material using the pressure provided by a vaccuum bag. Axial plies were substituted for ±45° plies in varying amounts so that the laminate's volume content of ±45° plies increased from 11.1-88.9%.

All surface-structured joints showed an increase in ultimate failure load against a reference joint without surface-structuring (adhesive only), with the maximum increase being 129%. Damage in the reference joint was categorised by rapid, catastrophic bond-line delamination. In contrast, damage for the structured joints varied between matrix crushing and compressive

failure of the composite for relatively low ±45° ply volume content; to bending and shear-off of the structured metal features without significant damage being initiated in the composite, as the number of ±45° plies was increased. This resulted in increases of elongation and energy absorption capacity for the structured joints with greater ±45° content, of 900% and 257%, respectively. No conclusions were made with regards to the mechanism that caused variation between laminate configurations, although it could be conjectured that the stiffness alteration of the composite may have been a factor. Also, the ±45 fibre directions may have resulted in an improved form fit around the metallic surface structures.

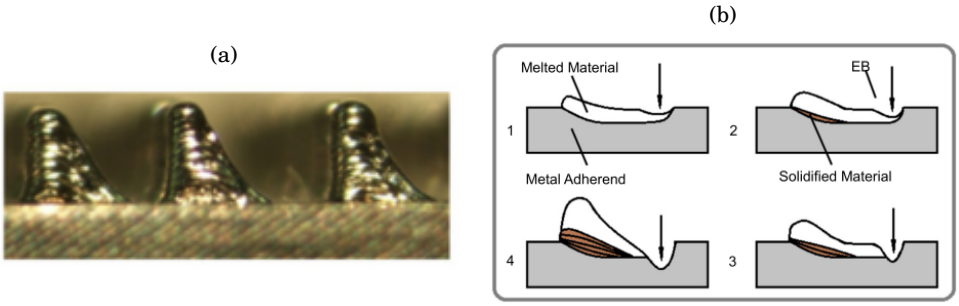

Figure 2.9: (a) Metallic surface protrusions manufactured using EBS. (b) An illustration of the manufacture process. [12]

2.4.1 Braided/surface-structured joints

The review of literature conducted thus far has focused on "planar" joints, few authors have attempted to study composite-metal joints for tubular structures similar to the hybrid strut examined in this work. However, braiding technologies has been utilised in the manufacture of tubular composite struts and drive shafts for rail and automotive applications. Challenges arise in effectively integrating the ends of the composite braid to the metallic yokes, end-caps or fittings, which connect the shaft to the torque actuator. For this, adhesive bonding is commonly used.

Investigations by Cinar *et al.* [56] found that failure in braided CFRP-metal drive shafts occurs with adhesive failure at the composite-metal interface prior to ply failure in the CFRP. The braided shaft displayed higher torsional stiffness against a fully metallic equivalent, but did not achieve the required torque value (3500Nm for passenger car drive-shafts) due to premature failure at the joint. Profiling of the metallic end-fittings was considered by Gude *et al.* [57] and Kim *et al.* [58] to improve the form-fit between the composite and metallic end-fittings in order to increase bond strength. However, this still relies upon a secondary joining mechanism using adhesive bonding after composite manufacture, and therefore the same limitations are apparent as with planar composite-metal adhesive joints examined in section 2.2.

Although current literature on the subject of braided/surface-structured joints is limited, surface-structuring offers the potential for improving coupling at such braid-metal interfaces. The braid can be continued over surface-structured metal end-fittings in order to initiate a mechanical form fit directly from the fabrication process. Co-curing of the matrix during consolidation then provides an adhesive bond, as with similar planar surface-structure/co-cured joint mechanisms.

This method has been utilised by TEUFELBERGER Ges.m.b.H [59] and its patented T-IGEL® connection technology, to integrate a braided composites with pin-structured metallic bodies, for applications including hybrid tubular drive shafts.

Sun *et al.* [6] developed a numerical tool to simulate the braiding of carbon-fibre over arrays of pentahedral-shaped pins distributed on tubular end-fittings. This allowed for the prediction of common manufacturing defects such as yarn twisting and puncturing (or splitting), and local misalignment in the braid angle. These occur due to interactions between the braid yarns, and the yarns and the braid ring, during the manufacture process, which cause variations in yarn positioning relative to the pins.

Defect position and frequency was found to correlate well with experimental trials. Pin density and arrangement (although pin shape was not examined) was determined to be critical with regards to the number of defects induced. However, defects occurred in all cases, in both the numerical simulations and physical reality, indicating a limitation in the application of braiding to establish the joining mechanism. Furthermore, once initiated, yarn puncture was found to propagate across the pins as the initial alteration of the intended yarn path (braid angle) remained uncorrected throughout fabrication.

Although the effect of such manufacturing defects on the mechanical properties of the joint was not examined, it can be conjectured that such defects may cause breakage of the fibre reinforcement and strength degradation in the composite part, potentially reducing the hybrid structure's performance capability.

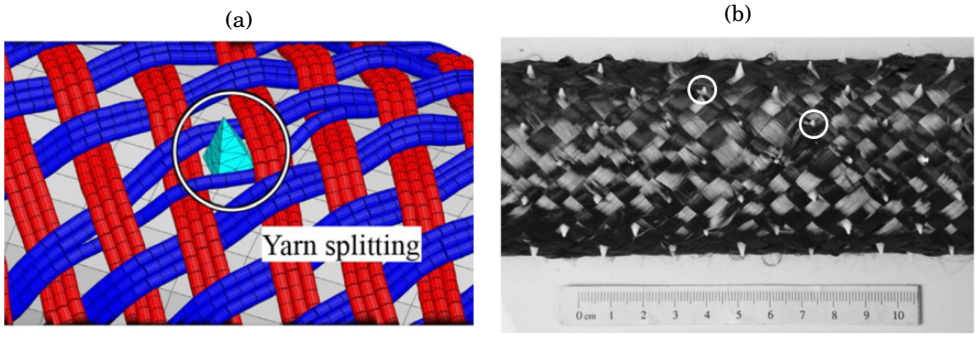

Figure 2.10: Yarn puncturing occurring in the (a) numerical model and (b) experimental procedure, during the braiding of fibre-reinforcement over pentahedral-shaped structured surface features [6].

2.5 Note on modelling methodologies

Modelling techniques used in this thesis to study the hybrid composite-metal joint and strut, have been adapted from the field of textile composite modelling. Research in this area is vast, and its content is, in general, beyond the scope of this thesis. For this reason, literature from this field is reviewed on an on-going basis as it is used in the work.

2.6 Summary

Conventional joining techniques, such as mechanical fastening, adhesive bonding, or combination of the two (bolted-bonded), typically display low efficiency when applied to composite materials. Methods such as the use of strain relief inserts or through-thickness reinforcement techniques, may offer improvements. However, these still consider joining as a secondary process, implemented after manufacture of the composite part. To increase coupling efficiency and structural integration, the fabrication and joining of composite materials should be undertaken simultaneously.

Co-cured/bolted-bonded approaches offer one such solution. Fasteners are inserted into dry composite fabrics and weaves prior to consolidation. In the absence of matrix, the fibre-reinforcement is free to move around the bolts, removing the requirement for damaging bolt-hole drilling. The joining mechanism is provided by a combination of a mechanical interaction due to the interlocking of the fibres around the bolt, and an adhesive bond initiated via the co-curing of the matrix. Improvements in joint strength and fatigue life were observed over joints using only bolting or adhesion.

Although promising, co-cured/bolted-bonded joints require the addition of the fasteners or bolts. This can add considerable parasitic weight to the structure, reducing the potential for a fully weight optimised solution.

Surface-structured joints do not have this limitation as joining material for the interlocking of the metal and fibre reinforcement can be fabricated directly from the surface of the metal. Additionally, as examined in this literature review, consideration of the geometric shape and distribution of these metallic surface features, or pins, allows for the possibility of improved structural tailoring.

Surface-structured joints and braiding technology have been combined in the manufacture of tubular, hybrid composite-metal struts and shafts. Although this may offer improvements against conventional adhesively bonded joints, defects arise during fabrication. Namely, reduced control of the path of the braid yarn due to complex inter-yarn interactions and contacts between the yarns and the braid ring may lead to yarn deflection, puncturing and fibre breakage.

Consequently, this work considers the use of filament winding to manufacture a similar hybrid strut. In filament winding, each tow is laid up individually and sequentially, improving precision and thereby reducing the likelihood of such manufacturing defects occurring.

Additionally, in a braided surface-structured joint, the mechanical bond relies upon the shear-locking of adjacent (non-axial) yarns around the metallic pins. In comparison, the fibre-tows can be reversed (pull-back) directly around the pins during the filament winding process. This provides a more direct and robust connection, which may improve the load transfer capability of the joint.

Finally, braiding also results in significant out-of-plane movement of the yarns (crimp) due to their relative positions in an undulating path. In filament winding, the tows can be laid flat to the mandrel's surface, resulting in significantly less crimping and improved alignment with the strut's loading direction (axial tension and compression). This offers the potential for improved structural properties.

CHAPTER 3

STRUT AND JOINT DESIGN

This chapter firstly introduces a novel composite-metal joining solution, for application to the manufacture of hybrid tubular struts or drive-shafts. The joint, occurring at the strut ends, is initiated via the filament winding of carbon-fibre tows around structured metallic surface features (pins).

Design parameters of the strut and joint are then considered. The layup sequence for the central part of the strut, which consists only of composite material, is firstly examined. Unique winding patterns are proposed for the theoretical manufacture of the hybrid composite-metal strut and joint. In order to avoid tow puncturing, neighbouring tows must be offset relative to each other by the separation distance between adjacent pins. This causes non-uniform coverage of the strut's central mandrel. For a strut loaded in tension and compression, maximum axial properties (stiffness and strength) are desirable, however, the effect of non-uniform tow content must be assessed, as large resin rich areas may constitute structural weak points. Analytical and numerical methods are adopted to study the effect of tow orientation angles and layup sequence on the mandrel, for a feasible range of layup sequences.

The properties of the hybrid strut will also be highly dependant upon the efficiency of the composite-metal joint. The tow's trajectory in the region of the metallic pins and the manner in which the tow's direction is reversed (pull-back) around the pins, may affect joint load transfer capability and strength. A number of practical joint configurations are examined using an analytical framework, in which the mechanical interaction between the fibre-tows and metallic pins is considered using a simple belt-and-pulley analogy.

These combined analyses provide a preliminary relative performance ranking of the possible strut and joint configurations. Five designs are continued through to assessment using Finite Element Methods (FEM) in chapters 4.

3.1 Strut and joint geometries

The initial structure prior to the filament winding process consists of a cylindrical "connector tube" spanning two surface-structured metallic end-fittings, as shown in figure 3.1(a). This "connector tube" provides a contact surface for the fibre-tows during fabrication, after which, it can either be removed or retained as a permanent part of the structure, possibly to improve strut properties under compression (this is briefly examined in section 4.8).

This initial structure would behave analogously to a conventional mandrel during the filament winding process. That is, this full structure would rotate about its longitudinal axis. However, for convenience, throughout this discourse only the cylindrical connector tube is referred to as the "mandrel".

The two metallic end-fittings would then be joined via the mechanical form fit provided by the filament winding of carbon-fibre tows around the metallic pins. An example of this is shown in figure 3.1(b). Finally, following matrix infiltration and consolidation the structure would appear as seen in figures 3.1(c) and 3.1(d). Carbon-fibre reinforced epoxy composite material would consequently span the full length of the strut, covering the pin-structured metallic end-fittings. However, the central part of the strut, overlaying the cylindrical connector tube, would consist of only composite material.

Each tow is reversed around a pin (or multiple pins), during a process referred to as "pull-back", as seen in figure 3.2. This provides a robust connection between the metal and fibre-tow directly from fabrication, which may improve structural integration, load carrying capability, strength and stiffness in the joint; as the high tensile strength of the fibre reinforcement is transferred directly into the joining mechanism. Initiation of pull-back in this way, may be considered unique to this work. As discussed in section 1.2, conventional filament winding typically utilises demi-spherical or domed-shaped end-caps to reverse the tow direction.

3.1.1 End-fittings and mandrel

The metallic end-fittings are tubular structures, with height H, outer radius ρ and wall thickness w, as illustrated in figure 3.3. The mandrel is also tubular in shape, with length L and equal outer radius. The cross section plane of the end-fittings and mandrel is the $x-z$ plane. The circumferential direction and angle are denoted by c and ϕ, respectively, with $\phi = 0$ at the positive x-axis.

3.1.2 Metallic pins and their distribution

In practice, pin shape and uniformity may depend upon the manufacturing technique employed, as discussed section 2.4. However, in this work the pins are assumed to be perfectly uniform and cylindrical in shape, with length, L_p and cross-sectional diameter, D_p. Cylindrical shaped pins are preferred as they provide a smooth contact surface for the fibre-tows. Pin shapes with sharp

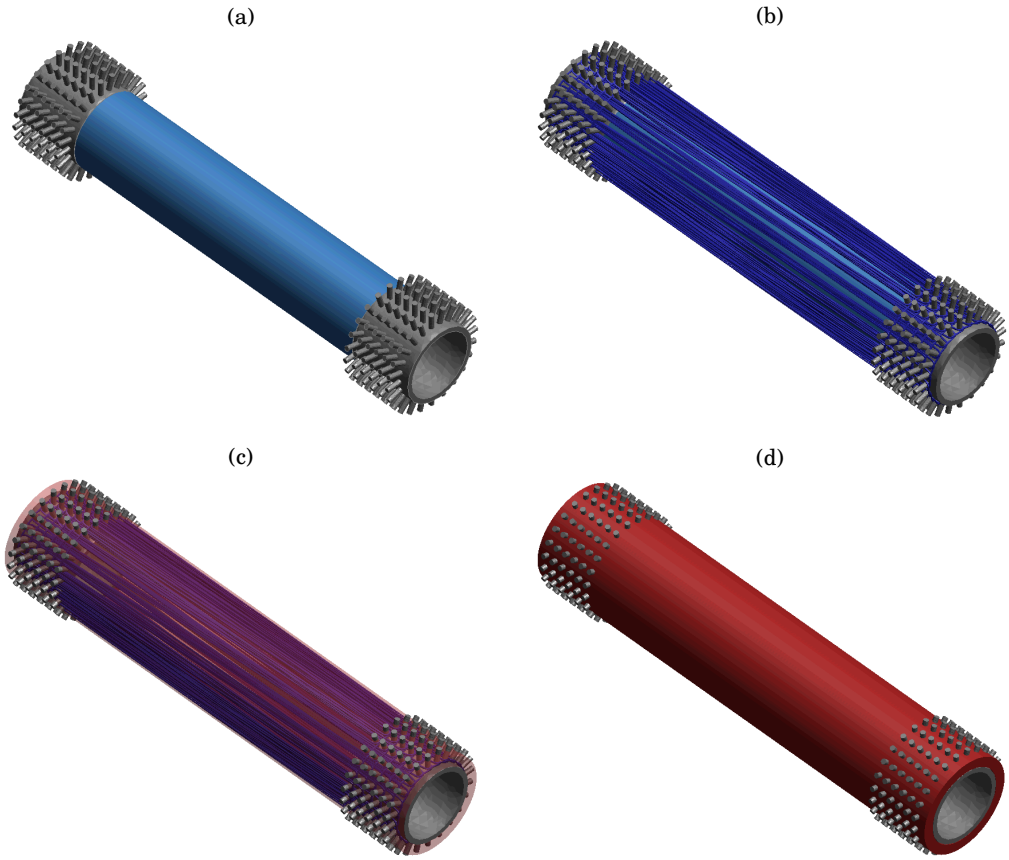

Figure 3.1: (a) Initial structure prior to fabrication, consisting of two pin-structured metallic end-fittings (grey) located at the ends of a tubular mandrel (light blue). (b) Structure after the filament winding process, carbon-fibre tows (dark blue) span the length of the structure, connecting the two end-fittings due to pull-back being initiated around the pins. (c) and (d) show the final consolidated component, including matrix material (red), which is made partially transparent in (c) so that the internal path of the fibre-tows can be seen. See chapter 4 regarding the construction of these models.

edges may cause undesirable effects, such as stress concentrations and fibre breakage in the tow, during the filament winding process.

To characterise the pin arrangement, or array, pins distributed around the end-fitting's circumference are referred to as pin "rows". The array would then consist of several rows of pins spanning the end-fitting's surface. Separation distances between pins in the array, in the circumferential and surface directions, are denoted by $\overline{\delta_c}$ and $\overline{\delta_s}$, respectively. The pin array is assumed to have either a "square" or "diamond" type distribution. A two-dimensional schematic of these pin arrangements is given in figure 3.4. Three-dimensional equivalents are shown in figure 3.5.

In order to avoid manufacturing defects, such as tow puncturing (which was found to occur in similar braided mechanisms, as discussed in section 2.4.1), during their placement, neighbouring

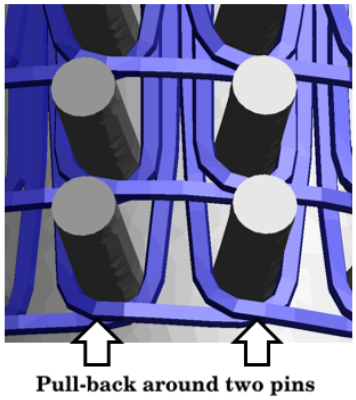

Figure 3.2: Model of the joining mechanism provided by reversing the tow (blue) direction, referred to as "pull-back", around two metallic pins (grey). (See chapter 4 for information regarding the model's construction).

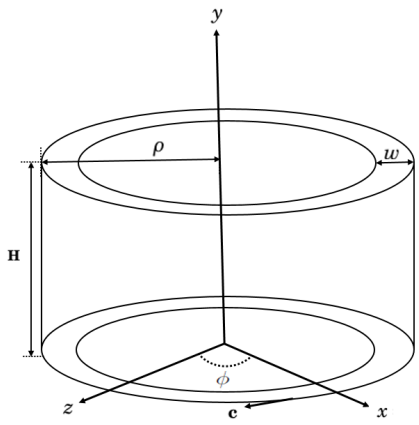

Figure 3.3: 3D diagram of a tubular end-fitting, with axes labelled.

tows must be offset relative to each other by the distance equal to the circumferential spacing between the pins. Defects may still be induced if spacing between the pins does not sufficiently exceed the tow diameter, and some imprecise in regards to tow placement around the pins occurs during the filament winding process.

Therefore, a maximum degree of pin density is established through specification of a minimum separation distance (δ_{min}) between pins in the array, in both directions c and s. Experimental work in chapter 6 uses a T-300 12k carbon fibre tows (supplied by Toray Industries Inc) carbon-fibre tow with an approximate cross-sectional width of 2mm. Consequently, a minimum pin spacing of 3mm is used. The difference, equivalent to 0.5mm at either side of the tow, provides a reasonable margin of error for tow placement without puncturing, whilst also not greatly reducing the total fibre volume content on the structure, due to overly large separation distances between adjacent tows, (non-uniform fibre coverage of the mandrel is examined in sections 3.4-3.7).

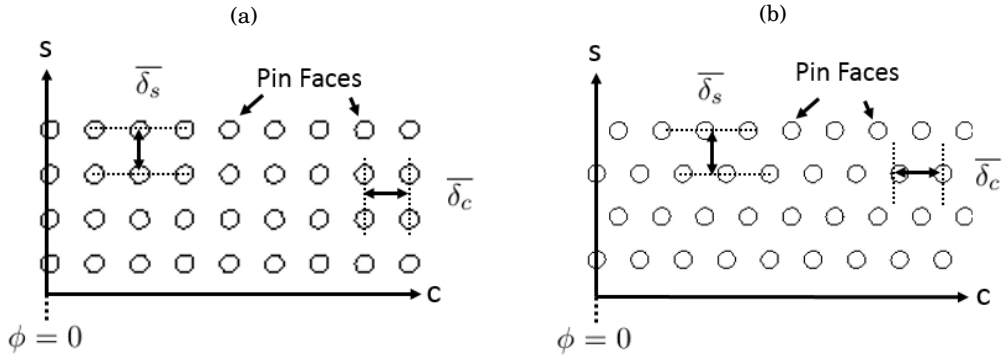

Figure 3.4: (a) Square type pin array. (b) Diamond type pin array. The abscissa and ordinate are equal to the end-fittings circumferential direction, c, and surface direction, s, respectively.

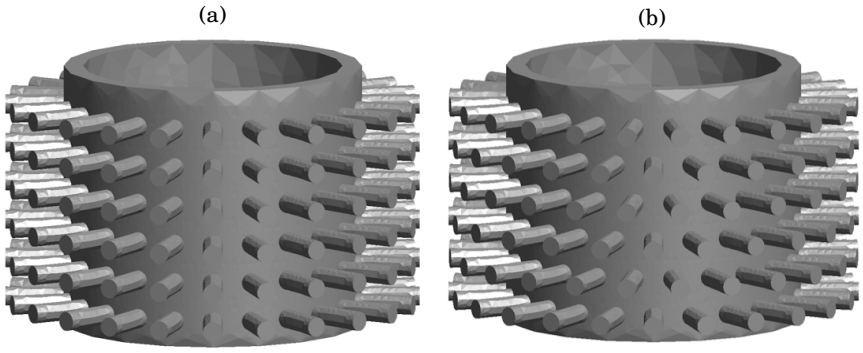

Figure 3.5: Tubular end-fittings with (a) square and (b) diamond type pin distributions.

Pin diameter and spacing will alter the effective turning radius that the fibre-tows undergo during pull-back. A relatively small turning radius, attributable to dense pin arrays with relatively small pins, may cause stress concentrations and possible micro-scale damage in the tows. This effect is not examined here, but is considered further in section 7.3. Instead, as discussed, the focus of the a-priori determination of a reasonable minimum degree of pin spacing is to prevent the occurance manufacturing defects such as tow puncturing, whilst maintaining a sufficient degree of tow coverage on the structure. That is, increased pin spacing will reduce the turning radius of the tows at pull-back but will result in poor tow converage of the strut and the strut's central mandrel. With regards to pin diameter, equal pin size is used from previous works on similar braided composite-metal joints, (as highlighted in section 3.2.2) so that their relative properties can be compared in section 5.9.

3.2 Design aims and performance requirements

Two main design aims are considered for this work. Firstly, the novel hybrid composite-metal joint should offer improved strength and load carrying capability over current joining technologies. To

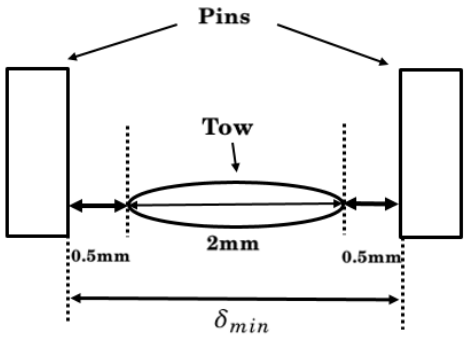

Figure 3.6: Diagram of minimum pin spacing. Condition is established to prevent tow puncturing.

establish this, comparison is made with an adhesively bonded joint, which serves as a reference case (section 3.2.1). Joint performance is also assessed against a similar joining mechanism using braiding technologies in section 3.2.2.

Secondly, the hybrid structure should offer weight saving benefits when compared to a fully metallic structure, and be offer comparable strength and stiffness, in order to justify the inclusion of composite materials in the design. Within these objectives, it is necessary to obtain joint configurations which maximise the strut's mechanical performance potential.

3.2.1 Adhesive joint

Minimum performance criteria is established against an adhesively bonded joint, this is compared against the hybrid composite-metal joint in section 5.9.3. No attempt is made to optimise the strength of the adhesive joint. Instead, where possible, parameters are maintained from the hybrid composite-metal joint in order to provide a fair comparison.

Adhesive joint strength is assessed using an analytical model. Actual joint formulation is not considered specifically for the tubular strut examined in this work. Joint analysis is instead simplified to a single lap-shear joint (figure 3.7), due to wide availability of analytical models to characterise stress analysis and failure criteria in such bonded joints [60], [61].

Volkersen's method [2] is used. This assumes that the adhesive deforms only in shear, and the adherends only in tension. Realistic non-uniform stress distribution in the adhesive is accounted for in the model, with maximum stresses at overlap ends. However, effects such as adherend bending, due to the eccentricity of the load path, are not considered. This should not offer significant limitations as bending moments are likely to be constrained in a cylindrical bonded joint.

The shear stress distribution in the adhesive ($\tau(x)$) is given by equation 3.1, where the x origin is the centre of the adhesive. E_i, t_i, for $i = u, l$ denote the moduli and thickness of the upper and lower adherend, respectively. Similarly, G_a and t_a denote the adhesive shear modulus and thickness, respectively. c denotes half of the overlap length ($l/2$), P the applied load, and ω

the stiffness ratio. Maximum adhesive shear stress, ($\tau_{\max}$) is given by equation 3.2, and occurs where $x = \pm c$.

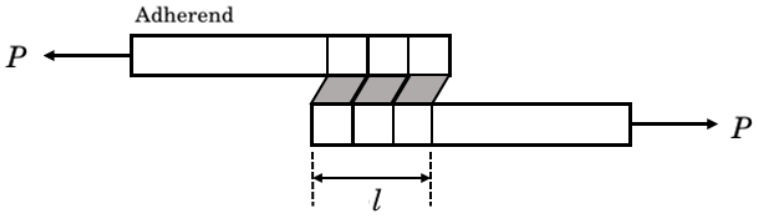

Figure 3.7: Single lap joint with sheared adhesive (grey).

$$\tau(x) = \frac{\omega P}{4}\left[\frac{\cosh(\omega x)}{\sinh(\omega c)} - \left(\frac{E_l t_l - 2E_u t_u}{E_l t_l + 2E_u t_u}\right)\frac{\sinh(\omega x)}{\cosh(\omega c)}\right]$$
$$\omega^2 = \frac{G_a}{t_a}\left(\frac{1}{E_u t_u} + \frac{2}{E_l t_l}\right) \tag{3.1}$$

$$\tau_{\max} = \frac{\omega P}{4\tanh(\omega c)}\left[1 - \left(\frac{E_l t_l - 2E_u t_u}{E_l t_l + 2E_u t_u}\right)\tanh^2(\omega c)\right] \tag{3.2}$$

In this work, an overlap length of 5% of the full mandrel length is assumed. Araldite® 2015 [62] epoxy adhesive (aerospace grade compatible with both metals and FRPs) is used. This has a shear modulus (G_a) of 0.9GPa and an approximate shear strength of 20 MPa at room temperature. Composite thickness is used for t_l, with the wall thickness of the metal end-fitting for t_u. An adhesive thickness (t_a) is considered to be 0.075mm, (median of 0.05-0.10mm recommended range).

3.2.2 Braided pin-structured joint

A similar joining mechanism using braiding technologies to manufacture hybrid composite-metal drive shafts, is used as a comparator. The number of manufacturing defects (such as tow puncturing), and defect severity, is compared in chapter 6 against that observed for the braided joint in [6]. Parameters for the end-fittings, such as the outer surface radii, (ρ), of 23mm, and wall thickness of 3mm, are maintained from [6].

However, the end-fitting's height is reduced to 40mm (from 150mm), and pin spacing is reduced to the established feasible minimum of 3mm (from 16mm). This results in an increased degree of pin density for the filament wound joint, with the pin array consisting of 6 rows of pins spanning the end-fitting's surface, and each row containing 24 pins (although the total number of pins is comparable, with 117 for the braided joint). The effect of pin shape is ignored (pentahedral-shaped pins were used in [6]). The total length of the drive shaft was not provided,

here an arbitrary strut length of 280mm is used for the strut (including end-fittings), with a mandrel length of 200mm.

The higher degree of pin density for the filament wound joint should promote the occurrence of manufacturing defects such as tow puncturing. However, as reviewed in section 2.5, it is hypothesized that defect occurrence is more likely for the braided joint due to the more complex interactions between the braid-yarns and braiding ring during fabrication. These may cause significant deviation from the intended yarn path or braid angle. Greater control, with regards to tow positioning, may be possible using filament winding as each fibre-tow is placed individually and sequentially.

As no assessment was made with regards to the mechanical performance of the braided joint in [6], a comparable mechanical model is constructed in section 5.9.2 and subjected to the same virtual testing scenario as the filament wound joint (see section 5.9). A tri-axial braid pattern is used with non-axial yarns at $\pm 45^{\circ}$ to the strut's longitudinal axis, as shown in figure 3.8(a). Two over-braids (for a total of 3 braided layers) are used in order to provide a comparable degree of tow density with the filament wound joint.

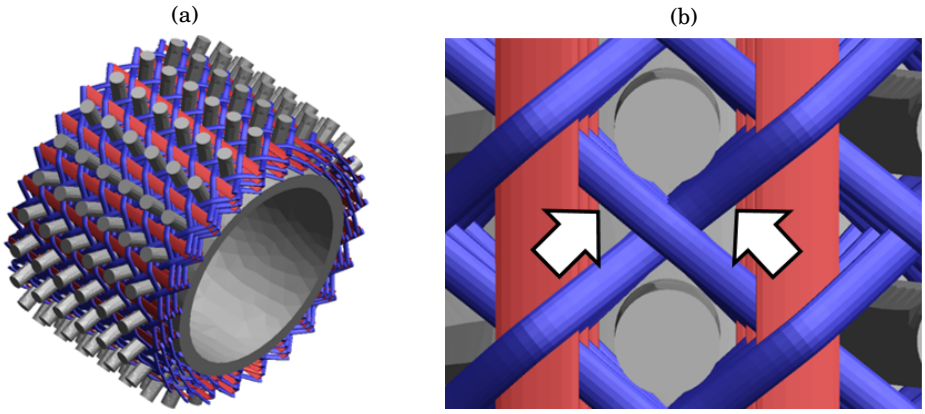

Figure 3.8: (a) Mechanical model of the tri-axial braided joint with 2 over-braids, for a pin-structured end-fitting (grey), and axial (red) and non-axial (blue) braid yarns. See section 5.9.2 for information regarding this model's construction. (b) Illustration of the shear-locking mechanism of adjacent (non-axial) yarns around the pins.

Improvements in joint properties, such as load transfer behaviour, stiffness and strength are expected for the filament wound joint over a braided equivalent. Firstly, from a manufacturing perspective, puncturing of the fibre-tows by the pins should be avoided, and consequently, the associated fibre breakage and strength degradation limited.

Secondly, in the filament wound joint, the fibre-tows are laid flat the strut's surface, with out of plane movement occurring only at tow crossing points. Braiding, in comparison, induces crimp (out-of-plane movement) of the yarns due to their relative interactions and the undulating path of the braid. This causes misalignment between the fibre reinforcement and the structure's

loading direction.

Finally, a braided joint relies on a shear-locking mechanism in which the angle of adjacent, non-axial, yarns is reduced to improve the form-fit with the metallic pins, as illustrated in figure 3.8(b). This results from an applied load, as opposed to one that is initiated immediately from manufacture. (Puncturing of the yarn by the pins may actually improve metal-fibre coupling in this regard, but at the expense of weakening the fibre reinforcement). In comparison, filament winding provides a robust connection between the metal and fibre-tow directly from fabrication. Pull-back of the fibre-tows around the metallic pins offers the potential for transferring the fibre reinforcement's high tensile strength directly into the joint.

3.2.3 Fully metallic strut

Comparisons of the hybrid strut's strength, stiffness and weight against a fully metallic component are made in section 4.7. In calculation of structural weight for both the hybrid and fully metallic strut, contribution from the lugs situated at the strut ends (see figure 1.2) are neglected. The metal strut is considered to be a uniform, cylindrical tube, with inner radius ρ, and consisting of the titanium alloy, Ti-6Al-4V (Grade 5), with properties as given in table 3.1. σ_Y denotes the yield stress and G, K, ETAN denote the shear, bulk, elastic (strain) hardening moduli respectively. This is a typical metallic alloy used in aircraft landing gear components [19].

Table 3.1: Material properties of metallic elements: pins and end-fittings.

	ρ (Kgm^{-3})	G (GPa)	σ_Y (GPa)	ETAN	K (GPa)
Ti-6Al-4V (Grade 5)	4420	43	1.1	0.20	0.25

3.3 Parameters of the hybrid strut and strategy for comparing possible configurations

For the hybrid strut and joining solution examined, there are a number of possible configurations that are created through variation of the parameters listed below:

(**1**) Tow layup sequence on the mandrel
(**2**) Tow pull-back and winding pattern around the pins
(**3**) Pin distribution (array)
(**4**) Pin size
(**5**) Pin angle (inclination)
(**6**) End-fitting shape

The remainder of this chapter consider items 1,2 and 3. Analysis of the strut is partitioned into two regions: the central composite part overlaying the mandrel, and the joining mechanism

at the pin-structured metallic end-fittings. These analyses combine to provide a preliminary performance ranking of strut and joint configurations, as presented in section 3.10. Items **4**, **5** and **6** are left for future consideration.

Firstly, the layup sequences for the mandrel are considered. An important factor effecting structural properties is the orientation of the fibre tows and possible non-uniformity of fibre coverage in this region. The mechanical interaction occurring between the filament wound fibre-tows and the pins at the joint is then considered. Load transfer capability and strength may be highly dependant upon the manner of tow pull-back, (where the tow reverses direction), and the tow trajectory in and around the pin array.

Design parameter I:

Tow winding angles and layup for the mandrel length

The elastic properties of a composite laminate can be calculated using Classical Lamination Theory (CLT) [63]. This considers the lamina (or ply) contribution to the properties of full the laminate, using the fibre-orientation of each ply and its position in the laminate, (known as layup or stacking sequence). Each lamina is regarded as homogeneous, with uniform fibre volume fraction and fibre arrangement throughout.

In this work, the layup sequence describes the orientation of the fibre-tows between the end-fittings, i.e. along the mandrel length only, for each filament wound layer and their order in the winding pattern. Adjacent tows are offset by the separation distance between the pins arrayed on the end-fitting's surfaces, in order to avoid puncturing of the tows during layup. Consequently, in a given filament wound layer, gaps may exist between adjacent tows, and therefore, assumption of uniform tow coverage and constant fibre volume fraction in the region of mandrel, is not representative. CLT therefore does not then provide a realistic prediction of the elastic properties of the central composite part of the strut overlaying the mandrel.

This section aims to offer an improved method for predicting the engineering, elastic constants of a three-dimensional tube representative of the central part of the strut spanning the two end-fittings, by accounting for the non-uniform fibre volume content in this region. For this, the part is subdivided into discrete sections, referred to as Individual Volume Elements (IVEs), as described in section 3.6. The path of the tow on the mandrel is mapped so that fibre volume fraction within each IVE can be calculated. CLT is then combined with a volume averaging method to calculate the unique elastic properties of each IVE, as seen in section 3.7.

3.4 Classical Lamination Theory

Classical lamination theory (CLT) is firstly discussed in order to provide a background. The stiffness of a composite laminate constructed from a number of perfectly bonded plies can be found using CLT. The stress-strain relationship in the principal material coordinate directions (1,2 and 3) for an orthotropic lamina under plane stress are given by equation 3.3.

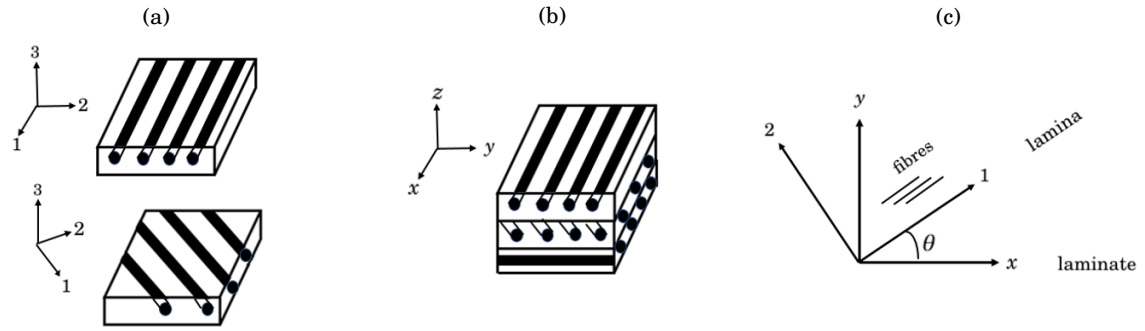

Figure 3.9: (a) Individual lamina coordinate systems. (b) Global laminate coordinate system. (c) Coordinate system transformation for fibres with orientation angle θ to laminate coordinates.

$$\begin{bmatrix} \sigma_1 \\ \sigma_2 \\ \tau_{12} \end{bmatrix} = \begin{bmatrix} Q_{11} & Q_{12} & 0 \\ Q_{12} & Q_{22} & 0 \\ 0 & 0 & Q_{66} \end{bmatrix} \begin{bmatrix} \epsilon_1 \\ \epsilon_2 \\ \gamma_{12} \end{bmatrix} \tag{3.3}$$

The reduced stiffness's, Q_{ij}, are defined in terms of engineering constants. Where ν_{12}, E_1, E_2 and G_{12}, denote the poissons ratio between directions 1 and 2, the longitudinal, transverse and shear moduli, respectively.

$$\begin{aligned} Q_{11} &= \frac{E_1}{1-\nu_{12}\nu_{21}} \\ Q_{12} &= \frac{\nu_{12}E_2}{1-\nu_{12}\nu_{21}} \\ Q_{22} &= \frac{E_2}{1-\nu_{12}\nu_{21}} \\ Q_{66} &= G_{12} \end{aligned} \tag{3.4}$$

The stress-strain relationship in the xy plane of the laminate coordinate system is then given by equation 3.5.

$$
\begin{aligned}
\overline{Q}_{11} &= Q_{11}\cos^4\theta + 2(Q_{12}+2Q_{66})\sin^2\theta\cos^2\theta + Q_{22}\sin^4\theta \\
\overline{Q}_{12} &= (Q_{11}+Q_{22}-4Q_{66})\sin^2\theta\cos^2\theta + Q_{12}(\sin^4\theta+\cos^4\theta) \\
\overline{Q}_{22} &= Q_{11}\sin^4\theta + 2(Q_{12}+2Q_{66})\sin^2\theta\cos^2\theta + Q_{22}\cos^4\theta \\
\overline{Q}_{16} &= (Q_{11}-Q_{12}-2Q_{66})\sin\theta\cos^3\theta + (Q_{12}-Q_{22}+2Q_{66})\sin^3\theta\cos\theta \\
\overline{Q}_{26} &= (Q_{11}-Q_{12}-2Q_{66})\sin^3\theta\cos\theta + (Q_{12}-Q_{22}+2Q_{66})\sin\theta\cos^3\theta \\
\overline{Q}_{66} &= (Q_{11}+Q_{22}-2Q_{12}-2Q_{66})\sin^2\theta\cos^2\theta + Q_{66}(\sin^4\theta+\cos^4\theta)
\end{aligned}
\tag{3.5}
$$

Where $\overline{Q_{ij}}$ denote the transformed reduced stiffnesses of a laminae with orientation θ. The stiffness of a laminate composed of N individual laminas, can then be calculated from equation 3.6.

$$
\begin{bmatrix} N_x \\ N_y \\ N_{xy} \\ M_x \\ M_y \\ M_{xy} \end{bmatrix} = \begin{bmatrix} A & B \\ B & D \end{bmatrix} \begin{bmatrix} \epsilon^0 \\ \kappa \end{bmatrix} = \begin{bmatrix} A_{11} & A_{12} & A_{16} & B_{11} & B_{12} & B_{16} \\ A_{12} & A_{22} & A_{26} & B_{12} & B_{22} & B_{26} \\ A_{16} & A_{26} & A_{66} & B_{16} & B_{26} & B_{66} \\ B_{11} & B_{12} & B_{16} & D_{11} & D_{12} & D_{16} \\ B_{12} & B_{22} & B_{26} & D_{12} & D_{22} & D_{26} \\ B_{16} & B_{26} & B_{66} & D_{16} & D_{26} & D_{66} \end{bmatrix} \begin{bmatrix} \epsilon_x^0 \\ \epsilon_y^0 \\ \gamma_{xy}^0 \\ \kappa_x \\ \kappa_y \\ \kappa_{xy} \end{bmatrix}
\tag{3.6}
$$

Where

$$
\begin{aligned}
A_{ij} &= \sum_{k=1}^{N} (\overline{Q}_{ij})_k (z_k - z_{k-1}) \\
B_{ij} &= \frac{1}{2}\sum_{k=1}^{N} (\overline{Q}_{ij})_k (z_k^2 - z_{k-1}^2) \\
D_{ij} &= \frac{1}{3}\sum_{k=1}^{N} (\overline{Q}_{ij})_k (z_k^3 - z_{k-1}^3)
\end{aligned}
\tag{3.7}
$$

For distances z_k and z_{k-1} of the k^{th} lamina, from the middle surface of the laminate.

In the $A-B-D$ matrix on the right-hand side of equation 3.6, the A_{ij} terms denote the extensional stiffness, with the 3 by 3 A matrix relating the in-plane stress to the mid-plane strains. Similarly, the D_{ij} terms denotes the bending stiffnesses and the D matrix relates the moment resultants to the curvatures. Lastly, the B_{ij} terms characterise bend-extension coupling.

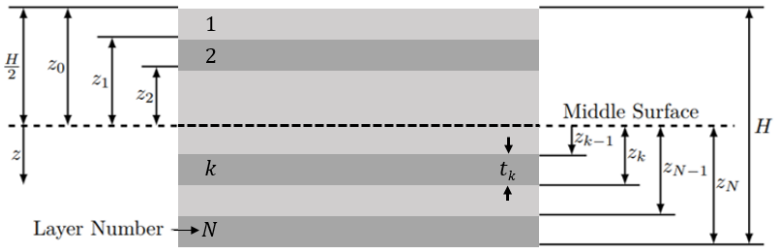

Figure 3.10: Geometry for a laminate consisting of N plies.

3.5 Hybrid structure layup sequence

The layup sequence for the strut describes the order and orientation of the fibre-tows for the region of the mandrel, only. That is, not including the tow in the region of the end-fittings and the joining mechanism at the strut ends. For characterisation of the tow path on the mandrel, it is necessary to specify a winding angle, (recall that this is the acute angle given by the tow trajectory and the strut's longitudinal axis).

However, the specified winding angle may have to be altered in order to allow the tow to pass through the pin array without puncturing occurring. Consequently, an alternate, feasible tow path and winding angle is found by a "nearest-pin" search. The method for calculating the nearest-pin angle is detailed in section 3.5.1.

A second consideration for tow layup on the mandrel is the attainment of full pin coverage. That is, during manufacture, the tow must be made to travel through all of the channels made by spacing between pins in the array. The fibre-tow then has the potential to interact with the full pin array, preventing redundancy of pins not involved in load transfer. To ensure this condition holds irrespective of the pin array and the winding pattern chosen (see section 3.9); pins in each row must be wound sequentially with the tow moving around the end-fitting's circumference.

These two requirements of a tow orientation on the mandrel that prevents puncturing and provides full coverage of the pin array, necessitate the definition of effectively two winding angles, θ_d and θ_u. Where, θ_d, and the subscript d denotes the layup of the tow "down" the mandrel, (or in the negative y direction), is equal to the nearest-pin angle and is determined to satisfy the first of these conditions, as detailed in section 3.5.1. Similarly, θ_u, with subscript "u" to signify a tow trajectory in the "up" direction fulfils the second criteria and is calculated as detailed in section 3.5.2.

It may be possible to instead offset, relative to each other, the end-fittings at the opposing ends of the strut, through application of a slight rotation about the strut's longitudinal axis. Their pin arrays may be offset in such a way so that θ_u and θ_d may become more equal (reducing asymmetry further, see section 3.7). However, it is preferred that control of the tow path is achieved through alteration of the tow winding angles directly (via definition of θ_u and θ_d) and the end-fittings are assumed to be perfectly aligned.

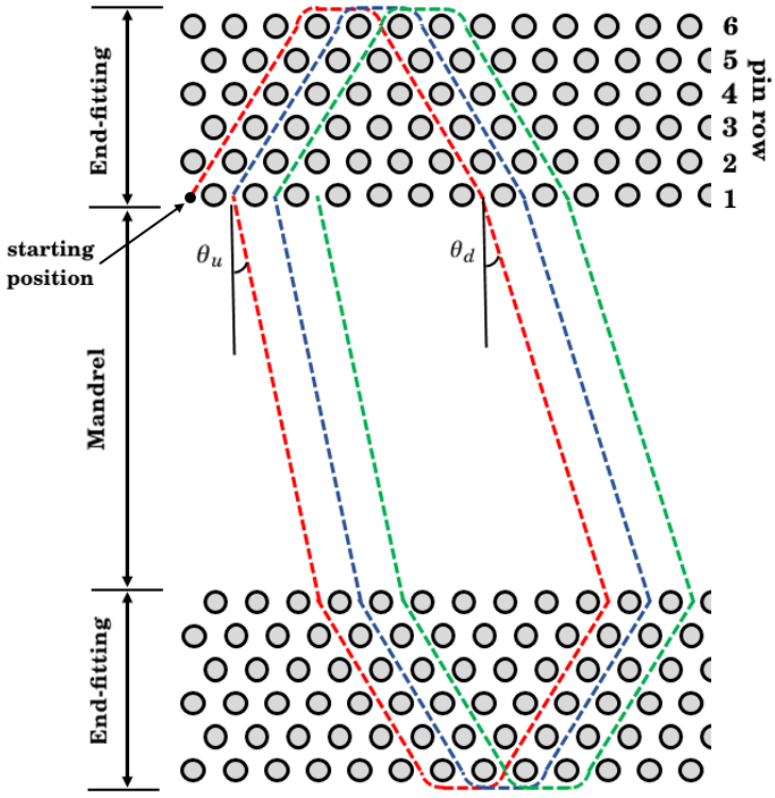

Figure 3.11: Illustration of the winding pattern for the hybrid strut, with orientation angles of θ_d and θ_u on the mandrel.

To define the layup sequence, the strut's central composite part overlaying the mandrel, is first viewed in an "unrolled" configuration, as shown in figure 3.12(b). Tows orientated at angles θ_d and θ_u are then considered as two, separate (non-uniform) lamina stacked in the positive radial (r) direction, with in-plane directions c and y. Each of these lamina has thickness equal to the thickness of the tow (T_t). This is estimated as described in appendix A.2. The N filament wound layers are then considered as a laminate with $2N$ lamina, thickness $2NT_t$ and a layup sequence of $[\theta_{1d},\theta_{1u},\theta_{2d},\theta_{2u},...,\theta_{Nd},\theta_{Nu}]$, as shown in figure 3.13.

3.5.1 Nearest-Pin Angle, θ_d, for prevention of tow puncturing

To find the nearest-pin angle, the struts circular cross-sectional face is divided into k sectors, as shown in figure 3.14. These are numbered sequentially in the clockwise direction with $\phi = 0$ at the positive x-axis. The total number of subdivisions is equal to the total number of pins in each row of the array (N_c, where subscript c denotes the pins around the end-fitting's circumference). That is, $1 \leq k \leq N_c$ and each sector has a interior angle of $\frac{2\pi}{N_c}$ radians.

Using results from [64], the total change in circumferential angle (ζ) of the tow due to its trajectory on the mandrel can be calculated from equation 3.8, where L and ρ_1 denote the

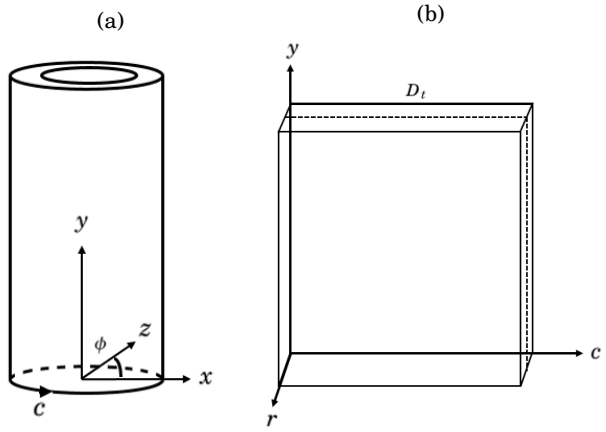

Figure 3.12: (a) Tubular central composite part overlaying the mandrel of the hybrid strut. (b) Equivalent 2D "unrolled" representation as a flat laminate. Filament wound layers are considered as lamina stacked in the positive radial (r) direction.

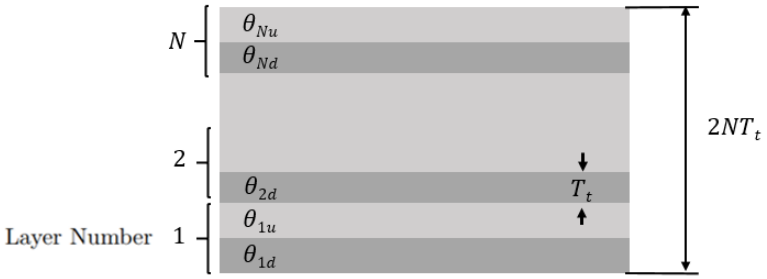

Figure 3.13: Equivalent laminate geometry for filament wound layers of fibre tows overlaying the mandrel part of the strut.

mandrel's length and radius, respectively. Let ϕ_k denote the circumferential angle at the start of sector k. The path of the tow will originate and terminate in a given sector at opposing ends of the mandrel, that is, $\zeta \in [\phi_{k-1},\ \phi_k]$ for some k. The nearest pin is then either the $k-1^{\text{th}}$ or the k^{th} pin.

$$\zeta = \frac{L\tan\theta}{\rho_1} \tag{3.8}$$

Suppose the nearest pin is denoted the K^{th} pin. Then the total change in circumferential angle as the tow traverses down the mandrel to the nearest pin, ζ_d, is given by equation 3.9. Re-arranging equation 3.8 using ζ_d, finds the effective winding angle, θ_d, required to wind the tow onto the K^{th} pin (equation 3.10).

$$\zeta_d = \begin{cases} K(\frac{2\pi}{N_c}) & \text{if } \zeta \geq 0 \\ N_c - K(\frac{2\pi}{N_c}) & \text{if } \zeta < 0 \end{cases} \tag{3.9}$$

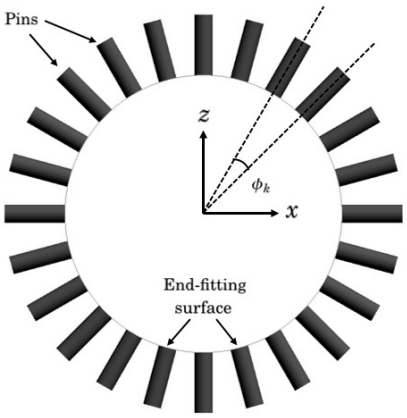

Figure 3.14: End-fitting cross-section subdivided by number of pins in each row and ϕ_k

$$\theta_d = \tan^{-1}(\frac{\rho_1 \zeta_p}{L}) \tag{3.10}$$

3.5.2 θ_u, for full pin array coverage

To ensure full coverage of the array, the tow must be returned on to either the $(K-1)^{\text{th}}$ pin, if $\zeta \geq 0$, or $N_c - (K+1)^{\text{th}}$ pin, otherwise. The change in the circumferential angle of the tow, ζ_u, due to its trajectory, is then given by 3.11.

$$\zeta_u = \begin{cases} (K-1)(\frac{2\pi}{N_c}) & \text{if } \zeta \geq 0 \\ (N_c - (K+1))(\frac{2\pi}{N_c}) & \text{if } \zeta < 0 \end{cases} \tag{3.11}$$

Again, re-arrangement of equation 3.8 allows for the calculation of the return (or up) winding angle, θ_u.

$$\theta_u = \tan^{-1}(\frac{\rho_1 \zeta_u}{L}) \tag{3.12}$$

3.6 Individual Volume Element (IVE)

3.6.1 Defining an IVE

Following definition of the layup sequence on the strut's mandrel, the position and trajectory of each filament wound layer, equivalent to two lamina with orientations angles θ_{id} and θ_{iu} $(1 \leq i \leq 2N)$, is known. The tow path can then be mapped on the mandrel's surface. The mandrel itself can then be subdivided into discrete sections, as shown in figure 3.15 using the 2D "unrolled" configuration referred to in section 3.5.

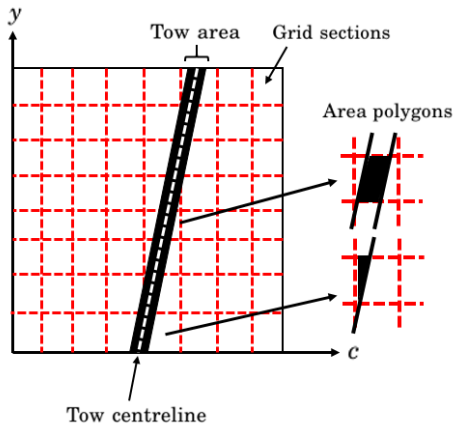

Figure 3.15: Meshed surface of the mandrel visualised in the 2D "unrolled" view. The centreline path and area of a given tow are also shown (not to scale). Area polygons define the total area of the tow with each section of the mandrel.

Parallel boundary lines can then be offset from the tow center-line by a distance equivalent to the tow radius. The area within these boundary lines defines the surface area of the mandrel occupied by a given tow due to its length and direction of travel. Intersections between the tow boundary lines and the gridded sections of the mandrel can then be found. These intersection points define a polygon with interior area equal to the area of the mandrel section that is occupied by the fibre-tow. It is possible for a section to not be intersected by the tow, or to be completely contained within the tow if the mandrel's mesh is sufficiently fine.

Calculation of the area of each grid section occupied by the fibre-tow can be repeated for each tow, forming each filament wound layer, as shown in figure 3.16. Consideration of thickness of the tow layers, projecting in the positive radial direction (r) from the mandrel's surface, defines an Individual Volume Element (IVE) that is a section of the central composite part spanning the two end-fittings and overlaying the mandrel. An IVE can be visualised as a section cut from this part of the strut, as shown in figure 3.17.

The total fibre volume fraction of each IVE, and the contribution from each layer of filament wound tows, can then be found accordingly. The remaining volume of the IVE consists of matrix material. Using CLT in combination with a method averaging the tow and matrix contributions to the properties of IVE based on their relative volume proportions (section 3.6.2.3) [65], the elastic properties of an IVE can be derived as described in section 3.6.2.

In effect, each IVE is considered as an individual laminate with unique elastic properties. Variation in the properties of the composite part overlaying the mandrel, due to the non-uniformity of fibre coverage, can be then be accounted for by considering this region as a mesh of IVEs.

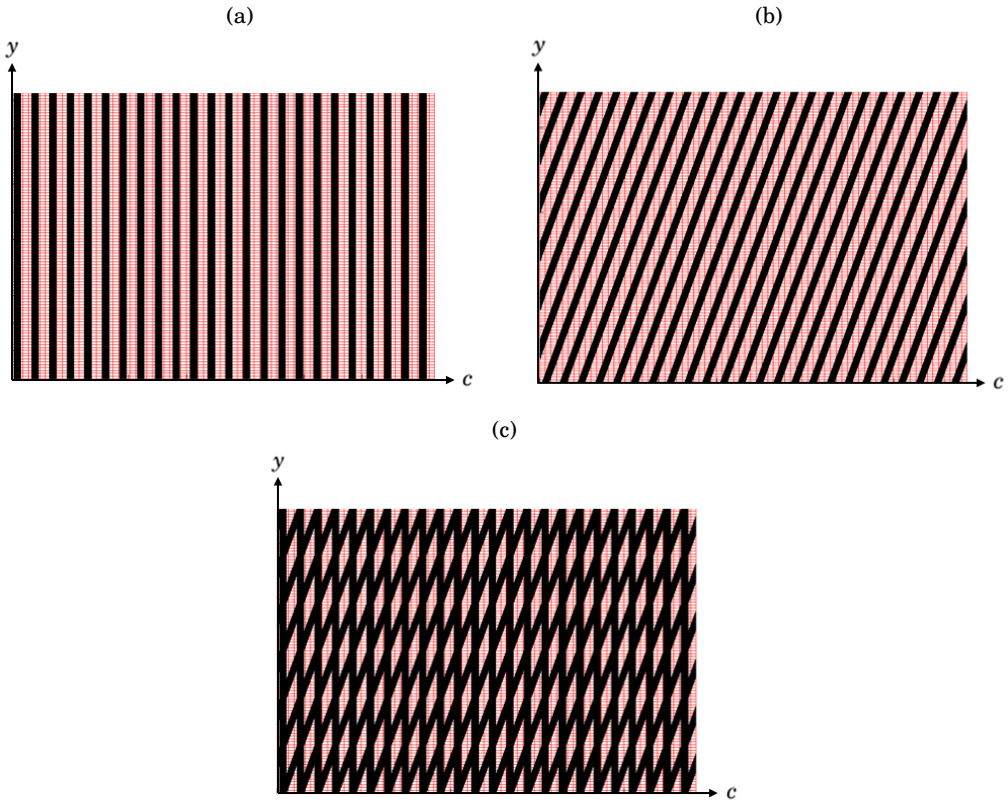

Figure 3.16: Area on a gridded (red lines) mandrel occupied by filament wound tows (black), for layers with a fibre orientation of (a) 0° and (b) 10° degrees, where spacing between tow centrelines exceeds the tow width. (c) The combined layup sequence.

3.6.2 Calculating the elastic properties of an IVE

3.6.2.1 Tow contribution

For the contribution of the fibre-tows to the elastic properties of an IVE, the tows are modelled as a transversely isotropic, linearly elastic material. The engineering constants of the tows are determined through use of the Chamis model [66]. As shown in equation 3.13, this uses the elastic properties of the fibres ($E_{f1}, E_{f2}, G_{f12}, \nu_{f12}$), matrix ($E_m, G_m, \nu_m$) and the intra-tow fibre volume fraction (V_f).

$$
\begin{aligned}
E_1 &= V_f E_{f1} + (1 - V_f) E_m \\
E_2 &= \frac{E_m}{1 - \sqrt{V_f}(1 - (E_m / E_{f2}))} \\
G_{12} &= \frac{G_m}{1 - \sqrt{V_f}(1 - (G_m / G_{f12}))} \\
\nu_{12} &= V_f \nu_{f12} + (1 - V_f) \nu_m
\end{aligned}
\tag{3.13}
$$

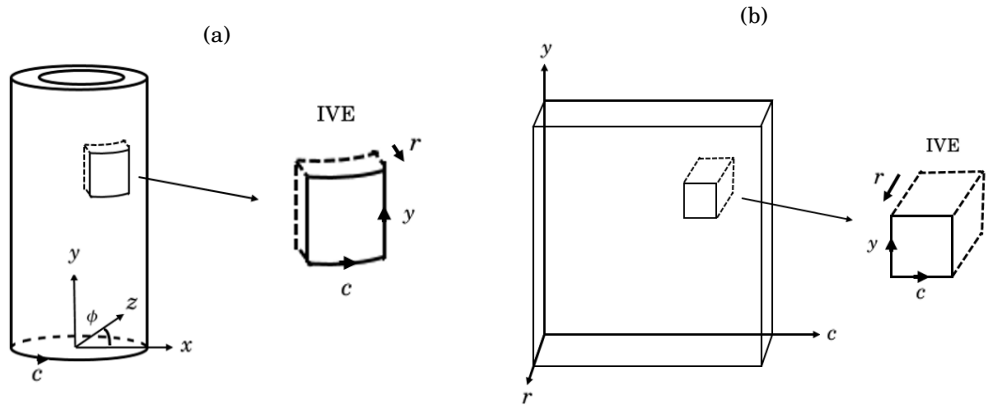

Figure 3.17: IVEs (not to scale) for (a) 3D tubular and (b) 2D "unrolled" representation of the central composite part of the strut overlaying the mandrel.

The local stiffness matrix, $[Q]$, of the tows with respect to the principal material coordinates of each lamina, defined by tows travelling in either the θ_d or θ_u directions, are given by equation 3.3. Global stiffness with respect to the laminate principal axes (x,y and z), equivalent to the filament wound layup of the mandrel, are therefore given by CLT and equations 3.5.

3.6.2.2 Matrix contribution

The matrix is considered to be a isotropic material with stiffness matrix, $[M]$, given by equation 3.14 [67].

$$[M] = \begin{bmatrix} M_{11} & M_{12} & 0 \\ M_{12} & M_{11} & 0 \\ 0 & 0 & M_{44} \end{bmatrix} \tag{3.14}$$

where

$$\begin{aligned} M_{11} &= \frac{(1-\nu_m)E_m}{(1-2\nu_m)(1+\nu_m)} \\ M_{12} &= \frac{\nu_m E_m}{(1-2\nu_m)(1+\nu_m)} \\ M_{44} &= G_m \end{aligned} \tag{3.15}$$

3.6.2.3 Volume averaging method

The volume of tow (V_t) within each IVE is calculated as detailed in section 3.6.1. The volume of the matrix (V_m) is then given by the total volume of the IVE, (V_{IVE}), less this value. (Note that the tow also contains matrix material proportional to the intra-tow fibre volume fraction and

given by $1-V_f$. This is, however, included in the calculation of the elastic properties of the tow, in accordance with equation 3.13). The volume proportions of the tow and matrix in a given IVE, V_{pt} and V_{pm} respectively, are calculated using equations 3.16.

$$V_{pt} = \frac{V_t}{V_{IVE}}$$
$$V_{pm} = \frac{V_m}{V_{IVE}} \tag{3.16}$$

The engineering elastic constants and Q-matrix of an IVE, $[Q_{IVE}]$, with respect to the laminate principal axes, is assembled from the stiffness of each constituent, matrix and fibre, using their relative volume proportions, as shown in equation 3.17. The A-B-D matrix of an IVE can then be calculated using equations 3.7.

$$[Q_{IVE}] = V_{pt}\left[\overline{Q}\right] + V_{pm}[M] \tag{3.17}$$

3.7 Relative performance ranking of layup sequences for the mandrel

3.7.1 Feasible layups and expected behaviour

According to CLT and equation 3.6, for the cylindrical coordinate system of the strut's mandrel, under axial loading, the resultant force N_y is related to the strains and curvatures by equation 3.18.

$$N_y = A_{11}\epsilon_y^0 + A_{12}\epsilon_c^0 + A_{16}\gamma_{yc}^0 + B_{11}\kappa_y + B_{12}\kappa_c + B_{16}\kappa_{yc} \tag{3.18}$$

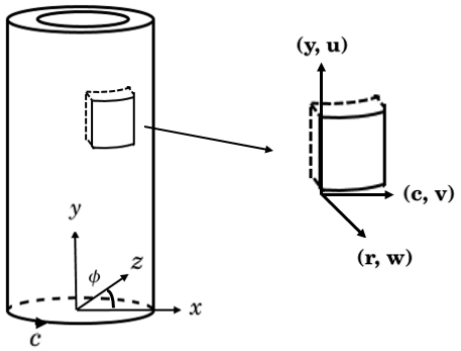

Figure 3.18: Axes y, c and r, and displacements u,v,w, respectively, for the composite tube (and IVE) spanning the two metallic end-fittings and overlaying the mandrel.

The A_{11} term of the A-B-D matrix denotes the axial (or longitudinal) stiffness and ϵ_y^0 the mid-plane axial strain. A_{12} denotes coupling between extension in the longitudinal and hoop directions, with ϵ_c^0 being equivalent to hoop strain. Finally, the A_{16} term represents hoop shear-extension coupling, with γ_{yc} denoting hoop-shear strain. This may lead to torsional stresses developing. For mid-plane displacements u^0, v^0 and w^0 in the y, c and r directions, respectively, the strain relations are given by equation 3.20.

The B terms that denote bending-extension coupling, are zero if a symmetric layup is utilised. For the component described in section 3.2, consisting of metallic end-fittings with 24 by 6 pin arrays and consequently 6 filament wound layers of fibre-tows; the possible symmetric layups L_i, $1 \leq i \leq 10$, are given by equation 3.19, (for fibre angle increments of $\pm 5°$). Note that these layups are also balanced, which is an equal consideration for layup determination at this stage in strut design. Unbalanced layups will produce torsional effects in strut following axial loading (tension and compression), which are to be avoided as these may induce additional stress in the structure.

$$L_i = \begin{cases} [0_6] & i = 1 \\ [\mp\theta_i \; 0_2 \; \pm\theta_i] & 2 \leq i \leq 10, \; \theta_i \in \{5, 10, ...45\} \end{cases} \tag{3.19}$$

However, recall that fibre orientations on the mandrel may not coincide with those prescribed due to the use of the altered angles θ_d and θ_u, in order to avoid puncturing of the fibre-tow and to ensure full coverage of the pin array. This may lead to some asymmetry and imbalance to the layup (see appendix A.5) for the resulting fibre angles θ_{di} and θ_{ui} for layups 1-10). Therefore, the B terms may be non-zero and the curvature relations given in equation 3.20 may apply.

$$\begin{aligned} \epsilon_y^0 &= \frac{\partial u^0}{\partial y} \\ \epsilon_c^0 &= \frac{1}{\rho_1}\left(\frac{\partial v^0}{\partial c} + w\right) \\ \gamma_{yc}^0 &= \frac{1}{\rho_1}\left(\frac{\partial u^0}{\partial c} + \frac{\partial v^0}{\partial y}\right) \\ \kappa_y &= -\frac{\partial^2 w}{\partial y^2} \\ \kappa_c &= -\frac{1}{\rho_1^2}\left(\frac{\partial^2 w}{\partial c^2} + w\right) \\ \kappa_{yc} &= -\frac{1}{\rho_1}\left(\frac{2\partial^2 w}{\partial y \partial c} + \frac{1}{\rho_1}\frac{\partial u^0}{\partial c} - \frac{\partial v}{\partial y}\right) \end{aligned} \tag{3.20}$$

B_{11} denotes extension-curvature coupling in the y-axis, with κ_y representing necking or funnelling of the composite cylinder. B_{12} is coupling between extension in the y-axis and curvature in the hoop direction, and κ_c denotes deviation from the circular cross-section, via wrinking or buckling of the cylinder around the circumference. Finally, the B_{16} term represents coupling between axial extension and curvature and κ_{yc} is twisting of the cylindrical cross-section.

3.7.2 Numerical model

An FE model of the central, composite part of the strut overlaying the mandrel, is constructed in Abaqus® Implicit [68] as a cylinder meshed with 0.5 by 0.5mm S4 type shell elements. Each element is equivalent to an IVE and is assigned an A-B-D matrix calculated using CLT and the volume averaging method described previously. The elastic properties of the cylinder and its IVEs vary due to the non-uniformity of fibre coverage of the mandrel and are dependant upon the layup sequence.

Material properties for the constituent tow and matrix are as seen table 3.2. These are derived using data from [69] and the Chamis model [66], for an assumed constant intra-tow fibre volume fraction of 70%.

Table 3.2: Material properties of carbon fibre, the virtual tow and matrix (resin) used in the numerical model of the central composite part spanning the two metallic end-fittings of the strut and overlaying the mandrel.

	E_{11} (GPa)	E_{22} (GPa)	$\nu_{12} = \nu_{13}$	ν_{23}	$G_{12} = G_{13}$ (GPa)	G_{23} (GPa)
Carbon Fibre (HTX40 F13 12k)	238	13	0.20	0.25	13	6
Virtual Tow	168	8.54	0.245	0.1771	5	3.6
Epoxy resin MVR444	3.1	3.1	0.35	0.35	1.2	1.2

A global tensile strain, equivalent to $2000\mu\epsilon$, is then applied to each cylinder constructed with layup sequences 1-10, by prescribing a y-direction (axial) displacement to nodes forming one end of the cylinder, and constraining the opposing end in all degrees of freedom. The maximum strains ϵ_y, ϵ_c and γ_{yc} are then extracted, as shown in table 3.4.

A relative performance ranking of the possible layup sequences for the mandrel is determined using the function F, as given in equation 3.21. An improved configuration is obtained through minimisation of F, using typical strain allowables for a carbon-fibre reinforced, epoxy plastic composite material, (table 3.3). The theoretical minimum value of F is 0.5, as the applied strain is 50% of the allowable axial strain. A value of F which is greater then 1 implies failure in one or more directions.

$$F = \max\left(\frac{\epsilon_y}{\epsilon_y^*}, \frac{\epsilon_c}{\epsilon_c^*}, \frac{\gamma_{yc}}{\gamma_{yc}^*}\right) \tag{3.21}$$

Table 3.3: Typical strain allowables for composite materials [1].

Strain Allowables	
ϵ_y^* ($\mu\epsilon$)	$\pm$4000
ϵ_c^* ($\mu\epsilon$)	$\pm$4000
γ_{yc}^* ($\mu\epsilon$)	$\pm$2600

Figures 3.19(a), 3.19(c) and 3.19(e) show the axial (ϵ_y), circumferential (ϵ_c) and hoop-shear (γ_{yc}) strain, respectively, in the strut's central composite part overlaying the mandrel, following axial tension, for layup 1 ($[0_6]$). Figures 3.19(b), 3.19(d) and 3.19(f), show likewise strain fields for layup 10 ($\mp 45/0_2/\pm 45$).

The axial paths of the fibre-tows can be seen clearly in the strain patterning for ϵ_c and γ_{yc}, as bands running length-wise down the longitudinal axis of the cylinder. Maximum absolute strain values occur in resin rich regions of the mandrel. For hoop-shear, large positive and negative strains appear in adjacent bands as significant imbalances occur in elastic properties between areas with a high volume content of axial fibres, and expanses of only matrix material. As evident in figure 3.20, the percentage of matrix only IVEs on the mandrel exceeds 60%, the constant fibre orientation through the layup results in poor coverage of the mandrel's surface.

For axial strain in layup 1, distribution is more uniform as the axial tow directions limit the strain in this direction in neighbouring parts containing only matrix material. However, some small areas of high strain occur at the ends of the cylindrical, as highlighted in the lower image of figure 3.21. These correspond to regions directly at, or underneath, the pins forming the first row of the pin-structured end-fittings. These have very low or no tow coverage (matrix rich) as they are "missed" by the fibre-tows due to their trajectories onto and off the pins.

For layup 10, tow coverage of the mandrel is improved from layup 1 due to the off-axis $\pm 45°$ fibre directions. These overlay a greater proportion of the mandrel's surface and cover areas of the mandrel not included by the axial fibre layers. Consequently, the number of matrix-only IVEs is less than and regions of high strain are, in general, significantly reduced from layup 1. However, as full mandrel coverage is not achieved, small resin rich regions appear along throughout the length of the mandrel.

Figures 3.22(a), 3.22(c) and 3.22(e) show ϵ_y, ϵ_c and γ_{yc}, respectively, for a composite tube with layup sequence $[0_6]$, following axial tension, but with assumed uniform tow coverage over the cylinder's surface, and elastic properties calculated using CLT only (i.e. without consideration of IVEs). Similarly, figures 3.22(b), 3.22(d) and 3.22(f) are equivalent strain plots for a cylinder with layup sequence $\mp 45/0_2/\pm 45$. A more homogeneous strain field is apparent due to the constant, uniform tow coverage of the cylinder's surface.

These uniform, composite tubes are not achievable for the central part of the hybrid strut following the filament winding process, because of the aforementioned precondition in which tow puncturing is prevented at the strut ends through offsetting neighbouring tows by the circumferential spacing between adjacent pins. (Possible methods for their manufacture include pultrusion methods [70] [71] or Automated Fibre Placement (AFP) [72], [73]). They are provided here to illustrate clearly that the strain distribution and structural behaviour of the strut's central composite part will be altered significantly due to non-uniformity of tow coverage, justifying the detailed approach in section 3.6 to consider this effect.

Table 3.4: Maximum strains ϵ_y, ϵ_c, γ_{yc} and F values for layups 1-10.

Layup No.	Layup Sequence	ϵ_y	$\frac{\epsilon_y}{\epsilon_y^*}$	ϵ_c	$\frac{\epsilon_c}{\epsilon_c^*}$	γ_{yc}	$\frac{\gamma_{yc}}{\gamma_{yc}^*}$	F
1	$[0]_6$	$3.00e-3$	0.75	$-1.35e-3$	0.34	$2.26e-3$	0.87	0.87
2	$[\mp 5/0_2/\pm 5]$	$4.38e-3$	1.10	$-1.68e-3$	0.42	$-5.89e-3$	2.27	2.27
3	$[\mp 10/0_2/\pm 10]$	$5.26e-3$	1.31	$2.26e-3$	0.57	$-6.81e-3$	2.62	2.62
4	$[\mp 15/0_2/\pm 15]$	$6.13e-3$	1.53	$-2.59e-3$	0.65	$-6.00e-3$	2.31	2.31
5	$[\mp 20/0_2/\pm 20]$	$6.33e-3$	1.58	$-2.82e-3$	0.70	$-5.18e-3$	1.99	1.99
6	$[\mp 25/0_2/\pm 25]$	$6.48e-3$	1.62	$-2.50e-3$	0.63	$-4.14e-3$	1.59	1.62
7	$[\mp 30/0_2/\pm 30]$	$5.64e-3$	1.37	$-2.46e-3$	0.61	$-3.45e-3$	1.33	1.37
8	$[\mp 35/0_2/\pm 35]$	$5.25e-3$	1.31	$-2.33e-3$	0.58	$-2.88e-3$	1.11	1.31
9	$[\mp 40/0_2/\pm 40]$	$4.43e-3$	1.11	$-2.06e-3$	0.52	$-2.45-3$	0.94	1.11
10	$[\mp 45/0_2/\pm 45]$	$3.97e-3$	0.99	$-1.73-3$	0.43	$-2.11e-3$	0.81	0.99

3.7.3 Additional hoop layer

An additional, outer hoop (with with fibre orientation of 90° to the strut's longitudinal axis) layer of filament wound tows could be included. This would be confined to the strut's central mandrel, with tow pull-back around the pins not occurring for this layer. Consequently, it would not directly influence the composite metal-joint at the strut ends, but as with its use in more conventional filament winding (see section 1.2), it may increase the strut's circumferential strength.

CLT can be used to analyse the contribution of this layer, as uniform coverage of the mandrel can be assumed. Table 3.5 displays the resulting strains and F values for layup sequences 1-10, with an outer hoop layer included. Circumferential (ϵ_c) strain is reduced for all layup sequences, with maximal strain reductions exceeding 50%. Axial (ϵ_y) and hoop-shear (γ_{yc}) are also reduced for layups 1-5, but for higher numbered layup sequences the benefit of an outer hoop layer becomes less obvious, as axial and hoop-shear stiffness are reduced, resulting in an increase in strain in these directions.

Table 3.5: Maximum strains ϵ_y, ϵ_c, γ_{yc} and F values for layups 1-10, including an additional, outer hoop layer.

Layup No.	Layup Sequence	ϵ_y	$\frac{\epsilon_y}{\epsilon_y^*}$	ϵ_c	$\frac{\epsilon_c}{\epsilon_c^*}$	γ_{yc}	$\frac{\gamma_{yc}}{\gamma_{yc}^*}$	F
1	$[0_6/90]$	$2.90e-3$	0.72	$-5.24e-4$	0.13	$1.96e-3$	0.75	0.75
2	$[\mp 5/0_2/\pm 5/90]$	$4.06e-3$	1.01	$-8.01e-4$	0.20	$-5.21e-3$	2.01	2.01
3	$[\mp 10/0_2/\pm 10/90]$	$4.91e-3$	1.23	$-1.04e-3$	0.26	$-6.35e-3$	2.44	2.44
4	$[\mp 15/0_2/\pm 15/90]$	$5.55e-3$	1.39	$-1.25e-3$	0.31	$-5.65e-3$	2.17	2.17
5	$[\mp 20/0_2/\pm 20/90]$	$5.85e-3$	1.46	$-1.33e-3$	0.33	$-4.99e-3$	1.92	1.92
6	$[\mp 25/0_2/\pm 25/90]$	$6.33e-3$	1.58	$-1.20e-3$	0.30	$-4.23e-3$	1.63	1.63
7	$[\mp 30/0_2/\pm 30/90]$	$5.78e-3$	1.45	$-1.35e-3$	0.34	$-3.56e-3$	1.37	1.37
8	$[\mp 35/0_2/\pm 35/90]$	$5.82e-3$	1.45	$-1.44e-3$	0.36	$-3.06e-3$	1.18	1.45
9	$[\mp 40/0_2/\pm 40/90]$	$5.17e-3$	1.29	$-1.31e-3$	0.33	$-2.60-3$	1.00	1.00
10	$[\mp 45/0_2/\pm 45/90]$	$4.64e-3$	1.16	$1.22-3$	0.32	$-2.27e-3$	0.87	1.16

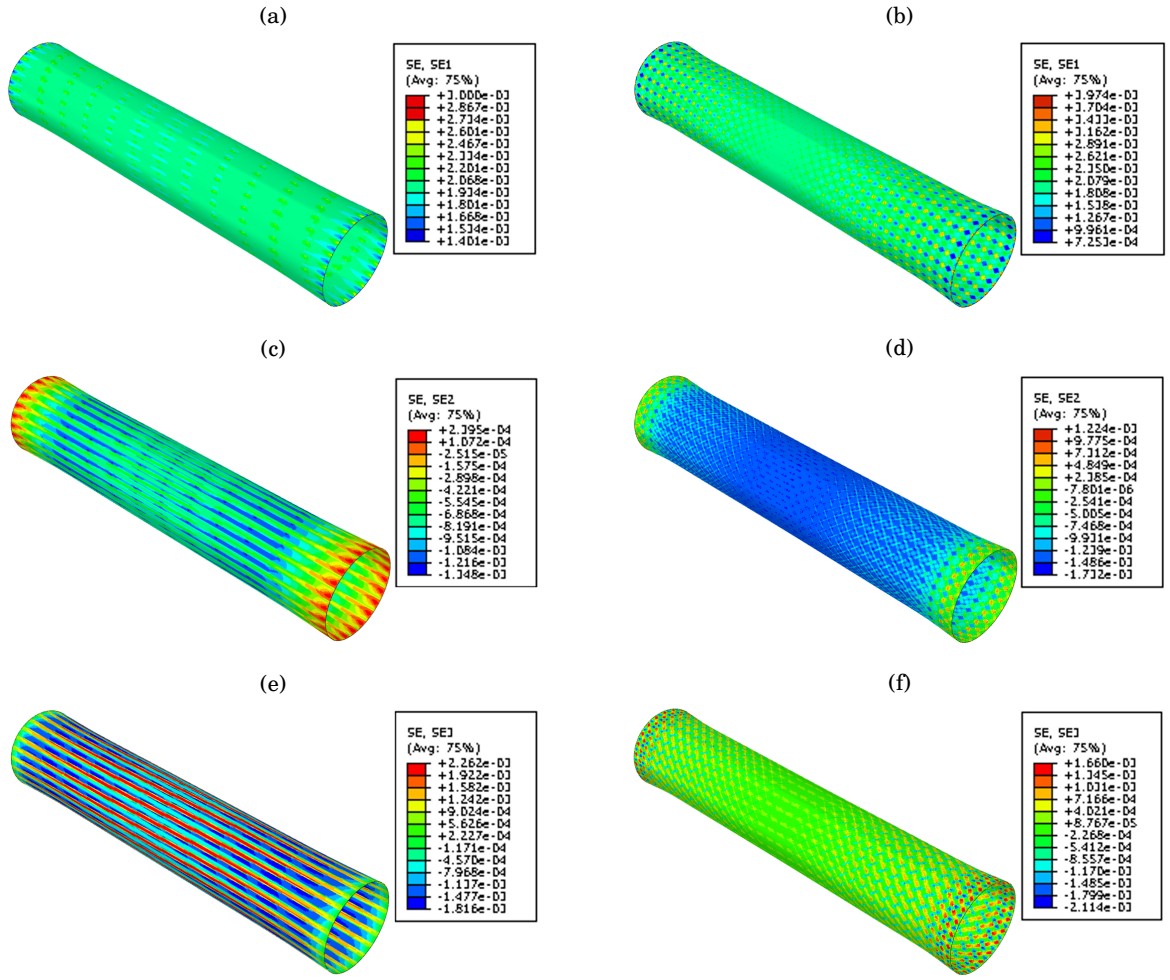

Figure 3.19: (a) Axial, (c) circumferential and (e) hoop shear strains of the central composite part of the strut overlaying the mandrel, for layup 1 ($[0_6]$), following an axial tensile strain of $2000\mu\epsilon$. (b), (d) and (f) are equivalent strain plots for layup 10 ($\mp 45/0_2/\pm 45$).

Design parameter II:

The pin array and tow trajectory in this region

3.8 Analytical pulley-and-belt model

In addition to the layup sequence on the mandrel, an important consideration for strut design is the winding pattern, or tow trajectory, for the region of the pin structured metallic end-fittings. This includes the manner in which tow pull-back is initiated around the pins. Joint efficiency and

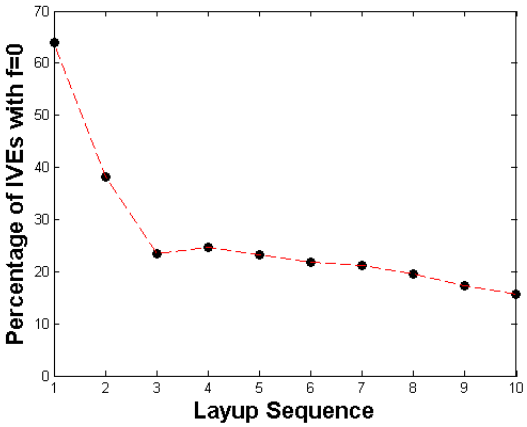

Figure 3.20: Percentage of matrix only (with fibre volume fraction $f = 0$) IVEs for each layup sequence 1-10.

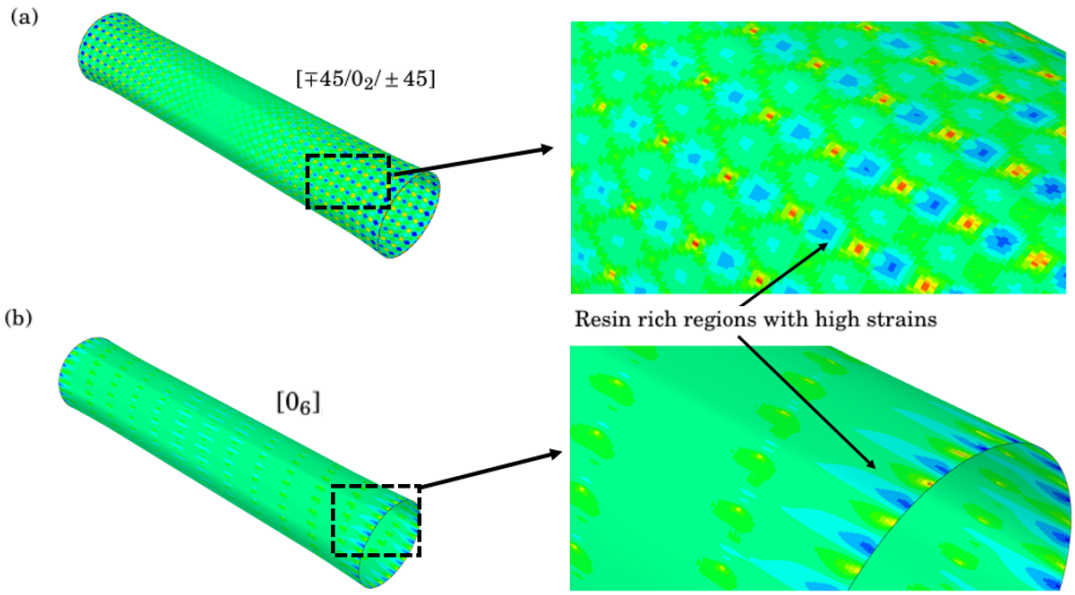

Figure 3.21: Areas of high (axial) strain in the central composite part of the strut, spanning the two end-fittings and overlaying the mandrel, with layup sequences (a) 1 and (b) 10. Areas of high strain correspond to areas with low or no fibre coverage.

the mechanical interaction between the fibre-tows and pins in the joint, may be highly dependent on the joint configuration. Load transfer potential should be maximised for joint designs in which load is evenly distributed across the pins in the array. This will act to prevent premature joint failure via over-loading, or redundancy, of given pins. As with the mandrel layup, it is therefore advantageous to develop a preliminary relative performance ranking of possible joint designs.

To accomplish this, the tow-pin interaction is reduced to a two-dimensional belt-and-pulley

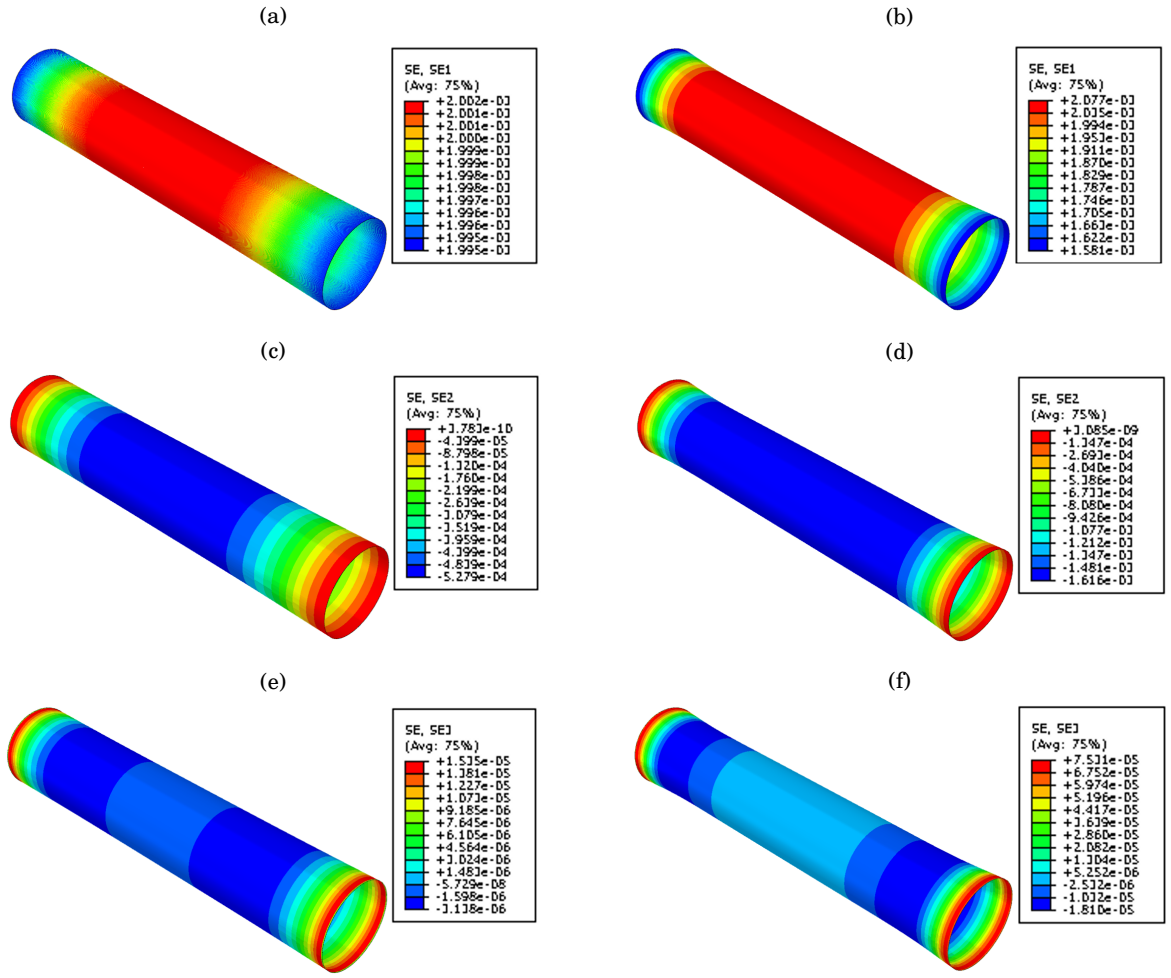

Figure 3.22: (a) Axial, (c) circumferential and (e) hoop shear strains in a uniform, composite tube with layup $[0_6]$, following an axial tensile strain of $2000\mu\epsilon$. (b), (d) and (f) are equivalent strain plots for a layup of $\mp 45/0_2/\pm 45$.

problem, which is examined using a simple analytical model. Each pin in the array is treated analogously to a frictionless point pulley (with zero diameter), and the fibre-tow is considered equivalent to a belt that wraps the pins, as shown in figure 3.23.

The case of joint and strut (axial) tension is examined only (i.e. not compressive loads, see section 4.8). Following tensile loads, force is exerted on the pins and tension is transferred to the tows due their mechanical interaction. The force exerted on a given pin is determined by the proportion of its surface that is in contact with a given tow, or a pin's degree of "wrapping" by the tow. More precisely, the force $\underline{F}$ exerted on a pin, wrapped on the interval $\psi \in [\theta_A, \theta_B]$, by a tow subjected to tension T, is given by equation 3.22.

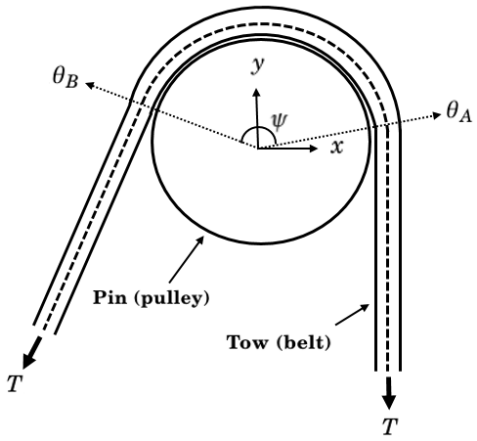

Figure 3.23: Illustration of the "wrapping" of a single pin (pulley) by the tow (belt).

$$\underline{F} = \left(-\int_{\theta_A}^{\theta_B} T\cos(\psi)d\psi, -\int_{\theta_A}^{\theta_B} T\sin(\psi)d\psi \right) \tag{3.22}$$

Tow tension (T) is treated as a variable scalar value, which is taken as unity for a pin array that is at the maximum feasible density, as established in section 3.1.2. The value of T is then increased proportionally to any decrease in pin density. As pin spacing increases, the number of tows spanning the strut length and connecting the two metallic end-fittings at the strut ends, would decrease, (as the tows are offset relative to each other by the circumferential separation distance between adjacent pins). Theoretically, the magnitude of tension per tow would then increase for an equal (global) tensile load applied to the full strut, and consequently, the force exerted on the pins would increase similarly, due to the pin-tow interaction in the joint.

Furthermore, in the analytical belt-and-pulley model, the aspect ratio of the pins (L_p/D_p) is assumed to be sufficiently small (< 3) such that load transference between the fibre-tows and the metallic pins results in only shear force being exerted on the pins, that is, induced bending moments are not considered.

3.8.1 Infeasible tow-pin interactions

Initial constraints are imposed upon the number of feasible winding patterns around the pin-structured end-fittings in order to limit the size of the design space. These may be less strict than those imposed by manufacturability, (see chapter 6).

Firstly, patterns in which the tow direction reverses whilst navigating the pin array are discounted. The level of articulation required by the tow delivery system to simultaneously reverse the direction of travel and lay up the tow precisely around the pins without puncturing occurring, is determined to be infeasible. Additionally, intuitively such tow trajectories may

induce a high degree of tow twist and fibre breakage during layup. Secondly, patterns in which the tow is made to contact the underside of the pin are limited to that discussed in section 3.9.4.

3.9 Tow-pin winding patterns and conventions

As established in section 3.1, each layer of fibre-tows would navigate the pin array, turn around a pin or group of pins, prior to reversing direction and transitioning down the mandrel length. The tow-pin interaction would then be repeated at the opposing end, to connect the two end-fittings and establish the strut. The top-most row of pins (row 6) forms the first "turn" row, with tow pull-back in the first layer being initiated around pins in this row. Each subsequent filament wound layer would then reverse direction around the next lower pin row, moving sequentially downwards to the pin row closest to the end-fitting's base (row 1).

3.9.1 Single-pin wrapping pattern

The simplest winding pattern is one in which each pin is wrapped individually by the tow, as shown in figure 3.24. Each pin has an angle of wrap of approximately 180°, and therefore, each pin is loaded equally. This holds for all possible layup sequences on the mandrel, due to the definitions of θ_d and θ_u within each filament wound layer.

However, no load sharing between pins occurs as each interacts singularly with the fibre-tow. Alteration of the winding pattern so that pull-back occurs around multiple pins (two or more), allows for the possibility of load sharing between pins. This may also provide a fail-safe mechanism in which pin-tow contact is maintained following failure of a given pin.

Only a square type array is considered for this particular winding pattern. Load sharing between pins is unaltered by the pin array type but a diamond patterned pin array will increase the necessary circumferential spacing between the pins, as seen in figure 3.25. This will increase the resulting tow tension (T) and magnitude of the force experienced in the pins.

3.9.2 All-row wrapping pattern

A second possible winding pattern is referred to as an "all-row" pin wrapping. This describes a trajectory in which the tow transitions onto the pin array around the first pin row. For this winding pattern, both diamond and square type pin arrays may be considered as minimum pin spacing and tow tension ($T = 1$) can be maintained.

The analytical model predicts that load sharing, within each layer, occurs only between first row of pins and the "turn" pin row, around which pull-back occurs. Transition pins between these two rows are unloaded as the tow passes tangentially and therefore their angle of wrap is zero.

Load distribution across the pin array will be effected by the layup sequence and the array type, as these both alter the relative degrees of wrapping of the entry and turn pins. Figure 3.27(a) displays the predicted variance (as a percentage of the total force exerted on the pin array)

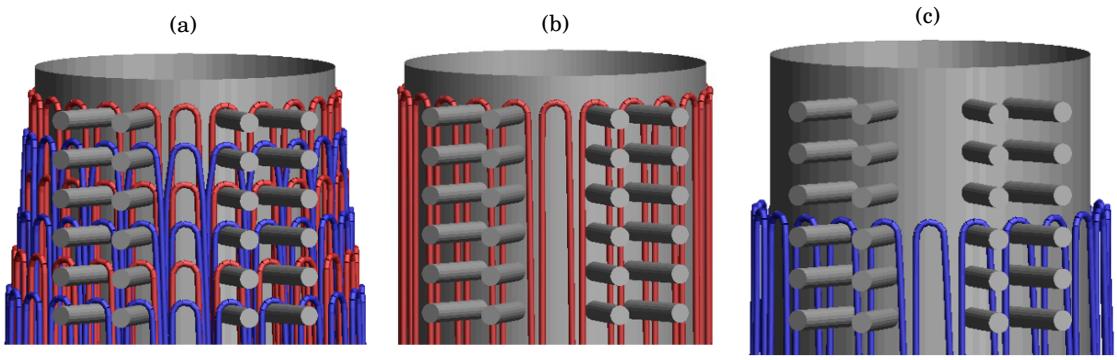

Figure 3.24: (a) Single pin wrapping pattern with six filament wound layers, coloured blue and red alternately. (b) First layer and (c) Fourth layers only. Some pins have been removed so that the tow path can be seen clearly. See chapter 4 for information regarding the construction of the model used in this figure.

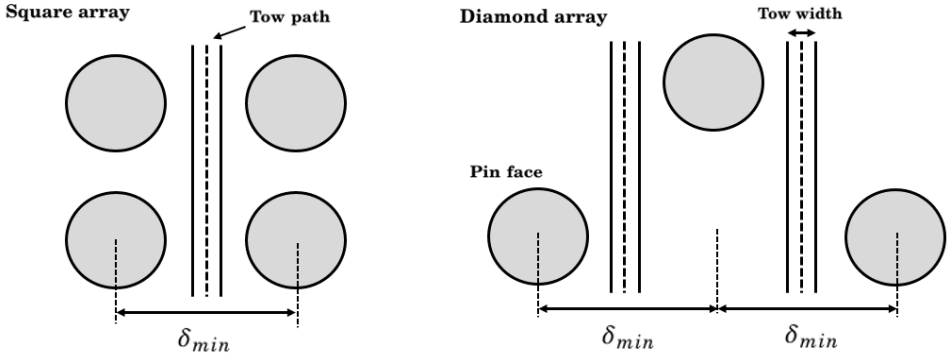

Figure 3.25: Minimum pin spacing for a single pin wrapping pattern of a diamond and square type pin arrays. Pin spacing is increased by a factor of two for a diamond array, when using a single-pin wrapping pattern.

in the shear force exerted on the pins for a diamond type array, for layup sequences 1-10. Figure 3.27(b) is a similar plot for a square type pin array.

Lower variance across all layups indicates improved load distribution for a diamond type pin array, compared with a square pin arrangement. For the diamond array, optimal load sharing is predicted to occur for layups 7 and 8, where the analytical model estimates a difference of less then 2% between the shear force exerted on the pins. Load sharing is improved between layups 1-7 as the force exerted on the first pin row is reduced. However, an inflection point occurs between layups 7-8, as the load on the first row of pins is reduced at the expense of increased loading of the upper pin rows, as shown in figure 3.28(a).

For the square array, load sharing is comparatively poor, with pins in the first pin row carrying the majority of the load, as highlighted in figure 3.28(b). Load sharing capability does improve for higher numbered layup sequences, as tows with orientation angles of 0° for the mandrel are

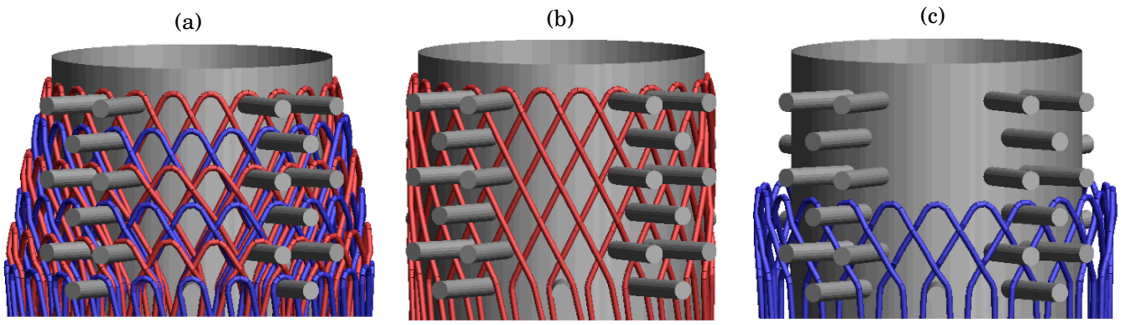

Figure 3.26: (a) All-row pin wrapping pattern with six filament wound layers, coloured blue and red alternately. (b) First layer and (c) Fourth layers only. Some pins have been removed so that the tow path can be seen clearly.

replaced by those with higher angles of approach. This reduces the degree of wrapping, and consequently force exerted, on pins in the first row.

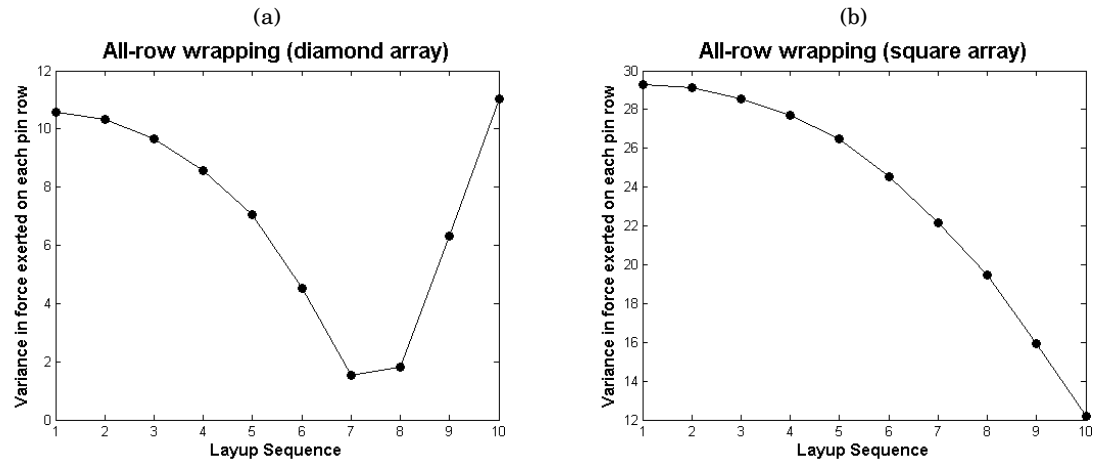

Figure 3.27: Variance (as a percentage of the total force exerted on the pin array) in pin shear force for a (a) diamond and (b) square type pin array, with an all-row winding pattern.

In general, this winding pattern is limited by the fact that load sharing occurs only between the first and "turn" pin rows, which results in overloading of the first row of pins, maximal tow density around the end-fitting's base and fibre volume content decreasing further up the structure.

3.9.3 Two-row wrapping pattern

A winding pattern in which each filament wound layer interacts with only two rows of pins is considered. This prevents the redundancy of the middle, (or transition), pins as evident in the all-row wrapping pattern examined previously. Overloading of the first pin row should be

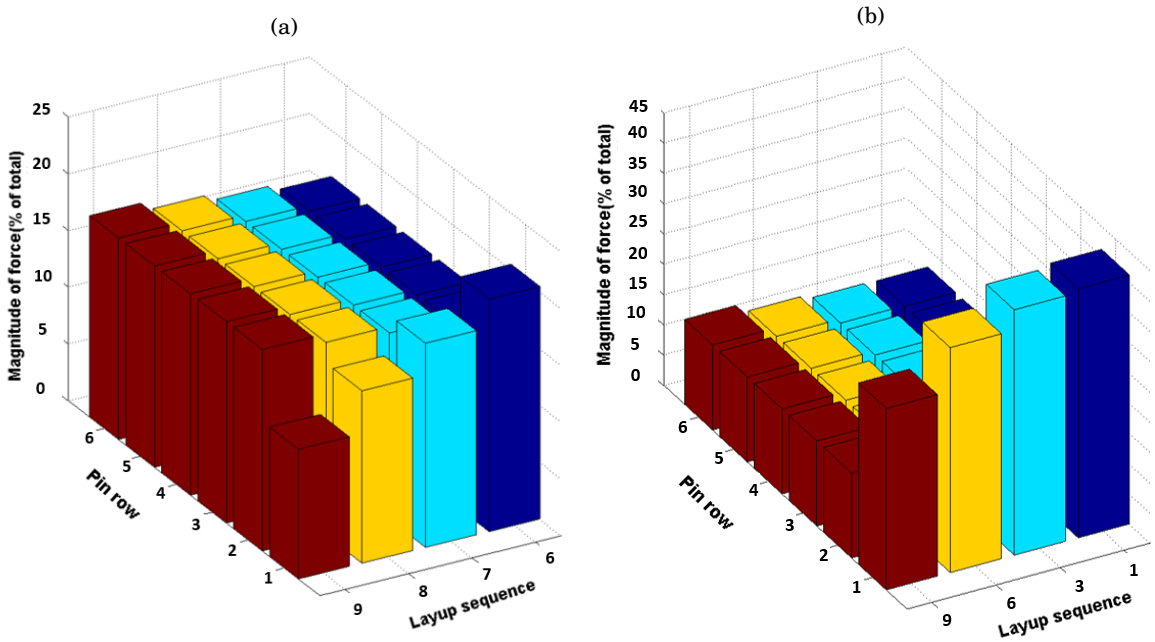

Figure 3.28: Percentage of the total shear force exerted on the pin array, by pin row, for (a) a diamond array and layups 6-9, and (b) a square array and layups 1,3,6,9.

removed as the lowest pin row interacting with the tows varies between each layer. Tow density should also be more evenly distributed on the end-fitting,

For the first filament wound layer of a cylindrical shaped end-fitting, the tow transitions vertically up to a pin in the row beneath the top-most pin row, as seen in figure 3.29(b). It then traverses diagonally to the top-most pin row, around which pull-back then occurs. Subsequent layers then interact with the next two adjacent pin rows, moving sequentially down the structure. The fourth layer can be seen in figure 3.29(c).

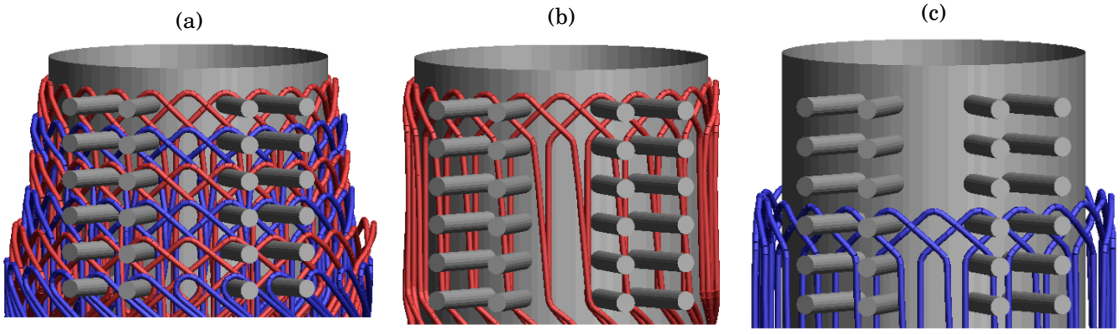

Figure 3.29: (a) Two-row pin wrapping pattern with six filament wound layers, coloured blue and red alternately. (b) First and (c) Fourth layers only. Some pins have been removed so that the tow path can be seen clearly.

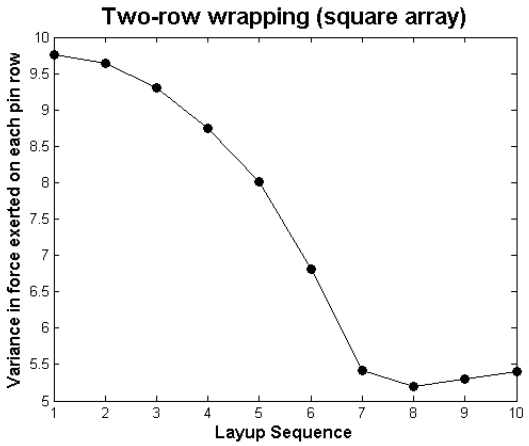

Figure 3.30: Variance in shear force as a percentage of the total, by pin row, for the two-row wrapping pattern, (only a square type pin array is considered).

As with the single-pin wrapping, only a square pin array is considered for this winding pattern. As shown in figure 3.30, the analytical model estimates that load sharing between pins in the array is improved as the layup number increases, and the inner and outer two axial tow layers are substituted for those with larger orientation angles. Load sharing is optimal for layups 7-10, in such cases, variance between the shear force exerted on each pin row is in the range of 5-5.5%. This is comparable with results for the all-row winding pattern with a diamond type array and for the optimal layup sequences.

3.9.4 Pin under-wind pattern

This winding pattern may be considered as an extension to those discussed previously rather than a separate alternative. It aims to reduce the magnitude of the load exerted on the pins in the array, but should have no effect on overall load distribution across the array.

Previously, the tow contacted only the top, or upper, surface of the pins. Following application of tension to the tow, shear force is exerted on the pins in only one direction, as shown in figure 3.32. If we consider a tow with a trajectory that contacts the underside of the pins, then the pins would then also experience a shear force in the opposing direction. The resultant force on a given pin should thereby be reduced.

3.10 Summary

In this chapter, joint and strut arrangement were considered to limit the size of the design space and to compare their relative performance. The objective was to develop an understanding of the factors that may effect the joining mechanism and to establish a preliminary ranking of feasible designs.

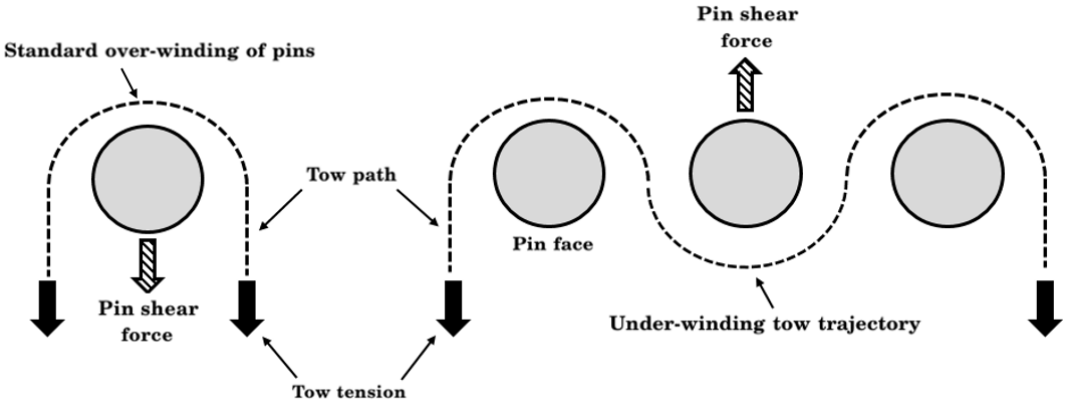

Figure 3.31: Diagram showing the tow path for a pin under-wind pattern. The opposing direction of pin shear force is indicated, for the middle "turn" pin.

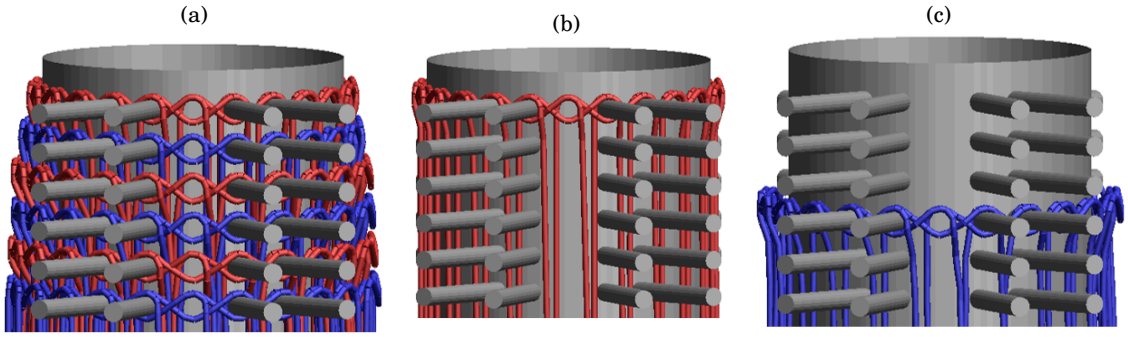

Figure 3.32: (a) Pin under-wind pattern for an end-fitting with six filament wound layers coloured blue and red alternately. (b) First layer and (c) fourth layers only. Some pins have been removed so that the tow path can be seen clearly.

Firstly, a method for calculating the relative volume proportions of the tow and matrix was used in combination with CLT, to calculate the elastic properties of the central composite part of the strut overlaying the mandrel. Structural behaviour was predicted to be greatly influenced by the non-uniformity of fibre coverage in this region. This was forced by the presence of the pins and pre-condition established to avoid tow puncturing. Layup sequences were compared using a numerical approach in Abaqus® Implicit, for strain allowables typical for a carbon fibre reinforced, epoxy composite material.

Secondly, the novel joining solution and the interaction occurring between filament wound fibre-tows and the metallic pins at the strut ends, was reduced to a simple analytical framework. This allowed for the examination of a number of feasible tow trajectories and winding patterns in the region of the pin array. Configurations were considered to be improved for cases where loading of the pins was most evenly distributed.

3.10.1 Final joint designs

A total of 5 joint configurations, as listed in table 3.6, are continued through to assessment by FEM in chapter 4. Types A-C should provide improved joint designs. They comprise of end-fittings with square type pin arrays and a layup sequence on the mandrel of $[0_6]$, which was found to be optimal in section 3.7.2. The winding pattern in the region of the pin array is an example of a single pin wrapping. This was predicted to provide equal load sharing across the pins and should therefore improve load carrying capability in the joint and strut.

Table 3.6: Joints designs for continuation through to mechanical performance assessment using FEM.

Joint configuration	Layup sequence	Array type	Winding pattern	Pull-back type
A	$[0_6]$	Square	Single-pin wrapping	2 over
B	$[0_6]$	Square	Single-pin wrapping	Under-wind
C	$[0_6/90]$	Square	Single-pin wrapping	2 over
D	$[\mp 45/0_2/\pm 45]$	Square	Two-layer wrapping	1 over
E	$[\mp 10/0_2/\pm 10]$	Diamond	All-row wrapping	1 over

In A, tow pull-back occurs around two adjacent pins. This is to provide a fail-safe mechanism, whereby tow-pin interaction is not lost through failure of a single pin.

Joint B uses the under-wind trajectory described in section 3.9.4. FEM can be used to assess if the magnitude of the load exerted on the pins is reduced as predicted by the analytical belt-and-pulley model. A uniform reduction of 64% in shear force is expected across the pins in the array, for this particular winding pattern and joint configuration. Also, it can be determined if tow pull-back in this manner leads to stress concentrations developing in the fibre-tow, due to the significant manipulation of its trajectory and relatively small turning radius. This was not considered in the analytical framework.

Joint type C includes an additional, outer hoop layer of filament wound tows. This is to assess if improvements in axial, hoop and hoop-shear stiffness of the central composite part of the strut, overlaying the mandrel, are observed, as predicted in section 3.7.3.

Joint type D consists of a strut with layup $[\mp 45/0_2/\pm 45]$. This was found to be the 2nd ranked layup sequence by F value. It is also of particular interest as its inner and outer layers have the largest fibre orientation angles, furthest from an axial fibre path. A two-layer winding pattern is used. This was found to provide reasonable load sharing across the pin array, for this particular layup sequence (5% variance in pin shear force). Pull-back is conducted around a single pin in this case. Loss of contact between the fibre-tow and pin array does not occur through failure of a given pin; material wastage and structural weight should therefore be reduced by initiation of tow pull-back around a single pin.

Joint E is predicted to provide reduced structural performance capability and is continued through for comparison purposes and to validate the predictions made in this chapter. The layup, $[\mp 10/0_2/\pm 10]$, is conjectured to fail both axially and in hoop-shear. The diamond type array, in

combination with the all-row winding pattern in section 3.9.2, is predicted to result in relatively poor load distribution across pins in the array, with some pins experiencing a 10% higher shear force.

3.10.2 Limitations

Some limitations may be apparent in the methods utilised in this chapter to compare designs for the hybrid strut and joining mechanism.

Firstly, for analysis of the non-uniform fibre coverage of the mandrel's surface, treatment of each filament wound layer as two laminates of thickness equal to an estimated tow thickness (appendix A.2), may lead to considerable overestimation of the final thickness of the strut's composite part. Also, the fibre-tow may spread significantly beyond its assumed diameter of 2mm, during fabrication.

These effects may combine to provide a considerable underestimate of the fibre coverage of the mandrel when compared to the as-manufactured, physical reality. This may affect calculation of the elastic properties using the volume averaging method and resin rich areas may be exaggerated. This will in turn effect the accuracy of the numerical models, in section 3.7, in providing a ranking of the feasible layups. Furthermore, the numerical model considered only the direct application of tensile strain to the central composite part of the strut. In reality, load would be transferred indirectly from the metallic end-fittings via the mechanical interaction between filament wound fibre-tows and the pins at the joining mechanism. Estimated strains such as hoop-shear may then be significantly less for the latter case, as the form-fit between the pins and fibre tows in the joint may limit any axial rotation or twisting of the strut, reducing extension hoop-shear coupling resulting from an applied axial load.

Secondly, for the winding pattern around the pin-structured end-fittings, reduction of the pin-tow interaction occurring in the joining mechanism to a 2-dimensional pulley wrapping problem, may be an oversimplification that does not accurately capture the behaviour of the physical, 3-dimensional structure.

CHAPTER 4

MESO-SCALE MECHANICAL PERFORMANCE ASSESSMENT OF THE HYBRID COMPOSITE-METAL JOINT AND STRUT

Chapter 3 considered design parameters of the hybrid composite-metal joint and strut. Particular attention was paid to the layup sequence for the strut's central mandrel, and the mechanical interaction occurring between the filament wound fibre-tows and the the metallic pins in the joining mechanism at the strut ends. From these preliminary design considerations, five strut and joint configurations were proposed for further analyses using Finite Element Analysis (FEA) [74].

A meso-scale modelling approach, with characterisation of individual tows within a matrix material, is necessary to capture tow pull-back around the pins and assess the mechanical interaction occurring in the joining mechanism at the strut ends. For this a two-stage modelling framework is implemented in explicit finite element solver LS-Dyna® [75].

Firstly, the Single Filament (SF) method is used in the "Tow Positioning" stage to predict the as-manufactured path of the fibre-tows on the strut, which would be expected following the filament winding process. Relative tow position and their degree of interaction with the pin-structured end-fittings will vary significantly between joint types A-E due to their different winding patterns.

The virtual tows are then converted to a 3D continuum (solid) elements for the tow cross-section, to allow for mechanical analyses in the "Strut Loading" stage. Matrix material is independently meshed and the two constituents are linked using a constraint-based coupling mechanism provided by LS-Dyna® function *CONSTRAINED_LAGRANGE_IN_SOLID (CLIS), so that the mechanical behaviour of the strut can be assessed in its final, consolidated operating form. Quasi-static virtual tests allow for the relative performance of strut configurations A-E to then be determined.

Stage 1: Tow Positioning

4.1 Single Filament (SF) Method

In the Single Filament (SF) method, a virtual tow is represented as a chain of truss elements with constant, circular cross-section (see figure 4.1(a)). Connectivity between the truss elements that comprise a virtual tow is established via the sharing of their end-nodes with adjacent elements in the chain. This approach is similar to the Digital Element (DE) method developed by Wang *et al.* [13], in which yarns were modelled as a chain of trusses connected by frictionless pins.

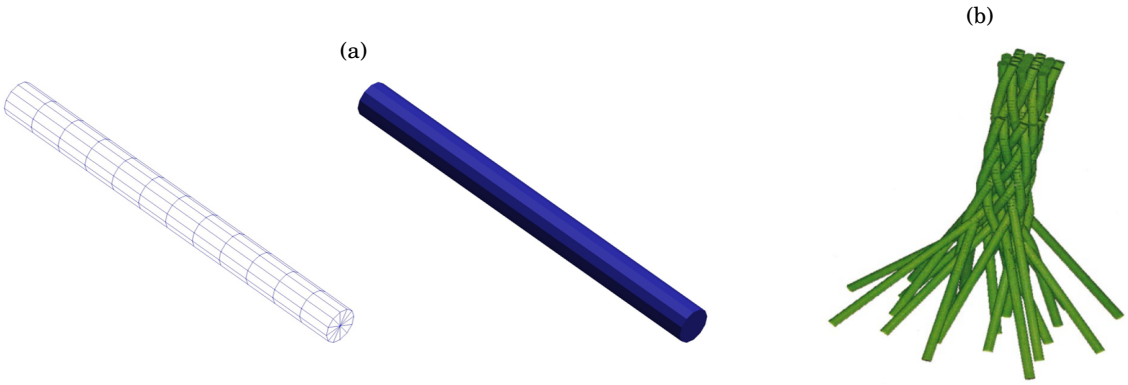

Figure 4.1: (a) Length of virtual tow consisting of a truss element chain with constant, circular cross-section. (b) Use of the Single Filament approach for 3D rope braid simulations in [13].

The discretisation of the tow, or yarn, into a series of trusses with minimal length, (when compared too the full length of the tow), allows the virtual tow to become fully flexible and thus imitate the flexural rigidity and bending behaviour of a physical fibre-tow. Tow movement resulting from interactions during textile production operations, such as weaving and braiding, can then be captured, as shown in figure 4.1(b). Note, however, that realistic material properties are not conserved in the SF approach, (see section 4.2.4). It is therefore unsuitable for mechanical analysis purposes.

In this work, the SF method is used to predict the as-manufactured path of the fibre-tow on the strut's surface, which would result following the filament winding process.

4.2 Modelling methodology

4.2.1 Model geometries

Construction of the model geometries is automated via a MATLAB® script that generates an LS-Dyna® input file. Recall, the initial structure prior to fabrication consists of a cylindrical mandrel partitioning two pin-structured metallic end-fittings. These three components (the mandrel, end-fittings and pins) are modelled using four-node rigid shell elements. It is sufficient to consider these parts as rigid bodies as they are used only as a contact surface for the virtual tows, in order to model the interactions between the physical carbon fibre and these structures, that occur during layup of the fibre-tows.

The virtual tow is assumed to have a nominal cross-sectional diameter of 1mm. The length of the individual truss elements forming a given virtual tow chain is set at 1mm so that the truss element aspect ratio is 1. It is not possible to accurately capture the cross-sectional dimensions of a physical tow, (whose cross-section shape may vary significantly due to factors such as tow tension, and the interactions and degree of entanglement between the fibres within the tow), into a virtual tow with a uniform, circular cross-section. Consequently, the SF method may both underestimate the degree of tow coverage of the strut's surface, and overestimate the thickness of the filament wound layers. These may combine to provide a relatively low total fibre volume fraction in the strut, when compared to the physical reality. This is a limitation to the approach. Efforts are made in chapter 5 to use a higher fidelity model of the fibre tow, to obtain more realistic tow geometries and fibre volume content in the region of the joint.

Additionally, there may also be some discrepancy with estimates of mandrel coverage and elastic properties as predicted in chapter 3, in which the tow is considered as a rectangular band of cross-sectional width and height, of 2mm and 0.42mm, respectively, (see appendix item A.2).

4.2.2 Tow path assignment

Initially, the position and trajectory of the virtual tows is determined analytically through designation of the tow centreline path. This path is described by a sequence of nodes which form the end-nodes of the truss elements in the virtual tow chain. Each wind layer forms a closed-loop by the equivalence of the first and last nodes of the virtual tows. Layers are placed individually and independently in a sequential manner moving radially outwards away from the mandrel surface, until a full wind sequence has been established.

The winding pattern is constructed by defining the tow position and trajectory at distinct regions on the strut's surface, namely, on the mandrel, in the pin array and during pull-back around the pins

For the mandrel, the tow centreline can be specified using a cylindrical coordinate system (equation 4.1) and the known winding angles, θ_u and θ_d. The tow path through the pin array can be constructed similarly using the pre-determined pin arrangement.

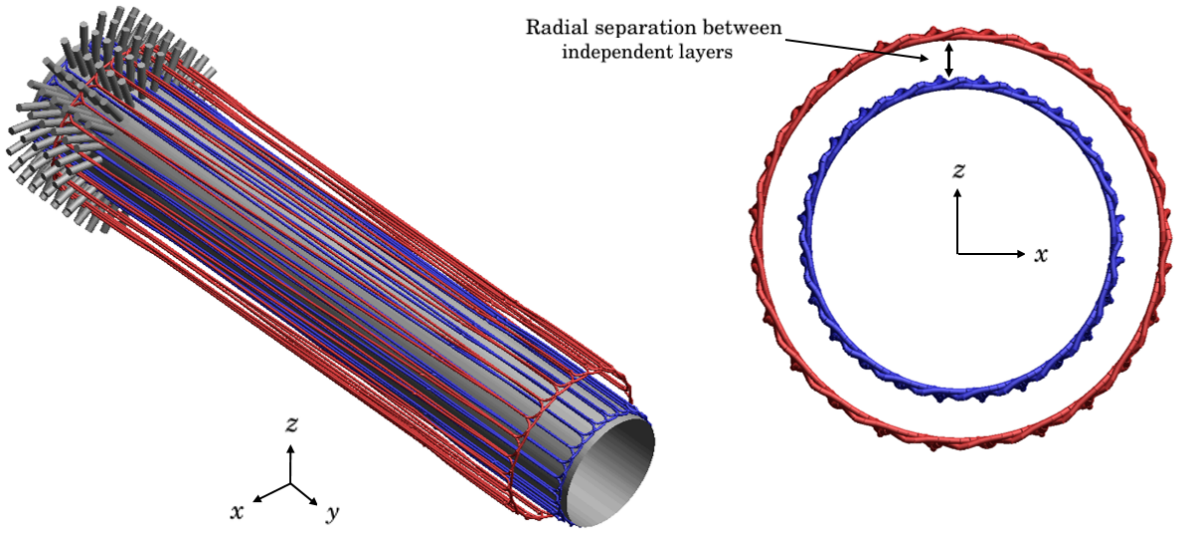

Figure 4.2: Radial separation between independently placed virtual tow layers 1 and 4, for strut configuration A. Full strut view with pins removed from nearest end-fitting for clarity (left) and x-z cross section view (right).

$$
\begin{aligned}
x &= \rho\cos(\phi) \\
y &= y \\
z &= \rho\sin(\phi) \\
\phi &\in [0, 2\pi]
\end{aligned} \tag{4.1}
$$

The path of the tow in the pull back region is assigned using two quadratic Bezier curves [76] $B_1(t)$ and $B_2(t)$, as seen in equation 4.2 and figure 4.3. These interpolate the tow centreline between points P_0 and P_2, and P_3 and P_5, respectively. The centreline approaches but does not intersect control nodes P_1 and P_4. These nodes instead determine the trajectory of the interpolation curve and are set at a position relative to the pin's surface to prevent penetration between the virtual tow and turn pin, whilst ensuring the tow path follows a smooth arc around the pin. For instances where pull-back occurs around multiple pins, the tow path also includes region R. Here the tow is travelling in a circumferential direction around the end-fitting's surface and between adjacent pins on a given row.

For the under-wind pattern described in section 3.9.4, the tow path is formed by a concatenation of Bezier curves whose control nodes are positioned so that the tow under-winds the central pin as shown in figure 3.31, whilst ensuring no tow-pin inter-penetrations and reasonable path smoothness.

$$
\begin{aligned}
B_1(t) &= (1-t)^2 P_0 + 2t(1-t)P_1 + t^2 P_2 \\
B_2(t) &= (1-t)^2 P_3 + 2t(1-t)P_4 + t^2 P_5 \\
&\text{for } 0 \le t \le 1
\end{aligned} \tag{4.2}
$$

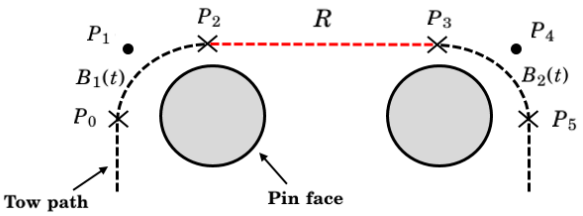

Figure 4.3: Two-dimensional representation of the tow trajectory during pull-back, with regions $B_1(t)$, $R(t)$ and $B_2(t)$ defining the tow path.

For a given wind layer, tow crossing points may occur, as seen in figure 4.4(a). The tow path must be corrected in order to prevent penetrations between virtual tows. Inter-penetrations are first detected by a node-to-node search procedure, using the truss end-nodes that describe the tow centreline path. If any two (non-adjacent) centre nodes lie within a distance less than the tow diameter from each other, penetration exists. These are then removed through translation of the centre-nodes of the (outer) virtual tows, as shown in figure 4.4(b).

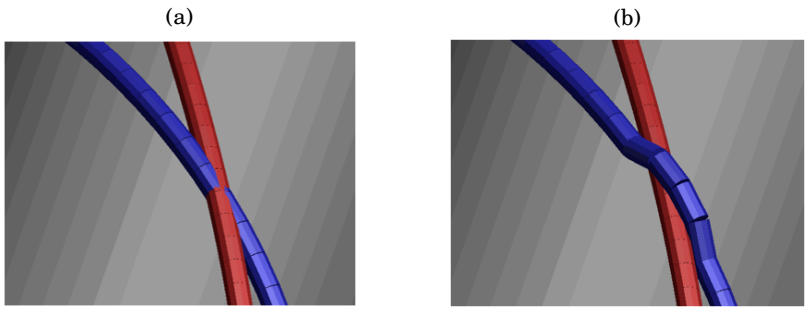

Figure 4.4: (a) Inter-penetration between virtual tows, coloured red and blue, at a tow crossing point on the surface of the mandrel (grey). (b) Corrected tow path to remove penetrations. Order precedence of the tows is established by the layup sequence.

Penetration correction may however lead to an unrealistic, undulating tow path, as seen in figure 4.5. Additionally, layer-by-layer sequential placement causes large radial separation distances between the filament wound layers. Therefore, following initial analytical assignment, a subsequent FE simulation is conducted in LS-Dyna® to smooth the tow path, increase radial density and to model the effect of tow-metal and inter-tow interactions on final path determination.

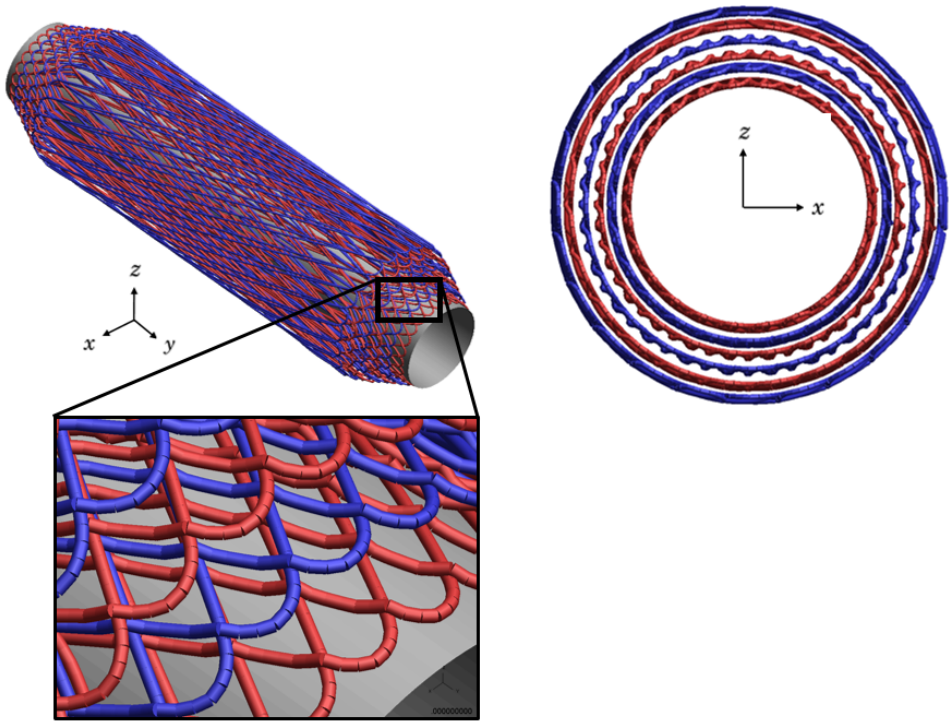

Figure 4.5: Initial, wavy tow path on the strut, with significant spacing between the virtual tow layers, coloured red and blue alternately. Pin surfaces have been removed so that the tow path can be seen clearly.

4.2.3 Tow path refinement

Mahadik and Hallett [77] modelled yarn crimp occurrence and severity in a layer-to-layer angle interlock, 3D woven fabric, using a variant of the Multi-Filament (MF) (see section 5.1). The fabric was initially assigned a loose topology, with unrealistic spacing between neighbouring yarns. The virtual yarns were then subjected to a tensile load through the assignment of a fictional coefficient of thermal expansion to the yarns, and subsequent application of a linear temperature gradient. This had the effect of reducing the length and straightening the warp and weft yarns, so that the model fabric approached a more realistic thickness.

Thompson *et al.* [14] implemented a similar technique in LS-Dyna® to simulate the as-woven state and thickness of biaxial tricot chain stitch non-crimp fabrics (NCFs), as shown in figure 4.6. The stitch yarn, modelled using a Single Filament (SF) approach, was subjected to tension via a temperature gradient, in order to reduce excess length and compact the yarns to a more representative thickness.

Here a similar methodology is used to refine the tow path on the strut. The virtual tow material is assigned an artificial coefficient of thermal expansion and a negative temperature gradient is applied to the model. A level of pre-strain is experienced in the tow structure, so that the effect observed is a reduction in excess tow length and the attainment of a smooth, realistic

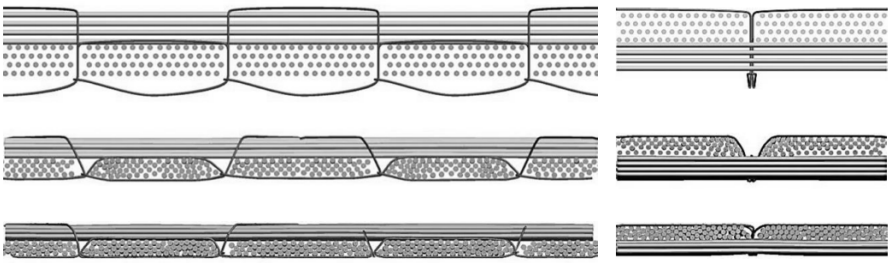

Figure 4.6: Compaction of an NCF from an initial loose topology to the physical fabric thickness, via tensioning of the stitch yarn using a temperature load [14].

tow path, as illustrated in figure 4.7. The virtual tows are pulled closer to the struts surface, encouraging nesting between layers and increasing the degree of radial tow density.

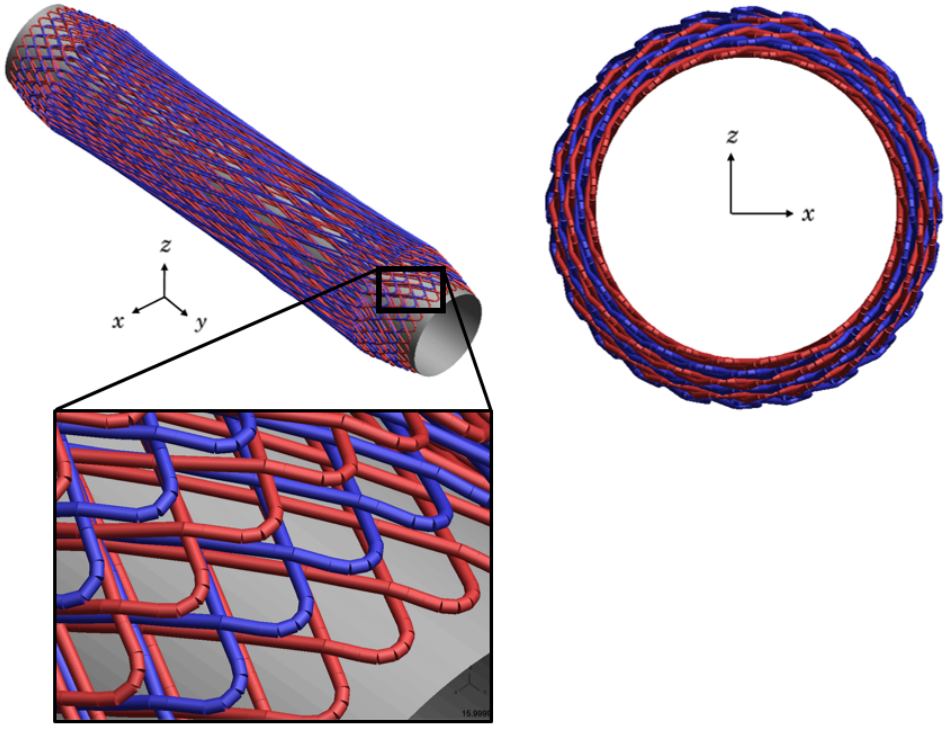

Figure 4.7: Final, smooth tow path on the strut, with improved radial density of the virtual tow layers, coloured red and blue alternately. Pin surfaces have been removed so that the tow path can be seen clearly.

4.2.4 Material parameters and contact definition

Model geometries (end-fitting, mandrel, pins and tow) are assigned fictional material densities and moduli of 5e-3 tonne / mm^3 and 200 GPa, respectively. Three separate contact definitions

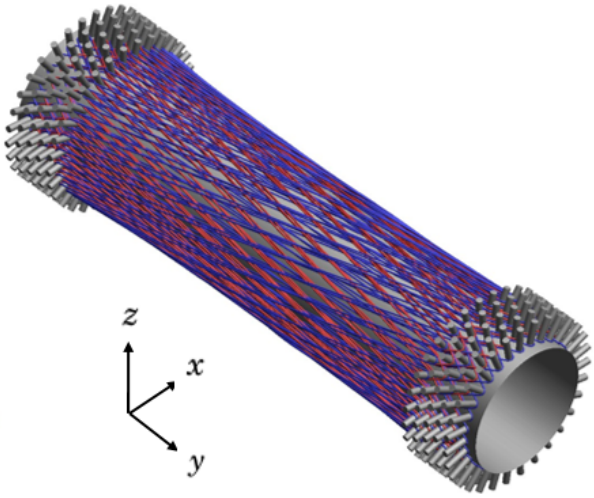

Figure 4.8: Final position of the virtual tow layers on the strut. With virtual tows modelled using the Single Filament (SF) method and following the simulation step in which the tow path was refined.

are utilised. BEAMS_TO_SURFACE contact is used to model interactions between the tow and pin surfaces, and between the tow and the mandrel and end-fitting surfaces. Contacts between virtual tows are established by type AUTOMATIC_GENERAL.

Material parameters are used to ensure adequate contact definition (minimal inter-penetrations between parts) and reasonable analysis times. Artificial material properties are acceptable as the Single Filament (SF) is not used for mechanical analysis purposes. Contact stiffness will be affected by choice of material properties but assigning material values so that model contact replicates the physical behaviour of the fibre-tow and metal during winding, is impractical for a virtual tow of constant, circular cross-section.

The tow-pin contact definition is assigned a low coulomb friction coefficient of 0.05. This is to encourage the virtual tows to slip down the pin surface's and consolidate around the end-fitting during application of the thermal load. Friction between the mandrel and end-fitting surfaces, and the virtual tows, is determined to be less important for determining the final tow path. Only the inner layers will be in contact with the mandrel and end-fitting, and the limited number of tow crossing points and circular cross-section result in the effect of inter-tow friction being negligible.

A temperature gradient of -1° is applied to the model over an analysis time period of 15 seconds. The temperature is then maintained for a further 5 seconds in order to reduce oscillatory effects in the virtual tow. A damping factor of 10 is also used via the LS-Dyna® keyword DAMPING_GLOBAL.

The virtual tow layers are assigned different thermal coefficient of expansion values dependant on their initial radial distance (layer order) and fibre orientation angle down the mandrel

length. The strain applied to the truss elements in the virtual tows is assumed to result in only a change in axial length (reduction) proportional to the product of the expansion coefficient and thermal load, as given by equation 4.3. Where L, ΔL, ΔT and α_T denote the initial truss length, the length change, temperature gradient and coefficient of thermal expansion, respectively.

$$\epsilon = \frac{\Delta L}{L} = \alpha_T \Delta T \tag{4.3}$$

Outer tow layers require a larger prescribed strain in order to consolidate more effectively towards the mandrel surface. Likewise, greater strain must be applied to layers with larger orientation angles, as these have more excess tow length due to their longer path. Determination of appropriate expansion coefficients values, can only be conducted qualitatively, by visual inspection of the final tow position and path smoothness. That is, if the tow structure appears to have significant excess length, (characterised by an undulating tow path with harsh out-of-plane change in direction, away from the strut's surface), the coefficient is increased by an appropriate factor and the model is re-run. The variability caused through this qualitative approach in determining a level of prescribed strain to achieve reasonable tow paths, is further discussed in section 4.6 as a possible model limitation. However, quantitative assessment of the tow paths obtained through the simulation can be conducted against the expected, prescribed winding angle along the length of the strut's central mandrel, as described in section 4.3. Note also that the outer hoop layer orientated at 90° to the strut's longitudinal axis, as used in strut configuration C, is not included in this simulation step. A smooth path can be assigned analytically.

4.3 Analysis of simulated tow paths

The local direction of a tow can be found, at points along its length, using the orientation of the individual truss elements that comprise the virtual tow chain. This analysis is useful for the mandrel section of the strut, as the local tow angle can be compared with the prescribed winding angles θ_u and θ_d, to determine if appropriate levels of tension have been applied to provide a smooth tow structure (which is qualitatively assessed), without significant alteration of its intended trajectory.

In the region of the pin-structured end-fittings, such analyses become less meaningful as the tow trajectory varies significantly throughout the pin array and cannot be compared against a prescribed angle. Also, substantial tow movement should constrained due to the presence of the pins.

Figure 4.9 shows the extracted local angles for a virtual tow as it transitions up and down the length of the mandrel in the first layer of the layup sequence for strut type A. The prescribed winding angles θ_u and θ_d are also plotted.

The local tow orientation differs minimally from the intended direction, (within ±2°), with maximum deviation occurring at tow-crossing points as the tow trajectory is altered due to

out-of-plane (radial) movement of the tow. This trend is consistent throughout the layup sequence and is also repeated in strut configuration B, which has an identical layup sequence, (note type C has an additional, analytically determined outer hoop layer).

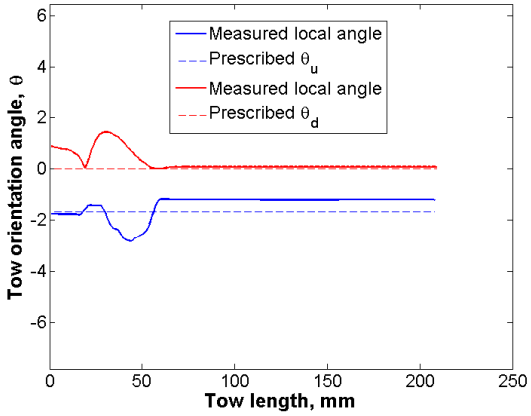

Figure 4.9: Variation of the local tow direction in the first filament wound layer of strut type A. Minimal deviation from the prescribed winding angles occur only at tow crossing points.

Figure 4.10 shows the extracted local angles for a virtual tow in layers (a) 1, (b) 2 and (c) 3 of strut type D. Recall, this strut configuration has an (unaltered) layup sequence of $[\mp 45\, 0_2 \pm 45]$.

Significant deviation from the prescribed angle is seen towards the ends of the tow in layers 1 and 2. This occurs as the relatively large (absolute) winding angles reduce the contact area between the virtual tow and pin, resulting in increased tow slippage as it transitions onto and off the pin array. This does not occur with small orientation angles as tension and the position of the tow is more readily maintained between the pins at opposing ends of the strut. This is observed for the third filament wind layer, as shown in figure 4.10(c).

Divergence from the prescribed winding angle, in this manner, for high angled tow trajectory's onto and off the pin array, is not thought to be a model limitation. These would be expected to occur also during the manufacture of the physical joint and strut. Therefore, it is possible to conclude that tow path assignment, and refinement, using the methods described in section 4.2, provide a reasonable approximation of the expected as-manufactured path of the tow, resulting from fabrication of the hybrid composite-metal joint and strut.

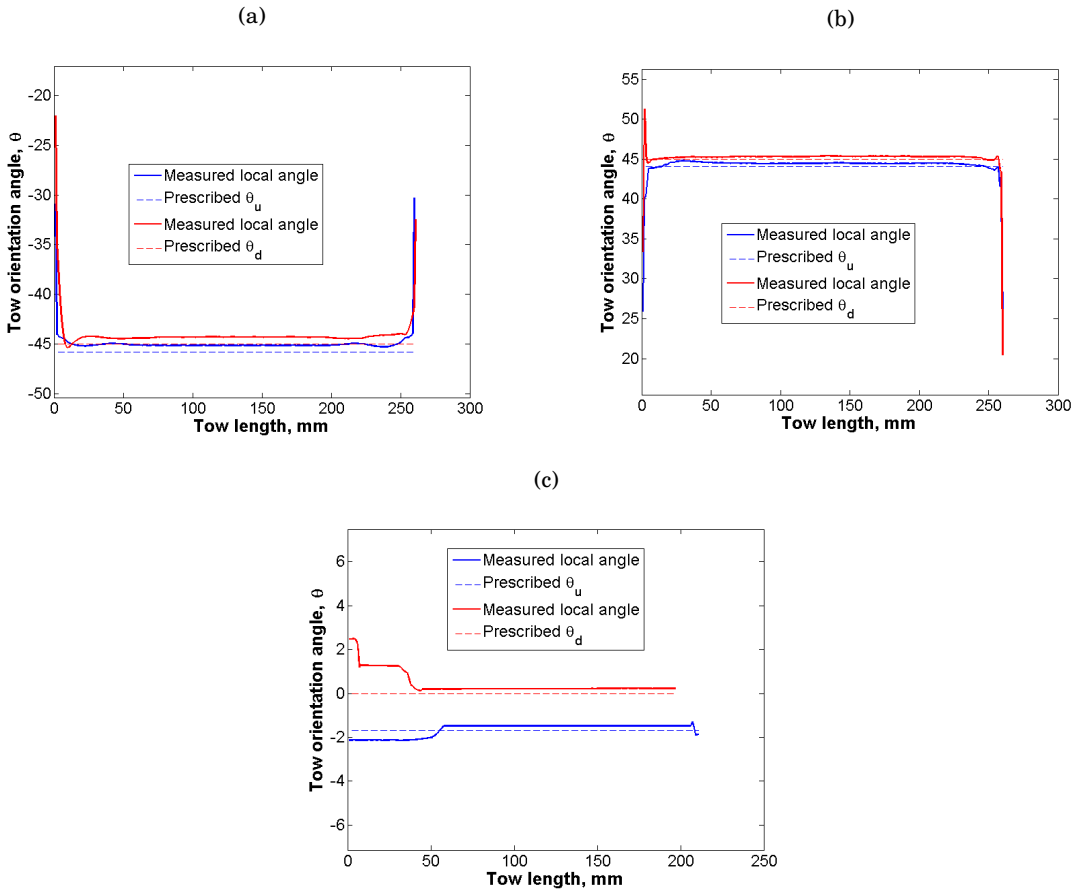

Figure 4.10: Local fibre orientation for strut D, layers (a) 1, (b) 2 and (c) 3. Significant deviation from intended tow direction occurs as the tow transitions off the pins, given by plot extremities, for large orientation angles.

Stage 2: Strut Loading

4.4 Methodology for meso-scale mechanical model

Recall, the Single Filament (SF) model is unsuitable for mechanical analysis purposes realistic material properties are not adopted for the virtual tows and pin structured end-fittings.

For mechanical performance assessment using Finite Element (FE) methods, yarns in composite fabrics and preforms are typically represented using 3D continuum (solid) elements [78], [17], [79], [18], [80]. The yarns are generally considered transversely isotropic, with transverse Young's moduli (E_2 and E_3) taking very small values in comparison to the longitudinal modulus (E_1),

which represents the fibre direction. Yarn paths are determined by the fabric's representative unit cell [81], [82].

For mechanical modelling of consolidated fabrics, it is necessary to include the matrix material. Response under loading may vary significantly from a dry fabric, as the matrix binds the fibre-reinforcement, restricts fibre movement and gives the composite its shape. It also carries a proportion of the load, depending on the fibre direction (alignment) and total fibre volume fraction.

A conformal mesh between the fibre reinforcement and the matrix can be used, in which nodes at the interfaces of yarn and matrix elements are shared [83], [84]. However, a large number of elements may be required in order to represent the individual constituents and the yarn-matrix interface, leading to significant computational cost even at the level of a representative unit cell.

Alternatively, voxel based techniques [85] can be employed for mechanical analysis of composite fabrics at the unit-cell level [86], [87], [88]. The domain of the unit-cell is meshed using regular 8-node (cubic) elements, or voxels. Voxel's are assigned material properties of the yarns if they are found to be contained within the yarn volume, otherwise the voxel consists of only matrix material. The voxel's must however be sufficiently small to prevent stepped element surfaces and stress discontinuities at yarn-matrix boundaries [69]. Voxel based techniques therefore also necessitate a large number of elements in the representative model, and significant associated computational cost.

For the case of the hybrid composite-metal strut examined in this work, resin infiltration and consolidation would be required for final component manufacture. Although these processes are not simulated, it is important that the mechanical behaviour of the strut is examined in its normal operating form, i.e. with matrix. However, model size, in terms of global volume and the number of finite elements required to represent the full strut, would incur infeasibly large computational cost, through adoption of either conformal meshing or voxel-based techniques.

Alternative strategies have been developed for modelling of textile composites. Jiang *et al.* [89] used the "domain superposition technique (DST)" to model the mechanical response of woven composite fabrics. Matrix was constructed for the model's global volume, as defined by a cubiodal ("box") region with dimensions equal to that of the full fabric unit cell. The yarns volumes were meshed independently, so that node sharing at the yarn-matrix interface was not enforced. Instead, stress transference between the two constituents occurred via a constraint equation coupling mechanism, in which local tow nodes were linked with the global mesh nodes. Virtual tests showed that results provided by DST, with respect to predicted stiffness and stress distribution in the fabric, correlated well with a conventional conformal mesh. This held even for relative coarse meshes for DST, indicating the potential for increased computational efficiency without significant reduction in accuracy; in addition to reduced mesh complexity as the need for node sharing at yarn-matrix boundaries is negated.

Tabatabaei *et al.* [90] also used a mesh superposition technique to conduct meso-scale FEA of a

reinforced composite fabric (5H satin weave). Matrix and yarns were coupled using the "Embedded Element (EE)" function in Abaqus ®. Good agreement (maximum difference of 12%) was observed for the fabric's predicted moduli and poisson's ratio, against a model using a conformal mesh. Stress/strain profiles (important for predicting damage initiation and propagation) also compared well. Mesh sensitivity analysis suggested that refinement of the host (matrix) part may improve accuracy of the fabric's predicted out-of-plane moduli (E_z, G_{yz} and G_{xz}). However, in-plane properties (E_x, E_y and G_{xy}) were found to be similar across all mesh densities, with a refinement factor of 200 yielding a difference of less than 5% in these values. Alteration of the yarn mesh density had no effect.

In this work, as described in section 4.4.2, the virtual tows are firstly converted to 3D continuum (solid) elements for the tow cross-section. The volume of the matrix material is made to completely contain the virtual tows (section 4.4.1). The virtual tows and matrix are independently meshed and linked via a constraint-based coupling mechanism provided by the LS-Dyna® keyword *CONSTRAINED_LAGRANGE_IN_SOLID (CLIS). This provides a computational efficient means for including matrix properties for mechanical performance assessment of the composite strut.

The coupling mechanism provided by CLIS can be either penalty or constraint based. Both methods, however, require an overlapping mesh but not shared nodal coordinates for the coupled entities, which are designated as either the "master" or "slave" parts in the interaction. In general, computational efficiency can be improved through avoidance of over-meshing via non-conformance of nodes, and the use of different mesh densities for the master and slave parts.

At each time step of an explicit finite element analysis, the coupling algorithm calculates the nodal forces for both the slave and master nodes. A penetration search is conducted at "coupling" points distributed over the surface of the slave segment and using the relative velocities ($vs-vm$) of the slave and master nodes, and the finite difference scheme given in equation 4.4. Here d is the penetration depth that represents the amount by which the coupling constraint is violated. As a rule, the slave node must be a Lagrangian mesh node, but the master node can be Eulerian, ALE or Lagrangian.

$$\underline{d}^{n+1} = \underline{d}^{n} + \left(\underline{v}_s^{\,n+\frac{1}{2}} - \underline{v}_m^{\,n+\frac{1}{2}}\right)\Delta t \tag{4.4}$$

Current literature on the use of CLIS to couple matrix and fibre-reinforcement in composite materials is not available. For this reason, several verification studies are first undertaken in section 4.5, prior to applying CLIS to the full joint model.

However, CLIS has been used extensively to model fluid-structure interaction (FSI) [91]. In such cases, the structure is modelled using a conventional Lagrangian formulation consisting of solid or shell element types, and the fluid is considered using an Eulerian or Arbitrary Lagrangian Eulerian (ALE) formulation, due to the potential for large mesh distortion and resulting instabilities.

Moreover, Moutoussamy *et al.* [92] used the CLIS function to provide a Lagrangian-Lagrangian coupling for reinforced concrete structures. The rebar reinforcement was modelled using beam elements contained within a 3D continuum element mesh of concrete. Good correlation with analytical calculations of resultant forces was found for a number of validation cases. Failure behaviour such as crack initiation in the concrete, was also found to be well represented.

4.4.1 Tow geometry conversion

The virtual tows are converted to 3D continuum (solid) elements for their cross-sections. Firstly, the paths of the virtual tows are extracted from the SF model, following the simulation step described in section 4.2.3, using the nodal coordinates that form end-nodes of the truss elements that comprise the virtual tow chains. These nodes define a centreline-path for each virtual tow forming a given filament wound layer. The virtual tows are then converted to 3D continuum elements for the tow cross-section.

Examples in literature often assume a virtual tow, or yarn, with elliptical [93], [94] or lenticular [95] cross-section shapes. Here, cross-section nodes are defined in a hexagonal pattern in two-dimensional plane, as shown in figure 4.11(b). This cross-sectional shape is chosen as it lies within the circular cross-section of the truss elements in the SF representation. This both limits initial penetrations (and associated numerical instabilities during FEA) between virtual tows following conversion to solid element types, and causes minimal loss to the tow's cross-section area, preserving the relative tow spacing apparent in the SF representation. Efforts are made in chapter 5 to account for more realistic tow geometries and cross-section shapes.

These cross-section nodes are then translated to the coordinates that define the extracted tow centreline path. The cross-section plane normal is then aligned with the tow direction at that point, defined as the vector a between two adjacent path nodes. Appropriate assignment of linkage between cross-section nodes gives four 8-node solid elements for each section, (figure 4.11(c)).

As in chapter 3, the tow is modelled as a linearly elastic, transversely isotropic material using element type SOLID_ORTHO and local material axes a,b and c defining the fibre direction and transverse directions, respectively. Material properties for the tow are calculated from the Chamis model [66], (which is restated below in equation 4.5 for a three-dimensional object, as opposed to the flat lamina considered in section 3.6.2.1), and the known material properties of carbon fibre (HTX40 F13 12k) and epoxy resin MVR444, stated in table 3.2. As in chapter 3, a constant intra-tow fibre volume fraction (V_f) of 70% is assumed for the tow.

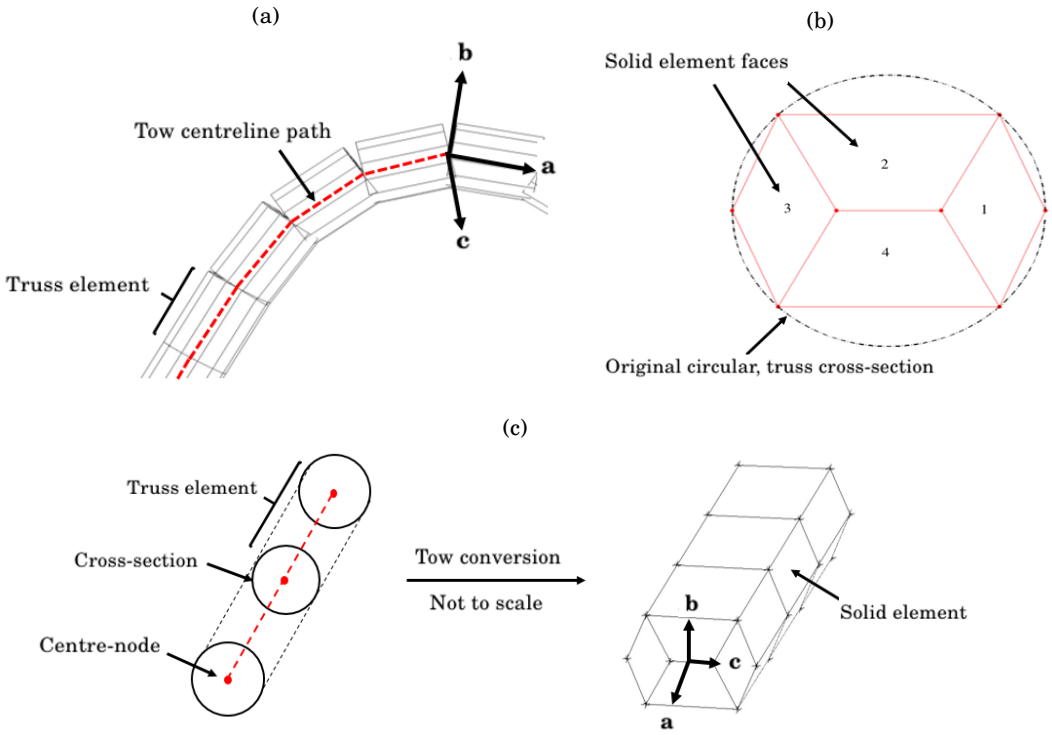

Figure 4.11: (a) Tow centreline path. (b) Tow continuum element cross-section mesh. (c) Tow conversion from SF representation to 3D continuum elements.

$$
\begin{aligned}
E_a &= V_f E_{f1} + (1 - V_f) E_m \\
E_b &= \frac{E_m}{1 - \sqrt{V_f}(1 - (E_m / E_{f2}))} \\
E_c &= E_b \\
G_{ab} &= \frac{G_m}{1 - \sqrt{V_f}(1 - (G_m / G_{f12}))} \\
G_{ac} &= G_{ab} \\
G_{bc} &= \frac{G_m}{1 - \sqrt{V_f}(1 - (G_m / G_{f23}))} \\
\nu_{ab} &= V_f \nu_{f12} + (1 - V_f) \nu_m \\
\nu_{ac} &= \nu_{ab} \\
\nu_{bc} &= \frac{E_b}{2G_{bc}} - 1
\end{aligned}
\tag{4.5}
$$

4.4.2 Matrix (resin) and End-fittings

The matrix (resin) is meshed as a uniform, cylindrical tube with an inner radius equal to the end-fittings' surface radius. The outer radius is determined by the wall thickness needed to completely contain the virtual tow layers, as shown in figures 4.12(c) and 4.12(d). This will vary between joint types A-E. The element mesh is generated in MATLAB® using 8-node solid elements. The matrix part is assigned an elastic material type with the material properties of Epoxy Resin MVR444, (a typical resin used in the manufacture of high performance composite aerospace structures), as seen in table 3.2.

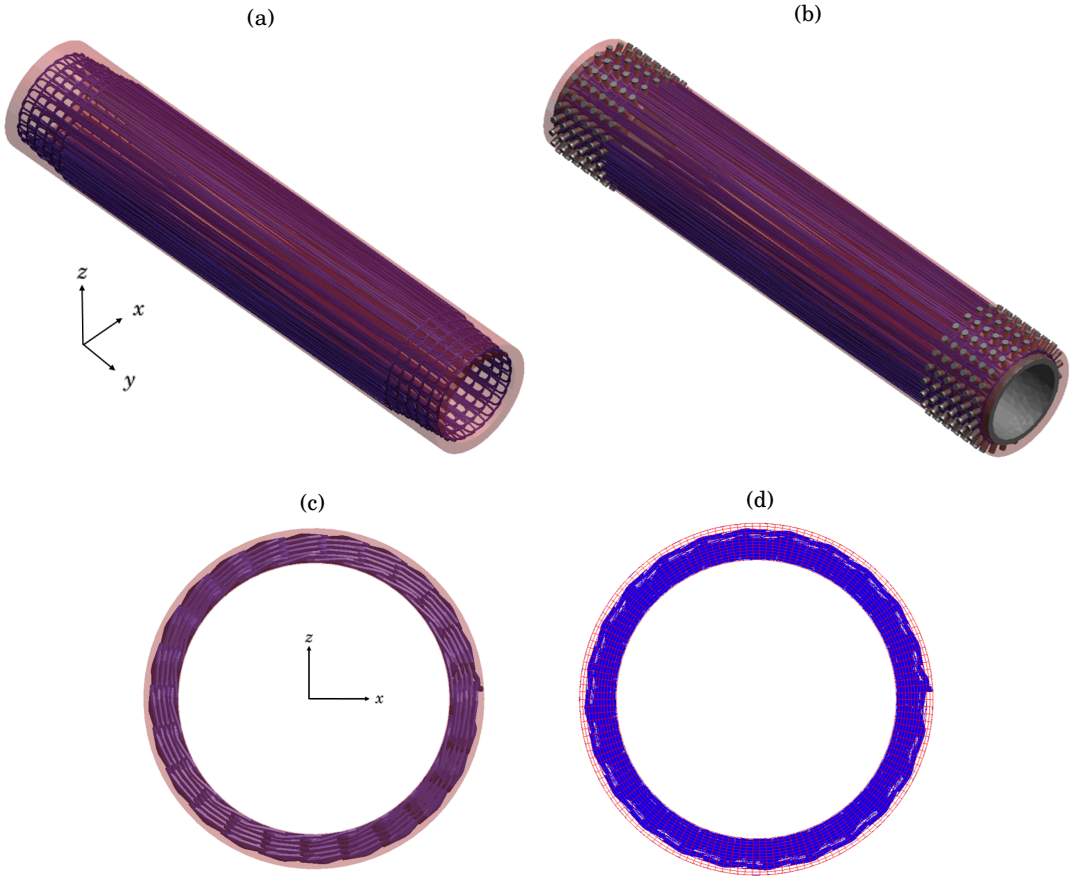

Figure 4.12: (a) Virtual tows (blue) contained within a matrix tube (red) for joint configuration A. The matrix is made partially transparent so the tow structure can be seen. (b) With end-fittings (grey) included. (c)-(d) x-z cross-section view, showing the tow layers completely contained within matrix material.

The end-fitting and pin geometries are meshed in the FE pre-processing software Patran® [96], before being exported to LS-Dyna®. Four-node, tetrahedral elements are used for the end-fitting and pins being considered as a single part. Stress transfer between the pins and the end-fitting's surface should then occur in a realistic manner. The pin-structured end-fitting is modelled using

material type ISOTROPIC_ELASTIC_FAILURE, with material properties of the titanium alloy, Ti-6Al-4V (Grade 5), as seen in table 3.1.

4.5 Qualification of *CONSTRAINED_LAGRANGE_IN_SOLID (CLIS)

Four verification studies are first conducted for the use of CLIS, prior to its application for mechanical performance assessment of strut types A-E in section 4.6.

Case 1 consists of single, straight tow constrained within matrix material. The stress magnitudes and distribution in the tow and matrix are compared against a conformal mesh model, in which node positions are shared between the tow and matrix. The ability of CLIS to accurately represent the load transfer mechanism between the fibre-reinforcement and the matrix is also assessed.

Case 2 is a single tow with hexagonal cross-section (as described in section 4.4.1) similarly embedded in matrix. This is used to clarify the required tow and mesh density, and the parameters assigned to CLIS, which allow for improved modelling of the composite's behaviour.

Case 3 consists of a virtual tow taking an arced path around a cylindrical pin. This is firstly used to assess if the mechanical interaction between the tow and pin is captured, when the tow and matrix are coupled using CLIS. Secondly, tow behaviour should be altered so that the tow and matrix reflect a consolidated composite part, i.e. tow movement should be constrained by the matrix, which should also offer some load carrying capability.

Case 4 is a representative full scale model of strut configuration A, with multiple layers of virtual tows. As in case 3, the action of the virtual tow should be altered by CLIS, so that under loading, strut behaviour is comparable with a final, consolidated component, as opposed to only a dry-fibre network. This is assessed via the movement of the virtual tows, and global strut behaviour.

4.5.1 Case 1. Straight tow

For verification case 1, as shown in figure 4.13(a), the matrix material forms a cuboidal region of cross-sectional width and height 3mm, and length 5mm. The tow is also cuboidal in shape, with cross-section 1mm by 1mm and length 5mm. The element mesh is constructed using regular 8-node (cubic) solid elements, with three different mesh densities consisting of elements of side lengths 1mm, 0.5mm and 0.25mm.

Two separate models are constructed. Model 1 has a conformal mesh, with node positions shared at the tow-matrix interface. In model 2, the node positions of the tow and matrix are deliberately offset from each other, as shown in figure 4.13(b). The tow and matrix are then coupled using CLIS, with the tow and matrix set as the master and slave parts in the interaction, respectively.

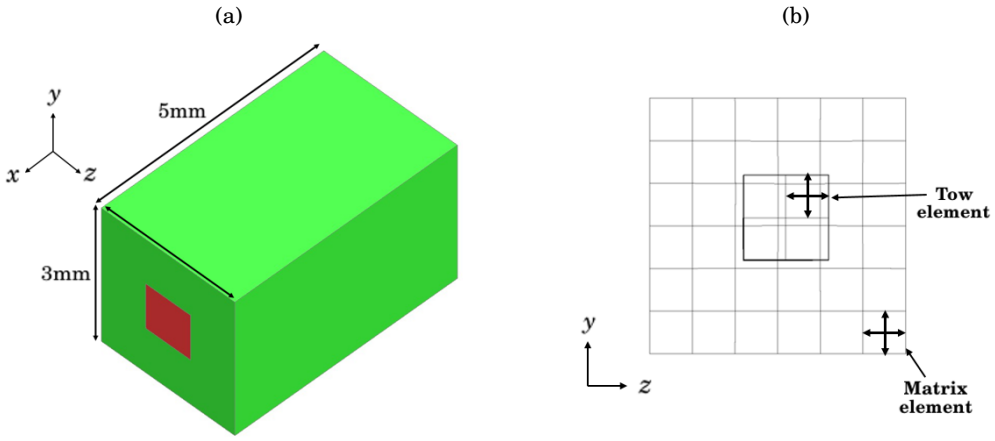

Figure 4.13: (a) Model 1 with shared nodes, tow (red) contained within matrix (green). (b) Cross-section (y-z) view of model 2 (for 0.5mm element side length), showing the offsetting of the virtual tow nodes from the matrix.

An elastic material of modulus 100GPa and 10GPa is assigned to the tow and matrix, respectively, for both models 1 and 2. Note that as in [89] and [90], for mathematical correctness, when employing a mesh superposition method, the tow's material properties should be calculated from material properties of the physical tow, less that of the matrix material, in order to prevent a "double-counting" of the matrix contribution. For simplicity, this is not done here, or during the mechanical analyses of strut types A-E in section 4.6. This simplification offers no constraint with regards to providing a qualitative and quantitative relative performance assessment of the different joint configurations, and removes the necessity of discounting matrix contributions to complex behaviour, such as shear.

A displacement of 0.1mm is then applied to one (y-z) cross-section face of the matrix, with the opposing end being fully constrained, so that an x-direction (length-wise) strain equivalent to 2000 $\mu\epsilon$ is simulated. All other outer faces of the matrix are constrained according to Dirichlet boundary conditions to limit poissons effects. For comparison with the conformal mesh in model 1, the tow in model 2 must also be fully constrained at one end.

Figures 4.14(a)-4.14(c) show the x-direction (length-wise) stress distribution in model 1 (conformal mesh) for the different mesh densities. Figures 4.14(d)-4.14(f) show similar plots for model 2 (using CLIS). The stress field, and load transfer between the tow and matrix, is similar for models 1 and 2, for element sizes of 0.5mm and 0.25mm. Maximum stresses occur in the (stiffer) tow and in the matrix in its proximity.

For the maximum element size of 1mm, stress patterns differ significantly between the conformal mesh in model 1 and the CLIS mesh in model 2. Load sharing is therefore determined not to be adequately captured in this case. Significant compression and distortion occurs at the tow end, as seen in figure 4.15(a). This is due to the relative sparsity of the matrix (slave) elements leading to fewer coupling points per given spatial volume (recall, coupling points are

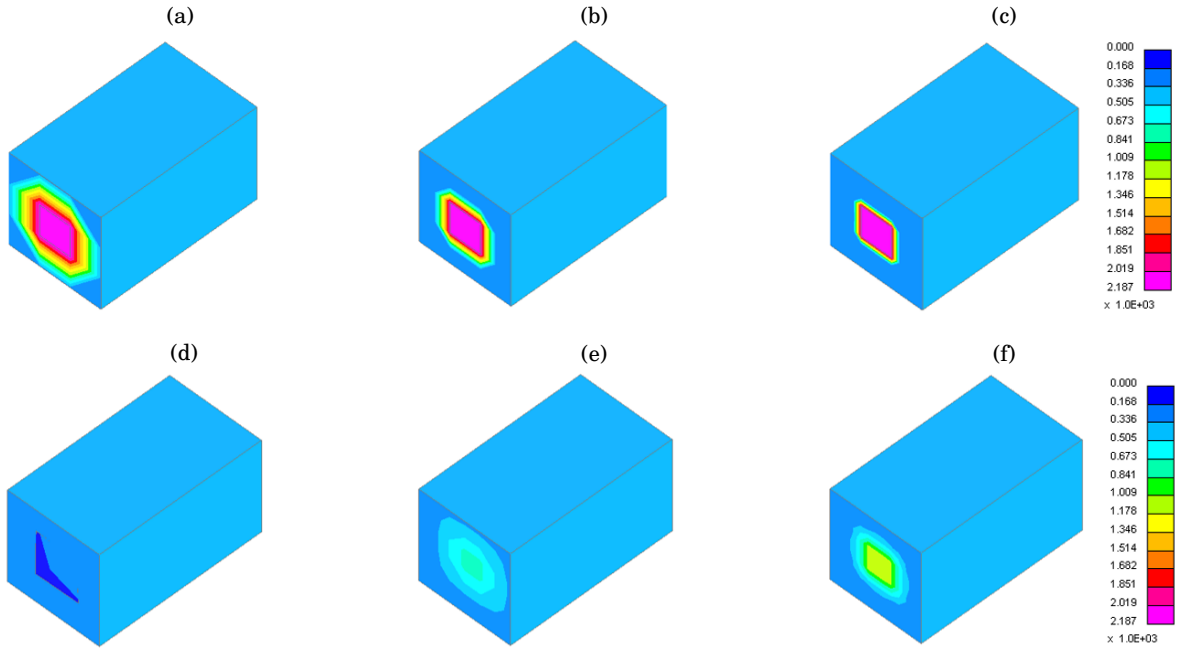

Figure 4.14: (a)-(c) x-direction (length-wise) stress (MPa) for model 1 (conformal mesh) for elements of side lengths 1 mm, 0.5 mm, 0.25 mm, respectively. (d)-(f) Likewise plots for model 2 using CLIS. An equi-scale is used for comparison purposes.

distributed over the surface of the slave segments). Penetration detection can then fail (referred to as leakage in FSI), resulting in unrealistic distortion of the slave (matrix) or master (tow) parts.

Some variation in the magnitude of the predicted stress in the tow and matrix, for all mesh densities, is observed between the conformal mesh and the use of CLIS, as shown in figure 4.16. Although this appears to be reduced for increasing levels of mesh refinement. For tow and matrix element length of 0.5mm and 0.25mm, maximum x-direction (length-wise) stress in the virtual tow is 25% and 16% less for those in model 2 using CLIS, when compared to the conformal mesh in model 1. Discrepancy is apparent because the equal-strain assumption only holds when the tow and matrix have a conformal mesh. This is not enforced through use of CLIS, which instead provides a coupling between the two constituents based on their relative penetration distances. The difference in the maximum stress in the matrix material is more significant between the CLIS and conformal mesh models, with a factor of 4 increase for CLIS, indicating that in this case, the CLIS models may not provide a reliable prediction of the absolute value of the matrix stress. However, further investigation is required to assess if the coupling of matrix and the virtual tows via CLIS, improves composite behaviour so that it more accurately reflects the final, consolidated component (as opposed to a dry-fibre network). This is conducted in sections 4.5.3

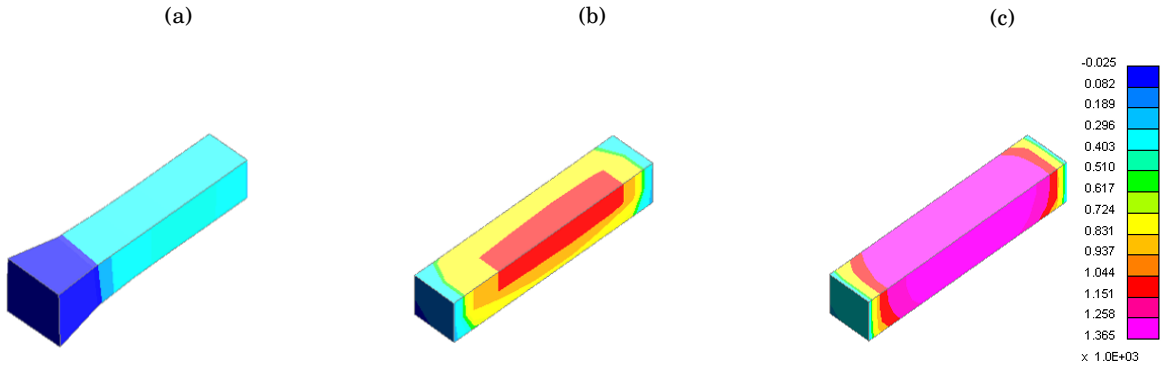

Figure 4.15: (a)-(c) x-direction (length-wise) stress (MPa) in the tow for the CLIS model, for elements with dimensions 1mm, 0.5mm and 0.25mm, respectively. Distortion to the (nearest) end of the tow is observed in (a), for the largest element size.

and 4.5.4. This is the primary aim for inclusion of matrix material in the full strut model, as detailed in section 4.4.

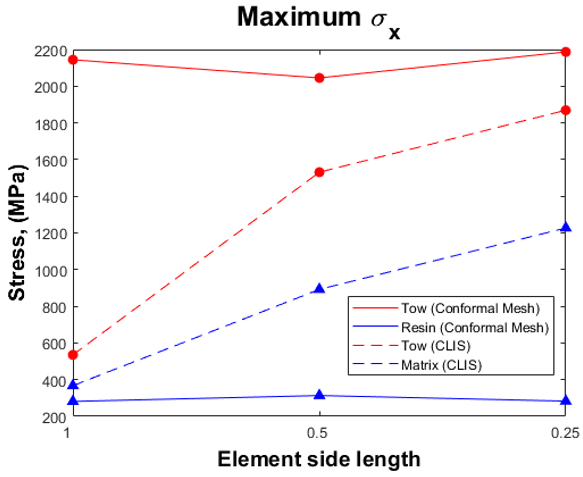

Figure 4.16: Maximum x-direction (length-wise) stress (σ_x) for the tow and matrix in models 1 (conformal mesh) and 2 (CLIS mesh), against mesh density.

Moreover, this case only considered equal mesh densities for the tow (master) and matrix (slave) parts. The principal advantage of the CLIS is that reduced mesh refinement can be used for the slave (matrix) part. Therefore, further investigation is required prior to application of CLIS to the full strut model, in which mesh density of the matrix is considered only. Additionally, material properties for the tow and matrix must also be consistent with those in sections 4.4.1 and 4.4.2. Finally, other input parameters for CLIS may also be important with regards to accurate modelling of the composite material's behaviour. These factors are now examined in case 2.

A formal convergence study is not attempted. Instead, we can conclude this case suggests

that CLIS provides a constrained based coupling mechanism sufficient to capture expected load transfer between the tow and matrix, provided matrix mesh density is sufficient so that unrealistic tow (master) behaviour does not occur due to failed penetration detection (leakage). The intended purpose of CLIS method is to provide a computationally efficient means for assessing mechanical properties of the composite-metal hybrid joint and strut, through avoidance of over-meshing and conformity of nodes at tow-matrix interfaces. Equal refinement of the CLIS and conformal mesh would defeat this objective.

4.5.2 Case 2. Hexagonal tow cross-section

Case 2 considers a single tow of length 10mm and hexagonal cross-section consistent with section 4.4.1, encased in a cuboidal mesh of matrix material and coupled using CLIS. Boundary conditions are applied to the matrix as described in the previous section to simulate an x-direction strain of 2000 $\mu\epsilon$. No additional constraints are applied to the tow, which is then free to move within the matrix according to the constraints imposed by CLIS.

CLIS requires input of a parameter NQUAD. This determines the number of coupling points per slave segment. For example, if NQUAD is 2, then there exists 2x2=4 coupling points for each slave segment. A higher NQUAD value reduces the likelihood of failed penetration detection (leakage), and possible subsequent element distortion. However, computational expense is increased and coupling forces may be excessive, which can lead to numerical instabilities. In general, guidance [97] suggests that for equally sized master and slave segments, an NQUAD value of 2 is sufficient. If slave segments are coarser, proper coupling may only be provided by increasing NQUAD to 3 or higher, although the effect of increased CPU time should be noted.

As both mesh refinement and increasing the value of NQUAD have the same effect of increasing the number of coupling points per given area, as illustrated in figure 4.17, only element size is studied. NQUAD is assigned a value of 2.

Unlike section 4.5.1, where mesh densities were adjusted proportionally for both master and slave parts to offer comparison with a regular, conformal mesh; here element size in the tow and matrix parts are considered independently. This is the advantage of the CLIS technique, with regards to increased computational efficiency via reduced mesh refinement for the slave (matrix) part.

As in [90], tow mesh density is kept constant. Regular 8-node (cubic) elements of side lengths 1mm and 0.5mm are constructed for the matrix in models 1 and 2. Model 3 has elements with dimensions 0.5 by 0.5 by 1mm. This more closely represents equal segment size between the tow (master) and matrix (slave) parts in the interaction. For consistency with later full strut models, the tow and matrix are assigned material properties as detailed in sections 4.4.1 and 4.4.2.

Figures 4.19(a)-4.19(c) show the x-direction (length-wise) stress in the virtual tow, for each different mesh density of the matrix. Figures 4.19(c)-4.19(e) show the likewise stress in the matrix. Stress distribution in the tow is similar across all three models, characterised by higher

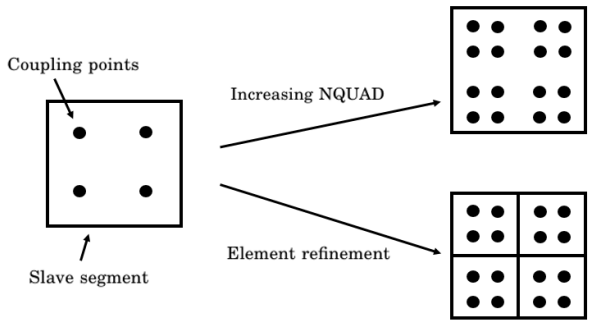

Figure 4.17: Diagram showing equivalence of increasing mesh density and value of NQUAD by a factor of 2.

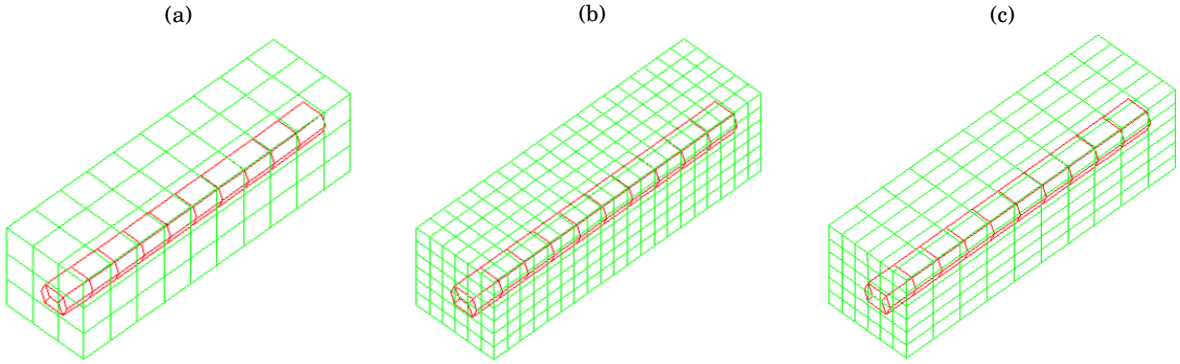

Figure 4.18: Single tow with hexagonal cross-section within a cubiodal mesh of matrix, for models (a) 1, (b) 2 and (c) 3, with element sizes 1mm, 0.5mm and in an approximate 1 to 1 with tow element size, respectively.

stress in the central part of the tow. For the matrix, higher stresses occur in the tow proximity, as load is transferred to the matrix (slave) from the stiffer tow (master) part. However, for the sparser mesh in model 1, comparatively poor stress distribution is observed in the matrix, with less concentrative stress in the region of the tow.

Although stress magnitudes in the matrix differ between models 2 and 3, the use of the "natural" model stress contour scales in figures 4.20(a) and 4.20(b), displays the similarity of stress distribution in the matrix for models 2 and 3. As concluded in section 4.5.2, dissimilar stress magnitudes offer no limitation with regards to predicting the mechanical performance of strut types A-E, provided consistent mesh densities are used for each simulation. Moreover, it cannot be concluded that the more refined matrix mesh in model 2, more accurately predicted stress in the matrix, as coupling forces may have been excessive, and an equivalent conformal mesh model was not constructed for comparison.

For the tow cross-section shape, and material properties for the virtual tows and matrix used in the full strut models, an NQUAD value of 2 and an approximate 1 to 1 ratio of the master and

slave segments gave reasonable representation of the expected stress distribution in the matrix, resulting from load transfer between the tow and matrix due to CLIS. Further mesh refinement of the matrix (slave) part (by a factor of 2) was found to offer limited improvement in this regard. The associated increase in computational cost will be important for the full strut models.

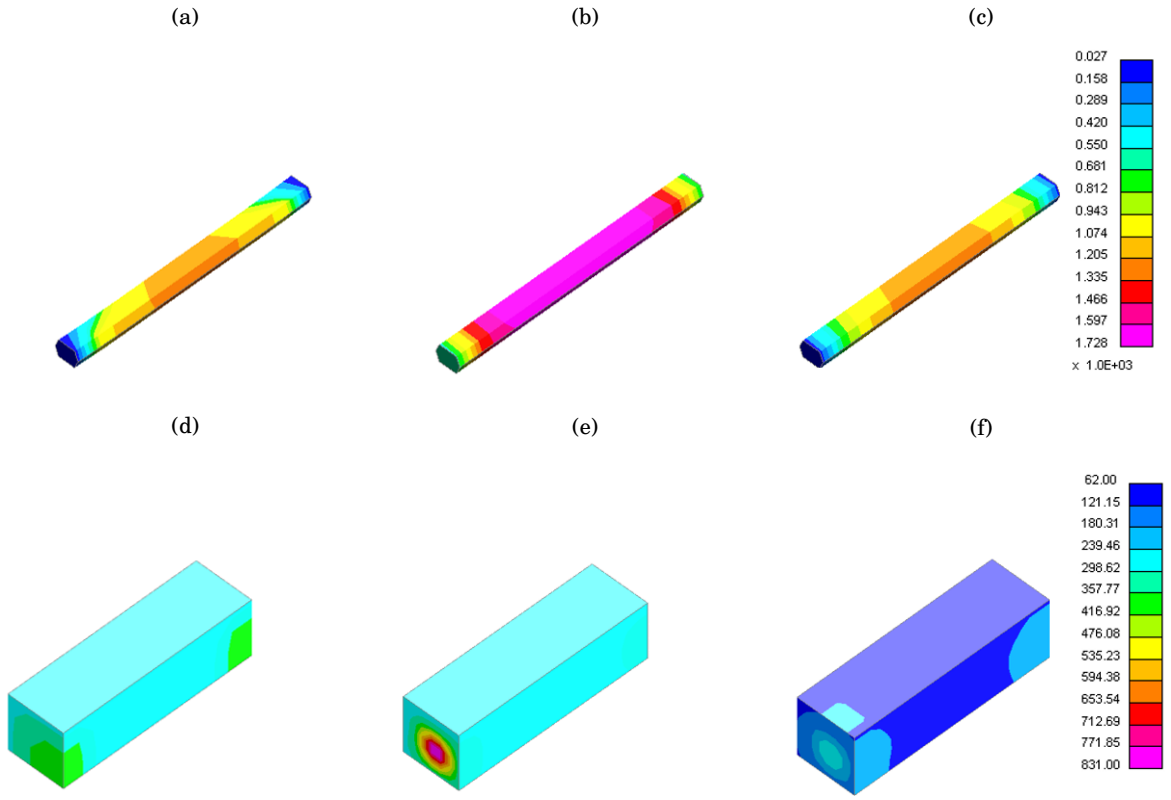

Figure 4.19: x-direction stress in the tow (a)-(c) and matrix (d)-(f), for models 1, 2 and 3, respectively. An equi-scale is used for comparison purposes.

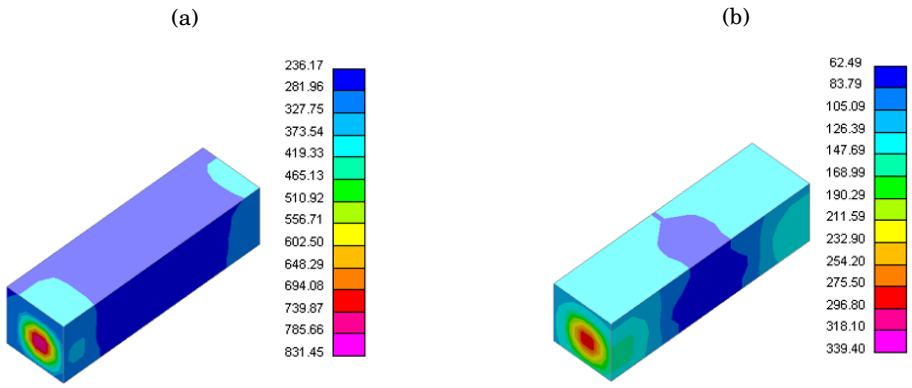

Figure 4.20: x-direction stress in the matrix for models (a) 2 and (b) 3, for the "natural" model stress scale, to highlight similar stress distribution in the matrix.

4.5.3 Case 3. Tow and pin interaction

For case 3, a virtual tow is made to take an arced path around a cylindrical shaped pin. Model 1 is constructed from only these parts. For model 2, the tow and pin are fully encased in matrix material, and the tow and matrix are coupled via CLIS. In both instances, the pin is assigned rigid material properties.

The end-nodes of the virtual tow are fixed and a displacement of 0.25mm is applied to the pin in the positive y-direction over an analysis time of 2 seconds. Contact type AUTOMATIC_GENERAL is used between the virtual tow and the pin, with a coulomb friction coefficient of 0.3. The matrix is excluded from the contact definition, so that stress is transferred to this part only via its coupling with the virtual tow using CLIS. This case considers the indirect application of load to the tow, in a manner similar to the mechanical interaction occurring in the joining mechanism at the strut ends. This differs from previous cases examined, in which loading was applied directly to the matrix material.

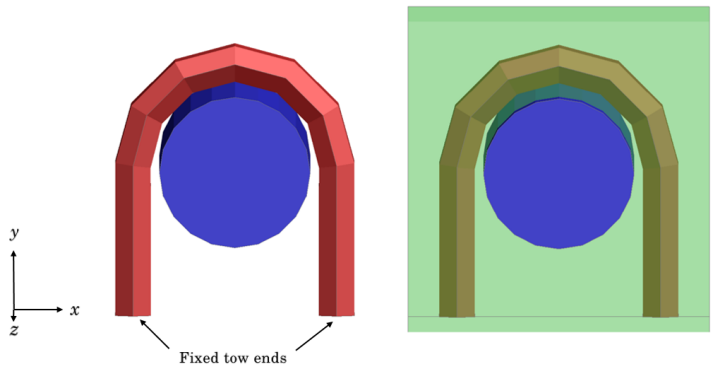

Figure 4.21: Tow (red) taking an arced path around a rigid, cylindrical pin (blue). Matrix (green) is made partially transparent.

Figures 4.22(a) and 4.22(b) show the local fibre-direction direction stress (along the path vector a as described in section 4.4.1) in the virtual tows for models 1 and 2, respectively. The magnitude of stress exerted in the virtual tow is reduced by 12% in model 2, although distribution is similar, with maximum stress occurring in the highlighted regions, at the underside of the tow as it transitions onto and off the pin. As shown in figure 4.23, stress is transferred to the matrix material in model 2. Peak stresses in the matrix occur in regions closest to the tow proximity and point of load transfer between the tow and pin, which reflects the expected reality.

Figures 4.24(a) and 4.24(b) display the resultant displacement in the tow for model's 1 and 2, respectively. Tow movement is reduced in model 2, as it is constrained by its coupling with the matrix via CLIS. This limits the inwards pinching of the free tow ends compared with model 1, resulting in reduced movement of the parts of the tow (highlighted) transitioning on and off the pin.

The combined effect of restricted tow movement and load carrying capability offered by the

matrix in model 2, suggests that the behaviour of the consolidated composite (as opposed to a dry-fibre tow) is represented through use of CLIS. Moreover, this occurred for the case of indirect load transfer to the matrix, via an interaction between a virtual tow and cylindrical pin.

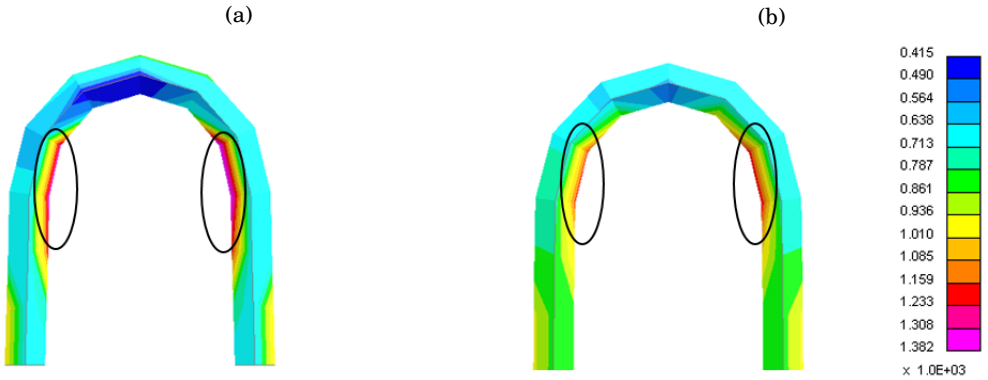

Figure 4.22: Local fibre direction stress (MPa) in the virtual tow for (a) Model 1 (tow and pin only) and (b) Model 2 (with matrix and CLIS). An equivalent-scale is used for purposes of comparison.

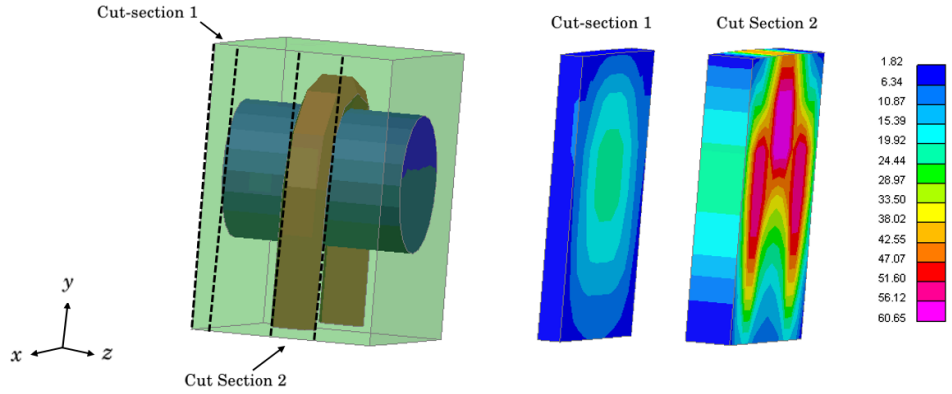

Figure 4.23: Von Mises stress (MPa) in the matrix at different positions relative to the tow position. Higher stresses are transferred to the matrix, closer to the region of the tow and pin interaction.

4.5.4 Full scale strut model with CLIS

A model of the full strut using CLIS is now considered, for configuration A. Construction of the model entities, namely the virtual tows, matrix and metallic end-fittings were detailed in sections 4.4.1 and 4.4.2.

As previously, two separate models are constructed. The first consists of only the metallic end-fittings connected via the virtual tow structure. This is more representative of a strut consisting of only a dry-fibre network, in which the fibre-tows are free to move in the absence of matrix.

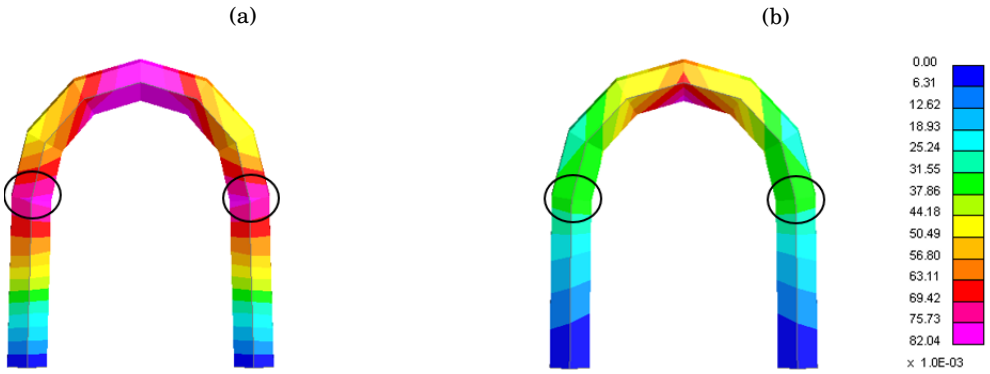

Figure 4.24: Resultant displacement (mm) of the virtual tow for (c) Model 1 (tow and pin only) and (d) Model 2 (with matrix and CLIS). An equi-scale is used for purposes of comparison.

Model 2 includes matrix material coupled with the virtual tows using CLIS. Parameters assigned to CLIS are maintained from cases 1 and 2.

A quasi-static tensile load, equivalent to a global strain of 2000 $\mu\epsilon$, is simulated in the strut by prescribing equal and opposing displacements to the end-fittings situated at the strut ends, over an analysis time of 5 seconds. As in verification case 3, contact type AUTOMATIC_GENERAL is used between the virtual tows and the pin-structured metallic end-fittings, with a coulomb friction coefficient of 0.3. Matrix is excluded from the contact definition.

Figures 4.25(a) and 4.25(b) show the circumferential (hoop) displacement (mm) of the end-fittings and virtual tows for model's 1 and 2, respectively. Resultant tow movement in this direction, due to rotation about the strut's longitudinal axis, is reduced by a factor of 3.5, through use of matrix and CLIS.

Furthermore, model 1 exhibits localised twisting at the strut ends, in the region of the joint. The end-fittings rotate in opposing directions as they attempt to become uncoupled from the virtual tow structure. In comparison, rotation at the strut ends is suppressed in model 2, by the matrix and its coupling with the virtual tows via CLIS. This also transfers and evenly distributes (minor) rotation along the length of the strut.

Similarly, figures 4.26(a) and 4.26(b) display the radial displacement (in mm) in the virtual tows, for models 1 and 2 respectively, (note that displacement in the end-fittings themselves is zero in this direction). Movement of the tows in this direction can be described as necking, funnelling or radial expansion of the tows along the strut length. Radial displacement is reduced by a factor of 5 in model 2, as the matrix constrains displacement of the fibre-tows in this direction.

The virtual tows are therefore constrained through used of CLIS in model 2, so that global strut behaviour more accurately reflects a final, consolidated component. The remaining, minimal axial rotation in model 2 is therefore more likely due to induced torsional effects (see section 4.6.2). Further, analyses of the mechanical response of the full hybrid strut (with configurations

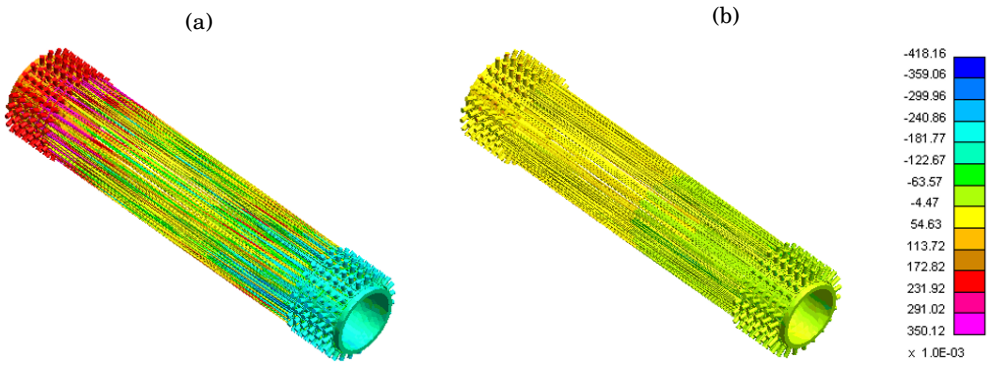

Figure 4.25: Circumferential (hoop) displacement (mm) in the end-fittings and virtual tows for strut type A. For (a) model 1, consisting of only the metallic end-fittings and virtual tows, and for (b) model 2, where matrix and CLIS have been included, (the matrix is omitted from the image).

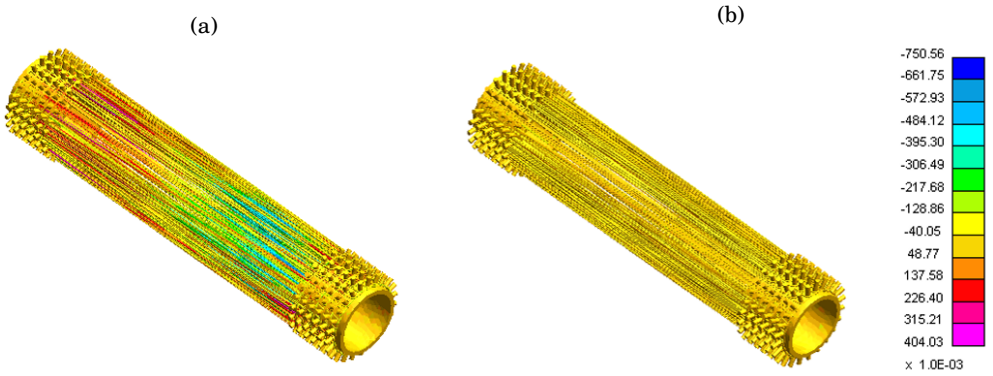

Figure 4.26: Radial displacement (mm) in the end-fittings and virtual tow structure for strut type A. For (a) model 1, consisting of only the metallic end-fittings and virtual tows, and for (b) model 2, including matrix and CLIS, (matrix is omitted from the image). Radial displacement of the virtual tows is minimal in model 2.

A-E) is conduced in sections 4.6 and 4.7.

4.5.5 Summary of *CONSTRAINED_LAGRANGE_IN_SOLID (CLIS)

Case 1 found that the coupling of the virtual tows (master) and matrix (slave), via the *CONSTRAINED_LAGRANGE_IN_SOLID (CLIS) function in LS-Dyna®, provided a realistic representation of load transfer between the reinforcement and matrix. Composite behaviour was well represented with higher stress in the stiffer tow (master part) and the matrix offering some load carrying capability. This was also apparent in case 2, in which realistic material properties were used for the virtual tow and matrix, and the relative mesh densities for the tow and matrix were similar to that used in the full strut models in section 4.6.

In case 3, realistic load transfer between a virtual tow and matrix was found to occur using

CLIS, for the instance where a mechanical interaction between the pin and tow was simulated. This reflects the interaction occurring between the filament wound tows and the pin-structured end-fittings in the composite-metal joining mechanism at the strut ends.

Additionally, in both cases 3 and 4, the virtual tows were found to be sufficiently constrained within the matrix, using the coupling mechanism provided by CLIS, so that composite, and global strut behaviour more accurately reflected the final, consolidated component as opposed to a dry fibre network.

As apparent in case 1, predictions of stress magnitudes in the virtual tows and matrix, may not be as accurate as a conventional FEA approach using a conformal mesh between the two constituents. However, the use of a conformal mesh for the full strut models examined in section 4.6 would have resulted in substantial mesh complexity and infeasibly large computational cost.

It can be determined that the methodology developed here, to couple matrix and reinforcement via CLIS, is sufficient to provide both qualitative and quantitative assessment of strut and configurations A-E, in their final consolidated and operating form. Their relative mechanical properties can be predicted and the performance capability of the composite-metal joining mechanism and hybrid strut can be established.

4.6 Virtual testing of strut configurations A-E

Quasi-static, global tensile strains of 2000 $\mu\varepsilon$ are applied to full strut models with configurations A-E. Compressive testing is examined separately in section 4.8. Contact formulations between the pin-structured metallic end-fittings and the virtual tows remain unchanged from sections 4.5.3 and 4.5.4. Use of CLIS to describe the matrix-reinforcement relationship is also unaltered.

Recall, strut type A, has a single-pin wrapping pattern (section 3.9.1), and an (unaltered) layup sequence $[0_6]$ for the strut's central mandrel. The model for this configuration is shown in figure 4.27(a). Strut type B, seen in figure 4.27(b), has the pin under-wind pattern (section 3.9.4) and an identical mandrel layup to A. Strut configuration D, as shown in figure 4.27(c) has the two-row wrapping pattern (section 3.9.3) for the pins, and a layup sequence of $\mp 45/0_2/\pm 45$ on the mandrel. The all-row pin wrapping pattern (section 3.9.3) and layup sequence of $\mp 10/0_2/\pm 10$ is used in strut E (figure 4.27(d)).

Finally, strut configuration C has both an identical layup sequence, and the same single-pin winding pattern used in strut A, but also includes an additional, outer hoop layer of virtual tows (orientated at 90° to the strut's longitudinal axis), as seen in figure 4.28.

For a strut which is predominately loaded in tension and compression, maximum axial, or longitudinal, properties are desirable. Layup sequences consisting of axial, or near-axial, tow trajectories, such as with configurations A, B and C, should therefore be advantageous. However, torsional effects may be more pronounced in such cases. These should be minimised as they can induce additional stresses in the structure.

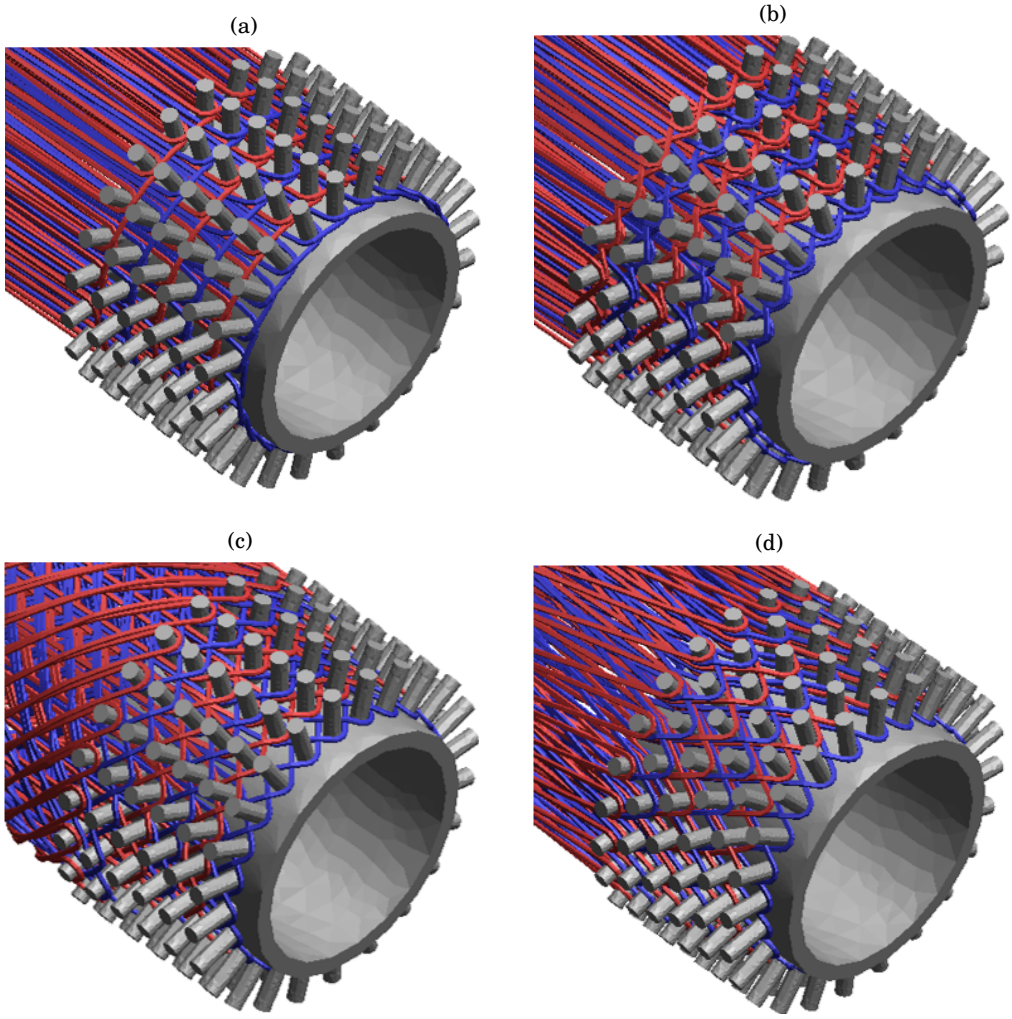

Figure 4.27: Models of strut configurations (a) A, (b) B, (c) D and (d) E. Virtual tow layers (described using solid element types) are coloured red and blue alternately. Matrix material is excluded from the image, so that the paths of the virtual tows can be seen clearly.

Torsion, or the occurrence of extension hoop-shear coupling in the strut under axial loading, should be reduced due to efforts made in section 3.7 to adopt only balanced and symmetric layup sequences on the mandrel. However, some asymmetry introduced for the altered orientation angles θ_d and θ_u may have an effect. Torsional effects may also be caused by the non-uniformity of tow coverage on the mandrel's surface, which may lead to more complex structural behaviour.

Additionally, strut properties will also be dependant on the joint configuration at the strut ends. Load is transferred to the composite part at this point, due to the mechanical interaction occurring between the filament wound fibre-tows and metallic pins. This interaction will be affected by the winding pattern in this region, and the manner in which pull-back of the tows is initiated around the pins.

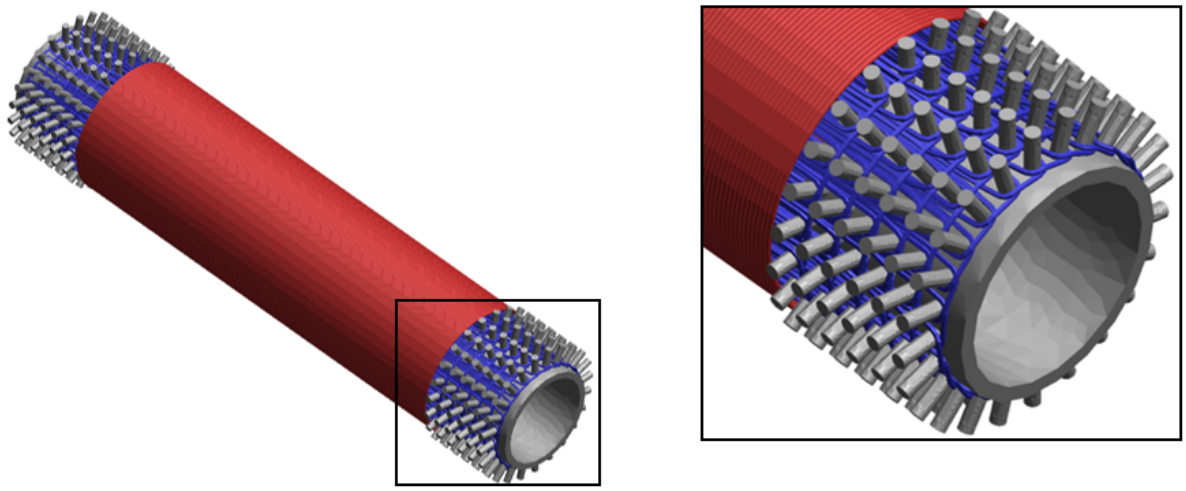

Figure 4.28: Model of strut configuration C, with an additional, hoop-layer of virtual tows (red) in the region of the mandrel. All other tow layers, coloured blue, have identical paths to that in strut type A. Matrix material is excluded from the image, so that the paths of the virtual tows can be seen clearly.

4.6.1 Axial stiffness of struts A-E

Figure 4.29 shows the force transferred to strut types A-E, against applied strain. This is the "reaction" load in the strut due to the prescribed tensile strain. A higher reaction load indicates higher axial stiffness for the strut. Initially, minimal reaction load is induced in the strut as an initial, small separation distance exists between the virtual tows and the pins, which results from conversion to 3D continuum elements for the tow cross-section (as described in section 4.4.1) and prevents penetrations between model parts. This is observed in a relatively flat load vs strain curve up to approximately 500 $\mu\epsilon$ for all strut configurations.

After this point, the tows and pins are brought into contact and load is transferred, and the gradient of the force vs strain curve increases. For applied strain in the range of approximately 500-1000 $\mu\epsilon$ strut stiffness increases at a higher rate. This is thought to be due to excess tow length on the strut (recall section 4.2.4). Once this has been taken-up, the high tensile stiffness of the virtual tows offers significantly higher resistance, resulting in stiffness increasing at a more linear rate for the remainder of the applied strain.

Note, however, that a degree of non-linearity persists throughout the loading range for the model struts. Excess tow length is not taken-up uniformly across the multiple layers of virtual tows, so some excess length may be maintained even at the later stages of the simulation. This also varies between strut configurations. Additionally, the degree of non-linearity in the force vs strain curve be exaggerated in the models as excess tow length may be bound more effectively by the matrix in the physical, consolidated strut, than that provided in the model through CLIS.

Figure 4.30(a) provides a comparison of the expected response of the physical strut and that

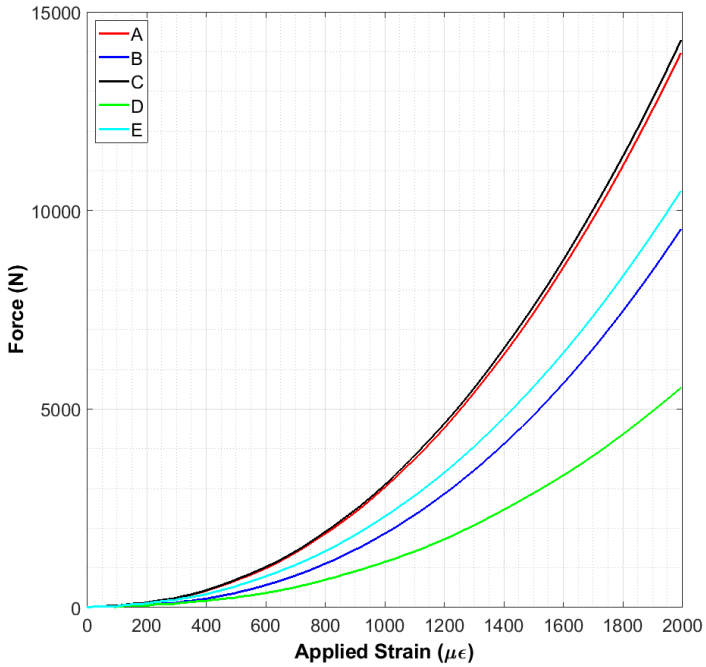

Figure 4.29: Force (N) against prescribed strain ($\mu\epsilon$) for joint types A-E. A steeper curve indicates increased "work", and consequently, axial stiffness.

observed in the models. The initial, minimal reaction load prior to establishment of contact between the virtual tows and metallic pins in the joint would not occur in the physical reality (although non-linearity may exist due to tow-matrix interactions and some excess tow length in the physical strut). As highlighted, inclusion of this region of the curve in the analysis leads to significant underestimation of the strut's stiffness response.

Therefore, as shown in figure 4.30(b), the strut's response up to 500 $\mu\epsilon$ is excluded. A linear fit is conducted on the data range between 1000-2000 $\mu\epsilon$, which is then extrapolated up to 2500 $\mu\epsilon$. The force vs applied strain curve in the range 500-2500 $\mu\epsilon$ is then considered as the strut's response for a prescribed strain of 2000 $\mu\epsilon$. Although extrapolation through use of a linear fit provides a non-exact solution (accuracy of the linear fitting can be assessed using the root-mean-square-error, as provided in the appendix table A.2), prediction of the relative performance of strut configurations A-E is not altered significantly.

Hooke's law is used to calculate strut stiffness's for the reaction load of 2500 $\mu\epsilon$ is used (minus the load at 500 $\mu\epsilon$ for an equivalent prescribed strain of 2000 $\mu\epsilon$). Assumption of non-linear behaviour over the prescribed strain should not provide a significant limitation as no attempt was made to model damage in the composite part of the strut and the initial, exaggerated non-linear behaviour is not has been removed from the analysis.

As expected, the strut's axial stiffness seems to be predominately determined by the fibre orientations and layup sequence on the mandrel. Joint configurations A and C displaying the

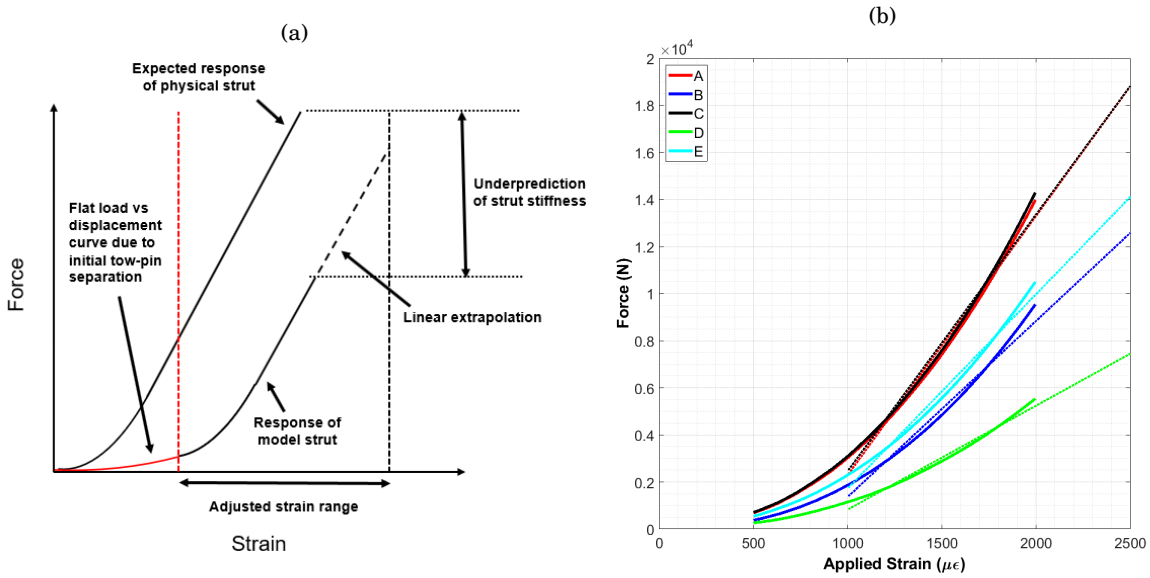

Figure 4.30: (a) Comparison of the Force (N) vs prescribed strain curve for that observed in the model, against an idealisation of the expected physical reality. (b) Adjusted Force (N) against prescribed strain ($\mu\epsilon$) for strut types A-E, after removing initial flat region of the curve between 0 - 500 $\mu\epsilon$.

Table 4.1: Predicted strut stiffness, for configurations A-E.

Strut Type	Reaction Load (N)	Stiffness, K (10^6Nm^{-1})
A	18125	44.2
B	12210	29.8
C	18113	44.2
D	7196	17.6
E	13568	33.1

maximum axial stiffnesses, as these strut types have layups consisting of only axial fibre directions, more aligned with the loading direction. Contribution to axial stiffness from the additional outer hoop layer in configuration C is not significant.

Similarly, strut type E has 25% lower axial stiffness than A (at 2000$\mu\epsilon$) due to its four $\pm10°$ filament layers. Configuration D has significantly reduced stiffness (-60% from A) because its layup includes layers with large orientation angles of $\pm45°$, further misaligned from the loading direction. However, joint configuration B displays a 33% reduction in axial stiffness from A despite having an identical layup sequence. This may be attributable to the difference in the pin-tow interaction at the strut ends. The under-wind pattern in B may have resulted in a slack tow contacting the underside of the pins, this may in turn have caused a reduction in load transfer to the tow structure, affecting prediction of axial stiffness.

Alternatively, the disparity may be due to model limitations. Recall from section 4.2.3, the final tow path on the strut is determined from a simulation step in which a small strain is applied

to the tow structure to reduce excess tow length, and thereby increase path smoothness and realism. The level of strain required to accomplish this effect was determined qualitatively by visual inspection of the virtual tow following the simulation. It may be the case that the strain applied to tow structure in configuration B left sufficient but non-obvious excess tow length, which decreased load transfer behaviour between the metal and tow, resulting in underestimation of axial stiffness.

4.6.2 Strut torsion

Table 4.2 shows the maximum twist angle, ψ, about the strut's longitudinal axis, occurring in strut types A-E due to an applied axial tension. This is calculated by considering the end-fitting's located at opposing ends of the strut, as rigid bodies. Following loading, their total displacement in the circumferential direction is used to find a resultant rotation angle, or twist angle, about the strut's longitudinal axis.

Table 4.2: Maximum twist angle (ψ) by joint configuration, following simulations of quasi-static tension.

Strut Type	Twist angle, ψ°
A	0.33
B	0.29
C	0.21
D	0.15
E	0.16

Minimal torsion is induced in all strut configurations, (section 4.6.5 considers if torsional effects result in increased stress in the matrix material). However, the degree of torsion does vary between each configuration. The use of an additional hoop wind layer on the strut's mandrel in configuration C reduced the maximum twist angle by 36% from type A. This is similar to the trend identified in table 3.5, in which hoop-shear strain was predicted to decrease by 14% with the introduction of an outer 90° layer for the $[0_6]$ mandrel layup.

The under-wind pattern in strut type B also produced a 12% reduction in twist angle from strut A. It is also conjectured that an improved form fit between the tow and pins is attained through adoption of the under-wind pattern, which decreases rotation and twist at the strut ends. Strut types D and E, with layup sequences $[\mp 45/0_2/\pm 45]$ and $[\mp 10/0_2/\pm 10]$, respectively, display the lowest twist angles. For D, this is expected as the $\pm 45^\circ$ layers should offer greater resistance to torsional effects. For E, minimal torsion is thought to be more attributable to the winding pattern in the region of the pin array, rather than the off-axis, $\pm 10^\circ$, fibre orientations on the mandrel. The all-row winding pattern, results in a tow trajectory that traverses the pin array at an angle, as shown in figure 4.31(a). In comparison, all other winding patterns have a vertical tow path for all, or part, of the tow trajectory through the pin array (figure 4.31(b).

As with configuration B, an improved form-fit between the filament wound tows and pins then results, which reduces torsional effects.

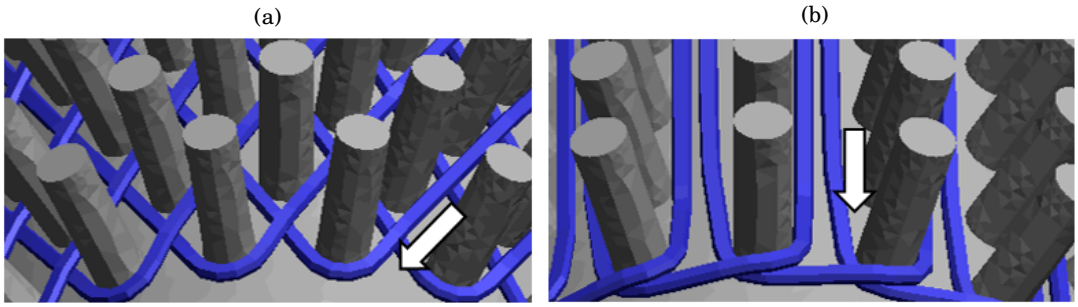

Figure 4.31: Tow (blue) trajectory around metallic pins (grey) for strut configurations (a) A and (b) E, respectively. The angle of the tow coincides with the pin array for E, resulting in an improved form-fit that reduces torsional effects in the strut.

Additionally, imbalance of the layups as a result of alteration of the winding angles on the mandrel to θ_u and θ_d was found to have minimal effect on strut torsion. For example, strut type A with layup sequence $[0_6]$ has the lowest relative degree of imbalance (see table A.1), but was the strut configuration observed to have the maximum twist angle.

4.6.3 Pin-structured end-fittings

Load distribution in the pin-structured metallic end-fittings, following strut and joint tension, is considered in this section. Similar examination of the stress distribution in the virtual tows and matrix are then conducted in sections 4.6.4 and 4.6.5, respectively. These combined analyses are then used to characterise the properties of the joint and strut (stiffness and strength) in section 4.6.6.

Recall, efforts were made in section 3.5 to consider the mechanical interaction occurring between the filament wound fibre-tows and metallic pins in the joint, using a simple analytical approach. Four different designs were then utilised in struts A-E, (the joint type in configuration C is equivalent to A).

The single-pin and two-row winding patterns in joints A and D, respectively, were predicted to display improved load distribution across the pin array. The under wind-pattern in B was expected to reduce the magnitude of the shear force exerted on the pins. Finally, for comparison purposes, the all-pin wrapping in joint E was intentionally chosen to provide inferior load distribution. A 10% variance in the shear force on the pins in different rows was expected, with significant overloading of the first row of pins.

Table 4.3 shows the maximum Von Mises stresses in the pin-structured metallic end-fittings, for strut configurations A-E. Figure 4.32 shows the stress distribution in one end-fitting of strut types A, B, D and E, respectively. Generally, load transfer in the joint, between the virtual

tows and pins, resulted in stress at the pin base and connection with the end-fitting's surface. The magnitudes of these stresses and the distribution across the pin array, vary between joint configurations.

Table 4.3: Maximum Von Mises stress (MPa) in the pin structured metallic end-fittings, for strut types A-E.

Strut Configuration	Maximum Von Mises stress (MPa)
A	993
B	866
C	999
D	649
E	1031

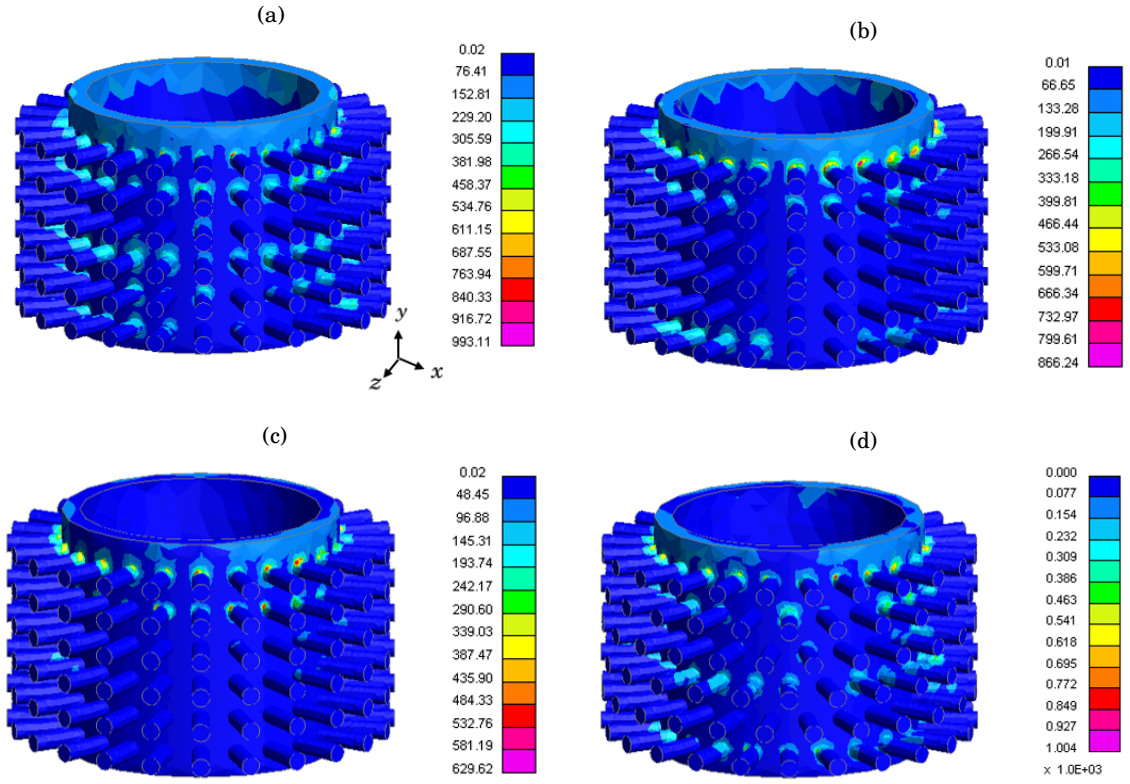

Figure 4.32: Von Mises stress in a pin structured metallic end-fitting located at the strut end, for joints (a) A, (b) B, (c) D and (d) E. Loading of the pins is most uniform for joint configurations A and E. In B, loading occurs predominately pin rows 1, 5 and 6. For D, loading is confined to rows 5 and 6.

Load distribution across the pins is most even for joint A. This agrees well with the predictions of the analytical model in section 3.5. However, loading of the pins for joint E is generally good and comparable with A, which is contradictory to the expectations of the analytical approach.

The maximum Von Mises stress in joint B is reduced by 33% from A. This trend was identified in the analytical model due to the under-wind pattern reducing the resultant shear force exerted on the pins. However, load distribution, in addition to magnitude, is also altered between the two cases, which was not predicted by the analytical approach. Pin loading for B, is predominately limited to the rows 1, 5 and 6 (i.e. the first, and the top-two most rows of pins).

Joint type D also displays a relatively poor distribution of load across the pin array, with stresses being confined to only rows 5 and 6. This was also not predicted by the analytical model. Further analysis of load transfer in the joint, between the filament wound tows and the metallic pins, is required. The stress distribution in the virtual tows is examined in the following section.

4.6.4 Virtual tows

Table 4.4 shows the maximum local fibre-direction (along the tow path vector, a) stress in the virtual tows, for each virtual tow layer of strut configurations A-E. Bracketed values indicate the (unaltered) fibre orientation angle on the mandrel, for that particular layer. 4.5

Table 4.4: Maximum local fibre direction stress (MPa) by virtual tow layer, for strut configurations A-E. Layer 7 corresponds to the outer hoop layer present only in strut type C. Bracketed values indicate the unaltered fibre-orientation angle of the virtual tow on the mandrel, for each layer.

Joint configuration	A	B	C	D	E
Virtual tow layer					
1	713 (0)	1217 (0)	723 (0)	775 (-45)	1107 (-10)
2	859 (0)	674 (0)	883 (0)	215 (45)	688 (10)
3	653 (0)	282 (0)	657 (0)	219 (0)	499 (0)
4	1004 (0)	436 (0)	1046 (0)	184 (0)	398 (0)
5	803 (0)	224 (0)	804 (0)	41 (45)	327 (10)
6	765 (0)	849 (0)	758 (0)	31 (-45)	285 (-10)
7	n/a	n/a	-1.09 (90)	n/a	n/a

Maximum stresses typically occur at the underside of the tows leading from the pins following pull-back. Highly concentrated stresses exists in these areas of the virtual tows, as this is the point of load transference. This is indicated by the significantly lower average fibre-direction tow stress, in the region of the joints only (i.e. excluding the tow elements forming the central composite part of the strut and overlaying the mandrel) given in table 4.5, and the maximum stresses in table4.4 . This can also be observed in figure 4.33, which shows the local fibre-direction stress distribution in the virtual tows in the proximity of the joint, for configurations A, B, D and E, respectively. Such stress concentration effects are not thought to occur due limitations in the analysis (i.e. resulting from single element skew due to poor contact definition), and would also be expected to occur in the physical joint.

The virtual tows also experience compressive stresses in the fibre direction, as their arced path around the pins lead to compression at the under-side of the tow contacting the pin, following

joint tension. However, as maximum compressive stresses in the tow are localised to this region, and are generally less than 20% of the maximum tensile stress in the fibre-tows for all joint configurations, the virtual tows are assumed to be predominately loaded in tension along the fibre direction.

Table 4.5: Average local fibre direction stress (MPa) by virtual tow layer in the joint region, for strut configurations A-E. Average stress in the virtual tows is significantly less than observed maximums, indicating highly concentrated stresses.

Joint configuration	A	B	C	D	E
Virtual tow layer					
1	190 (0)	226 (0)	194 (0)	181 (-45)	222 (-10)
2	169 (0)	125 (0)	170 (0)	30 (45)	133 (10)
3	157 (0)	110 (0)	157 (0)	127 (0)	120 (0)
4	164(0)	107 (0)	164 (0)	125 (0)	120 (0)
5	155 (0)	103 (0)	156 (0)	41 (45)	119 (10)
6	153 (0)	108 (0)	155 (0)	31 (-45)	105 (-10)
7	n/a	n/a	-13 (90)	n/a	n/a

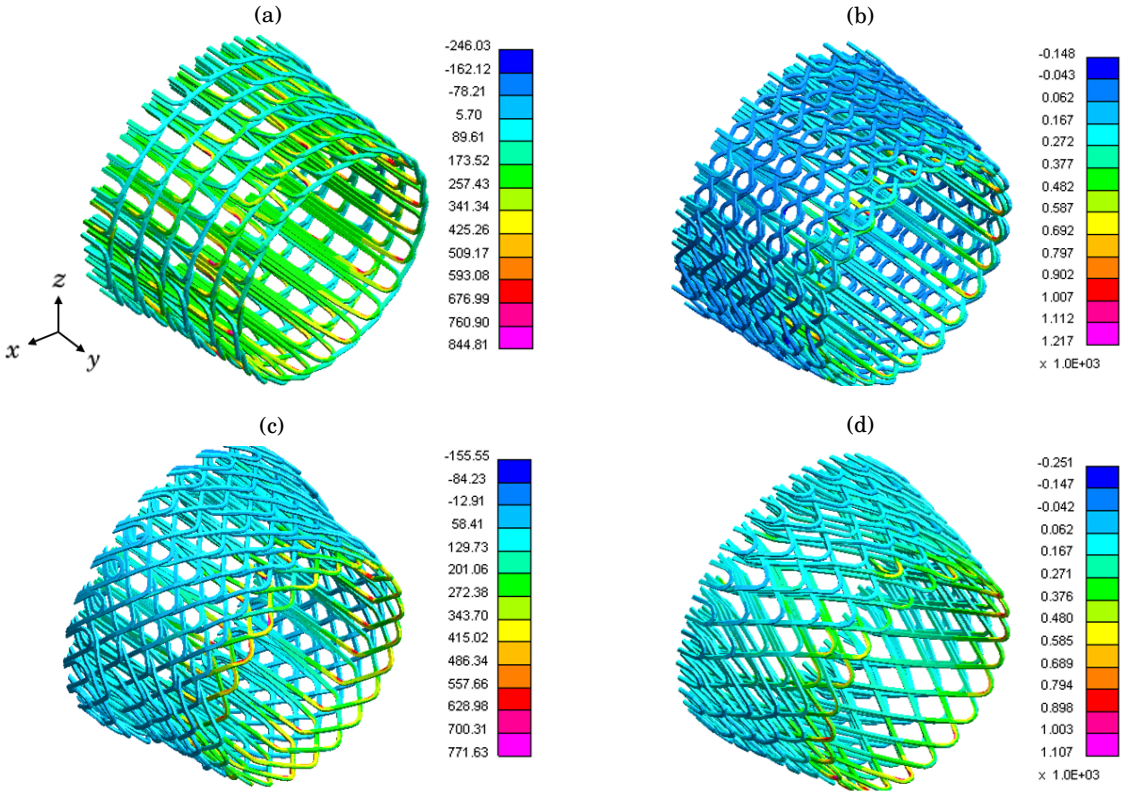

Figure 4.33: Local fibre direction stress in the virtual tows for the region of the joint, for configurations (a) A, (b) B, (c) D and (d) E.

Configurations A and C have a more even distribution of loading in the virtual tow layers,

with standard deviations of maximum tow stress of 123 MPa and 138 MPa, respectively, about the mean maximum layer stress. This may be due to their constant angle layup for the central mandrel. In comparison, strut types D and E have greater variance in stress values across the virtual tow layers, (with standard deviations of 329MPa and 388MPa, respectively), due to their varying tow orientations on the mandrel. In particular, the outer $\pm 45°$ layers in D are only minimally loaded, (at 41MPa and 31 MPa).

However, strut configuration B also displays large variance (standard deviation of 379MPa) in stress between the virtual tow layers, despite it having only axial tow orientations on the mandrel. Therefore, the winding pattern in the region of the pin array also has significant effect on load transfer to the virtual tows, and stress magnitudes in the virtual tow layers.

This is most apparent for the inner-most layer of strut D, which is more highly stressed than the remaining layers despite having an orientation angle of $-45°$ for the mandrel. Large (absolute) orientation angles for the first two layers of strut D, result in an increased contact area and improved form fit between the pins in the first row and the virtual tows as they transition off and onto the pin array, as illustrated in figure 4.34. Load transfer to this layer may be higher compared to a virtual tow that takes an axial direction on the mandrel.

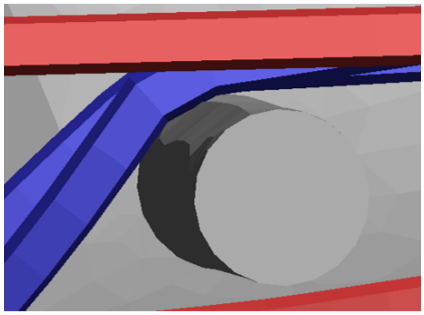

Figure 4.34: Virtual tow in the first (blue) and third (red) layers of strut type D. The improved form-fit between the inner $-45°$ layer and the pin as it transitions from the end-fitting, may lead to significant load transfer to this tow, despite its off-axis orientation.

For the mandrel region, as highlighted in figures 4.35 and 4.36, loading of the virtual tows is more synchronous with the principles of composite materials and fibre-load alignment; as the virtual tow layers in A have approximately equal loading due to their equal (axial) orientation angles, where as the axial layers in D are significantly more highly stressed that the $\pm 45°$ layers.

It was hypothesised that adoption of the under-wind pattern in joint configuration B, may lead stress concentrations in the virtual tow, due to its high degree of manipulation. Although maximum stress increased by 21% from joint A, it is not conclusive that this was due to higher, or more concentrative stresses, in the pull-back region. For struts B, D and E, tow stress is generally maximal for the two inner-most layers, interacting with pins in rows 5 and 6, respectively. This was apparent in the poor stress distribution across the pins observed for these joint types in section 4.6.3, with loading of the pins predominate for these rows.

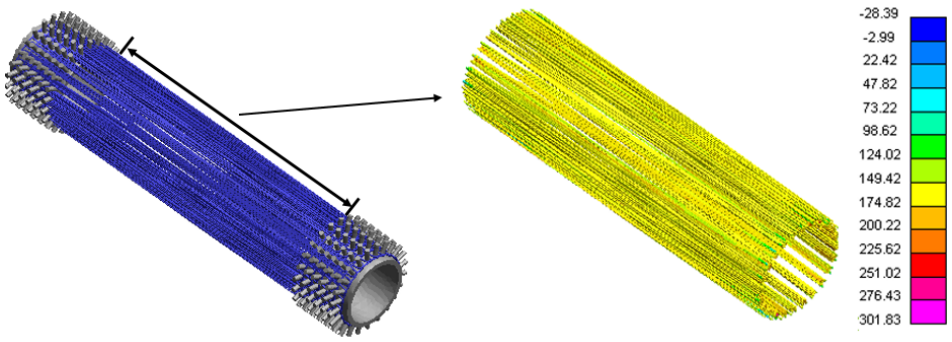

Figure 4.35: Local fibre direction stress in the virtual tow structure spanning the mandrel, for strut type A.

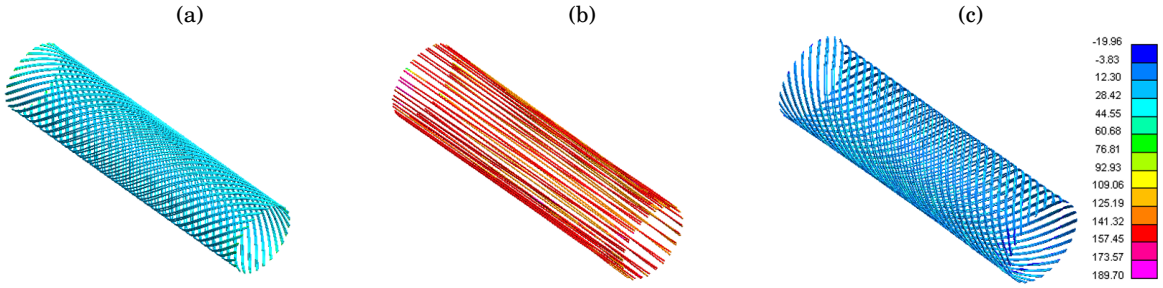

Figure 4.36: Local fibre direction stress in the virtual tow structure spanning the mandrel, for layers (a) 1, (b) 3 and (c) 5. of strut configuration D. Virtual tow layers with axial orientations (such as layer 3) experience significantly higher loading.

The models may offer some limitations with regards to representing the load transfer behaviour in the joint with precise realism. These may also be the cause of the discrepancy, with respect to load distribution in the virtual tows and pins virtual, against the analytical approach adopted in section 3.5. For example, the use of virtual tows with uniform, circular cross-section and diameter of 1mm, will significantly overestimate the thickness of the composite part. The outer tow layers will then be both, significantly longer in length and at a relatively large radial distance from the strut's surface, and will be poorly loaded as a consequence. This effect is exaggerated in the outer two $\pm 45^{\circ}$ layers of strut type D. Also, non-realistic virtual tow shape and composite thickness, also necessitate the use of model pin lengths significant longer than the physical joint, which can in turn lead to higher bending loads and stresses at the pin base.

These observations motivate work in chapter 5 to study the joining mechanism using a higher fidelity approach, which includes realistic tow geometries in the region of the composite-metal joint.

4.6.5 Matrix

Table 4.6 displays the Maximum Principal stress in the matrix, for joint configurations A-E. As highlighted in figure 4.37, higher stresses are observed in the region of the joint (and point of load transfer between the virtual tows and pins) at the strut ends, for all configurations. This is consistent with the expected reality.

A detailed approach was used in sections 3.4-3.7 to study the complex behaviour and stress distribution of the central composite part overlaying the mandrel, due to non-uniform fibre content in this region. The use of CLIS to couple the virtual tows and matrix for the full strut models, did not highlight similar stress concentrations in matrix rich regions of this part of the strut. Instead, loading of the matrix is predicted to be more significant for the joint at the strut ends.

However, it should be noted that this may also be a limitation to the CLIS approach, i.e. load cannot be transferred to the matrix (slave) if no interaction with the tow (master) occurs in regions of the strut consisting of only matrix material. Stress distribution, in these matrix rich areas, may not then be well represented with CLIS. This model limitation should however be mitigated, with regards to assessing the effect of mandrel layup sequence on joint and strut properties, due to the detailed approach developed in chapter 3 to capture the complex stress distribution caused by non-uniform fibre coverage of the strut's central mandrel; prior to defining the layup sequences for strut configurations A-E.

Table 4.6: Maximum Principal stress (MPa) in the matrix, for strut types A-E.

Strut Configuration	Maximum Principle stress (MPa)
A	20.7
B	38.5
C	20.8
D	29.6
E	29.7

Torsional effects, as examined in section 4.6.2, not determined to have a significant effect on matrix stress. For example, strut type A exhibited the largest twist angle (ψ), but the lowest predicted stress in the matrix. In the physical strut, rotation of the strut's end-fittings may be constrained by their connections to other structural parts (via the pin-lug joints highlighted in chapter 1). This may lead to increase matrix stress in the physical structure. However, in this work, it was necessary to not constrain (the minimal) end-fitting rotation in order to assess the effects of CLIS on strut behaviour (section 4.5.4).

4.6.6 Strut and joint strength

Strut and joint strength is assessed by calculating reserve factors for the fibre-tows (R_t), metallic pin-structured end-fittings (R_{mt}) and matrix material (R_{ma}), as shown in table 4.7. This is the

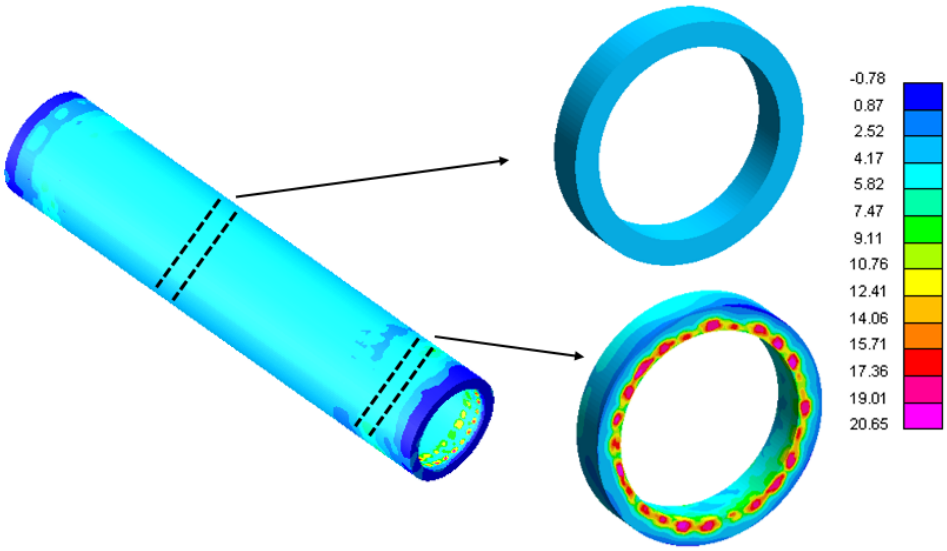

Figure 4.37: Maximum Principal stress (MPa) in the matrix, for strut configuration A. Highest stresses are observed at the strut ends, in the region of tow-metal interaction.

ratio of the component stress (σ_i) over strength (S_i), as shown in equation 4.6. A joint may be considered optimal when $R_t = R_{mt} = R_{ma} = 1$, that is, when joint and strut failure occurs in all its constituents (fibre, matrix and metal) simultaneously, and at their ultimate failure loads.

Table 4.7: Reserve factors for the tow, metal and matrix, and the reaction load (N) of strut configurations A-E.

Strut Type	R_t	R_{mt}	R_{ma}	Reaction Load (N)
A	0.31	0.90	0.34	18125
B	0.38	0.79	0.63	12210
C	0.32	0.91	0.34	18113
D	0.24	0.59	0.48	7196
E	0.34	0.94	0.48	13568

$$R_i = \frac{\sigma_i}{S_i}$$

$$\text{for } i = t, mt, ma \tag{4.6}$$

For the titanium alloy (Ti-6Al-4V, Grade 5) end-fittings, a yield stress of 1100MPa (from table 3.1) is used for denominator in calculation of R_{mt}. For calculation of the reserve factor of the fibre tows, a tow tensile strength of 3234MPa is used (taken from [69], for a tow/yarn with assumed 70% intra-tow fibre volume fraction). A matrix (epoxy resin MVR444) strength of 61.5MPa is used, also from [69].

For all joint configurations, high reserve factors for the metallic pins (R_{mt}) indicate that joint and strut failure is likely to occur via pin failure (possible failure mechanisms include pin elongation, bending and shear-off). The virtual tows are loaded to 24%-38% of their tensile strength, across all joint configurations, with the maximum occurring in joint B.

Different axial stiffnesses were observed in section 4.6.1, for strut configurations A-E, due to their varying layup sequences on the mandrel and disparate winding patterns around the pin-structured end-fittings. Therefore, application of a constant axial strain to each strut type, will naturally give different stress levels in the strut, and its constituents (matrix, tow and metal). For fair comparison, each strut must be assessed in terms of its approximate "failure" load.

A failure load is obtained by re-scaling the reaction load until the first reserve factor reaches one, and strut (joint) failure has therefore occurred. As reserve factors were highest for the metal part, this is equivalent to dividing the reaction loads by R_{mt}. Reserve factors of the tow ($\overline{R}_t$) and matrix ($\overline{R}_{ma}$) can also be re-stated for this failure load, as shown in table 4.8. Strut stiffness is also included from section 4.6.1, for comparison purposes.

Table 4.8: Restated reserve factors for the tow and matrix, and the predicted failure load (N) of strut configurations A-E.

Strut Type	$\overline{R}_t$	$\overline{R}_{ma}$	Failure Load (N)	Stiffness, K ($10^6 \mathrm{Nm}^{-1}$)
A	0.34	0.37	20139	44.2
B	0.42	0.7	15456	29.8
C	0.36	0.38	19904	44.2
D	0.27	0.53	12197	17.6
E	0.38	0.53	14434	33.1

As examined in section 4.6.1, strut stiffness is highest for A and C. These also display the highest failure load, indicating joint and strut properties are more optimal for these strut configurations. Joints B and E display similar stiffness and failure load, although both the fibre-tows and matrix are more highly loaded (proportionally to their maximums) in B. This perhaps reflects the increased stress due to the under-wind trajectory of tow pull-back in configuration B. Type D is predicted to provide the lowest stiffness due to its $\pm 45^\circ$ fibre orientations on the mandrel. Joint strength is also comparably poor for D, as the pins are overloaded relative to the tows.

Across all strut configurations matrix failure is likely to follow pin failure, with the virtual tows loaded between 27% and 42% of their maximums at the joint failure load. This highlights the potential for improving joint strength, if configurations could be designed in which loading of the tows is increased, and the pin stress reduced, (see section 7.3).

However, prior to adoption of a formal optimisation strategy, it is first necessary to develop modelling frameworks capable of assessing the joint's mechanical properties, which include more realistic tow geometries. As stated in sections 4.6.3 and 4.6.4, some limitations may have been apparent with regards to capturing of joint load transfer behaviour, and the stress distribution

in the tows and the pin-structured end-fittings, with sufficient realism, through use of the SF method.

4.7 Comparison with fully metallic strut

Comparisons of the hybrid composite-metal strut, and a fully metallic equivalent can be made with regards to strut stiffness, strength and weight. Approximate weights for hybrid struts A-E are firstly calculated. The total length of the virtual tows are extracted from the SF models (section 4.2), for each strut configuration. This is then used with the tow cross-sectional area given in appendix A.1, to provide an estimate of the total tow volume in each strut. The volume of fibre can then be found for an assumed intra-tow volume fraction of 70%.

The total volume of the composite, can be considered as the volume of the model part representing the matrix (section 4.4.2). However, the SF method assumes a virtual tow with cross-sectional diameter of 1mm. This leads to overestimation of the thickness of the virtual tow layers, the volume of matrix material needed to completely contain them (prior to coupling via CLIS), and consequently, also the strut's composite part. Therefore, thickness of the strut's composite part is re-scaled (along with the pin length necessary to provide sufficient contact surface for the virtual tows), from 9mm to 4mm, in order to gain a more realistic prediction of strut weight.

The volume of the matrix is then given by the composite's total volume, minus the fibre volume, and including an assumed 30% of the intra-tow contribution. Weight of the composite part can then be found using material densities of 1750Kgm^{-3} [69] and 1140Kgm^{-3} [98], for carbon fibre and epoxy resin MVR44, respectively.

The average estimated weight of the hybrid strut is 0.4Kg. The heaviest is strut type C (at 0.41Kg), due to the additional, outer hoop layer of filament wound tows (although weight increase in this configuration is offset by the reduction in matrix material).

Hooke's law is used to calculate the cross-sectional area of a fully metallic, tubular strut, consisting of the titanium alloy, Ti-6Al-4V (Grade 5), and with equivalent (tensile) axial stiffness to strut configuration C (which was predicted to be maximal). The cross-sectional area is given by 108.6mm^2, which equates to a wall-thickness of 0.74mm (for an cross-section inner radius of 23mm) for the metallic tube.

Using the strut length of 280mm and material density of 4420Kgm^{-3} in table 3.1, the total weight of the metal strut can be estimated at 0.13Kg. This cross-sectional area can be multiplied by the yield stress of 1.1GPa (also from table 3.1) to provide an approximate failure load of 119kN.

The increased tensile strength (by a factor of 6) and reduced component weight (by 68%) (for an equivalent stiffness) of the titanium strut would imply that significant improvements are required to justify the use of composite materials in the design. This is discussed further in section 7.3 . However, the weight of the pin structured end-fittings is predicted to account for, on

average, approximately 44% of the total weight of the hybrid strut, but only 12% of the hybrid strut's total volume. As no attempt was made to optimise end-fitting weight (a wall thickness of 3mm was used from [6]), this indicates the potential for a more weight optimised hybrid strut. Furthermore, if the hybrid strut was scaled to the physical component size (such as a landing gear lower side-stay), possible weight reduction and improved specific strength and stiffness through use of composite materials may become apparent against the fully metallic equivalent.

Additionally, properties of the novel hybrid composite-metal joint must also be assessed against other possible composite-metal joining techniques, (see sections 5.9.2 and 5.9.3). If performance improvements are predicted, then benefits are apparent to the use of the proposed joining solution in the design of hybrid structures, against other currently available joining methods.

4.8 Virtual compressive tests

For the case of axial (or longitudinal) compression, load transfer between the metallic pins and tows in the joint, is comparatively poor compared to tension. Using an equivalent methodology to section 4.6.1 for calculation of strut stiffness, axial stiffness is reduced by a factor of 200 for strut configurations A and C when loaded in compression (versus tension). As figure 4.38(a) illustrates, the pin-tow mechanical interaction is generally only maintained for tension. Compressive loads result in loss of the contact between the virtual tows and pins, as the tow slips vertically from the pin's surface.

However, as illustrated in figure 4.38(b), the exception is the under-wind pattern used in strut configuration B. For this strut type, axial stiffness is reduced by less than 30%. The pull-back trajectory under the middle "turn" pin maintains contact and load transfer following application of compressive loads to the strut and joint. This results in the compression of the section of the tow contacting the under-side of the pin, as shown in 4.39.

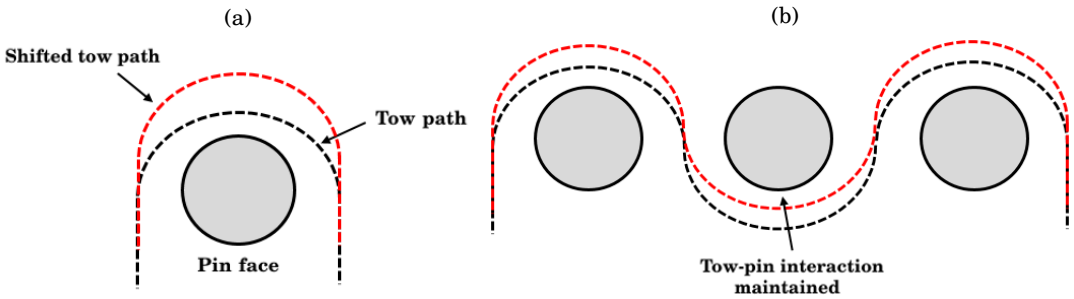

Figure 4.38: Illustration of the tow path (black) during pull-back around the metallic pins in the joint, for a (a) standard over-wind and (b) under-wind trajectory. The shifted tow path resulting from a compressive load being applied to the pin-structured metallic end-fittings at the joint ends is shown (red). The tow-pin interaction is maintained for configuration B due to its under-cutting trajectory around the middle "turn" pin.

Figures 4.40(a) and 4.40(b) show the local fibre direction stress in the virtual tows for the region of the mandrel, for strut configurations A and B respectively, following application of an (global) axial compressive strain equivalent to 2000$\mu\epsilon$. Compressive stresses in the virtual tows for strut configuration A are relatively low (<5MPa) in comparison to B, despite the strut types having identical layup sequences along the length of the mandrel ($[0_6]$). This reflects reduced load transfer in joint type A, for the case of axial compression.

Figure 4.39: Local transverse direction stress in the virtual tows in the pull-back region for strut configuration B, using the under-wind pattern. High compressive stress is located for the part of the tow contacting the underside of the middle "turn" pin.

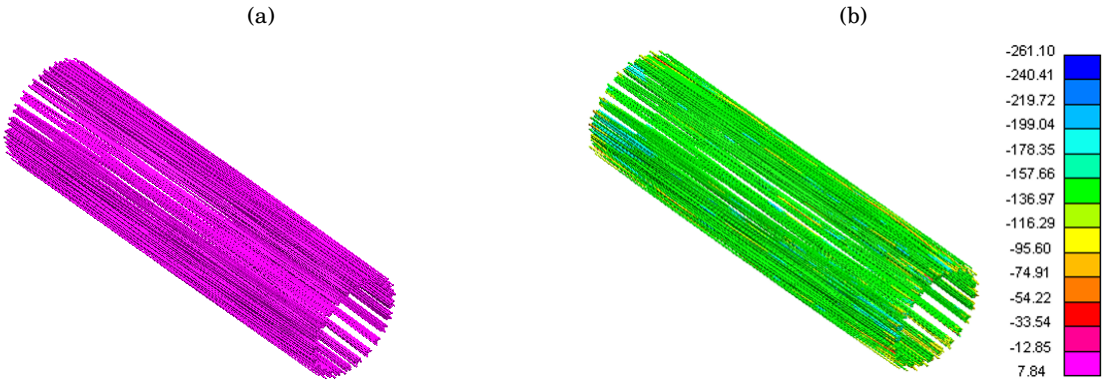

Figure 4.40: Local fibre-direction stress in the virtual tow structure spanning the mandrel, i.e. not including the region of joining mechanism and pin-structured metallic end-fittings, for strut types (a) A and (b) B, following axial compression. Stress magnitudes for the virtual tows in A are relatively low, generally less than 5MPa, reflecting poor load transfer to the tow structure in the joint.

Minor compressive load is also transferred to the virtual tows in strut configurations D and E, as shown in figures 4.41(a) and 4.41(b).This, however, is not due to the pin-tow mechanical interaction initiated via tow pull-back. Instead, as illustrated in figure 4.42, following joint compression, load transfer occurs as the virtual tows shift to contact neighbouring pins. The angled path of the tows through the pin array, in joints D and E, encourage this type of tow-pin interaction, which is more analogous to the shear-locking mechanism occurring in similar

braided/surface-structured joints, as described in section 3.2.2. Consequently, strut axial stiffness is reduced by factors of 12 and 40 for configurations D and E respectively, for the case of compression.

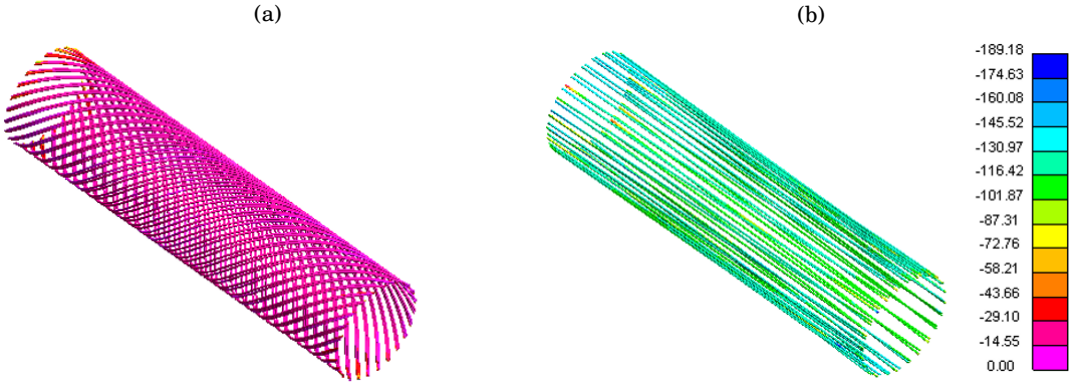

Figure 4.41: Local fibre-direction compressive stress in the virtual tows spanning the mandrel, in layers (a) 1 and (b) 3, of strut configuration D. Compressive load is transferred to the virtual tows due to the mechanism described in figure 4.42, with axial tows experiencing higher (absolute) loads.

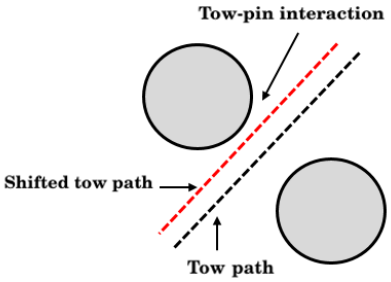

Figure 4.42: Illustration of the angled tow path (black) between the pin array, present in joint types D and E. Following joint compression, the shifted tow path (red), leads to contact with neighbouring pins.

For the case of joint and strut compression, load transfer behaviour may generally be improved in the physical joint. In the modelling framework, no attempt was made to include the adhesive bond occurring between the matrix and the surface of the pin-structured metallic end-fittings, which would result following curing of the composite part of the strut. In the physical reality, following strut compression, surface attachment at the matrix-metal interface should maintain load carrying capability in the joint and operate similiarly to a conventional adhesive joint until bond failure, as reviewed in section 2.2. In such instances, the fibre reinforcement may not contribute directly to load transfer in the joint, but will reinforce the central composite part of the strut.

4.8.1 Additional supporting mandrel

As hypothesised in section 3.1,the central mandrel of the strut could be left as a permanent part, as opposed to being removed following the filament winding process. This may be useful for improving strut properties in compression and mitigating the poor properties observed for the proposed joining mechanism, with regards to compressive loads. A pultruded or braided composite tube could be used for the central mandrel, with an adhesive bond at the mandrel/end-fitting interface. Detailed examination of this concept is beyond the scope of this thesis.

4.9 Summary

A two-step modelling approach was used to study the hybrid composite-metal strut and joining mechanism at the strut ends. Firstly, the tow path on the structure was predicted using the Single Filament (SF) approach. The virtual tows were then converted to 3D continuum elements to allow for modelling of the strut's mechanical performance. Matrix material was included and coupled with the virtual tows via CLIS, so that the strut's behaviour and response under loading more accurately reflected the strut's final operating form.

Quasi-static virtual tensile and compressive tests were conducted on strut configurations A-E. In general, load transfer was predicted to occur mainly via the metallic pins and the fibre-tow reinforcement, due to their direct connection initiated by reversing the tow direction (pull-back) around one, or multiple, pins. This is comparable with aim of the proposed joining mechanism.

Properties of the hybrid strut, with respect to tensile stiffness, strength and susceptibility to torsional effects, were found to be well captured in the simulations. Variation between different strut and joint configurations was inherent, which allowed for discussion of their relative performance ranking. Poor load transfer in the joint was observed for the case of axial compression, although mandrel retention may provide a simple system for improving the strut's compressive properties.

Stress distribution in the virtual tow structure overlaying the mandrel and spanning the two metallic end-fittings at the strut ends, was found to be well represented, with stress magnitudes varying between fibre orientation and layer order in the sequence, in accordance with the principles of composite materials and fibre-load alignment.

Comparison with a fully metallic strut found that inclusion of composite materials in the strut design is not yet justified, as no weight saving benefits were apparent against a metal strut with equal (or greater) (tensile) stiffness and strength. However, this may be attributable to limitations with the Single Filament (SF) method. The SF approach, and the mechanical model of the strut developed following the conversion of the tow structure to solid element types, both explicitly assume that the virtual tow has a constant, uniform, circular cross-section.

This may consequently lead to overestimation of the thickness of the hybrid strut's composite part, thereby contributing to over-prediction of structural weight, (despite efforts made in section

4.7 to take this into account), underestimate tow coverage on the strut's surface, and provide a less realistic representation of the load transfer mechanism between the tows and pins in the joint.

Moreover, load transfer between the fibre tows and pins in the joint may not be captured with sufficient realism, which may under-predict the performance potential of the hybrid composite-metal joint and strut. For example, stress distribution in the pins was found to have limited agreement with the that predicted using the analytical model in section 3.8.

In the physical joint, tow cross-section geometry is likely to vary significantly due to interactions with the pin-structured metallic end-fitting. For example, the tows may become compacted or flattened during pull-back around the pins, and exert load over a larger area of the pin's surface. Realistic tow geometries must be taken into account in order to more accurately represent load transfer and stress distribution in the physical joint.

Methodologies are developed in chapter 5 to include these effects, and to model the fibre-tows with improved realism. This is necessary to develop sufficient modelling tools to characterise the hybrid composite-metal joint and strut, prior to adoption of a formal optimisation strategy in which joint performance is maximised so performance is comparable (or improved) against a fully metallic strut component. Also, joint potential must be assessed against other available composite-metal joining techniques.

CHAPTER 5

MESO-SCALE MECHANICAL ASSESSMENT OF THE COMPOSITE-METAL JOINT USING A HIGHER FIDELITY APPROACH

In chapter 4, the properties of the hybrid strut, and the joining mechanism at the strut ends, were assessed using a virtual tow with a uniform, constant cross-sectional shape. In physical reality, the tow shape may change significantly between different points on the strut.

For example, as the fibre-tow is manipulated around the cylindrical pins during pull-back, the tow may become significantly deformed as it is flattened and pressed onto the pin's surface. In order to form a detailed understanding of the interaction occurring in the joint, between the filament-wound fibre-tows and the metallic pins, it will be important to account for such variations in the tow geometry and internal architecture, in the development of a model that studies the mechanical properties of the joint with improved realism. Load transfer behaviour and stress distribution in the fibre-tows and metallic pins, are likely to differ compared with the case in which the tow cross-section is assumed to be both constant and circular.

Consequently, this chapter proposes a multi-stage modelling framework to predict the performance of the composite-metal joining mechanism occurring at the ends of the hybrid strut. Firstly, the Multi-Filament (MF) method is used in a "Forming" simulation to obtain tow geometries that more accurately reflect the expected structure of the physical fibre-tow, in the region of the joint, following the filament winding process. Deformations and distortions that are likely to be induced in the tow due to the interactions with the pin-structured end-fittings, are captured.

Following which, information regarding the tow's variable geometric shape and internal architecture are then utilised in the construction of a higher fidelity model to assess the joint's mechanical performance. As previously, the virtual tows are represented using 3D continuum (solid) elements, which are coupled with independently meshed matrix material via the LS-Dyna®

function *CONSTRAINED_LAGRANGE_IN_SOLID (CLIS).

Quasi-static virtual tensile tests are conducted on joint designs A and E to demonstrate the results of this detailed joint model, against those obtained in section 4.6, using a virtual tow with constant, circular cross-section.

Finally, the novel composite-metal joint that has been proposed, designed and examined in this work, is compared against two alternate joining techniques. The first is a reference joint established using adhesive bonding (see section 5.9.3). The latter is a similar joining mechanism created using braiding technology (section 5.9.2).

Stage 1: Tow Forming

5.1 Multi-Filament (MF) Method

Recall that in the Single-Filament (SF) method (section 3.1), the virtual tows are modelled as a chain of truss elements with constant, circular cross-section. In comparison, the Multi-Filament (MF) method describes each virtual tow as a bundle of such truss chains, as shown in figure 5.1(b). This approach is similar to the Multi-Chain Digital Element (MDE) method developed by Zhou *et al.* [15] to study yarn deformations induced during composite textile production processes, such as weaving and braiding.

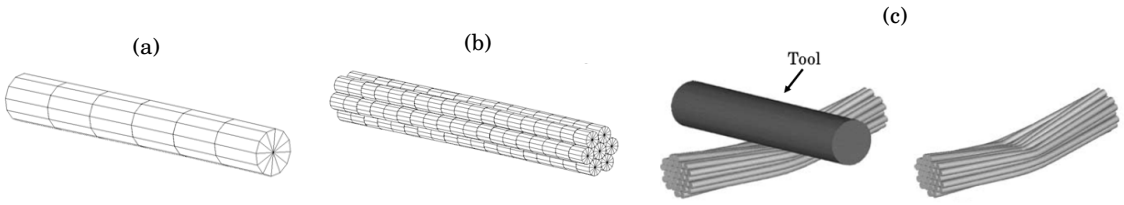

Figure 5.1: Length of a virtual tow modelled using the (a) Single Filament (SF) and (b) Multi-Filament (MF) methods. In this example the MF virtual tow is consists of 7 filaments, or virtual fibres. (c) Deformation being induced to a straight virtual tow, or yarn, due to it contacting a cylindrical rigid tool [15].

Each truss chain, filament, or virtual fibre, homogenises the behaviour of a number of fibres within the physical tow, or yarn. (For example, for a 12k carbon fibre-tow modelled using 12 filaments, each virtual fibre approximates the behaviour of 1000 physical fibres). As relative contacts and displacements between the virtual fibres within the tow structure are possible, a variable tow internal architecture and geometric shape can be captured, as shown in figure 5.1(c).

In this work, the MF method is used to predict as-manufactured geometries of the fibre tows for the region of the joint, resulting from interactions with pin-structured end-fittings during

the filament winding process (see section 5.4). However, prior to applying the MF method to simulations involving the full composite-metal joint, the simple case of an individual fibre-tow reversing direction (pull-back) around a single cylindrically shaped pin, is firstly examined in section 5.2. Furthermore, the effect of model parameters is examined in section 5.3 using this simple case.

5.2 Single Pin Forming

A virtual tow, represented using the MF method, is placed on an arced path around a pin, as shown in figure 5.2(a). Within the tow, the virtual fibres are initially arrayed in a circular patterned cross-section, as illustrated in figure 5.2(b). Modelling techniques for the pin (shell elements) and virtual fibres (truss elements) remain unchanged from those used in section 4.2. Similarly, contact between the virtual fibres is modelled using LS-Dyna® contact type BEAMS_TO_SURFACE and inter-fibre contact is handled with contact formulation AUTOMATIC_GENERAL. A coulomb friction coefficient of 0.1 is used in the contact definitions.

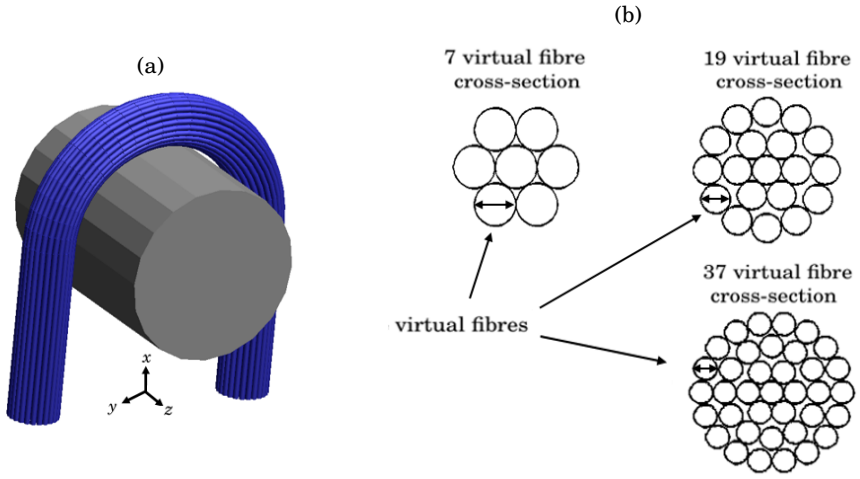

Figure 5.2: (a) MF tow consisting of 37 virtual fibres (blue), with an arced trajectory around a cylindrical pin (grey). Initial tow cross-section, prior to the forming simulation, is perfectly circular due to the arrangement of its constituent virtual fibres. (b) 2D representation of the initial arrangement of the MF tow's virtual fibres, for a tow consisting of 7, 19 and 37 virtual fibres.

In order to obtain a realistic representation of the physical tow, a degree of deformation must be induced to the virtual shape to alter its geometry and internal architecture via the relative movement of its constituting virtual fibres. For this, a load of 0.5N is applied to the end-nodes of each of the virtual fibres, in the negative x-direction, over a time period of 2 seconds. This has the effect of pulling the virtual tow onto the pin. The as-simulated tow shape, seen in figure 5.3(a), provides an approximation of the physical tow structure that would be expected if a

single fibre-tow was manipulated onto a cylindrical pin. The tow's cross-sectional shape is altered throughout its length so that it forms a more elliptical configuration, as shown in figure 5.3(b),

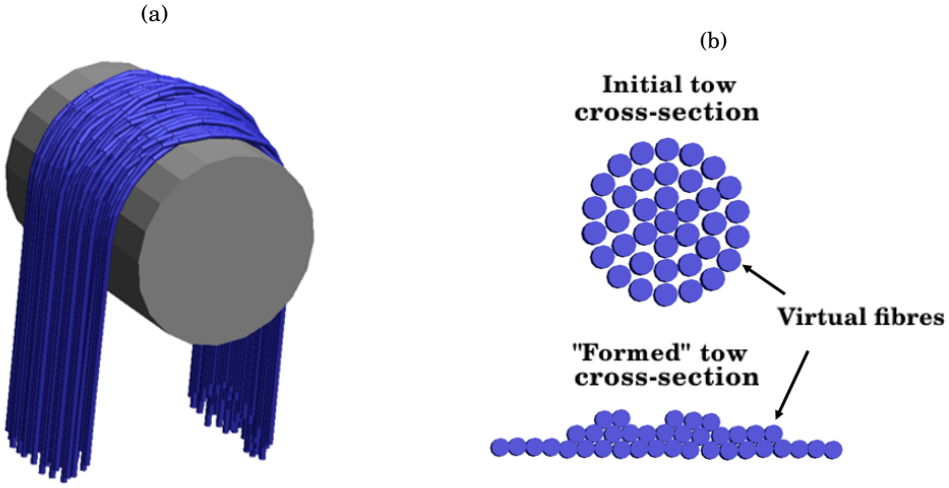

Figure 5.3: (a) Final tow geometry obtained from the forming simulation. (b) Deformation of an virtual tow cross-section, from the initial, circular patterned distribution of its virtual fibres.

The "formed" tow can be analysed through calculation of an intra-tow fibre volume fraction (section 5.2.1) and approximation of the cross-section shape (section 5.2.2). The values, and their variation along the length of the tow, develop an understanding of the level and type of deformation induced in the MF virtual tow during the forming simulation.

Although the mechanism by which tow deformation is induced, is relatively simple for the case of an individual tow forming around a single pin, characterisation and analysis of the alteration to the tows' geometric shape and internal architecture is more complex in the full joint model in section 5.4, due to the tow interacting with multiple pins, the end-fitting's surface and also other virtual tows. This detailed description of the tows' geometry is also necessary to construct a model capable of assessing the joint's mechanical performance (see sections 5.7 and 5.8).

5.2.1 Calculating the intra-tow fibre volume fraction

The internal architecture of the MF virtual tow, following the forming simulation, can be assessed using the predicted values of the intra-tow fibre volume fraction at discrete sections of the tow.

For this, the tow geometry is firstly extracted via cross-sections at points along the length of the tow, using the nodal coordinates of the end-nodes of the truss elements that define the virtual fibre chains, as shown in figures 5.4(a) and 5.4(b).

A 3D orthonormal system (a,b,c) is then constructed using the vector, a, which defines the tow centreline path spanning the geometric centres of adjacent cross-sections. Vector b is found using the procedure detailed in [16] and c is given by the cross-product of a and b. Each extracted cross-section is then mapped to a two-dimensional x-y plane, as shown in figure 5.4(c). Additional

nodes are then projected from the cross-section nodes in order to account for the radius of the virtual fibres prior to defining the tow cross-section shape. A convex hull algorithm [99] is then used to "wrap" these projected nodes. The outlining polygon, given by the hull nodes, defines each tow cross-section shape, figure 5.4(d).

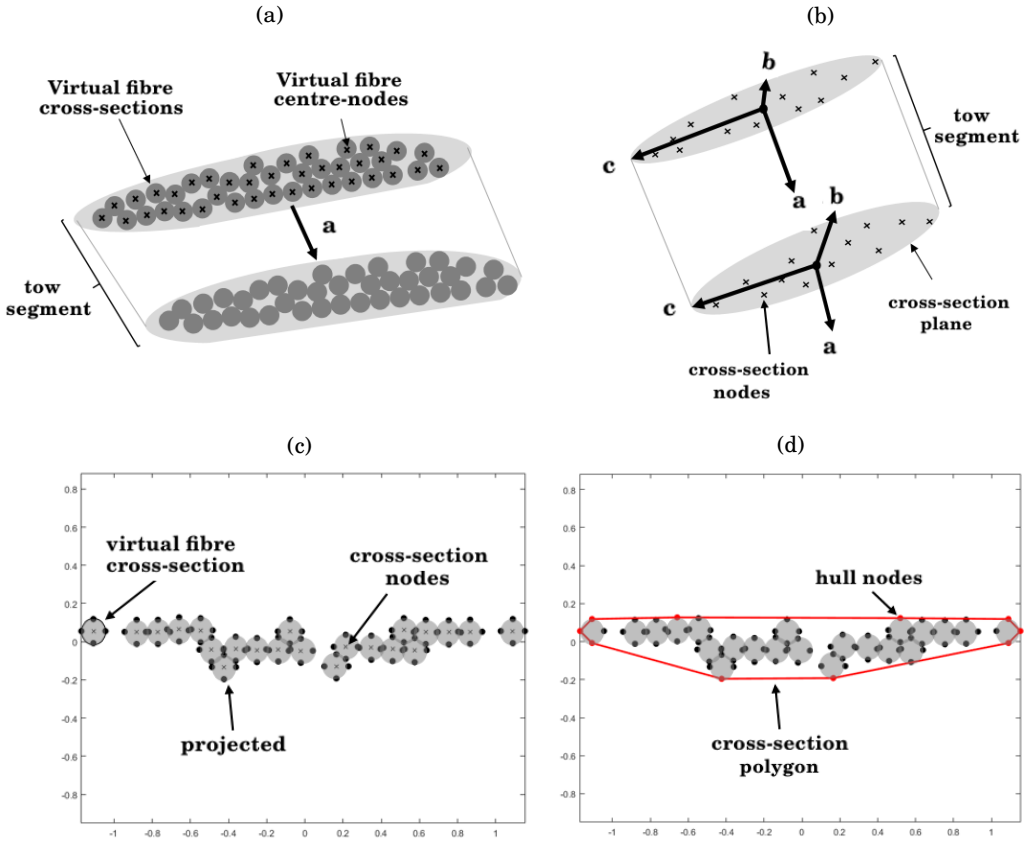

Figure 5.4: (a) Extraction of a deformed tow segment via the virtual fibre positions in two adjacent cross-sections. (b) 3D cross-section nodes, with vector "a" defining the tow centre-line path. (c) Mapped 2D cross-section nodes, with projected nodes to account for radius of the virtual fibre cross-section prior to defining cross-section shape. (d) Hull nodes selected by the convex hull algorithm. These define a polygon representing the cross-section's shape.

The average area of two adjacent cross-section polygons, (each of area Ap_i and Ap_{i+1}), provides an estimate of the cross-sectional area of a given segment of the tow, A_{Ts}, as illustrated in figure 5.5. The volume, V_{Ts}, of the tow segment is then equal to A_{Ts} multiplied by the segment length, L_{Ts}. This is given by the length of the vector, a, between the two adjacent cross-section centre nodes. The volume of the virtual fibres contained with the tow segment, V_f, is given by the product of the cross-sectional area of an individual fibre, A_f, with the number of fibres, N_f, and the segment length. Taking into account the maximum packing factor of physical fibres within each virtual fibre, the intra-tow fibre volume fraction for a given segment of the tow length, is then given by f in equation 5.1.

$$
\begin{aligned}
A_{Ts} &= \frac{Ap_i + Ap_{i+1}}{2} \\
V_{Ts} &= L_{Ts} A_{Ts} \\
V_f &= A_f N_f \\
f &= 0.91 \frac{V_f}{V_{Ts}}
\end{aligned} \tag{5.1}
$$

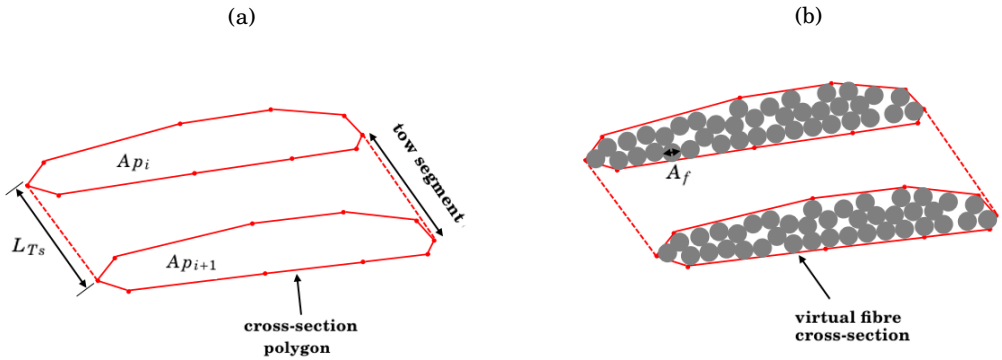

Figure 5.5: (a) Adjacent cross-section polygons, whose areas (A_{Ts}) are used with the segment length (L_{Ts}) to define the total volume of the tow segment (V_{Ts}). (b) Virtual fibre cross-sections, each of area A_f, contained within each cross-section polygon.

5.2.2 Approximated the "formed" tow cross-section shape

An representation of the geometric shape of the virtual tows, following the forming simulation, can be determined by fitting an ellipse to each cross-section polygon, as shown in figure 5.4(a). This determines an approximate height and width for each tow cross-section. The deviation in these values provides an understanding of the variability in the tow shape along its length.

The shape of a cross-section ellipse is determined by dividing the x-y cross-section plane into four quadrants, $Q_1 \in [0, \frac{\pi}{2})$, $Q_2 \in [\frac{\pi}{2}, \pi)$, $Q_3 \in [\pi, \frac{3\pi}{2})$) and $Q_4 \in [\frac{3\pi}{2}, 2\pi)$. The major and minor axes lengths of the cross-section ellipse are given by $b = |b_1| + |b_2|$ and $a = |a_1| + |a_2|$, respectively. The values of a_1, a_2, b_1 and b_2 are determined independently using the extreme x and y coordinate positions of the convex hull nodes that define the cross-section polygon.

This allows for the use of non-symmetric ellipses, which more accurately fit non-uniform and irregular cross-sections (represented by irregular cross-section polygons). For example, one side of the tow may be significantly flattened as it is pressed to the surface of a pin during pull-back, in which case the values of a_1 and a_2 may differ significantly as the tow cross-section is more accurately reflected by a semi-ellipse . Additionally, pinching and narrowing of the tow cross-sections (as observed in section 5.4 for the case of multiple layers of virtual tows in the full

joint) are accounted for by more circular cross-sections where the major and minor axes lengths (a and b) take similar values.

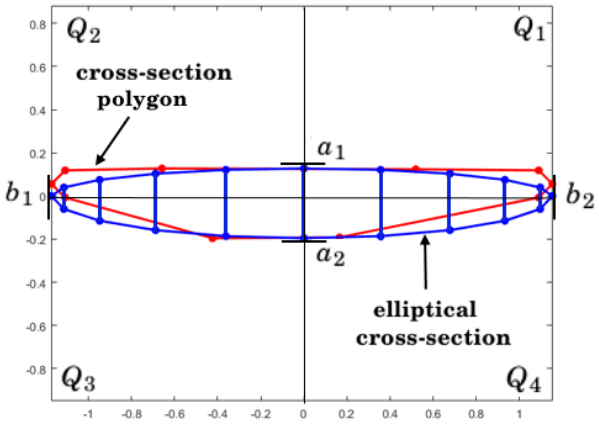

Figure 5.6: Elliptical fitting to the cross-section nodes. This allows for an approximate of the tow height and width at discrete points along the length of the virtual tow, so that its geometric shape can be assessed and described.

5.2.3 Analysis of the "formed" tow geometry

From the single pin forming simulation, the tow is predicted (using the major and minor axes lengths of the fitted ellipse) to have average cross-section width, height and aspect ratio (width/height) of 2.36mm, 0.35mm and 6.74, respectively. The virtual fibres spread significantly resulting in a very flat, wide tow cross-section. This effect is exaggerated for regions of the tow contacting the pin's surface, as observed in figure 5.7, which shows the variation in the intra-tow fibre volume fraction. Lower fibre volume fractions are present for sections of the tow around the pin, this is due to increased lateral dispersion of virtual fibres along the pin's surface and a less compacted tow cross-section.

5.3 Forming Parameters

The final tow geometry and internal architecture gained from the forming simulation, is dependent upon the choice of several model parameters. Green *et al.* [100] conducted a study into the effects of parameters including material density (degree of mass scaling), the number of filaments (virtual fibres) per yarn and model friction, for the forming of a 3D woven fabric unit cell using a Multi-Chain Digital Element (MDE) approach implemented in LS-Dyna ®. The simulated tow geometries were compared against x-ray computed tomography (μCT) scan images of the physical fabric. Model friction and the number of virtual fibres used for the tow cross-section, were determined to be the most influencing factors on the simulated yarn geometries. Friction

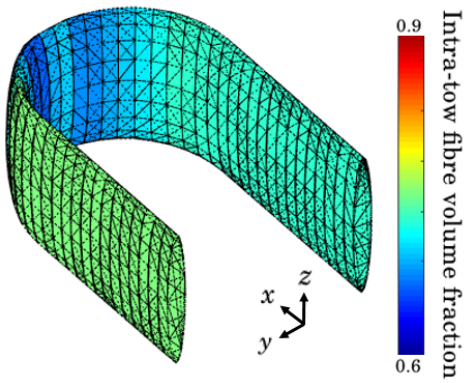

Figure 5.7: Variation in the predicted intra-tow fibre volume fraction along the tow length. Lower values, for the region of the tow contacting the pin, are caused by increased spreading of the virtual fibres as the tow is pressed onto the pin's surface.

was important for determining the degree of yarn crimp and waviness in the fabric, while the use of fewer virtual fibres resulted in comparatively poor prediction of the yarn's cross-section shape.

In this work, the effect of model friction is assessed used in section 5.3.1. As two contact definitions are used to govern inter-fibre and fibre-to-pin contact types, these must be considered independently.

The number of virtual fibres in the tow cross-section is examined in section 5.3.2. In general, the accuracy of the MF method should improve as the virtual tow is refined with an greater number of virtual fibres for its cross-section [101]. The difference between the number of virtual and physical fibres is reduced and physical tow behaviour is more realistically modelled. However, significant refinement of the virtual tow leads to increased computational expense as the number of elements is increased. This will become more of a consideration for the case of the forming of multiple layers of virtual tows in the full composite-metal joint, (see section 5.4).

Conversely, fewer virtual fibres in the MF tow representation may result in less accurately defined cross-section polygons (section 5.2.1), as the convex hull algorithm has fewer nodes from which to select to determine the outlining shape. The cross-section polygon's shape is more easily skewed by outlier virtual fibre positions, so that significant overestimation of the polygon's size and area can occur as local concavities are ignored to a greater extent, resulting in a relatively low predicted value for the intra-tow fibre volume fraction.

Other model parameters such as material density, modulus and truss element length are not considered here. Nor are they assigned values representative of physical parameters. Instead, their values are collectively determined to provide a combination of good contact definition, minimal dynamic effects and reasonable analysis times. Material densities and moduli of $5e^{-3}$ tonne/mm^3 and 25 GPa are used, respectively. Within the virtual fibres, the truss element length is determined by their cross-section diameter and the use of a maximum aspect ratio of 4. Additionally, as in section 4.1, a damping factor of 10 is maintained using LS-Dyna® keyword

*DAMPING_GLOBAL.

For the single pin forming, the magnitude of the pull-force applied to the end-nodes of the virtual fibres to induce deformation to the tow structure, is also not a considered model parameter. This, however, may have a significant effect on the final tow geometry obtained. For example, a comparatively low applied force may not cause sufficient deformation to the virtual tow, leaving it relatively unchanged from the initial, unrealistic circular cross-section. Use of physical forces, such as the tension applied to the fibre-tow during the filament winding process, would be impractical as non-physical values are used for both the stiffness and density of the virtual fibres. Instead, the effect of the applied force is monitored to ensure that its application results in an approximate, realistic tow geometry (with appropriate model friction values). In section 5.4, a displacement controlled mechanism is utilised for an equivalent effect.

5.3.1 Contact Friction

Three separate single-pin models are constructed to study the effect of contact friction in the forming simulation. As shown in table 5.1, model 1 has relatively low values of 0.1 assigned to both inter-fibre (μ_{IF}) and fibre-pin contact types (μ_{FP}). Model 2 has a high value of 1, for contact between the virtual fibres and the pin, and a low value of 0.1 to govern inter-fibre contact. Model 3 has the inverse relationship to model 2.

Table 5.1: Coulomb friction coefficients assigned to the inter-fibre (μ_{IF}) and fibre-pin (μ_{FP}) contact definitions in three separate models 1, 2 and 3.

Model	1	2	3
μ_{FP}	0.1	1.0	0.1
μ_{IF}	0.1	0.1	1.0

Figure 5.8 shows the final tow geometries for models (a) 1, (b) 2 and (c) 3, respectively. The virtual tow geometry in model 3 is practically unchanged from the initial configuration of a circular patterned cross-section. High inter-fibre friction prevents separation between the virtual fibres and alteration of the tow's cross-sectional shape. Similarly for model 2, deformation in the tow structure is limited by the high friction between the virtual fibres and the pin, although tow deformation is slightly increased over model 3, indicating that inter-fibre friction has the greater influence with regards to inhibiting movement of the virtual fibres within the tow. Model 1, shows a simulated tow geometry that is more representative of the expected form of the physical tow, with an approximate elliptical cross-section that is formed due to it being pressed onto the pin.

It can be concluded that contact friction has a significant influence on the degree of deformation induced in the virtual tow, and its final simulated geometry. The use of physical friction values would be infeasible, as number of virtual fibres is significantly less than the number of physical fibres in the tow. Instead, frictions values should be used that do not inhibit relative displacement of the virtual fibres within the tow and provide realistic spreading of the tow cross-

section shape during forming. This occurred with a relatively low coulomb friction coefficient of 0.1.

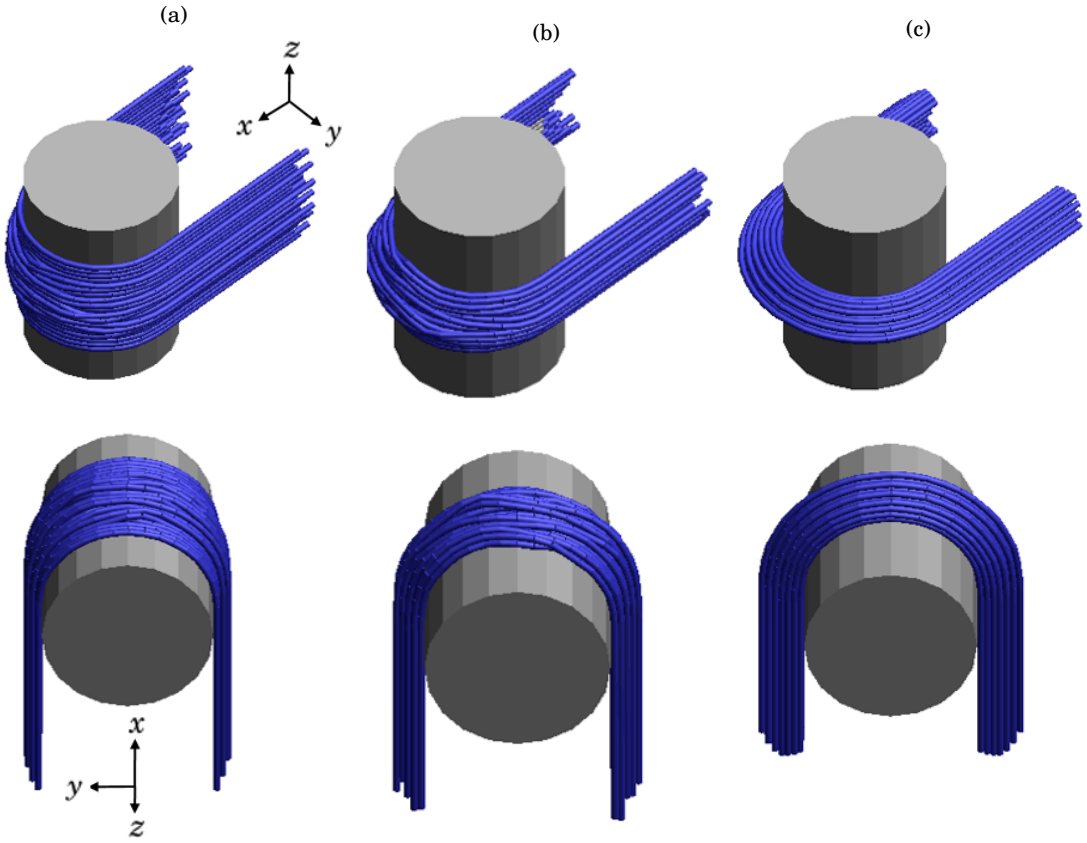

Figure 5.8: Final tow geometries from the forming stage of the simulation of a single tow around a cylindrically shaped pin for models (a) 1, (b) 2 and (c) 3, using different friction values for inter-fibre (μ_{IF}) and fibre to pin (μ_{FP}) contact definitions.

5.3.2 Number of virtual fibres per tow

The number of virtual fibres used to describe the tow is now examined. Three models are constructed for a virtual tow consisting of 19, 37 and 61 fibres, respectively. Friction parameters are consistent with model 1 of section 5.3.1.

Table 5.2 lists the range in the intra-tow fibre volume fractions for virtual tows consisting of 19, 37 and 61 virtual fibres. As similar intra-tow fibre volume fractions are indicative of similar internal architectures, little obvious difference can be observed between the use of 19 and 37 virtual fibres, however, the case of 61 virtual fibres does predict a greater (+15%) maximum volume fraction.

Figure 5.9 displays the variation in the intra-tow fibre volume fraction along the length of the tow. Similar variation in the intra-tow fibre volume fraction is displayed in the three cases, with relatively low values for the sections of the tow around the pin, as the virtual tow is pressed onto the pin's surface, causing increased spreading of the virtual fibres within the tow cross-section. For the 61 virtual fibre case, this region is predicted to encompass a larger proportion of the pin's surface, where as for fewer virtual fibres, this is confined to the section of the tow contacting the top part of the pin. Relatively high volume fractions occur at the tow ends, where the applied load limits relative displacement of the virtual fibres. The virtual tow consisting of 61 virtual fibres predicts greater compaction of the virtual fibres in this region.

For the case of a single pin, expected variation in tow shape and internal architecture (as observed by the predicted variation in the intra-tow fibre volume fraction), such as increased flattening of the tow cross-section and spreading of the virtual fibres around the pin , was well captured for a virtual tow consisting of 19 virtual fibres. Increase computational cost associated with using a higher number of virtual fibres in the tow cross-section will take more importance for the case of the full joint forming simulation in section 5.4.

Table 5.2: Range in intra-tow fibre volume fractions (2 d.p.) for a virtual tow formed around a cylindrical shaped pin and represented using 19, 37 and 61 virtual fibres, respectively.

Number of virtual fibres	19	37	61
Range in intra-tow fibre volume fraction	0.61-0.75	0.67-0.75	0.61-0.86

5.4 Full joint forming

Having established "ideal" forming parameters (accuracy of the predicted tow geometry against computational expense) for the case of individual tow wrapping a single pin, the more complex case of the forming of six layers of virtual tows around pin-structured end-fittings, in the joining mechanism at the strut ends, is now considered.

The methodology adopted is similar to that utilised by Huang *et al.* [16], to obtain realistic yarn architectures in a 3D woven fabric unit cell, using a MF approach. Yarn representation

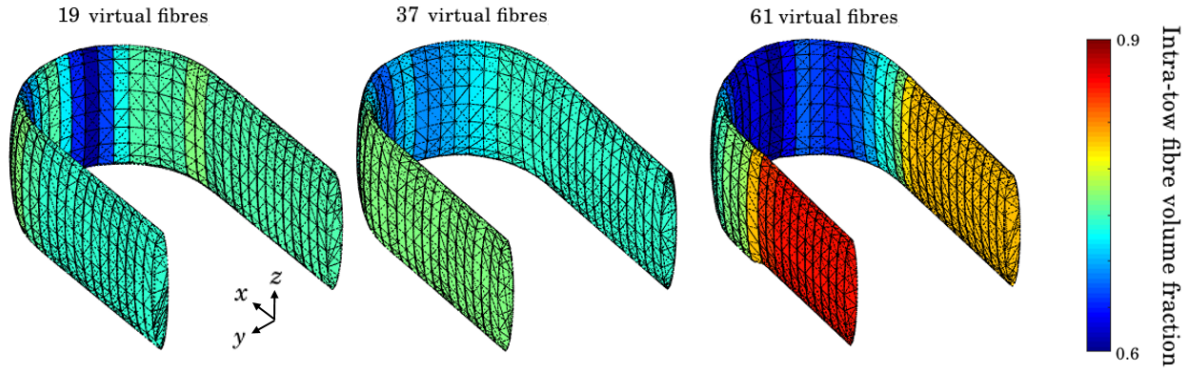

Figure 5.9: Variation in the intra-tow fibre volume fraction along the length of the tow, using 19, 37 and 61 virtual fibres per tow.

was progressively refined through increasing the number of virtual fibres at each stage of the fabric forming simulation, as seen in figure 5.10. In such forming simulations, yarn deformations were found to be initially minimal, with yarn movement being the predominate behaviour as the yarns position progress from an approximate assigned path, or topology (top left image). Significant computational cost can be saved through use of a single filament yarn for the initial stages of the simulation, as the model contains fewer contacting elements. The number of virtual fibres can then be increased at later stages as the fabric approaches a more realistic thickness (proceeding clockwise through the images) and modelling of yarn geometric effects takes increased importance.

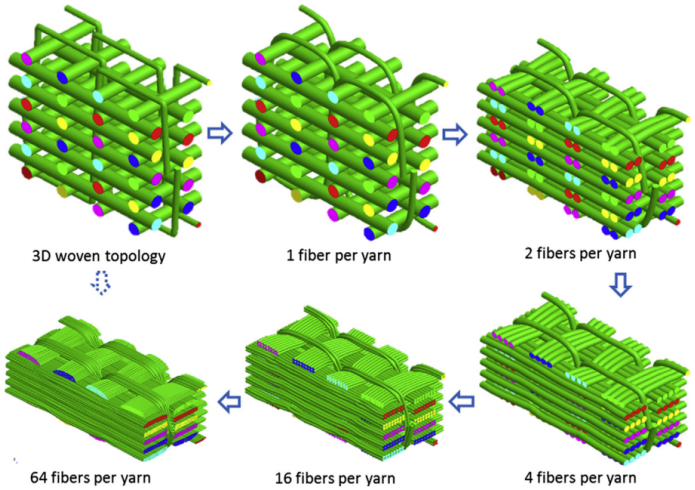

Figure 5.10: Multi-stage yarn refinement for 3D woven fabric unit cell [16]. The top left image shows the initial, assigned topology of the unit cell. Moving clockwise the yarn cross-section is refined with an increasing number of virtual fibres as the fabric approaches a more physical thickness, allowing for yarn geometric effects to be modelled.

As described in section 5.4.1, firstly, the Single-Filament SF method is used to predict the as-manufactured path of the tows, in the region of the joint. Similarly to sections 4.2, this uses an initial, approximate analytical designation of the tow path, which is then refined through assignment of a fictional coefficient of thermal expansion to the virtual tows, and subsequent application of a temperature gradient. This has the effect of generating a level of strain in the virtual tows, thereby reducing excess tow length and providing smoother, realistic tow paths, which are consolidated closer to the end-fitting's surface.

Once more realistic tow paths and degree of radial tow density has been achieved using the SF approach, the virtual tows are then refined so that their cross-sections are represented as a bundle of virtual fibres, in accordance with the Multi-Filament (MF) method. As with the case of a individual tow forming around a single pin, deformations are induced in the virtual tows due to their relative interactions and contact with the pin-structured end-fittings. The simulated tow geometries and internal architectures should then more accurately reflect the expected form of the physical tow, which would result from the layup of the fibre-tows in the joint region, during the filament winding process.

Model constructs for the pin (shell) and virtual fibres (truss) are maintained from the single pin forming simulations in section 5.2. Similarly, the contact definitions are unchanged and a coulomb friction coefficient of 0.1 is used. The virtual tows are represented using 19 virtual fibres per tow cross-section.

5.4.1 SF method for tow path prediction and radial consolidation

The virtual tows are constructed using the SF method, as seen in figure 5.11. Only one end of the strut is represented, so that the model considers a pin-structured end-fitting and 10mm of the central mandrel (5% of the full mandrel length). Consequently, unlike the full strut model developed in section 4.2, the virtual tow layers do not form a closed loop via the equivalence of the first and last centre-nodes of the truss elements in a virtual tow chain. Therefore, appropriate boundary conditions must be assigned to the free tow ends, so that tension is maintained following thermal loading.

As illustrated in figure 5.12, a local orthonormal coordinate system is defined at each tow end-node via the LS-Dyna® keyword *DEFINE_COORDINATE_SYSTEM. Movement along the vector X', which is the radial direction at that end-node relative to the end-fitting's x-z cross-sectional plane, is permitted using the keyword *BOUNDARY_SPC. All other translation and rotational degrees of freedom are constrained. This allows the virtual tows to consolidate towards the end-fitting's surface, whilst maintaining an unaltered tow trajectory for the mandrel length so that the winding angle is preserved.

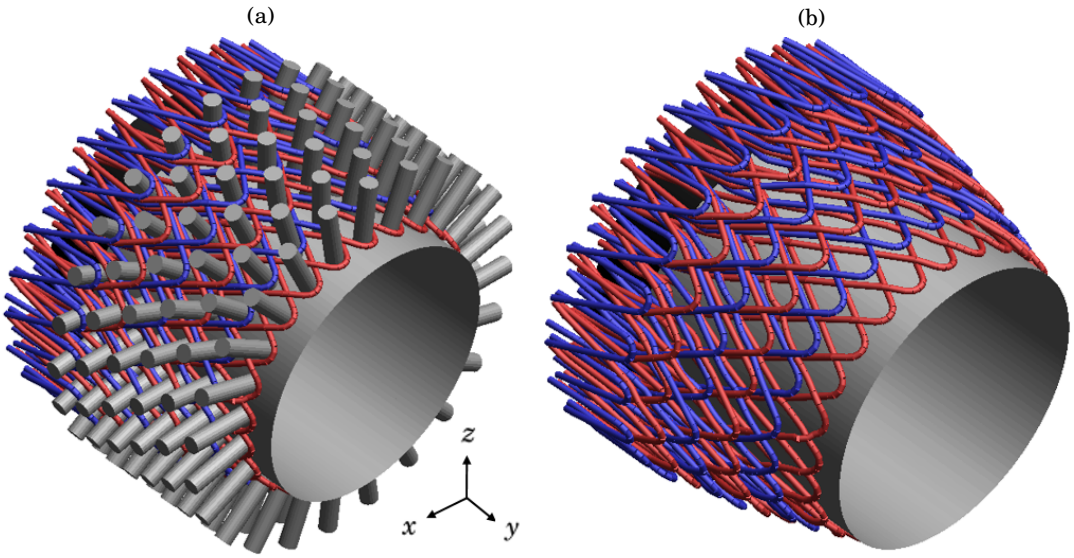

Figure 5.11: (a) The final position of the SF following the simulation, for joint configuration E, in the region of a pin-structured end-fitting (grey) and part (10mm) of the mandrel length (black). (b) With pin surfaces omitted from the image so that the path of the tows can be seen more clearly. The virtual tow layers are coloured red and blue alternately.

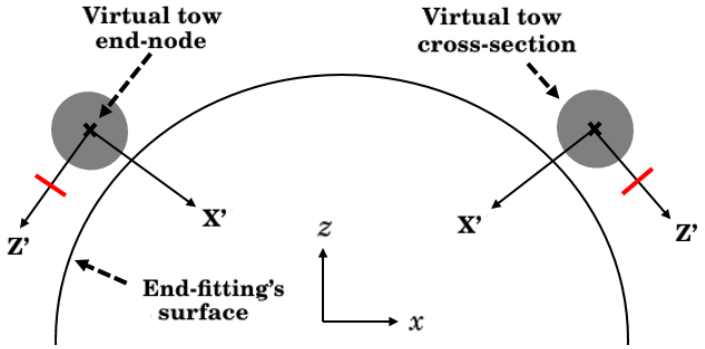

Figure 5.12: Schematic (not to scale) of the boundary conditions at the end-ndoes of the virtual tows in the SF stage model of the full joint. x and z defines the cross-section place of the end-fitting. The virtual tows are free to move in the radial direction, X', which allows them to consolidate towards the end-fitting's surface.

5.4.2 MF method for tow forming

As in section 4.4.1, the path of the virtual tow is extracted from the SF model using the centre-nodes of the truss elements that describe the virtual tow chains. This centre-line path is then refined by linearly interpolating between adjacent nodes, as shown in figure 5.13. This refinement is necessary to establish an aspect ratio of ≤4 for the truss elements in the virtual fibre chains, in order to ensure good contact definition (minimal interpenetrations) is maintained during forming.

Deformation is then induced in the MF virtual tows by maintaining the boundary conditions

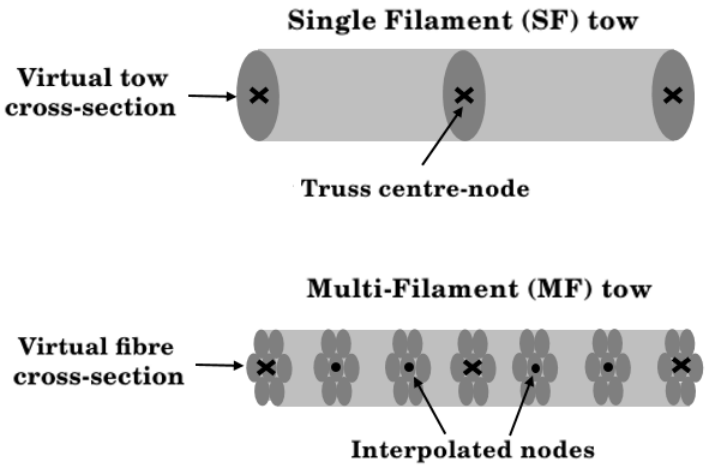

Figure 5.13: Schematic of the conversion of the SF tow to a MF representation. The tow path is refined by interpolating between adjacent path nodes, so that the aspect ratio of the virtual fibres in the MF method does not exceed 4.

on the free ends of the virtual fibres, and prescribing a displacement of 0.5mm to the pin-structured end-fitting in the positive y-direction over an analysis time period of 20 seconds, so that the virtual tows are brought into contact with the pin surfaces. The relative displacements of the virtual fibres within the tow cross-sections causes alteration from the initial, perfectly circular tow geometry, seen in figure 5.14(a); to one that more accurately represents the expected shape of the physical fibre-tow, resulting from the filament winding process, as seen in figure 5.14(b).

This can be observed by the flattening and spreading of the virtual tows around the "turn" pins utilised for pull-back, as highlighted in region 1. Also, in the pinching and deflection of the tows due to intra-layer interactions at tow crossing points (region 2) and due to inter-layer nesting effects (region 3). Further analyses of the simulated tow geometries and internal architectures, for joint configurations A and E is conducted in section 5.5.

A non-physical structure, referred to as a "band tool", is utilised in the model to compact the virtual tow layers to a radial thickness of 2.4mm (or 0.4mm per layer). This should provide a better approximation of the thickness of the physical filament wound fibre-tows. The "band tool" consists of an open-ended ring of shell elements, which envelops the virtual tows for part (5mm) of the mandrel length, as seen in figures 5.14(c) and 5.14(d). Following tow forming, opposing circumferential displacements are applied to the nodes at the open ends of the tool over an analysis time of 10 seconds (for total analysis time of 30 seconds in the full joint forming simulation) to decrease its radial distance relative to the end-fittings surface. The virtual tow layers are thereby consolidated to a thickness given by the final radial distance between the tool and the end-fittin's surface (contact between the tool and the virtual fibres is also established via contact type BEAMS_TO_SURFACE, with a friction coefficient of 0).

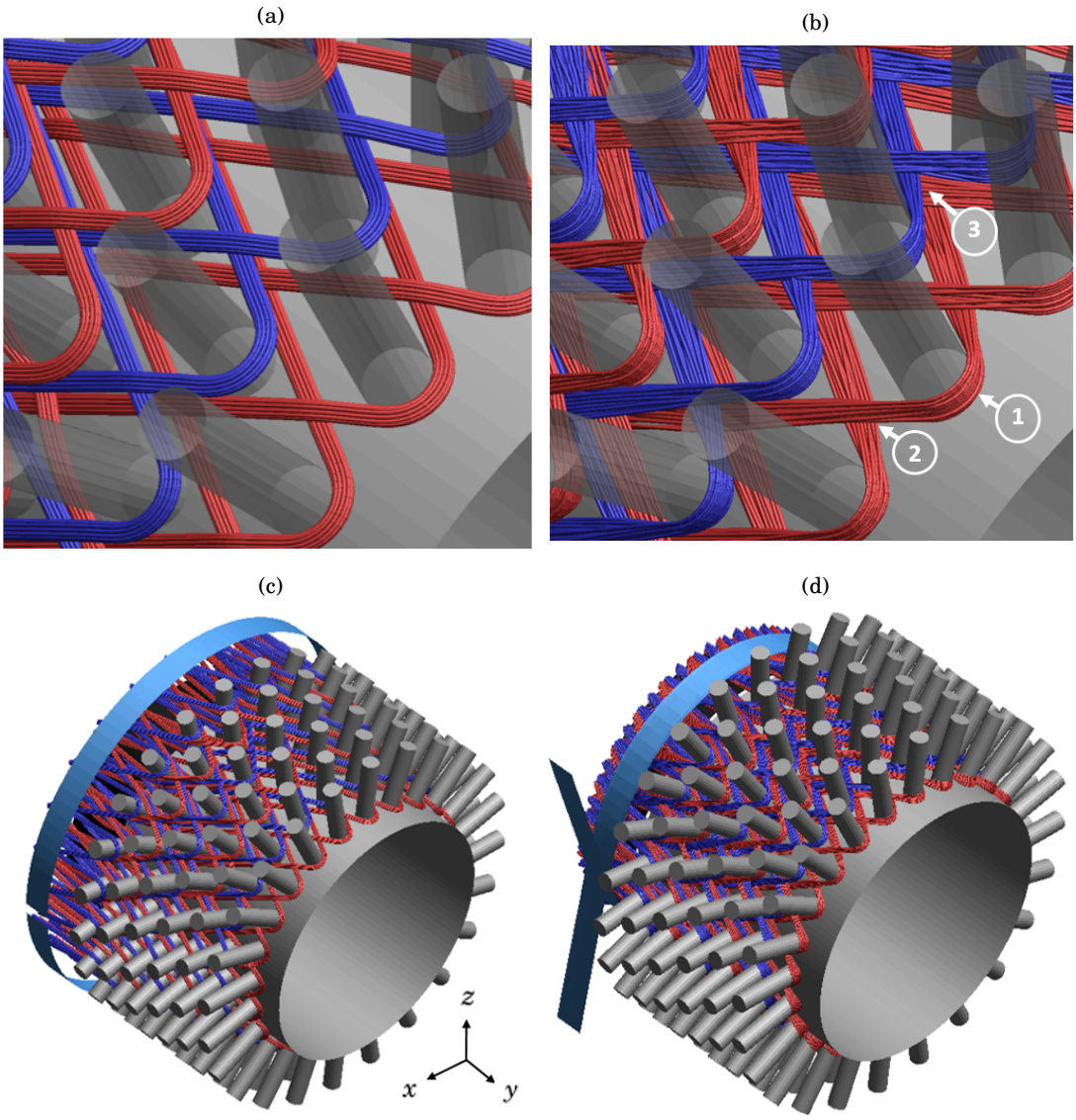

Figure 5.14: (a) Close view of the initial tow structure, prior to forming, on part of the pin-structured end-fitting (grey). The virtual tow layers are coloured red and blue alternately. Pin surfaces are made partially transparent so that the tow path and shape can be seen clearly. (b) Close view of the final tow geometry following the forming stage. (c) Initial full model configuration for the part of the strut including one pin-structured end-fitting, 10mm of the mandrel (black), and the "band tool" (cyan), prior to the forming stage. This example is for joint type E. (b) Final full model configuration following the forming stage. The "band-tool" is tightened so that the virtual tow layers have a radial thickness of 2.4mm in the region of the tool.

5.5 Geometric analysis of the formed virtual tows for joints A-E

The "formed" tow geometries and internal architectures, for the case of the full joint model, are evaluated using estimates of the tow's cross-section shape and the intra-tow fibre volume fraction,

calculated using the methods described in sections 5.2.1 and 5.2.2. Analysis of the virtual tows is restricted to the region above the band-tool, i.e. for the part of the virtual tow around the pin-structured end-fitting and 2.5mm of the mandrel length. Although the band-tool enabled the consolidation of the virtual tow layers to a more realistic degree of radial thickness, tow deformations due to contact with this "model-only" structure would not occur in the physical reality, therefore its effects on the tow geometry must be excluded.

A single virtual tow is considered within each of the first 3 filament wound layers. Tow deformation is approximately consistent within a given layer, as the repeating pattern of the tow placement ensures similar effects of inter-tow interactions, and contact with pin structures is replicated, moving circumferentially around the end-fitting. Between each layer, the level of tow interactions, particularly as the tow transitions onto and off the pin array, are highly dependant upon the winding angles for the mandrel (θ_d and θ_u). All strut configurations A-E have utilised symmetric layup sequences, (for example, type E had a layup of $\mp 10/0_2/\pm 10$). Therefore consideration of the first 3 layers, includes all winding angles used in the full sequence. The geometries and internal architectures of the tow as it transitions onto and off the pin array are therefore assumed equivalent for layers 1 and 6, 2 and 5, and 3 and 4.

5.5.1 Joint configuration A

Recall, the tow trajectory in the region of a pin-structured end-fitting, for joint configuration A, is an example of a single-pin winding pattern (section 3.9.1), with pull-back initiated around two adjacent pins. This winding pattern is illustrated in figure 5.15(a). The tow geometries, resulting from the forming simulation for this joint type, are shown in 5.15(b).

In order to examine the variation in the virtual tow's geometry and internal architecture throughout its length, the tow path, (as determined by the winding pattern), is subdivided into 9 distinct regions R_i, $1 \leq i \leq 9$. These consider separate areas of the tow, in which the degree of deformation and alteration of the tow's geometric shape may diverge significantly, due to varying levels of interactions with the pins. A description of the individual tow regions is provided in table 5.3.

Figure 5.16(a) displays the predicted average intra-tow fibre volume fraction for a virtual tow in layers 1, 2 and 3, across regions R_i. An inter-layer average line is also plotted. Figure 5.16(b) shows the predicted inter-layer average tow height and width (as estimated using the major and minor axis lengths of the fitted ellipse in section 5.2.2) for a virtual tow in layers 1-3, across regions R_i.

Relatively low volume fractions and consistent tow shape (with similar height and width) is observed between regions $R_1 - R_3$. Strut configuration A has a layup sequence with constant fibre orientations on the mandrel, consisting of axial (or near axial due to adjustment of the prescribed angle θ, to θ_d and θ_u) tow directions. As the tows transition onto the pin array and up to the point of the first pin turn, little deformation is induced as they pass tangentially to the

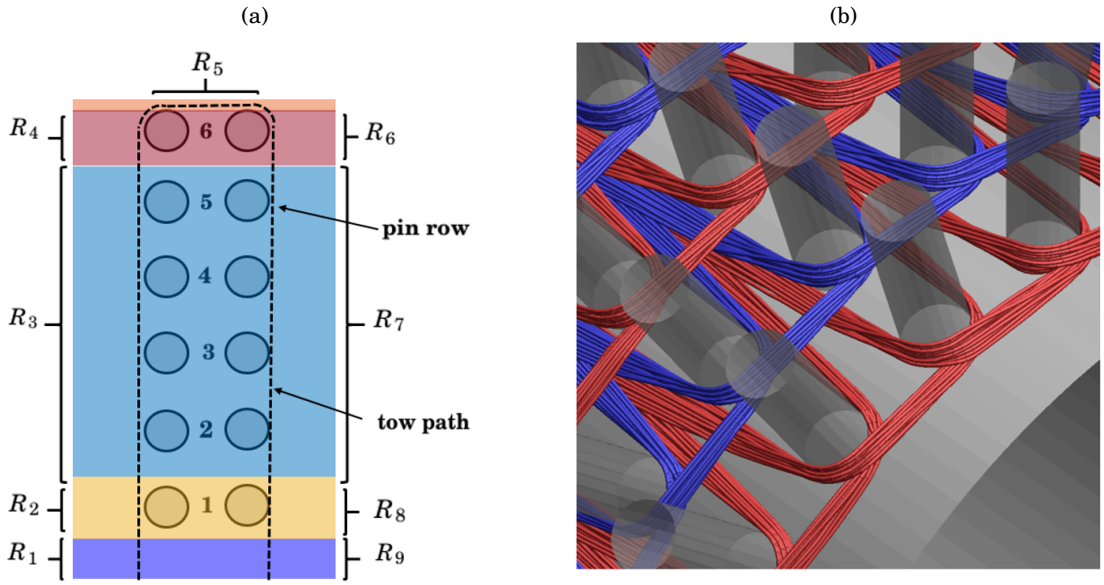

Figure 5.15: (a) 2D schematic of tow trajectory in the region of the joint, for configuration A. (b) Tow geometries obtained from the forming simulation for joint configuration A.

Table 5.3: Description of the tow trajectory and degree of interaction with the pins for each region of the winding pattern, for joint type A.

Region	Description of tow trajectory
R_1	Transition onto pin array
R_2	Contact with "on" pin
R_3	Transition up the pin array to first "turn" pin
R_4	Contact with first "turn" pin
R_5	Transition between "turn" pins
R_6	Contact with second "turn" pin
R_7	Transition down the pin array from second "turn" pin
R_8	Contact with "off" pin
R_9	Transition off pin array

pins, as illustrated in figures 5.17(a) and 5.17(b). An approximately flat elliptical cross-section, characterised by a comparatively large aspect ratio (width/height) in the range of 2.7-3.3, is then maintained across regions $R_1 - R_3$ for all layers. This is repeated in an approximate symmetrical manner for regions $R_7 - R_9$, as the tow transitions from the second pin turn and down the array also with an axial path.

High fibre volume fractions are observed during pull-back, with an average of 85% between regions $R_4 - R_6$. This is in contrast to the case of a individual tow forming around a single pin in section 5.2, in which lower intra-tow fibre volume fractions were observed for the region of the tow contacting the pin, resulting from increased spreading of the virtual fibres on the pin's

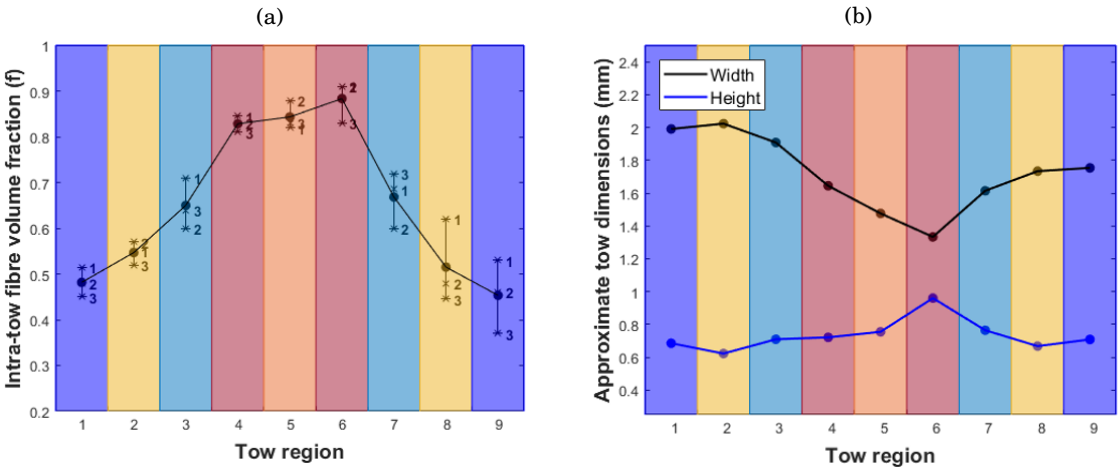

Figure 5.16: (a) The average predicted intra-tow fibre volume fractions, in regions $R_1 - R_9$ for layers of virtual tows in joint configuration A. An inter-layer average line is also plotted. Inter-layer average tow (b) width and (c) height, tow shape is consistent through the layers due to constant fibre-orientation in the layup sequence for A.

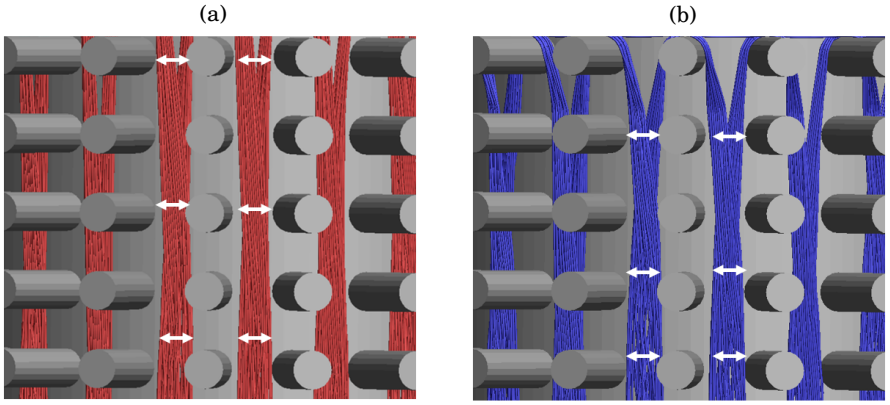

Figure 5.17: Regions R_1-R_3 and R_7-R_9 of the virtual tows in layers (a) 1 (red) and (b) 2 (blue), for joint configuration A. An approximate flat elliptical shape is maintained throughout, as deformation induced due to interactions with the pins is minimal due to their axial paths.

surface. This difference is due to the more complex inter-tow interactions occurring in the full joint forming model.

The virtual tows are compacted and pinched around the "turn" pins, resulting in a more circular tow cross-section in regions R_4 and R_6. This pinching effect is more pronounced for the second pin turn (R_6), for which an average aspect ratio of 1.4 is predicted, against 2.3 for the first pin turn (R_4). This is due to the relative positioning of the tows in the winding pattern, as shown in figure 5.18. As pull-back occurs around two pins, a given virtual tow is on the outside (relative to the end-fitting's surface) of the preceding tow, for the first pin turn (region R_4). For the second pin turn (region R_6), it is then on the inside of the subsequently placed tow so that its degree of

spreading on the pins surface is reduced, resulting in more compacted cross-section shape.

This trend does not however hold for first tow that to be placed during the filament winding process. Here the tow is positioned on the inside of neighbouring tows in both regions R_4 and R_6, closer to the end-fitting's surface. The opposite holds for the relative position of the final virtual tow in a given layer.

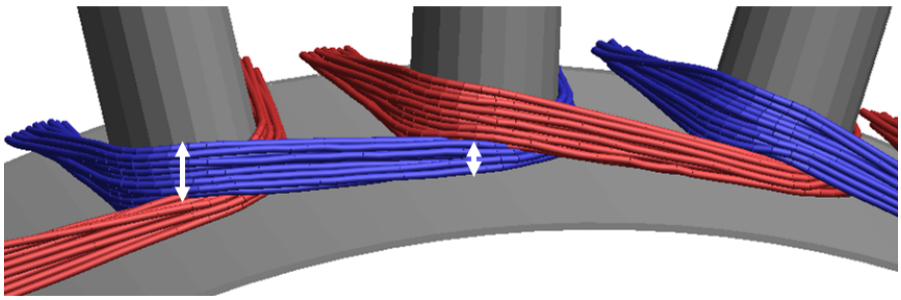

Figure 5.18: Cut-section of the pin-structured end-fitting, showing pull-back of the fibre-tows (coloured red and blue alternately) around the pins in joint configuration A, for the first filament wound layer. The virtual tow's are more highly compacted at the point of the second pin turn, due their relative positions.

As the tow transition betweens the adjacent turn pins, in region R_5, the tow becomes twisted and its major axis its orientated along the length of the pin, as it flattens to the pin's surface. Although significant spreading (against the virtual tow in the single pin forming simulation in section 5.2), which would result in a noticeable increase in tow width against regions R_4 and R_6), is limited by contacts with neighbouring tows.

5.5.2 Joint type E

The tow trajectory in the region of a pin-structured end-fitting, for joint configuration E, is an example of an all-row winding pattern, with pull-back occurring around a single pin (section 3.9.2). This winding pattern is illustrated in figure 5.19. The tow geometries, resulting from the forming simulation for this joint type, were shown previously in figures 5.14(a) and 5.14(b). In this case, the winding pattern is divided into 7 distinct regions R_i, $1 \leq i \leq 7$. Each region is described in table 5.4.

Figure 5.20(a) displays the predicted average intra-tow fibre volume fraction for a virtual tow in each layer 1, 2 and 3, across regions R_i. An inter-layer average line is also plotted. Figure 5.20(b) is a similar plot for the tow height and width.

Unlike, configuration A, strut type E has a layup sequence $(\mp 10/0_2/\pm 10)$ with non-constant fibre orientation angles. The tow trajectory onto and off the pin array therefore varies between each layer, which effects the level of deformation experienced in the virtual tows due to their interactions with the "on" and "off" pins, in regions R_1 and R_7, respectively.

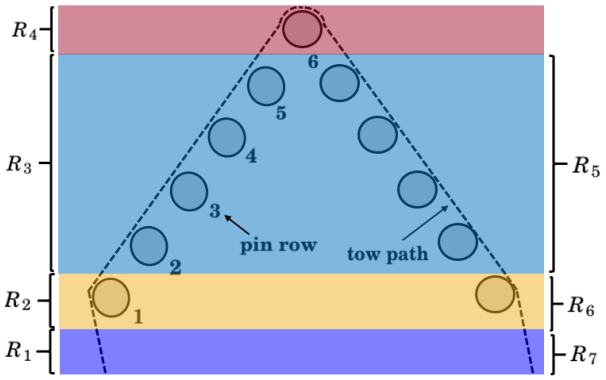

Figure 5.19: 2D schematic of tow trajectory in the region of a pin-structured end-fitting, for joint configuration E. This is an example of a all-row winding pattern, with pull-back occurring around a single pin. Tow geometries resulting from the forming simulation for this joint configuration can be seen in figure 5.14.

Table 5.4: Description of the tow trajectory and degree of interaction with the pins, for each region of the winding pattern for joint type E.

Region	Description of tow trajectory
R_1	Transition onto pin array
R_2	Contact with "on" pin
R_3	Transition up the pin array to "turn" pin
R_4	Pull-back around "turn" pin
R_5	Transition down the pin array from second "turn" pin
R_6	Contact with "off" pin
R_7	Transition off pin array

As illustrated in figure 5.21(a), minimal alteration of the tow trajectory occurs from the $-10°$ winding angle and the diagonal path of the tow through the pin array. Deformation due to the contact with the "on" pins is therefore also minimal, and the tow maintains an approximate flat elliptical cross-section shape, with an average aspect ratio of 2.6 in regions R_1 and R_2, respectively.

Conversely, the $10°$ orientation angle for the second virtual tow layer, results in significant deviation in the tow's trajectory between regions R_1 and R_2, as it the transitions from underneath the "on" pin. The virtual tow forms an approximately circular cross-section as it is compressed to the pin's surface, with an average aspect ratio of 1.41 for the tow cross-section in these regions.

Tows in the third layer take axial paths onto the pin array and so experience some deformation to one side of the virtual tow as the tow direction deviates around the pin, as shown in figure 5.21(c). An approximate elliptical cross-section shape is, however, maintained with the dimensions comparable with the virtual tows in the first layer. A lower fibre volume fraction is observed in regions R_1 and R_2 for this layer, however, relatively consistent predicted intra-tow fibre volume

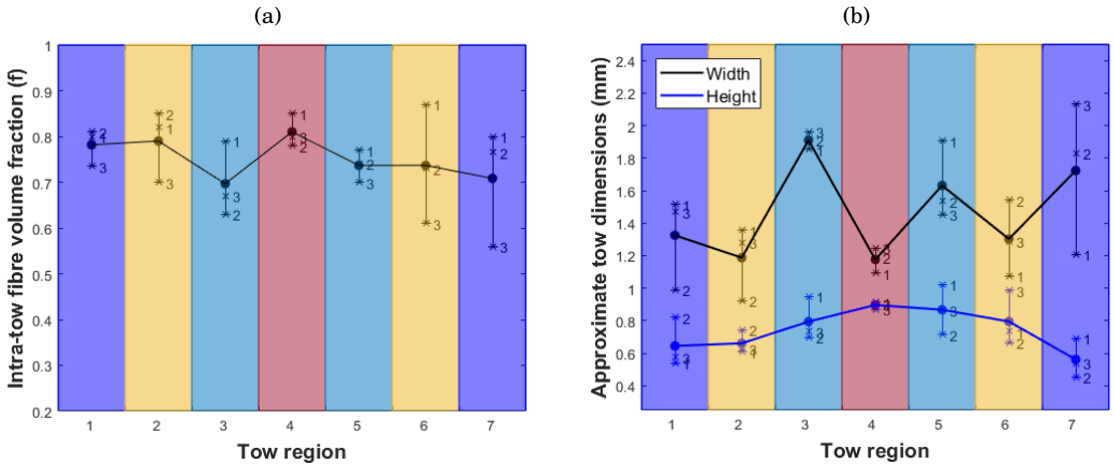

Figure 5.20: The average predicted (a) intra-tow fibre volume fraction, tow (b) width and (c) height, in regions R_1-R_7, for layers of virtual tows in joint configuration E. An inter-layer average line is also plotted.

fraction is observed between the layers, indicating a similar degree of virtual fibre compaction, despite the observed alteration in cross-section shape.

In regions R_6 and R_7, as the transitions off the pin array, the relationship is reversed due to the definitions of θ_u and θ_d. The virtual tows in layer 1 now experience similar deformations to layer 3 in the first layer, with an approximately circular cross-section shape (average aspect ratio of 1.47). The tow in layer 3 undergoes little deformation an maintains an flat elliptical shape for its cross-sections (aspect ratio 2.94). However, perfect symmetry of the tow shape and internal architecture is not observed between regions R_1 and R_7, and R_2 and R_6. This indicates that tow position (in the layup sequence) also has significant effect of the degree of deformation and final geometry.

As the virtual tows transition diagonally through the pin array in regions R_3 and R_5, they generally form an elliptical tow cross-section shape, flat to the surface of the end-fitting, as shown in figure 5.22(a). This is consistent for all three layers, with average aspect ratios of 2.39 and 1.97 for the tow cross-sections, and intra-tow fibre volume fractions of 70% and 74%, for regions R_3 and R_5, respectively.

The virtual tow in the pull-back region R_4, becomes pinched to an approximately circular cross-section (with average aspect ratio of 1.3), for all layers. Spreading of the tow cross-section in region R_4 is reduced from joint configuration A, due to the interlocking of the virtual tows at crossing points resulting their diagonal paths prior through array, (as illustrated in figure 5.22(b)), which restrict radial movement of the tows. This results in a comparatively high intra-tow fibre volume fraction of 81% for this region of the tow.

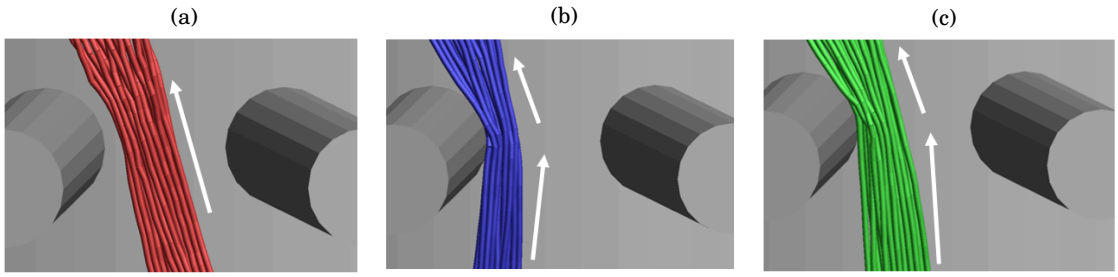

Figure 5.21: Deformation induced in the virtual tows due to their contact with the "on" pin of the array, in layer (a) 1 (b) 2 and (c) 3, respectively. The variable tow trajectory, for each layer, results in different levels of induced tow deformation and alteration to the tow shape and internal architecture.

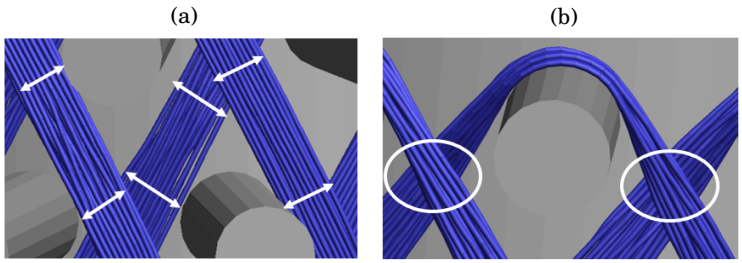

Figure 5.22: (a) Consistent flat, elliptical tow cross-sections for regions R_3 and R_5 of joint configuration E. (b) Tow crossing points due to their diagonal paths through the pin array.

Stage 2: Joint Loading

5.6 Methodology for tow geometry conversion

The description of the tow geometries and internal architectures obtained in the forming stage, (using the MF method), are now used in the construction of a more detailed mechanical model for the joint, than that provided through the SF method in chapter 4. As previously, for mechanical analysis purposes, the virtual tows must be converted to 3D continuum (solid) elements.

Thompson *et al.* [17] adopted a similar two-stage modelling approach in which a MDE method was first used to obtain a detailed description of yarn geometries and internal architectures, for a 2D woven fabric unit cell (figure 5.23). The yarn geometries were extracted via their cross-sections at discrete points along the yarn length. A meshing algorithm was then implemented to convert the exact simulated yarn geometries to 8-node continuum (solid) elements, so that the fabric's mechanical response under compressive loading could be studied.

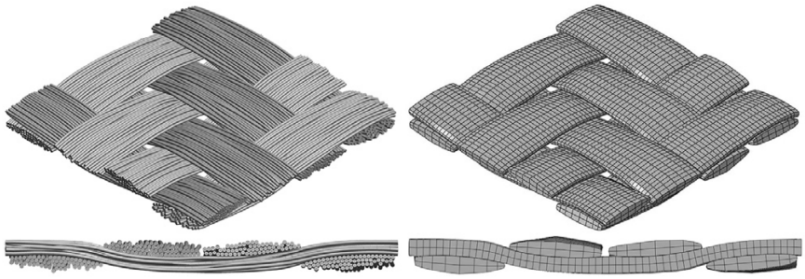

Figure 5.23: Conversion of simulated yarn geometries in a 2D woven fabric (2/2 twill) unit cell, from an MDE representation to 3D continuum (solid) elements [17].

Yarn geometry extraction and re-meshing (with 3D continuum elements) methodologies have also been developed for more intricate composite fabrics, such as non-crimp, 3D orthogonal weaves [18]. The complex path of the yarns within the fabric, and their significant interactions with neighbouring yarns, result in a high degree of irregularity and variability in yarn shape. Yarn meshing procedures therefore display increased complexity as they have to account for substantial heterogeneity in the yarn geometry. The resulting continuum mesh requires a relatively large number of elements in order to adequately represent the yarn's topology.

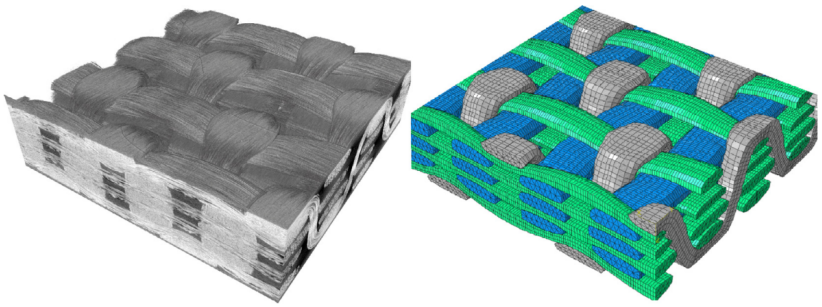

Figure 5.24: Conversion of yarn geometries gained from post-processing of Computed Tomography (μCT) scan images of a 3D orthogonal, non-crimp weave, to continuum (solid) elements [18].

As discussed in 5.5, the paths, geometric shape and internal architectures of the virtual tows in the full joint forming simulation, were found to display a large degree of variability and complexity. Therefore, exact conversion of the virtual tows to continuum element mesh, will require a relatively large number of elements per tow. Model size in this instance, in terms of the number of virtual tows represented in the model and its global volume (in comparison to a fabric unit cell), may therefore incur high computational cost.

Additionally, significant intermingling of the virtual fibres, between neighbouring virtual tows, was observed at points on the structure, as highlighted in figure 5.25. Intermingling of the virtual fibres was facilitated by the repeating nature of the winding pattern, in which virtual tows with identical trajectories were made to directly overlay each other, with a relatively high

degree of compaction, both for virtual tows within a given layer and between separate layers. Relative displacements of the virtual fibres was therefore more likely to result in such co-mingling between neighbouring tows, in comparison with textile fabrics in which neighbouring yarns often take different trajectories (as determined by the weave) and spacing between yarns is conserved to a greater extent.

In such instances, definition of tow cross-section shapes using the cross-section polygon found via the convex hull algorithm (section 5.2.1), would result in significant unrealistic inter-penetrations between the tows following conversion to solid elements for their cross-sections. This may lead to numerical instabilities during subsequent FE simulations.

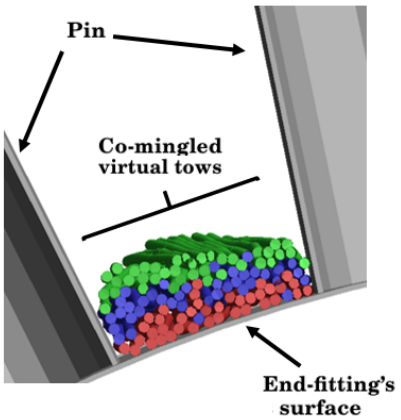

Figure 5.25: Intermingling of the virtual fibres with neighbouring tows (individually coloured red, blue and green), resulting in co-mingled virtual tows. Direct conversion of the tow geometries to 3D continuum elements using the cross-section polygons, would result in inter-penetrating virtual tows.

This work seeks to develop a modelling framework capable of assessing the mechanical behaviour of the composite-metal joint using a more realistic representation of the fibre-tow in this region (as opposed to the use of a virtual tow with constant, circular cross-section). Consequently, it is sufficient to construct a tow structure that includes a realistic, variable cross-sectional shape and material properties (as determined by its internal architecture), as opposed to the direct extraction of the tow geometries (as conducted for the case of woven textiles) obtained from the forming simulation, which for the reasons discussed, would be infeasible for this particular application.

The tow shape, and variation along its length, can be extracted from the forming simulation, via the dimensions of a fitted ellipse, as seen in section 5.1. These can be used to construct a virtual tow with a more realistic and non-uniform cross-section shape, which varies between regions R_i of the winding pattern due to interactions with the pin-structured end-fittings and neighbouring tows. This process is described in section 5.7, using a novel Single Filament Superposition (SFS) approach.

Furthermore, information regarding the variation in the intra-tow fibre volume fractions across the regions R_i, can be used to construct a virtual tow with more accurate material properties (and variation along the tow length) relative to the physical tow. This is detailed in section 5.8.2.

5.7 Single Filament Superposition (SFS) method

In the Single Filament Superposition (SFS) method, each virtual tow is represented as two superimposed chains of 2D beam (truss) elements with circular cross-sections. End nodes of truss elements in different chains are shared so that the virtual tow behaves as a single filament. A truss element in one chain is assigned a cross-sectional diameter equal to the tow width. The other is assigned a diameter that is representative of the tow height. As illustrated in figure 5.26, a virtual tow with an elliptical cross-section can be represented via the superposition of the two truss elements. This offers a more realistic geometric shape for the virtual tow in comparison to the Single-Filament (SF) method, in which the cross-section is assumed circular.

Moreover, the diameters of the truss elements can be varied along the length of a given truss element chain (which represents either the tow height or width) to construct a virtual tow with variable and non-uniform cross-section shape.

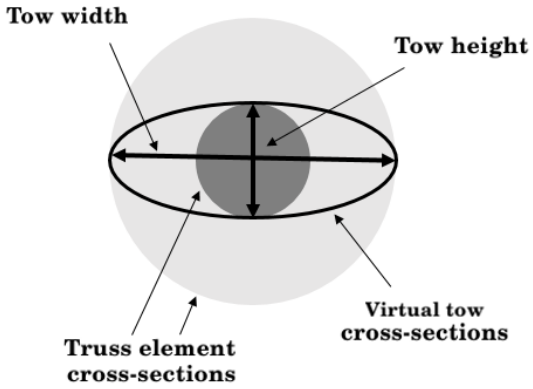

Figure 5.26: Illustration of a SFS virtual tow cross-section, consisting of two superimposed truss elements.

As described in the following section, the Single Filament Superposition (SFS) method is used to construct a model capable of assessing the mechanical properties of the composite-metal joint, which takes into account realistic tow geometries in this region.

5.8 Meso-scale mechanical model of the composite-metal joint

5.8.1 Joint model using SFS method

Analysis in section 5.5 of the virtual tow geometries obtained from the MF method, provided the average tow cross-sectional dimensions (width and height) in regions R_i of the winding pattern. These predicted dimensions are used to construct virtual tows with non-uniform and elliptical cross-section shape, for the region of the joint, using the SFS method.

Truss elements forming a given chain and comprising "one half" of a given virtual tow, and which lie in region R_i of the winding pattern, are assigned diameters equal to either the average tow height, or width, in that region. An example of this is shown in figures 5.27(a) and 5.27(b), for a virtual tow in joint configuration A. Truss elements within a given truss element chain, which are positioned at either the start or end of a given region (R_i) of the winding pattern, are assigned interpolated dimensions, so that the tow cross-section shape transitions smoothly between the different tow dimensions attributable to different regions of the winding pattern, as shown in figures 5.27(c) and 5.27(d).

In this way, virtual tows are constructed with non-circular and non-uniform geometries. Moreover, their cross-sectional shape have been gained directly from the simulations using the MF tow, in which induced deformations due to inter-tow interactions, and interactions with pin-structured end-fittings were captured. The resulting virtual tow geometries should therefore offer improved realism against the SF method.

As with the determining the as-manufactured path of the SF tows (section 5.4.1), an approximate, coarse tow path is firstly assigned analytically, and subsequently refined with a simulation step in which a thermal gradient is applied to the virtual tows. However, for the SFS tows, three separate contact definitions are required for this simulation. Firstly, one truss element chain, which partially defines the virtual tow, is used to determine both inter-tow contact, via LS-Dyna® contact algorithm *AUTOMATIC_GENERAL, and contact between the virtual tows and the end-fitting's surface, via type *BEAMS_TO_SURFACE. The remaining truss element chain is used to define contact with the pins, again via the *BEAMS_TO_SURFACE algorithm.

During the simulation used to refine the tow path, due to the contact definitions established, the different diameters of the two superimposed truss element chains maintain separation distances relative to the end-fitting, pins and other truss element chains, in proportion to the diameters of the truss elements used in that particular contact. As the end-nodes are shared between the two truss element chains, the combined effect of the multiple contact definitions, provide a smooth path for the virtual tows that accounts for its elliptical and non-uniform cross-sectional shape.

For example, as shown in figures 5.28(c) and 5.28(d), during tow-pull back, the tow cross-section was found to be flattened to the pin's surface (section 5.5.1). The truss elements forming the chain used to determine tow-pin contact therefore have relatively small diameters. In comparison,

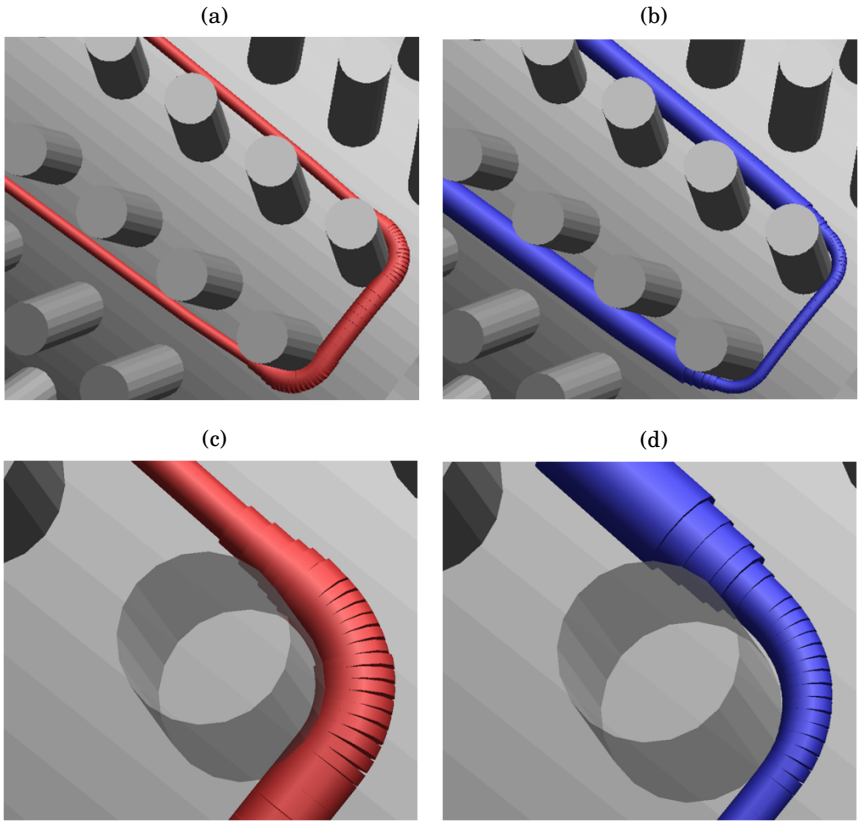

Figure 5.27: Truss element chains, with variable cross-section dimensions, used to provide (a) inter-tow and tow to end-fitting, and (b) tow to pin, contact definitions. A single virtual tow is formed from the superposition of these two chains. The example here is joint configuration A. (c) and (d) show region R_6, the second pin turn. The diameters of the truss elements are interpolated between regions R_5, R_6 and R_7 to smooth transition of the tow dimensions between distinct regions of the winding pattern.

contact with the end-fittings and other truss element chains, is established through use of larger truss element, which reflects the spreading of the tow cross-section radially, along the length of the pins.

The cross-section shape and orientation of the virtual tows is therefore accounted for through use of the SFS method, and the simulation step provides smooth, realistic tow paths in the region of the joint. As with the SF model described in section 4.4.1, the tow paths are then utilised for the generation of a mechanical model, in which the virtual tows are represented as a mesh of 3D continuum (solid) elements.

5.8.2 Solid element joint model

As in section 4.4.1, the path of the virtual tow is extracted from the SFS model. Each virtual tow cross-section is meshed for the tow width (along the major axis of the cross-section ellipse) using

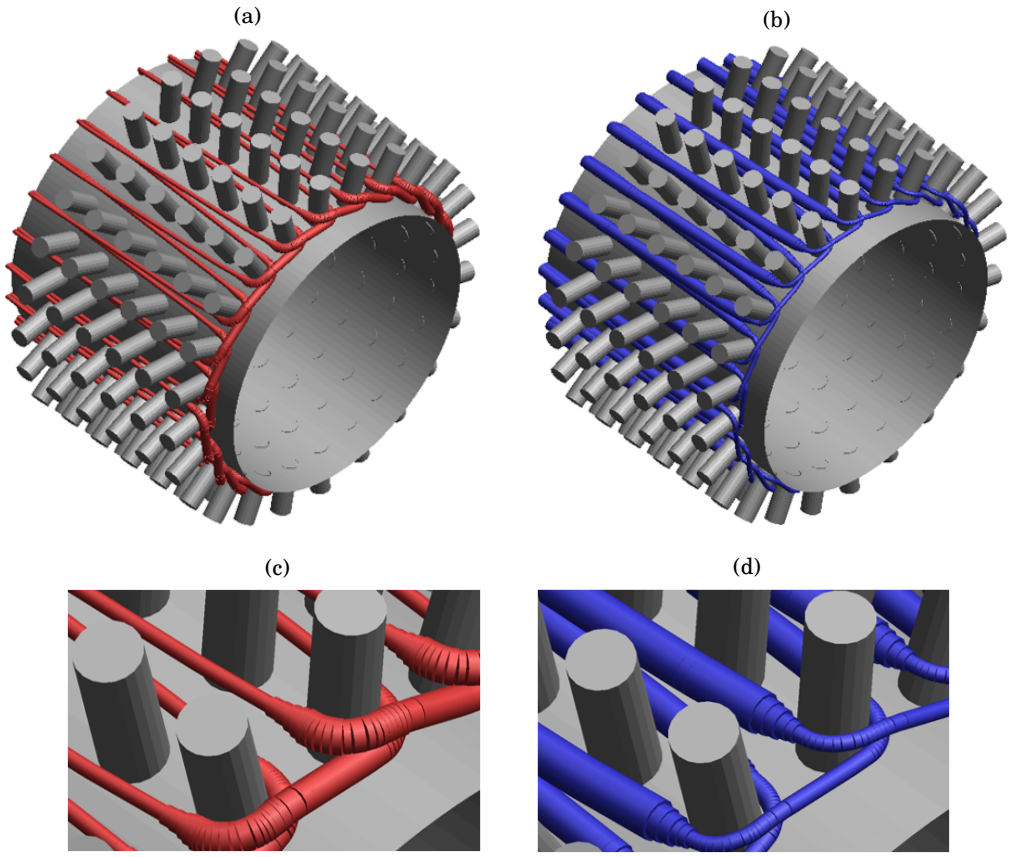

Figure 5.28: Final simulated positions of the SFS virtual tows comprising the first filament wound layer in joint configuration A, with truss elements used in (a) inter-tow and tow to end-fitting, and (b) tow to pin, contact algorithms. (c) and (d) show the pull-back region.

eight 8-node solid elements, as shown in figure 5.29. Elements at the extremes of the elliptical cross-section face are excluded to prevent virtual tows with sharp edges. Figures 5.30(a) and 5.30(b) show the full joint model, following tow conversion to solid elements, for configurations A and E, respectively.

Figures 5.30(c) and 5.30(d) show the converted virtual tows on part of the pin-structured end-fitting. For joint A, the flat elliptical cross-section of the tow can be seen prior to the pin turn. The tow then twists, as predicted from the MF model in section 5.5, so that it is flat to the surface of the "turn" pins. Similarly for joint E, the tow cross-section shape is again elliptical prior to pull-back. The tow then spreads less around the single "turn" pin in this winding pattern so that it instead forms a more circular cross-section shape, although orientation is again changed so that the major axis is orientation along the pin, away from the end-fittings surface.

As in section 2.4.1, the tow is modelled as a linearly elastic, transversely isotropic material, using element type SOLID_ORTHO and local material axes a, b and c defining the fibre direction and transverse directions, respectively. Similarly, material properties for the tow are calculated

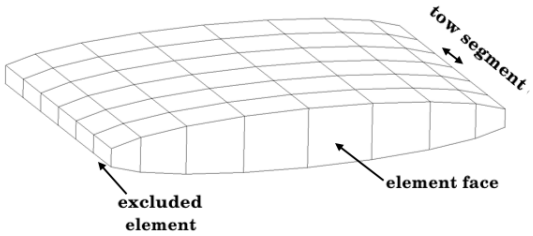

Figure 5.29: Segment of a virtual tow described using 3D continuum (solid) elements for its cross-sections.

from the Chamis model [66], (see equation 4.5) and using known material data for carbon fibre (HTX40 F13 12k) and epoxy resin MVR444, stated in table 3.2.

However, unlike previously, a uniform fibre volume fraction (of 70%) is not assumed throughout the length of the tow, and in the assignment of the virtual tow's material properties. Instead, the average intra-tow fibre volume fractions in regions R_i, are used to define individual material properties for each section of the tow. For example, as illustrated in figure 5.31, each of the 9 regions in the virtual tow for joint configuration A, has an individual material model, each with individual material parameters calculated using the average intra-tow fibre volume fraction in that particular region. Model realism is therefore improved as the tow's variable internal architecture in the region of the pin-structured end-fitting (in addition to geometric shape), is accounted for in its assigned material properties.

Properties of the matrix and metallic end-fittings are maintained from section 4.4.2. Similarly, the independently meshed matrix material is coupled with virtual tow using the constrained-based coupling mechanism provided by LS-Dyna® keyword *CONSTRAINED_LAGRANGE_IN_SOLID, (section 4.5).

5.9 Virtual testing

The mechanical properties of the composite-metal joint can now be assessed. A quasi-static tensile strain, equivalent to a global strain of $2000\mu\epsilon$ for the full strut, is applied to the joint by prescribing a displacement to the end-fitting in the positive y direction, over a analysis time of 5 seconds. The open ends of the virtual tows are fixed in the y degree of freedom to simulate their connections with the end-fitting at the strut's opposing end.

As in section 4.6, contact between the virtual tows and the pin-structured end-fitting (and inter-tow interactions) is established with type *AUTOMATIC_GENERAL, using a coulomb friction coefficient of 0.3. Matrix material is excluded from the contact definition, and consequently, stresses are transferred to it only via its coupling with the virtual tows using CLIS.

Joint compression is not considered. As examined in section 4.8, load transfer capability

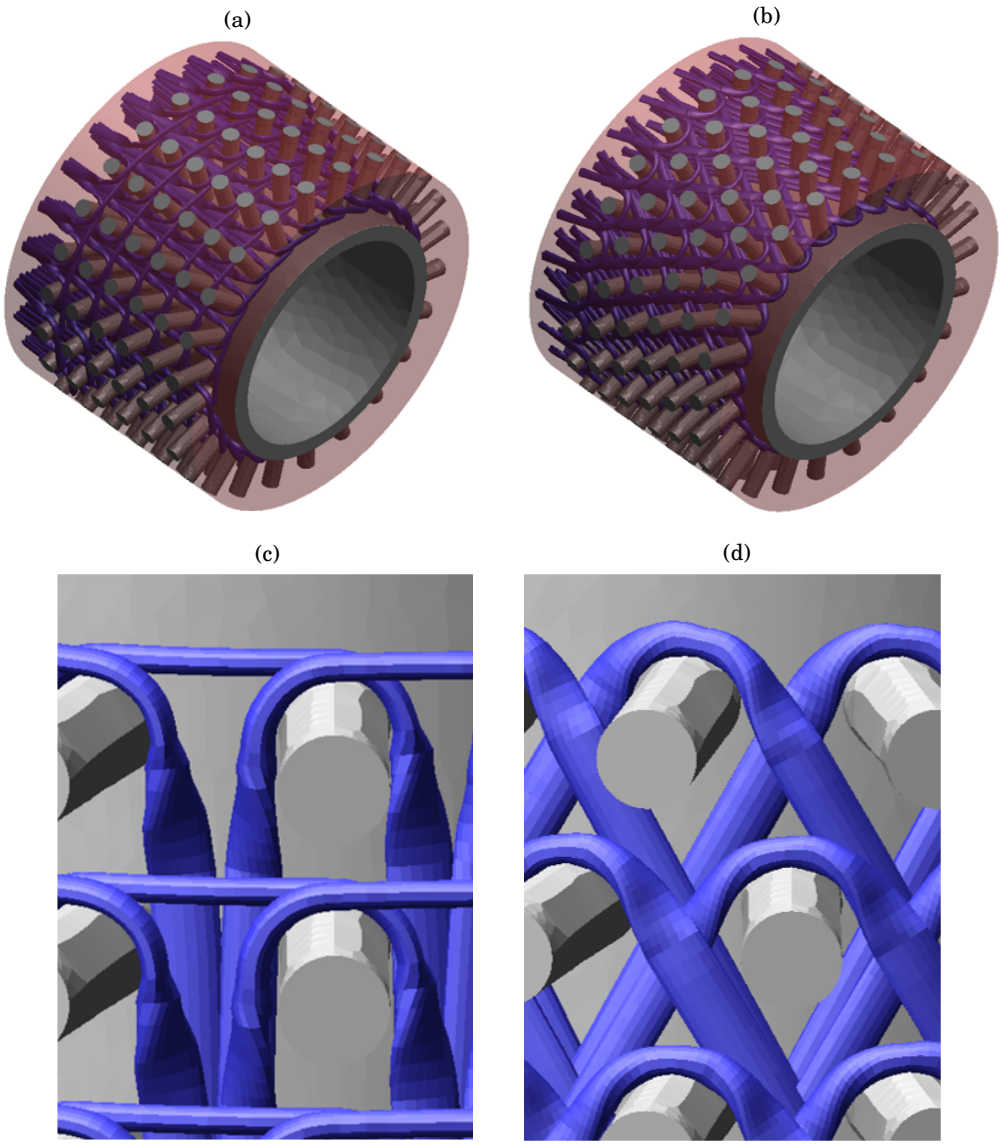

Figure 5.30: (a) and (b) full joint models for virtual testing, with configurations A and E, respectively. Virtual tows (blue) are meshed using 3D continuum (solid) elements. Matrix material (red) is made partially transparent so that the path of the virtual tows can be seen. (c) and (d) close up views for a region of the pin-structured end-fitting (grey).

between the filament wound fibre-tows and the pin-structured metallic end-fitting was found to be limited for compressive loads. As discussed in section 4.8.1, properties of the strut in compression could be improved through use of a permanent mandrel structure.

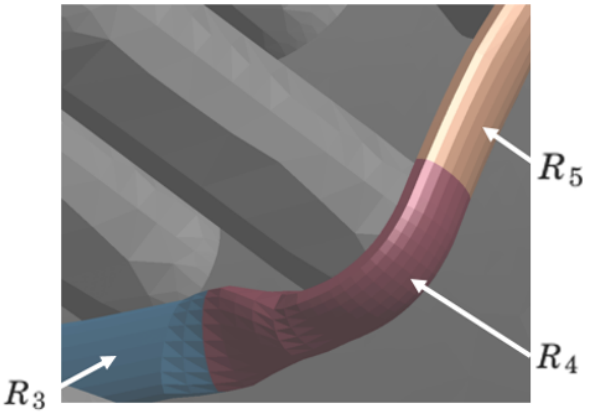

Figure 5.31: Sections R_3, R_4 and R_5 of a virtual tow in joint type A, with each of the individual tow regions is assigned material properties depending on the average intra-tow fibre volume fraction in that region.

5.9.1 Comparison of strut configurations A and E

Table 5.5 shows the maximum local fibre-direction stress in the virtual tows, for each virtual tow layer of joint configurations A and E. Bracketed values indicate the (unaltered) tow orientation angle for the mandrel. Figures 5.32(a) and 5.32(c) show the stress distribution in the virtual tows for these joint types. For comparative purposes, also included in the table are the predicted stress magnitudes for the same joint types studied using the SF approach, (as examined in section 4.6.2). Figures 5.32(b) and 5.32(d) show the stress distribution for the SF virtual tows.

Table 5.5: Local fibre direction stress (MPa) by virtual tow layer, for joint configurations A and E. Also shown are the predicted stress magnitudes for the virtual tow layers using the Single Filament (SF) approach.

Joint configuration	A	A (SF)	E	E (SF)
Virtual tow layer				
1	1275 (0)	713 (0)	1067 (-10)	1107 (-10)
2	999 (0)	859 (0)	700 (10)	688 (10)
3	453 (0)	653 (0)	514 (0)	499 (0)
4	297 (0)	1004 (0)	316 (0)	398 (0)
5	372 (0)	803 (0)	330 (10)	327 (10)
6	241 (0)	765 (0)	330 (-10)	285 (-10)

For joint type A, maximum (tensile) stress in the virtual tows is predicted to be 21% higher than the equivalent joint modelled using a SF tow. The flattened shape and increased contact area of the virtual tows against the turn pins, as observed in figure 5.30(c), may have contributed to increased load transfer to the tows, than compared to a tow shape with a circular cross-section. This effect is less pronounced for joint E, as tow pull-back around a single does not result in significant flattening and compaction of the tow cross-section around the pin, as seen in figure

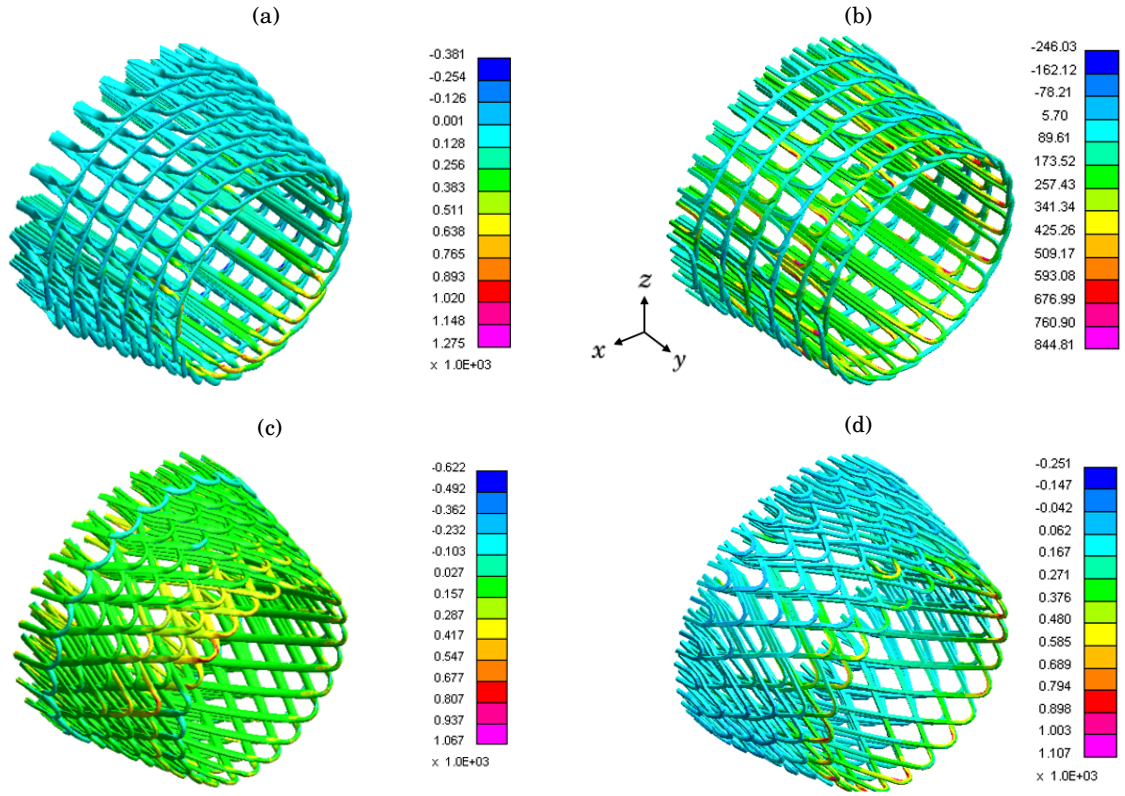

Figure 5.32: Local fibre direction stress in the virtual tows for the joint, with configurations (a) A, (b) A using the SF method, (c) E and (d) E using the SF method.

5.30(d). For joint type E, maximum loading of the virtual tows is comparable between the SF approach, and the joint model using more realistic tow geometries, (4% difference).

In general, as stated in section 4.6.4 for the SF models, concentrative stresses are observed as the virtual tows transition off and onto the turn pins. Localised compressive stresses are observed at the under-side of the tow contacting the turn pins, as tow tension results in pinching of this region of the tow due to its arched path around the pins. Also, a clear trend in the loading of the virtual tow layers can be identified here, in comparison to the SF models. Maximum loading occurs in the first layer and the degree of loading decreases for higher numbered virtual tow layers, as they are positioned further from the end-fitting's surface and point of loading.

Moreover, the maximum stress in the virtual tows may vary significantly in given layers, between the SF strut model and joint model. For example, the maximum stress in the virtual tows in layer four of joint type A, has increased by a factor of 3 from strut configuration A. Load transfer behaviour between the virtual tows and metallic pins, and the concentrative stresses occurring in the virtual tows as they transition around the pins, are highly influenced by tow shape. As observed using the MF approach, inter-tow interactions result in deformation and alteration to the tow cross-sectional shape (tow spreading, pinching, and twisting), which in turn

alters the stress distribution in the virtual tows in response to applied load.

Table 5.6 shows the maximum Von Mises stress in the pin-structured end-fittings for joint types A and E. Also included are the predicted stresses from section 4.6.3, using the SF model for the virtual tow. Figures 5.33(a) and 5.33(c) show the Von Mises stress distribution in the pin-structured end-fittings for joint types A and E, respectively. Figures 5.33(b) and 5.33(d) show likewise stress for joints A and E, with virtual tows modelled using the SF approach (as previously examined in section 4.6.3).

Table 5.6: Maximum Von Mises stress (MPa) in the pin structured metallic end-fittings, for joint types A and E. Also shown are the predicted stress magnitudes using the Single Filament (SF) approach.

Strut Configuration	Maximum Von Mises stress (MPa)
A	1100
E	1043
A (SF)	993
E (SF)	1031

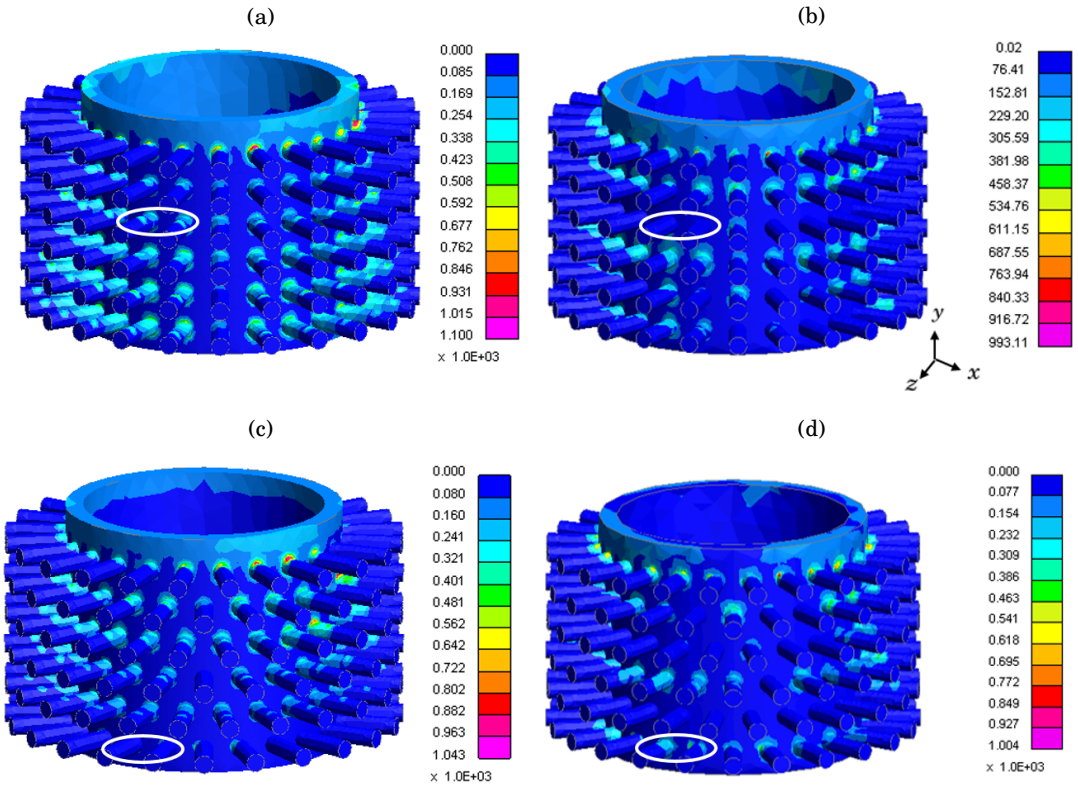

Figure 5.33: Von Mises stress (MPa) in the pin-structured metallic end-fitting for joint (a) A, (b) A using the SF model, (c) E and (d) E using the SF model.

Stress distribution across the pins is improved for both joints A and E, using the higher

fidelity model of the virtual tow developed in this chapter, against the SF method utilised in chapter 4. The number of pins experiencing negligible loading is reduced. An example of this is highlighted in figures 5.33(a) and 5.33(b), for pins in row 4 of joint A. This may also be due to the increased contact area between the virtual tows and the pins for the flatter, elliptical tow cross-section shape.

However, pins in row 1 of joint type E, as indicated in figures 5.33(c) and 5.33(d), exhibit reduced loading against the SF method. This may be due to a limitation in the construction of the higher fidelity tow model, for the last virtual tow layer in joint type E. Only the first three filament wound layers in the layup sequence were analysed in section 5.5. The symmetric nature of the layup sequence is then used to provide the tow geometries and internal architectures for layers 4-6. That is, the virtual tows in layer 6 is constructed using information from layer 1 (4 from 3 and 5 from 2).

However, for the last virtual tow layer turning around the first pin row, as observed in the MF model in figure 5.34(a), the shape of the tow during pull-back more closely resembles the flattened elliptical cross-section present in the "single-pin" winding pattern for joint type A; as the tows in this layer do not transition diagonally through the pin array prior to pull-back. The virtual tow structure is therefore poorly represented in the model, with an exaggerated arced path (figure 5.34(b)) around the pins in row 1, reducing load transfer. Future work should aim to account for the distinct tow geometric effects observed for the final filament wound layer of some joint configurations.

(a)

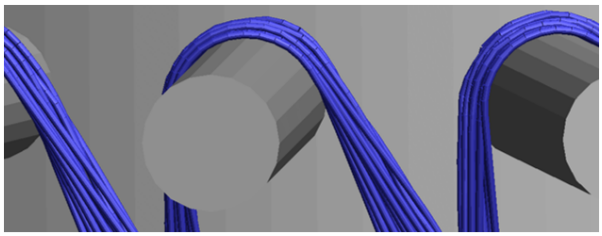

(b)

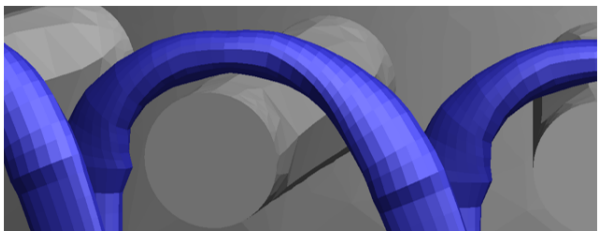

Figure 5.34: Virtual tow structure for the last layer in joint configuration E, predicted from the (a) MF method and (b) SFS method (using the same tow structure for layer 1).

Stress is transferred to a greater proportion of the pin length than in the SF tow representation. This also reflects the increased contact area between the virtual tows and the pins.

Pins in row 6, interacting with the first layer of virtual tows, experiences maximum loading, following the highest observed tension in these virtual tows in both joint types A and E. The yield stress (1100MPa) of the titanium alloy (Ti-6Al-4V, Grade 5) was reached in joint A, indicating joint failure load was achieved at a tensile (global) strain equivalent to $2000\mu\epsilon$ for the full strut. Further analysis of joint strength is conducted in section 5.9.3.

Table 5.9 displays the Maximum Principal stress in the matrix resulting from the virtual testing of joint types A and E. Also included are the stress magnitudes for the SF tow model, repeated from section 4.6.5. The joint model using a higher fidelity tow representation predicts increased stress in the matrix material. This may be due to the larger cross-sectional areas (and volumes) of the virtual tows compared to SF representation, which may increase load transfer to the matrix via CLIS. Also, the increased tow volumes and higher degree of total tow volume content in the region of the joint, may have resulted in fewer "empty" matrix elements, which do not containing any virtual tows. Coupling forces due to CLIS may therefore be increased, resulting in higher load transference and stress in the matrix.

Table 5.7: Maximum Principal stress (MPa) in the matrix, for joint types A and E. Also shown are the predicted stress magnitudes using the Single Filament (SF) approach.

Strut Configuration	Maximum Principle stress (MPa)
A	54.4
E	40.8
A (SF)	20.7
E (SF)	29.7

5.9.2 Braided joint

As reviewed in section 2.4.1, braiding technologies have been used in the manufacture of similar composite-metal joining mechanisms. Improvements with regards to load transfer capability, strength and stiffness were hypothesised for the filament wound joint in section 3.2.2. A braided joint is also constructed using the same techniques developed in this chapter. This is then subjected to an equivalent (global) tensile strain of 2000μ and its properties and performance is assessed against joint types A and E in section 5.9.3.

For the braided joint, a tri-axial braid pattern is used for the region of a pin-structured end-fitting. The end-fitting is equivalent to that used for joint type A, with a square patterned pin distribution, 3mm spacing between adjacent pins and a total of 144 pins arranged in 6 rows. "Ideal" placement of the braid yarns is assumed to result from manufacture, so that yarn puncturing is not included in the model. In reality, as found in [6], yarn puncturing was found to be a common defect resulting from the fabrication of braided/surface-structured joints.

Spacing between axial yarns, as seen in figure 5.35(a) is determined by the circumferential spacing between the pins. Yarn cross-sectional shape was assumed to be elliptical and constant along the length of the yarn. It was assumed that axial yarns would spread to cover the area of the

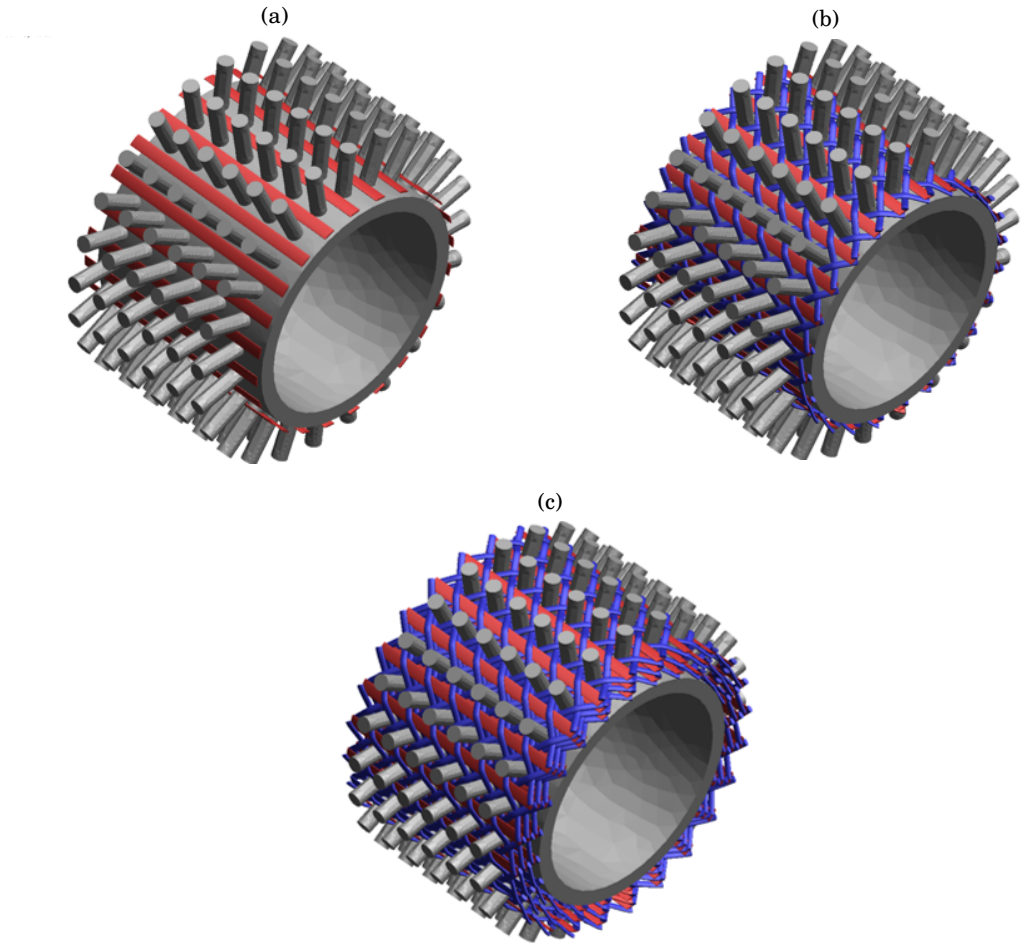

Figure 5.35: (a) Path of the axial yarns (red) on the pin structured end-fitting (grey). (b) Tri-axial braid pattern, with non-axial braid yarns (blue) orientated at ±45°. (c) Three layers of the tri-axial braid for the joint. Matrix is omitted from the figure so that the yarn paths on the structure can be seen clearly.

end-fitting's surface, spanning its length and between adjacent pins. This gave an approximate yarn width of 2.6mm. The yarn's cross-sectional height (of 0.34mm) could then be determined using appendix item A.2, for an assumed intra-yarn fibre volume fraction of 70%.

The non-axial braid yarns, seen in figure 5.35(b) are orientated at ±45° to the end-fitting's longitudinal axis. Their paths on the end-fitting's cylindrical surface are designated using results from [102] and [72]. The yarns are constructed from a concatenation of cubic Bezier curves [76], which determined their out-of-plane radial movement. Control nodes (see section 4.2.2) are placed in order to minimise penetrations between the virtual yarns. Yarn width is set at 1.3mm for the non-axial yarns, this is determined by the maximum feasible yarn width that did not result in unrealistic, inter-penetrations between the pins and yarns in the model, due to the yarn paths through the pin array. Yarn height (0.65mm) was calculated similarly to the axial yarns, using

appendix A.2, and assuming a 70% intra-yarn fibre volume fraction.

Two over-braids are also constructed (for a total of three braid layers) in order for yarn volume in the joint region to be comparable with the filament wound joints, A and E. Perfect alignment of the over-braid layers is assumed. Also, similarly to the filament wound joints, matrix is included as a tubular mesh completely containing the virtual yarns. These are then coupled via CLIS. Material properties for the yarns are used from table 3.2, (with an assumed intra-yarn fibre volume fraction of 70%).

Following the applied strain, relatively minimal load is transferred to the virtual yarns, in comparison to the virtual tows in the filament wound joint. This is reflected in the comparably low Von Mises stress in the end-fitting, as shown in figure 5.36. Moreover, load transfer occurs due to contact between the non-axial braid yarns and the pin, in the regions highlighted. This results in compressive loads for the yarn's transverse directions, as shown in figure 5.37, and local fibre directions stress in the virtual yarns that is higher in compression (at 244 MPa) than tension (125MPa).

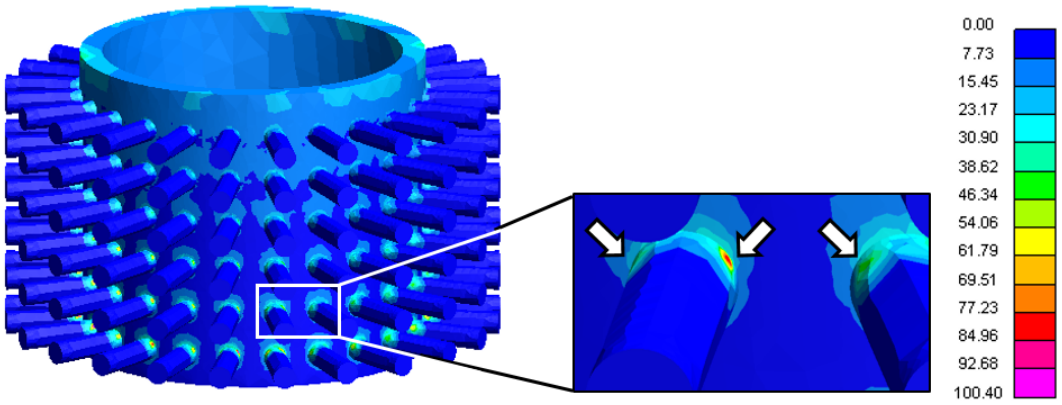

Figure 5.36: Von Mises stress distribution in the pin-structured end-fitting for the braided joint.

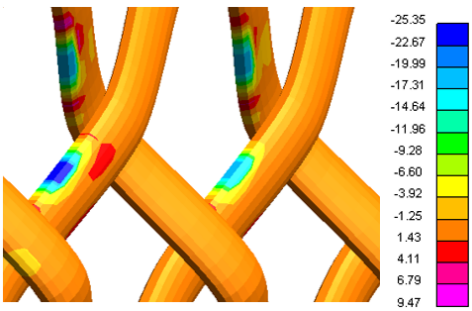

Figure 5.37: Local transverse direction stress in the virtual yarns due to contact with the pins.

5.9.3 Joint stiffness and strength

Similarly to section 4.6.1, a reaction load (due to the applied tensile strain) is extracted from the models of joints A and E, and the braided joint constructed in section 5.9.2. Figure 5.38 shows the force vs strain curve for the braided joint, and joint types A and E.

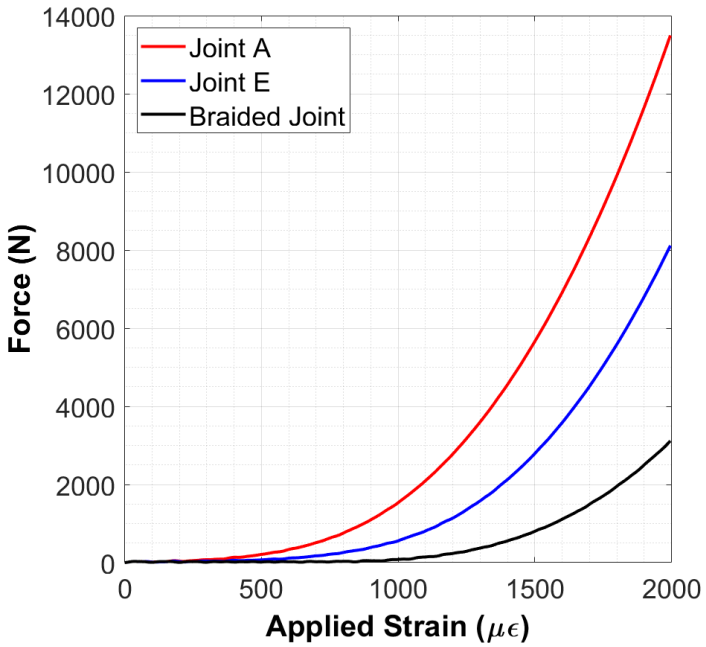

Figure 5.38: Force (N) against prescribed strain ($\mu\epsilon$) for joint types A, E and braid.

Figure 5.39(a) shows the normalised force vs strain curves for strut and joint type A. In both instances, a minimal initial reaction load is induced as the virtual tows and pins are not in contact at the start of the simulation. After prescribed strains of approximately 500$\mu\epsilon$ and 750$\mu\epsilon$ for the strut and joint respectively, the tows and pins are brought into contact and load is transferred between the two components and joint stiffness increases. Establishment of contact between the virtual tows and pins is delayed for the joint model. Larger initial separation distances exist between the virtual tows and pins due to the non-uniform tow cross-sectional shape and size attributable to the SFS tow representation, and the interpolation of the tow cross-section orientation in the region of the pins.

The gradient of the joint force vs strain curve then increases between 750 - 1250 $\mu\epsilon$ at an observably faster rate than the 500 - 1000 $\mu\epsilon$ loading range for the full strut model. This is because the joint model has significantly less excess tow length, therefore the high tensile stiffness of the virtual tows are exploited at a lower prescribed strain. Joint stiffness increases at a more linear rate at a lower applied load when compared to the full strut model.

However, as with the full strut model, a degree non-linearity persists throughout the full loading range. This because use of the SFS tow representation for the joint model has the same

limitation as SF method for the full strut model, in that, the magnitude of the thermal gradient applied to the virtual tows to obtain a smooth, realistic tow path, is assessed qualitatively. Excess tow length may not then be taken-up uniformly across the multiple layers of virtual tows, so some excess length is maintained even at the later stages of the simulation.

Using the same methodology as that applied to the full strut models in section 4.6.1, the joint model's unrealistic response up to 750 $\mu\epsilon$ is excluded. A linear fit is conducted on the data range between 1250-2000 $\mu\epsilon$, which is then extrapolated up to 2750 $\mu\epsilon$, (accuracy of the linear fitting can be assessed using the root-mean-square-error provided in the appendix table A.2). The force vs applied strain curve in the range 750-2750 $\mu\epsilon$ is then considered as the joints' response for a prescribed strain of 2000 $\mu\epsilon$. These reaction loads are used to estimate joint stiffness, as shown in table 5.10.

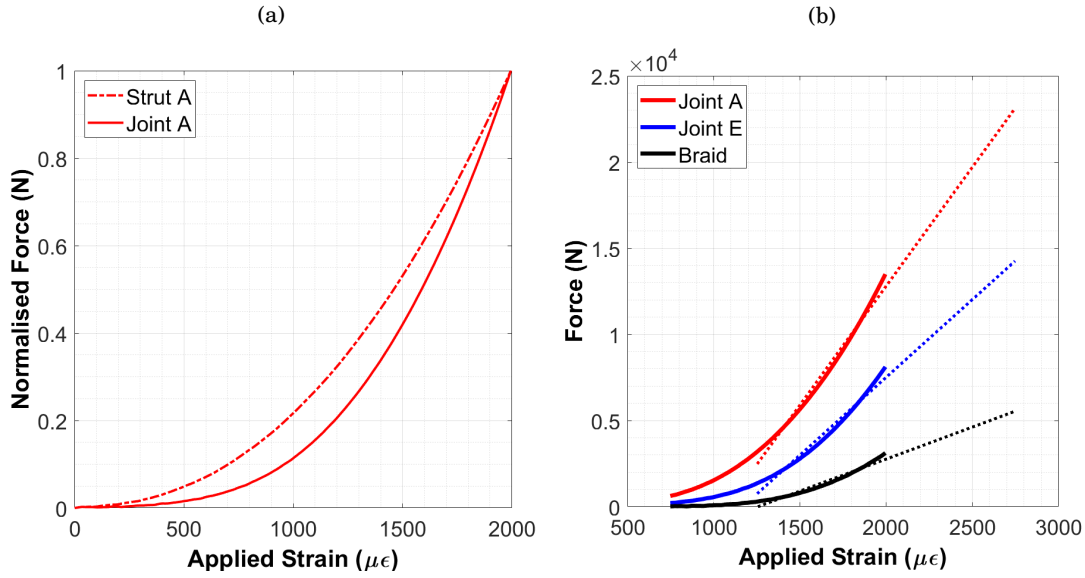

Figure 5.39: (a) Comparison of the Force (N) vs prescribed strain curve for strut and joint type A, using a SF and SFS tow representation, respectively. (b) Adjusted Force (N) against prescribed strain ($\mu\epsilon$) for joint types A, E and braid.

Table 5.8: Reserve factors for the tow, metal and matrix,; the reaction load (N) and predicted stiffness of joint configurations A, E and the braided joint.

Joint Type	R_t	R_{mt}	R_{ma}	Reaction Load (N)	Joint Stiffness, K (10^6Nm^{-1})
A	0.39	1.0	0.88	22493	112
E	0.33	0.95	0.66	14041	69
Braid	0.21	0.21	0.34	5521	27

The filament wound joints A and E display significantly greater axial stiffness compared to the braided joint (factors of 4.3 and 2.6, respectively). This is principally due to the disparity between the form of the pin-tow connection established using the two different fabrication techniques.

As stated section 3.2.2, the filament wound joint establishes a robust connection between the fibre-tows and the pins, with tow pull-back around the pins transferring the high tensile strength and stiffness of the fibre-reinforcement directly into the joint. In comparison, the braided joint relies upon the "shear-locking" of adjacent (non-axial) yarns around the pins to maintain load transfer in the joint.

Moreover, as apparent in figure 5.38, joint stiffness for the braided joint is minimal even at applied strains in the range of 1000-1500$\mu\epsilon$, in comparison to the filament wound joints A and E. Shear-locking of the tows results from an applied load rather than resulting from immediately from joint manufacture. Therefore, load transfer between the metallic pins and virtual tows is initially poor and the high tensile stiffness of the fibre-tows is only exploited later in the simulation, when joint stiffness increases significantly between 1500-2000 $\mu\epsilon$.

Consequently, joint stiffness could be overestimated for the braided joint through exclusion of the initial part of the loading curve (between 0-750$\mu\epsilon$) for its calculation. The model response in this region of the strain vs load curve may be more representative of the physical joint, than compared with the filament wound joints (with disparity between the physical and model responses being attributed to the initial contact gap between the pins and virtual tows). However, this effect is ignored as other limitations to the braided joint model may actually contribute to underestimation of joint stiffness and strength. These include the reduced yarn coverage of the pin-structured end-fitting in comparison to the physical joint, or the assumed "ideal" placement of the yarns around the pins (without puncturing), which may both reduce the degree of interlocking and form-fit between the yarns and pins.

As in section 4.6.6, a predicted joint failure load can be calculated via the re-scaling of the reserve factors, as shown in table 5.9. Joint type A has a failure load 62% and 39% greater than E and the braided joint, respectively. This indicates the potential for improved strength for the filament wound joint (in addition to stiffness), provided more optimal joint configurations are used.

However, the higher predicted strength for the braided joint against configuration E may be due to model limitations. The low reaction load and stiffness observed for the braided joint, leads to a high degree of scaling to obtain the predicted failure load in this case. Thus, a high margin for error can be assumed in deriving the failure load in the braided joint, as joint behaviour and response under loading is assumed linear for a significantly larger loading range, between the reaction and failure loads.

Moreover, unlike the pin failure observed for the filament wound joints, matrix failure is predicted to occur in the braided joint. Matrix failure is more likely to initiate joint failure at significantly lower loads. This is inferred by the 50% higher restated reserve factor for the yarns in the braided joint (at 0.6) against the tows in the filament wound joints, despite comparatively poor load transfer behaviour (and low reserve factor of 0.17) being observed for the yarns in the braided joint in the simulation; which was attributable to the less robust connection provided by

the shear-locking mechanism.

Table 5.9: Restated reserve factors for the tow and matrix, and the predicted failure load (N) of joint configurations A, E and the braided joint.

Strut Type	$\overline{R}_t$	$\overline{R}_{ma}$	Failure Load (N)
A	0.39	0.88	22493
E	0.35	0.69	14780
Braid	0.60	0.60	16238

Finally, joint strength can be compared against a reference case of a adhesive joint. Equation 3.2 can be re-arranged to find the predicted failure load for a single-lap shear joint using Volkersen's method [2]. A summary of the model parameters is given in table 5.10.

To offer a fair comparison with joint type A, the composite adherend is considered to be a uniform laminate, consisting of 6 lamina with fibre orientations of 0°. Laminate and composite thickness (t_l) is determined to be 2.4mm, using a tow thickness (T_t) as calculated in appendix A.2 and utilised in section 3.7 for the strut's central composite part overlaying the mandrel. The modulus of the composite adhered (E_l) is calculated for this laminate using CLT (section 3.4). All other parameters are taken from material data, previously stated in section 3.2.1 and table 3.1.

A failure load of 320N is predicted for the adhesive joint, and consequently, joint strength should therefore be increased by a factor of 70 through use of the filament wound joint, with configuration A. Although no attempt is made to optimise the adhesive joint's configuration, the large difference apparent in joint strength would indicate significant improvements in joint properties could be attained through use of the novel filament wound joint.

Table 5.10: Parameters used to calculate joint strength for an equivalent single-lap shear joint, using Volkersen's method [2].

Model parameter	Value	Description
c	5 (mm)	Half overlap length l = 10mm
t_l	2.4 (mm)	Lower adherend (composite) thickness
t_u	3 (mm)	Upper adherend (metal) thickness
t_a	0.075 (mm)	Adhesive thickness
E_l	423 (GPa)	Lower adherend (composite) modulus
E_u	114 (GPa)	Upper adherend (metal) modulus
G_a	0.9 (GPa)	Adhesive shear modulus
$\tau_{\max}$	20 (MPa)	Adhesive shear strength

5.10 Summary

In this chapter, a higher fidelity modelling framework was developed to study joint strength and load transfer behaviour with improved realism. This was motivated by the limitations imposed by the Single-Filament (SF) approach used in chapter 4 to assess the mechanical properties of the hybrid composite-metal strut. Assumption of a virtual tow with perfectly uniform and circular cross-section did not provide a realistic description of the virtual tow geometries in the region of the joint.

The Multi-Filament (MF) method was first used to predict realistic tow geometries and internal architectures in the joint region. Deformations are induced in the fibre-tows due to their relative interactions, and interactions with the pin-structured end-fitting, during the filament winding process. This detailed description of the tows was then used in the Single-Filament Superposition (SFS) approach to develop a mechanical model for the joint. The virtual tows were represented as a mesh of 3D continuum (solid) elements, and as previously, the virtual tows were coupled with matrix material via CLIS, so that joint's response under loading reflected the final, consolidated joint and strut component.

Mechanical properties of joint types A and E, following application of quasi-static tensile loads, were then assessed using the higher fidelity joint model. Noticeable difference, with regards to stress magnitudes and distribution, in the virtual tows and pin-structured metallic end-fittings, was observed against the SF model in chapter 4. This highlighted the importance of including realistic tow geometric effects for the joint.

Joint performance was also assessed against a reference joint using adhesive bonding and a braided/surface-structured joint. Significant improvements in joint stiffness and strength were predicted for the filament wound joint. This was conjectured to be predominately attributable to the robust connection established via direct pull-back of the tows around the pins, which exploits the high tensile stiffness and strength of the fibre reinforcement. The level of improvement against the braided joint was, however, found to be dependant upon the joint configuration. This supports the efforts made in chapter 3 to develop a preliminary performance of joint and strut configurations.

Joint and strut failure, for the filament wound joint, was predicted to occur via pin failure in both the higher fidelity model developed in this chapter, and in chapter 4. Moreover, at the joint's predicted failure load, reserve factors for the tow were in general less than 40%. This indicates the potential for further improvements joint strength (and stiffness), if configurations could be designed in which the high tensile strength of the fibres is exploited more efficiently in the joint. For example, the use of larger pins (and possibly also alteration of their shape) may both increase loading of the tows, and reduce stresses in the pins. The reserve factors for the tows (R_t) and pins (R_{ma}) would then be more equal, improving joint efficiency. Further discussion is provided in chapter 7.

However, the work so far has focused on the theoretical capabilities of the hybrid composite-

metal joint and strut. Before attempting to optimise strut and joint design, greater importance must be placed on assessing its manufacturability. If manufacture of the hybrid strut is infeasible, the joining mechanism becomes non-viable irrespective of the predicted performance improvements. Consequently, chapter 6 considers manufacturability via the fabrication of an early-stage, conceptual prototype hybrid composite-metal strut, using a 4-axis filament winding machine. This will also provide opportunity to validate the tow geometries predicted using the MF method.

CHAPTER 6

A MANUFACTURING CONCEPT FOR THE NOVEL HYBRID COMPOSITE-METAL JOINT

The chapters thus far have considered only theoretical concepts for a novel hybrid composite-metal joint solution. Whilst this can demonstrate the potential benefits of the direct load transfer between the pin-structured end-fittings and the carbon fibre tows, if it is not feasible to manufacture the final concept, then it becomes non-viable, regardless of the performance gains. This chapter considers manufacturing trials for the proposed composite-metal joining solution in the fabrication of a prototype hybrid strut. The manufacturability of the joining mechanism is assessed using current, commercially available technologies. Limitations imposed by manufacturing constraints are also quantified and discussed.

For the manufacturing trials, a 4-axis filament winding machine is used to layup dry, carbon-fibre tows onto a 3D printed polylactide (PLA) initial structure, consisting of a cylindrical mandrel spanning two pin-structured end-fittings. Novel winding patterns, in which the tow direction is reversed around cylindrically shaped pins, are constructed via the numerical control programming language, G-code, which coordinates the movements of the filament winding machine.

Matrix infiltration and consolidation of the strut is beyond the intended scope of this work. Similarly, validation of mechanical performance predictions made in chapters 3, 4 and 5, is not attempted. However, the manufactured dry tow strut allows for the verification of the tow geometries obtained using the Multi-Filament (MF) method, as detailed in chapter 5. This is conducted both by visual inspection and through use of x-ray computed tomography (μCT) scans of the hybrid strut. These analyses are then used to validate the MF approach, to confirm that it is able to capture realistic tow geometries for the region of the joint, with induced deformation due to the interactions between the filament wound fibre-tows and the metallic pins.

6.1 Experimental procedure

The strut's central mandrel and two end-fitting's are 3D printed [103] as PLA based, cylindrical tubes with outer radii 23mm, and lengths 200mm and 40mm respectively. These form the initial structure prior to the filament winding process. Dimensions are consistent with those used in chapters 3, 4 and 5.

Recall, this initial structure as seen in figure 6.1, behaves analogously to a traditional mandrel in conventional filament winding, in that, it is this structure that rotates about its longitudinal axis. To maintain the distinction between the use of "mandrel" to describe the central part spanning the two end-fitting's of the strut, this complete initial structure is referred to as the "Full Mandrel Structure" (FMS), to reflect its role during the filament winding process.

The end-fitting's are printed with an array of holes of depth 2mm and diameter 3.2mm. Cylindrical, acrylic pins with diameters 3mm and lengths 10mm are then fixed into these holes to form pin-structured end-fittings. This method of producing the pin structures was preferred against 3D printing the pin-structured end-fittings as a single piece. In such instances, the pins protruding from the end-fitting's surface require supporting material (scaffolding) during printing, as layers of PLA are built up from the end-fitting's base. The supporting structures have to be removed post-print. During detachment some material may remain on the pin surfaces leading to a rough exterior. This is to be avoided as it was found to cause splitting, fraying and breakage of the fibre-tow as it reversed direction around the pins during pull-back.

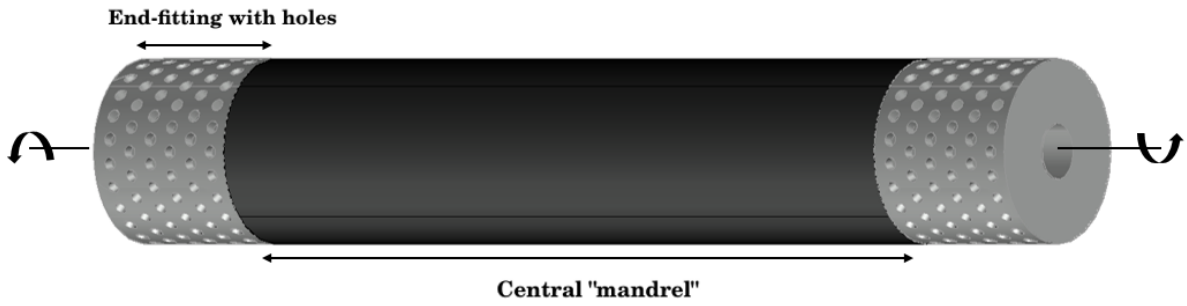

Figure 6.1: CAD drawing of the "Full Mandrel Structure" (FMS), which forms the initial structure behaving analogously to a conventional mandrel during the filament winding process (rotation direction is indicated). End-fittings located at the ends of the FMS are manufactured with holes into which cylindrical acrylic pins are inserted to form the pin-structured end-fittings of the strut.

The two pin-structured end-fittings are then fixed to the mandrel and connected to the mechanical chucks that control the rotational degree of freedom of the filament winding machine, as highlighted in figure 6.2. Custom modifications to the machine are also discussed in the following section, which aim to improve the manufacture process, in particular, the precision of the tow placement around the pin-structured end-fittings.

6.1.1 Filament winding machine - X-winder 4.0 ®

The 4-axis, desktop filament winding machine X-winder® 4.0 [104] [105], as shown in figure 6.2, was used in this work. Its four relative directions of motion, or degrees of freedom, are given by linear delivery carriage movement (Z), rotation of the mandrel (C) about its longitudinal axis and linear movement (Y) and rotation (B) of the tow delivery roller. Further details of the control axes are given in section 6.3.

Control axes Z and C form the essential degrees of freedom associated with a 2-axis filament winding machine. Linear movement of the tow delivery roller (Y) controls the position of the tow feed point relative to the mandrel's surface. Rotation of the roller adjusts the angle of the tow as it laid up on to the mandrel. Both of these additional axes of control are useful for preventing tow twisting during layup and for maintaining uniform thickness, as typically utilised in the conventional filament winding of domed-end composite pressure vessels [24] [25].

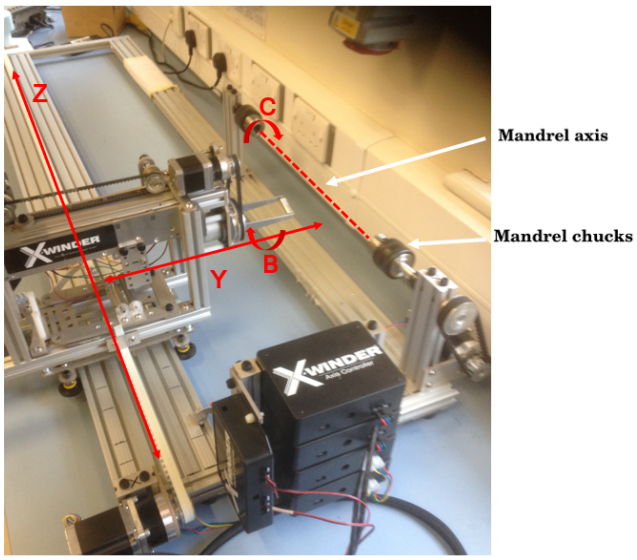

Figure 6.2: The X-winder® 4.0 4-axis, desktop filament winding machine. Control axes Z, C, Y and B are labelled.

Modifications were made to the tow delivery apparatus that feeds the fibre-tow onto the mandrel during fabrication. Originally a concave roller, as shown in figure 6.3, was used. During layup, the tow passes over the roller's surface to encourage flattening and spreading of the tow prior to placement on the mandrel.

During trials, transverse slippage of the tow along the length of the roller was found to occur, reducing the precision of the tow position. In the region of the pin structured end-fittings, exact placement of the tows is necessary to prevent puncturing by the pins. This was an important design consideration outlined in chapter 1.

Consequently, the tow delivery system was altered to a conically shaped structure that tapers to a eyelet, as shown in figure 6.4. The fibre-tow is passed through this delivery eye prior to

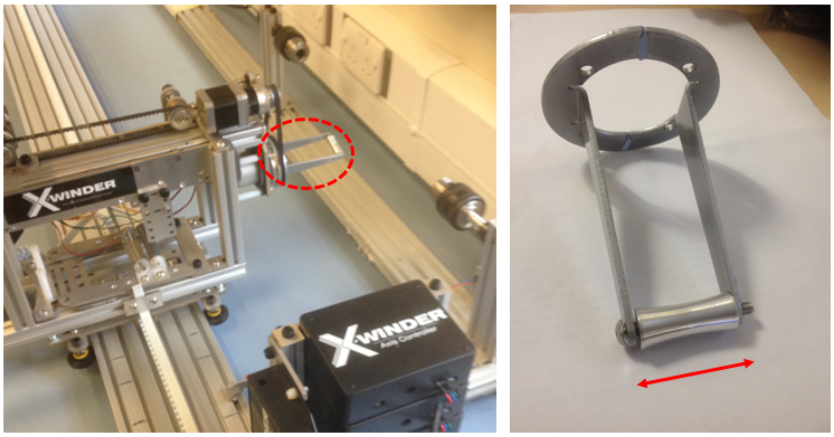

Figure 6.3: Concave roller position on the X-winder® 4.0. This apparatus provides the mechanism for feeding the fibre-tow onto the mandrel during the filament winding process. Close view of the roller, with the direction of tow slippage indicated.

placement onto the mandrel. During layup, deviation from the intended tow position is then limited to the diameter of the delivery eye, resulting in increased precision. The open end of the conical structure allows for easier access as the fibre-tow is threaded through the delivery eye by hand prior to winding. Friction between the walls of the delivery eye and the fibre-tow was reduced through inclusion of a low friction, silicon carbide guide ring. This was sufficient to prevent splitting and fraying of the tow as it passed through the delivery eye. Figure 6.5 shows the modified tow delivery system mounted of the X-winder. Fibre tows are pulled through the inner low friction ring (pink) during the winding process.

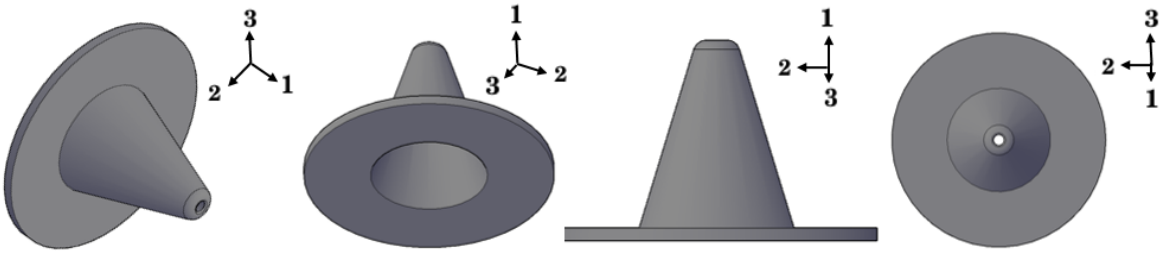

Figure 6.4: CAD drawings of the modified tow delivery system. A delivery eye of approximately 3mm in diameter allowed for improved control of tow placement over the concave roller.

6.2 Winding pattern determination

As described in sections 3.5 and 3.9, determination of the winding pattern necessary to fabricate the novel composite-metal joint and hybrid strut, required separate consideration of the tow path

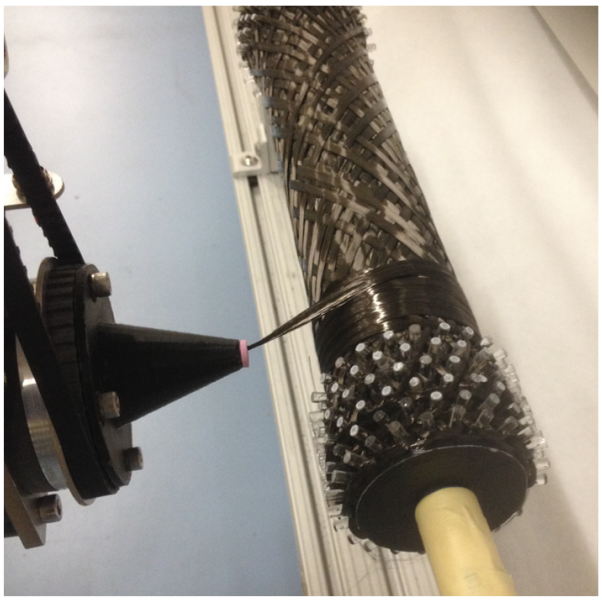

Figure 6.5: Modified tow delivery system mounted on the X-winder.

in two regions: in the proximity of the pin-structured metallic end-fittings and along the length of the mandrel forming the central part of the strut.

For the pin array, the tow path is determined by the array type, the chosen tow trajectory (section 3.9) through the pin array and the manner in which pull-back is initiated. The tow path on the mandrel is determined through alteration of the prescribed winding angle, θ, to θ_d and θ_u in the "down" and "up" directions between the end-fitting's at the strut ends. These alternative orientation angles prevent puncturing of the tow by the pins and ensure full coverage of the pin array, respectively.

Winding patterns of this type require a reversion of the FMS's direction of rotation between regions R_1 and R_2, as indicated in figure 6.6(a). That is, if the FMS is rotating in the anti-clockwise direction about its longitudinal axis for R_1, to place the tow along path R_2 it must then rotate clockwise.

Although this capability is not infeasible, the X-winder 4.0 cannot reverse the direction of the mandrel's rotation during execution of a given winding pattern. This limitation necessitates the development of an alternate winding pattern for the manufacturing trials, in which the rotation direction of the FMS is constant.

As previously, the prescribed winding angle on the mandrel (θ) can be adjusted to determine a path through the pin array and prevent tow puncturing, through calculation of the nearest-pin angle (θ_d), as described in section 3.5.1. However, as illustrated in figure 6.7, the return path of the tow in the "up" direction has opposing orientation due to FMS's constant rotation direction. That is, if the down angle is positive, then the return angle is negative, and visa versa. If symmetry is maintained at each end-fitting, then a given filament wound layer (within a full

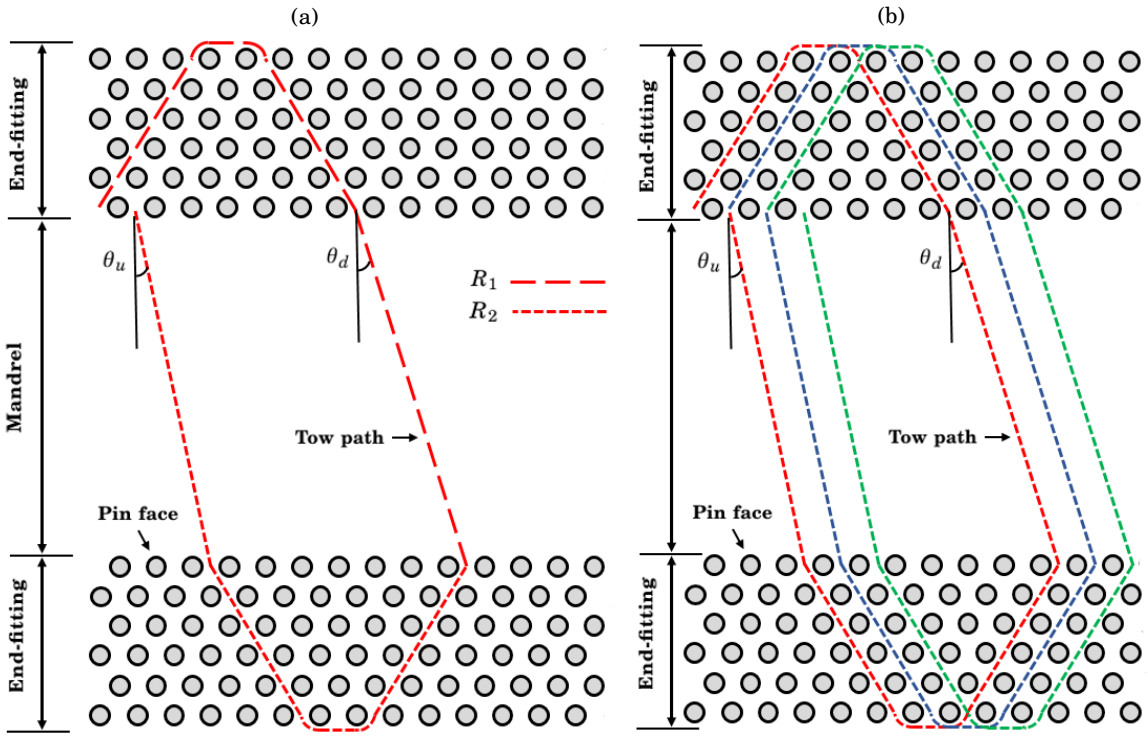

Figure 6.6: (a) Illustration of the tow path for a single iteration of the first filament wound layer onto the FMS with layup sequence detailed in section 2.5, for a diamond patterned pin distribution and an all-row winding pattern with pull back around 2 pins. (b) Three iterations of the winding pattern within a given layer, sequentially coloured red, blue and green.

sequence) consists of fibre tows with both positive and negative orientation angles.

This offers an immediate disadvantage in the respect that the number of tow crossing points is increased for the mandrel length. Significantly more undulation and out of plane movement of the tow may then result following layup when compared to the previous winding sequence devised, which reduces alignment with the strut's loading direction (axial tension and compression). Consequently, structural properties may be negatively affected. The interlocking manner of the filament wound tows may then more closely resemble a braided part at the tow crossing points. However, reversal of the tow direction (pull-back) around the pins still distinguishes it from a braided joint.

Additionally, the alternative winding pattern does not automatically return the tow to the next pin in the array, moving sequentially around the end-fitting's circumference. Full coverage of the pin array is not then immediately assured independently of the tow trajectory on the mandrel and around the pin-structured end-fittings. As detailed in section 6.2.1, achievement of full pin coverage becomes a more complex consideration requiring more detailed consideration.

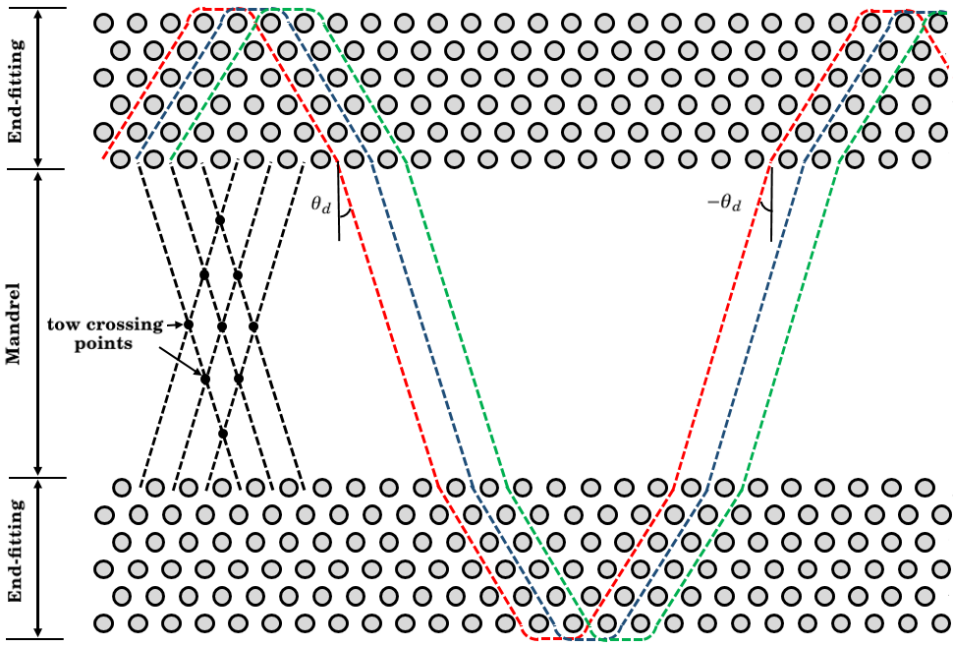

Figure 6.7: Illustration of the alternative winding pattern for a constant FMS rotation direction. Positive and negative fibre orientation angles exist (for the mandrel length), increasing the number of tow crossing points.

6.2.1 Methodology for full coverage of the pin array

Let us consider a worked example of the second layer of an all-row winding pattern, for a diamond type pin array consisting of 6 pin rows, each with 24 pins, (equivalent to the structure examined in this work). Suppose the tow enters the pin array at pin number 1, in the first row of the upper end-fitting in figure 6.8(a). It then leaves the array at pin 6, having reversed direction around pins in row number 5 (beneath the top row).

The prescribed winding angle for the mandrel length is $\theta = 15°$. The down angle, θ_d, is then given by 15.2°. The tow would transition onto the first row of the opposing pin-structured end-fitting at pin number 17, and then exit at the 22nd pin. An equal and opposite return angle of $\theta_u = -15.2°$ then places the tow on pin number 9, completing a single iteration of the filament wound layer.

As shown in figure 6.8(b), after three iterations of this winding pattern the tow returns to the starting position at pin number 1, of the first pin row of the upper end-fitting. Continued repetition of this winding pattern would result in additional fibre-tows being placed along this trajectory. The tow would contact only these pins, leaving 75% of the pins redundant in the mechanical interaction occurring between the fibre-tows and pins in the joint.

To prevent this, the return angle in the third iteration of the winding pattern is modified so that the tow is instead returned to pin 2, with an effective angle of −16.8°, as shown in figure 6.9(a). Every 3rd iteration of the winding pattern must be altered in this way to ensure full

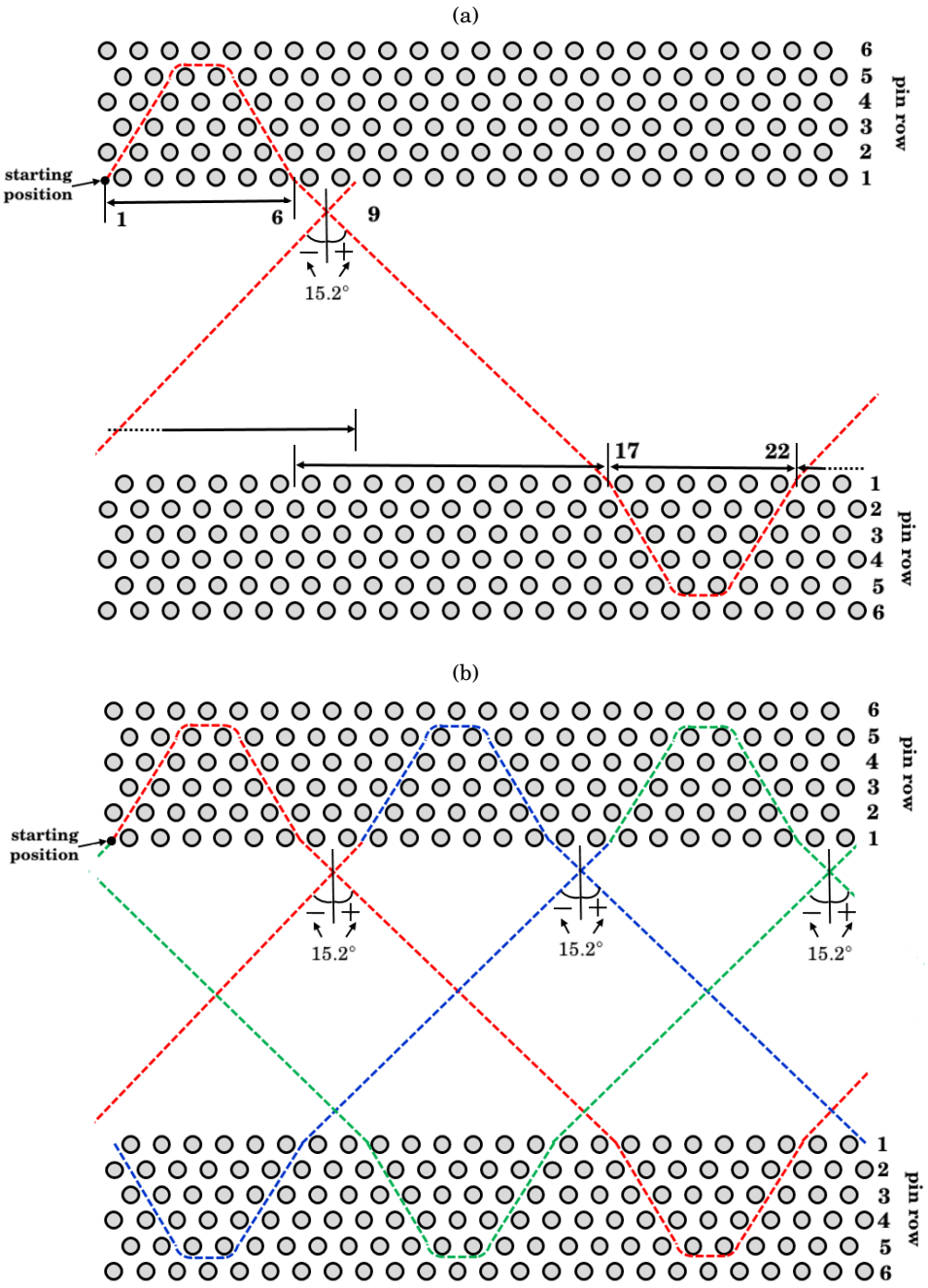

Figure 6.8: (a) Single iteration path of the second layer of an all-row winding pattern with pull-back around two pins, for a cylindrical end-fitting with a 24 x 6 diamond type pin array. The tow transitions on and off the pin array's at given pins in the first row, numbered sequentially preceding around the end-fitting's circumference. (b) Three iterations of the modified winding pattern for this filament wound layer, sequentially coloured red, blue and green. Without modification, only the pins along this tow path would interact with the filament wound fibre-tows in the joint.

coverage of the pin array.

Intuitively, when either the prescribed winding angle (θ) for the mandrel, or the tow trajectory through the pin array, are changed, the winding sequence must be modified at different points, after a given number of iterations. For example, for a third layer of an all-row winding pattern with $\theta = 30$ and pull-back occurring around two pins in row number 4, the down angle is $\theta_d = -29.8°$ and the return angle $\theta_u = -29.8°$ is altered to $-31.1°$ at every 12th iteration, (i.e only one modification is required for a pin row consisting of 24 pins).

Therefore, the path of the tow for a given filament wound layer requires independent consideration. An algorithmic or sequencing approach must then be used to map the path of the unmodified winding pattern, in order to determine an appropriate point in the sequence for path correction to ensure full coverage of the pin array. Complexity is thereby increased as this must be calculated prior to the winding process, so that path corrections can be automated in the G-code scripts (discussed in section 6.3).

6.3 G-code construction

To experimentally replicate the novel winding patterns detailed in section 6.2, custom G-code scripts are written and run in the X-Winder® Executor software. Table 6.1 shows the references for the relative degrees of freedom, movement (velocities) and acceleration rates of the X-Winder® 4.0.

Table 6.1: X-winder® 4.0 axes control references. Note X is a non-movement axis and is denoted to complete the right-hand orthogonal system.

	Linear degrees of freedom		
	Non-movement	Delivery head	Delivery carriage
Position (in)	X	Y	Z
Linear rate (ins^{-1})	D	E	F
Linear acc (% of full)	I	J	K
	Rotational degrees of freedom		
	Non-movement	Delivery head	Mandrel
Angular position (°)	A	B	C
Angular rate ($revmin^{-1}$)	Q	R	S
Angular acc (% of full)	N	O	T

The X-winder® 4.0 uses absolute positioning. Each assigned movement is completed relative to the origin and starting position of the control axes at the beginning of the G-code script. This is as opposed to incremental positioning, where movements are completed relative to the previous position, as designated in the preceding line of G-code. A full example of a G-code script used for the manufacture of the 2nd filament wound layer in section 6.4, can be seen in appendix A.6.

Lines of G-code containing movement commands can invoke individual or multiple machine movements. Figure 6.10 shows a line of G-code in which mandrel rotation (C), linear movement

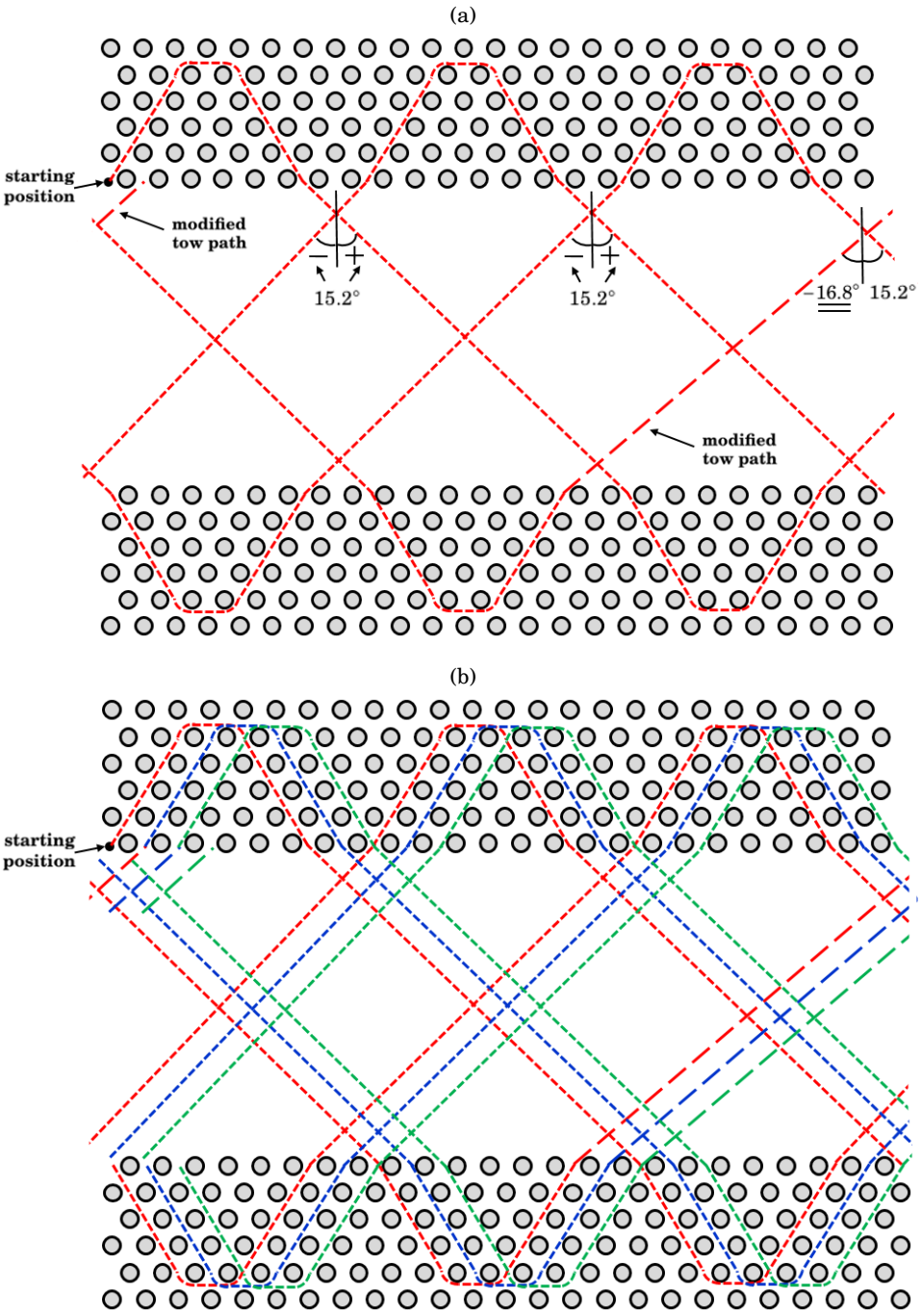

Figure 6.9: (a) Modified tow trajectory at 3rd iteration of winding pattern with constant mandrel rotation direction. Modification is required to ensure full coverage of the pin array. (b) Three iterations of the modified winding pattern for this filament wound layer, sequentially coloured red, blue and green.

of the delivery carriage along the FMS's longitudinal axis (Z), and rotation of the delivery eye (B), are called simultaneously. The "G1" term confirms a movement command to the executor.

The numerical values following the letter references denote the magnitudes of the velocities and displacements undertaken in that line of G-code. For example, "F0.12 C2.83" describes a linear movement of the delivery carriage of 2.83 inches at a rate of 0.12 inches per second. The value following the reference, "A", denotes the cumulative rotation angle of the FMS, following execution of the movements in that particular line of G-code, (this is required by X-Winder® operating system).

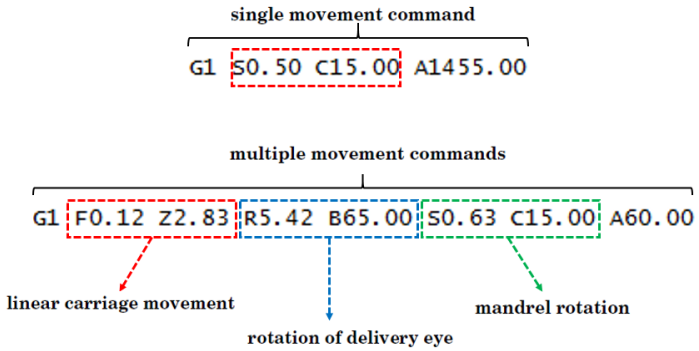

Figure 6.10: Lines of G-code containing both a single movement command and multiple movement commands. Multiple movements must be made coordinate over a given time interval.

In general, multiple movements within a given line of G-code must be made coordinate so that they are completed simultaneously. This prevents inaccuracies propagating in the tow placement during the winding sequence due to overlapping movements across given time intervals.

Lines of G-code were coordinated against a specified rate of 3 and 25 $\text{mm}s^{-1}$ (or 0.12 and 0.98 $\text{in}s^{-1}$) for the linear delivery carriage movement, in the region of the pin-structured end-fittings, and for the mandrel, respectively. The carriage position at given points in the winding pattern can then be used in combination with these prescribed velocities to define time intervals other which all over movements are then coordinated. A relatively slow carriage velocity was used in the proximity of the pins to improve the precision of the tow layup in this region. Less precision was required for the mandrel length so the carriage speed was increased to improve total fabrication time.

Acceleration rates J, K, O and T were initialised at the start of the G-code scripts. These are values representing a percentage of the permissible maximums, as determined by the tolerances of the X-Winder® 4.0.

6.3.1 Tow reversal (pull-back)

During experimental trials, it was found that direct navigation of the delivery eye through the channels between pins in the array, was infeasible. Even small imprecision with regards to the position of the delivery eye relative to the pins resulted in contact, forcing cessation of the trial. Instead, the Y axis, controlling the position of the tow delivery eye relative to the mandrel's

surface, was invoked only at the start of the G-code scripts, in order position the tow delivery eye as close as possible to the FMS's surface without contacting the pins. The mechanism for placing the tow between the pin array, and around the pins during pull-back, therefore replied upon the low friction of the pin surfaces and the tension in the filament wound tows, to allow the tows to slip down the pin length and consolidate closer to the end-fitting's surface.

A degree of manual manipulation of the fibre-tows was required at points during manufacture in order to aid this process. This particularly held for layups with low orientation angles on the mandrel. In such cases, the tows were prone to slipping in the opposing direction away from the end-fitting's surface, resulting in loss of contact between the fibre-tows and pins during pull-back. Difficulties also arise in avoiding contact between the tow and pins neighbouring the "turn pin", both for the case of adjacent pins in the same row, and for pins in rows above and below the turn pin row. These were exacerbated by the multi-row pin array and relatively high degree of pin density used in this work. Such contacts would reduce accuracy of tow placement and may induce manufacturing defects such as tow fraying and puncturing.

A two-dimensional illustration of the reversal of the tow direction (pull-back) around the pins is given in figure 6.11, for the case in which two adjacent "turn" pins are used. Initiation of tow pull-back in this way can be considered unique to this work. P_0 denotes the starting position of the tow, following navigation through the pin array, but prior to initiation of tow pull-back. The delivery carriage was advanced along the FMS's longitudinal axis (Z), so that the delivery eye was positioned 10mm above point P_0. The distance of the delivery eye along the Y axis, relative to the end-fitting's surface, mean that the tow then occupied a position between the turn-pin row, and the row directly above. A Z translational distance of 10mm was found to be optimal with regards to providing sufficient tow length to promote slipping down the pin's surface, without the tow interacting with pins in row above. The mandrel was simultaneously rotated about its C axis to position the tow at point P_1. An equal mandrel rotation, and opposing displacement of the delivery eye, placed the tow at position P_2, completing tow pull-back.

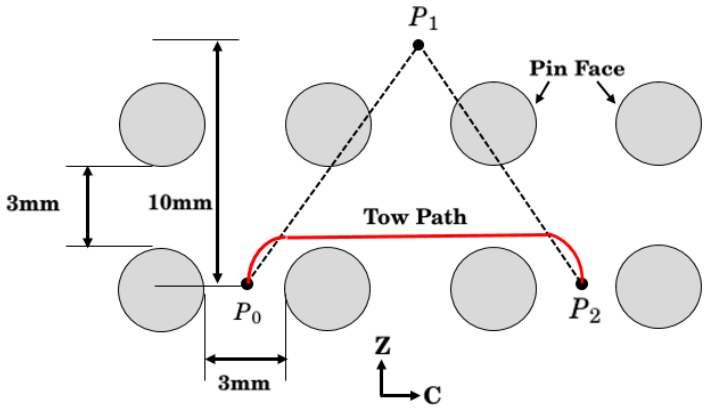

Figure 6.11: Illustration of the mechanism for reversing the tow direction (pull-back).

6.4 Prototype manufacture

The manufacture of a conceptual, prototype hybrid strut was completed. For this, T-300 12k carbon fibre tows (supplied by Toray Industries Inc) were wound onto the FMS using the winding pattern devised in section 6.2, using single direction mandrel rotation, and through direct assignment of the G-code scripts to coordinate the machine movements for each layer, as detailed in section 6.3.

Three filament wound layers were produced with prescribed orientation angles (θ) for the mandrel length at 5°, 15° and 30°, respectively. The actual orientation angles were given by ±5.2°, ±15.2° and ±29.8°, when their trajectories were adjusted to prevent tow puncturing by the pins, and a constant FMS rotation direction was assumed. The return angle θ_u was modified at various points in the winding sequence to ensure full coverage of the pin array, as detailed in section 6.2.1. The tow path through the pin array was an example of an all-row trajectory, described in section 3.9.2. This was thought to being the simplest pattern to produce from an experimental perspective as the tow direction remains constant through the pin array until the point of pull-back.

In each layer, pull-back was initiated around two adjacent pins. Pull-back around more than two pins would also have been possible, although this would have resulted in material wastage. Reversal of the tow direction around a single pin was found to be difficult to replicate experimentally, with the fibre-tow often slipping from the pin's surface due to the relatively small turning radius and reduced contact area between the tow and the pins. Similarly, the level of tow articulation required to produce the under-wind pattern described in 3.9.4, was determined to be infeasible with the apparatus available.

Figure 6.12(a) depicts the first filament wound layer on the FMS. Figures 6.12(b) and 6.12(c) include the 2nd and 3rd layers, respectively. Tow coverage of the mandrel surface increased with each subsequent layer due to the varying fibre orientation angles on the mandrel. However, as highlighted in figure 6.13, some small regions of the mandrel remained uncovered even after the application of the third layer, although these appear to be fewer and less regularly distributed on the mandrel's surface than that predicted using the analytical and numerical methods described in section 3.6, and shown in figure 6.14. This was due to the physical fibre-tow spreading beyond the assumed diameter of 2mm utilised in the modelling approach, resulting in increased coverage of the mandrel's surface.

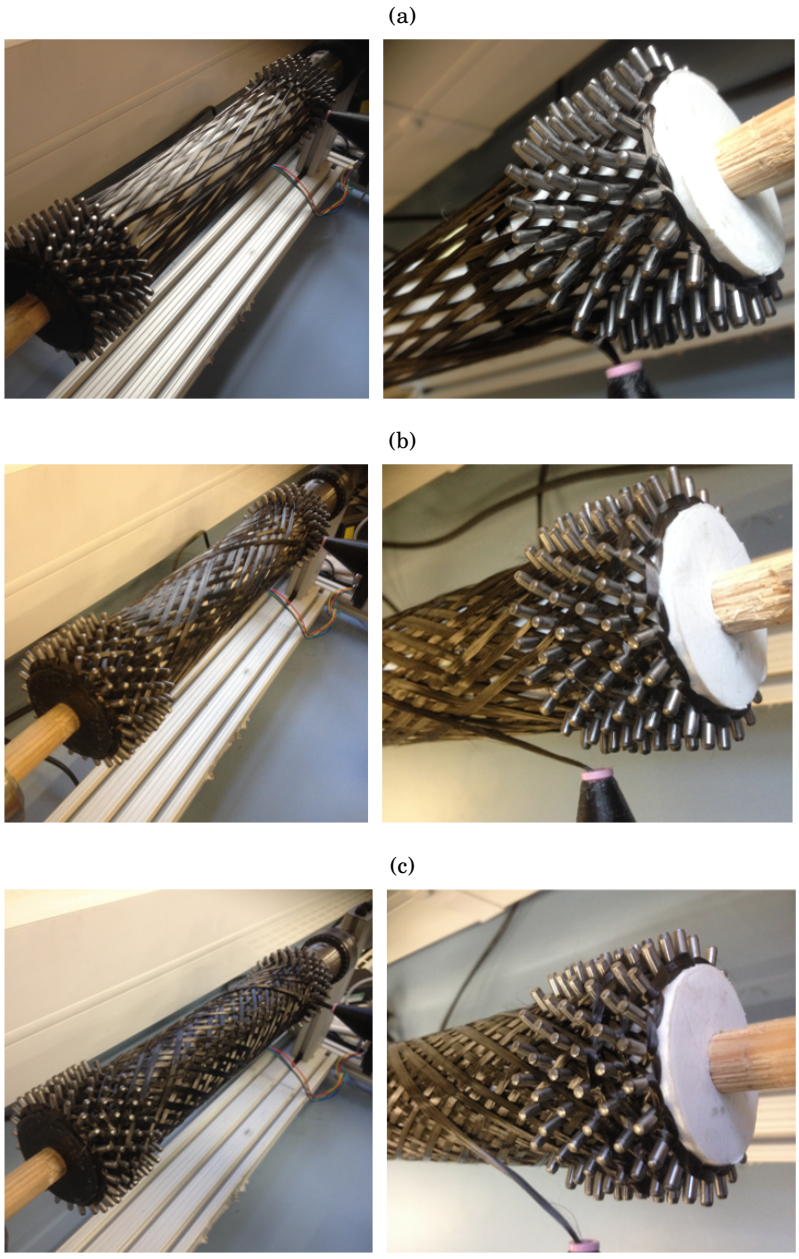

Figure 6.12: (a) FMS after a single filament wound layer with a prescribed orientation angle (θ) of 5° on the mandrel. (b) and (c) include the 2nd and 3rd layers, with orientation angles of 15° and 30°, respectively. The tow trajectory through the pin array is an example of an all-row winding pattern, with pull-back initiated around two pins.

Fabrication was halted after three filament wound layers were completed. It was theoretically feasible to have a total of 6 layers with pull-back occurring on pins in each row. Further layers with different orientation angles will have contributed to improved coverage of the mandrel. However, it was anticipated that μCT image clarity (see section 6.5), with respect to the visualisation

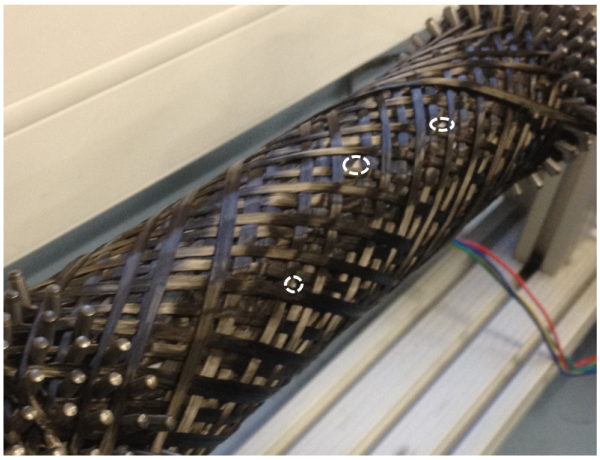

Figure 6.13: Uncovered regions of the mandrel after the application of three filament wound layers. Tow coverage was greater than that predicted using the analytical approach in section 2.6, due to increased spreading of the physical tow on the mandrel's surface.

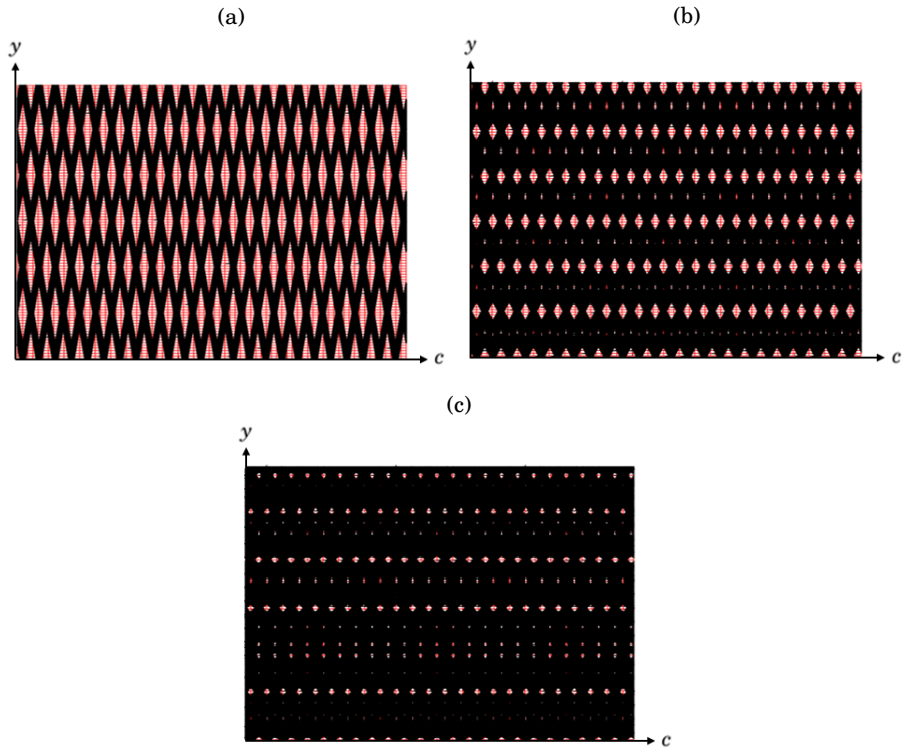

Figure 6.14: Tow coverage (black) of a gridded (red lines) mandrel's surface in the "unrolled" configuration, as predicted with the analytical and numerical approach utilised in section 3.6, for (a) 1 and (b) 2 and (c) 3 filament wound layers (cumulative). Areas of no tow coverage are overestimated and more regular in their distribution, when compared to the physical reality.

of the tow paths, geometries and areas of low fibre coverage of the FMS, would be improved for fewer layers. Furthermore, the completion of three filament wound layers with different fibre orientation angles for the mandrel length, was determined to be sufficient for proving the manufacturability of the novel composite-metal joining solution and hybrid strut examined in this work.

6.5 Analysis of x-ray computed tomography (μCT) images and comparison with the Multi-Filament (MF) Model

The Multi-Filament (MF) method (section 5.1) was used to predict position and shape of the fibre-tows in the region of the joint, as shown in figures 6.15. The results of the simulation are compared against the physical tows via μCT scan images in figures 6.16. μCT Scans were conducted for a region on the strut's longitudinal axis including an end-fitting and part (40mm) of the mandrel length.

For fair comparison, the MF model in this instance accounts for the modified winding pattern used in the experimental procedure. Additionally, the virtual tow layers were compacted, (using the "band-tool" as described in section 5.4.2), to the average measured thickness of the physical tows overlaying the mandrel (0.95mm).

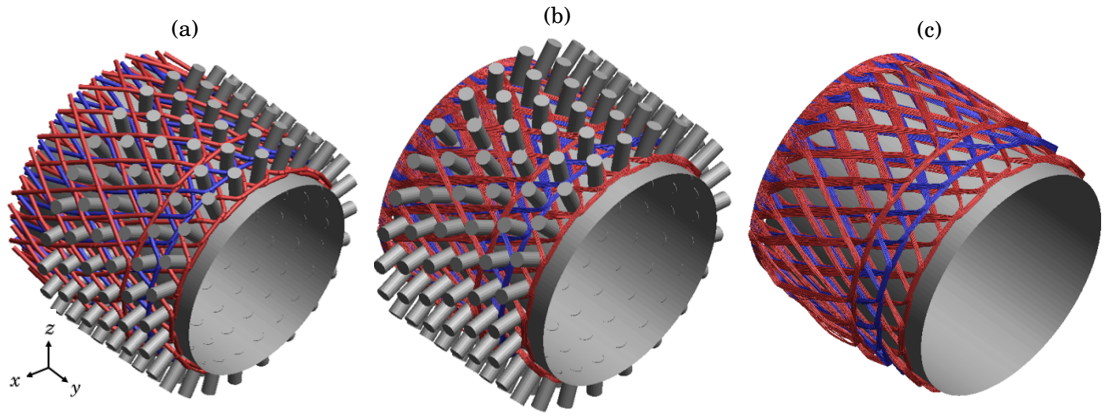

Figure 6.15: (a) Single Filament (SF) model of the composite-metal joint, this forms the first stage in the development of the Multi-Filament (MF) model. (b) The MF model of the joint with the final simulated tow geometries. (c) With pin surfaces removed so that the tow path and shape can be seen clearly. The three filament wound layers are coloured red and blue alternately.

As illustrated in 6.17, the MF method is capable of capturing realistic representations of the tow shape in the region of the end-fitting. Deformations that are induced in the fibre-tows due to their relative positions and interactions at crossing points were in good agreement with the physical reality (see region 1). Similarly, predicted gaps in tow coverage, in terms of size, frequency and position, correlated well with the experiment, particularly for those occurring at

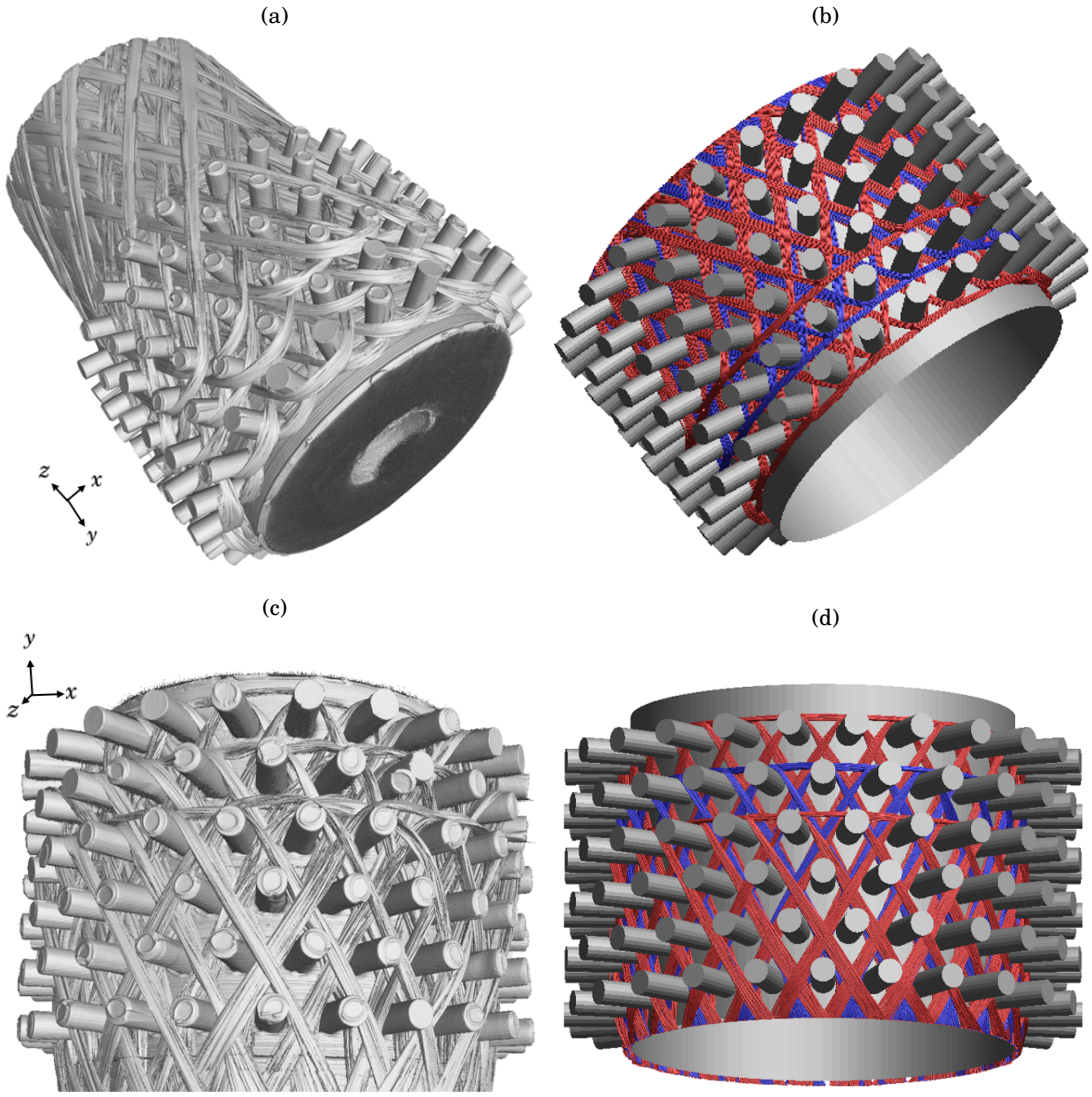

Figure 6.16: Comparison of the μCT images (a) and (c), with the Multi-Filament (MF) model (layers of virtual tows are coloured red and blue alternately) of the composite-metal joint (b) and (d). Note that the perspectives are not exactly equal.

the underside of the pins, as highlighted in region 2. As found in section 5.9.1, the inclusion of realistic tow geometries was important for detailed modelling of the stress distribution in the metallic pins and filament wound tows, and the load transfer behaviour in the joint.

Variation in tow geometry due to interactions with the pins during pull-back was also observed in the MF model. In particular, the spreading and thinning of the tow cross-section as it was compacted onto the surface of the pin. However, as indicated in region 3, the degree of tow spreading on the pins was predicted to be significantly less than compared to the physical reality. As tow spreading along the pin was reduced, the virtual tows tended to consolidate closer to the end-fitting's surface, as highlighted in figures 6.18 and 6.19. The physical tows are typically

located at a increased radial position relative to the end-fitting's surface.

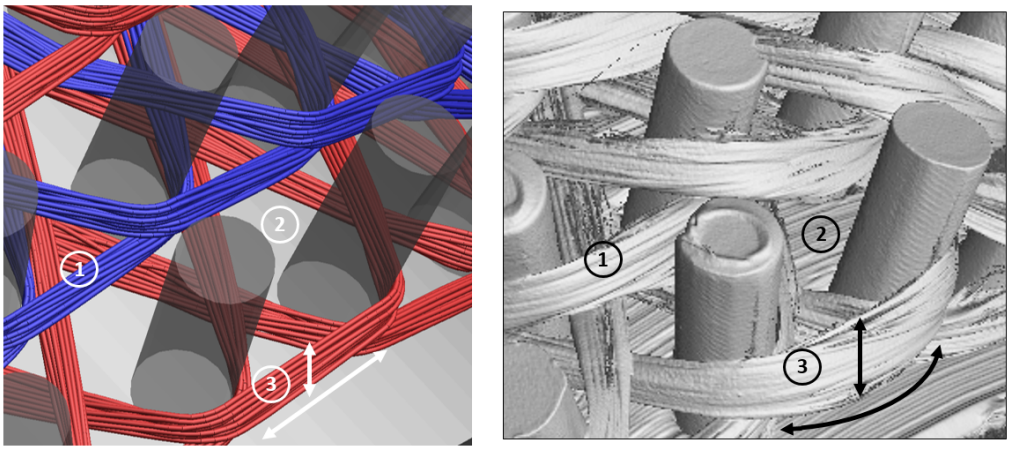

Figure 6.17: Close view of a region of the pin-structured end-fittings. Good agreement between the MF method and the experimental procedure was observed with regards to (1) the relative tow positions and interactions and (2) uncovered areas of the end-fitting located at the underside of the pins. Although tow deformation due to contact with the pins during pull-back was well captured using the MF method (3), the degree of spreading of the tow along the pin surfaces was underestimated when compared with the physical joint.

This discrepancy between the model and physical tow position occurred despite the use of very low coulomb friction coefficients (0.1) in the model's contact definitions, which should not inhibit tow spreading via the relative displacements of its virtual fibres.

Moreover, the shape and path of the tow structure also varies between the model and the μCT image in region 3. The virtual tows take a straighter path between the adjacent turn pins, in comparison to the physical tows which follow a more curved, bow-shaped trajectory.

These differences may be attributable to several factors. Firstly, due to the dynamic nature of the filament winding process, during pull-back, the tow is manipulated and dragged onto the pin in a more forceful fashion than that utilised in the modelling approach, where deformation is gradually induced in the tow structure so that good contact definition (minimal interpretations) is maintained between the virtual fibres. This may have caused significantly more spreading and alteration to the tow's shape than that predicted using the MF approach.

Additionally, spreading of the physical tow during the filament winding process was predominately determined by the degree of tow tension. During pull-back, tow tension control was significantly variable. Tension was generally only maintained at the point of tow reversal around the "turn" pins. As the tow travelled between the two adjacent turn pins used in the experiment, the tow was relatively un-tensioned, with some excess tow length. This may have contributed to both, increased spreading of the tow along the pin length, and its curved path, in comparison to the model in which tension was applied more uniformly to the virtual tows.

Finally, the flexural rigidity of the physical tow was approximated in the MF via the discreti-

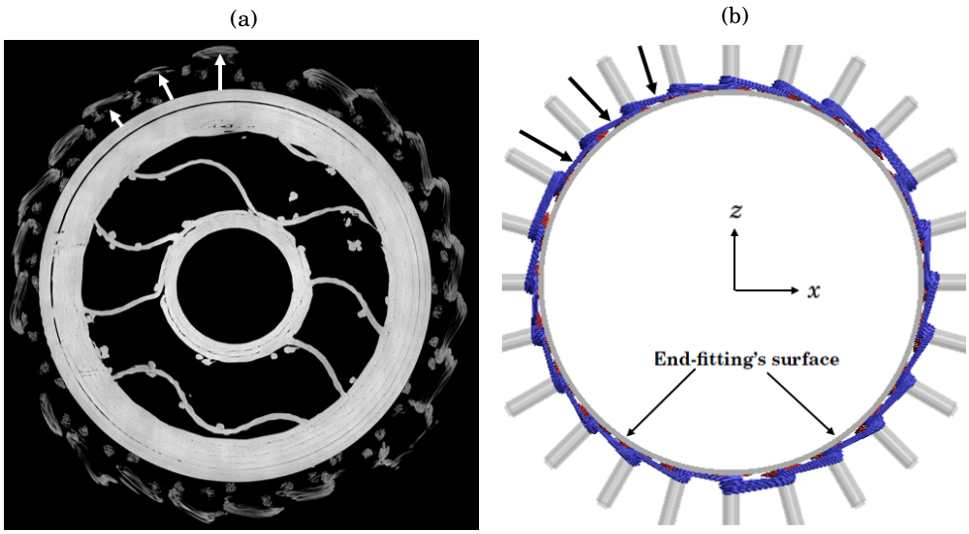

Figure 6.18: Cross-section view (x-z) of the (a) physical and (b) model structures, at the point of pull-back for the second filament wound layer. The degree of tow consolidation to the surface of the end-fitting was overestimated by the models. Increased tow spreading along pin length was found to occur in the experimental procedure, resulting in tow positions at a greater (radial) distances from the end-fitting's surface.

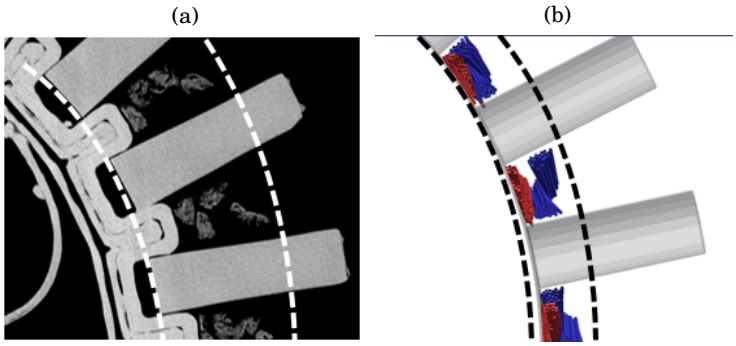

Figure 6.19: Part of the $x-z$ cross-section view, for the (a) physical and (b) model structures. As highlighted, a higher degree of radial compaction is observed in the MF model.

sation of the virtual fibres into individual truss elements, each of minimal length in comparison to the full length of the tow. The use of the physical tow's very low bending stiffness for truss element's material properties would have led to poor contact definition (in addition to not being representative of the tow's significantly higher axial stiffness). Consequently, the flexural rigidity of the virtual tow may have been greater than the physical reality, contributing to the discrepancy observed between curved, bow-shaped path of the physical fibre-tows, and the straighter path of the virtual tows, in region 3.

In its construction, the MF model also assumed "ideal" or "perfect" placement of the tows around the pins. Consequently, it was therefore unable to predict the presence of manufacturing

defects such as tow puncture, as shown in figure 6.20, due to poor tow positioning relative to the pins. However, these defects were found to be infrequent occurrences, and typically only observable from the μCT images, as opposed to visual inspection.

It should be noted that the pin array used for the experimental procedure was at the maximum feasible degree of density, using the condition established in section 3.1. Therefore, tolerances for erroneous tow placement were at a minimum and such defects therefore most likely to occur, compared to other configurations. The fact that frequent, significant defects were not observed, supports the hypothesis that establishing the joining mechanism via filament winding, as opposed to braiding technologies, may reduce such manufacturing defects as placement of the individual tows (or yarns) can be achieved with a higher degree of accuracy.

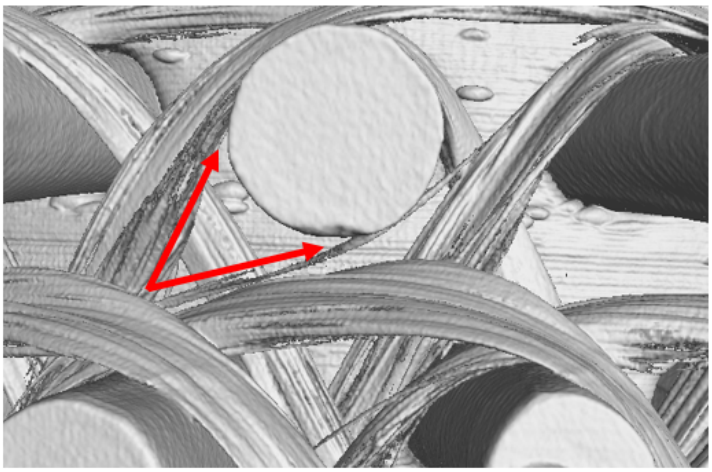

Figure 6.20: Tow puncture occurring at the point of pull-back around a cylindrical pin during the experimental procedure. Puncture in this case is minor, as only a small section of the tow separates to take a path around the underside of the pin, which was only observable in the μCT scan images.

6.6 Summary

6.6.1 Experimental Procedure

The manufacturability of the proposed composite-metal joining solution, for a early-stage, prototype hybrid strut, was explored using a commercially available 4-axis filament winding machine. Modifications to the tow delivery system were made to improve precision of tow layup around the pins, in order to prevent manufacturing defects such as tow puncturing. Furthermore, alterations were made to the winding patterns designed in sections 3.5 and 3.9, in order to account for experimental limitations.

The numerical control programming language, G-code, was used to coordinate the movements of the filament winding machine, in order to fabricate novel winding patterns in which the tow

trajectories were reversed (in a process referred to as "pull-back") around cylindrical shaped pins located at the strut ends. The layup of three filament wound layers was conducted, each with different fibre orientations angles along the mandrel length. Although some manual manipulation of the fibre-tows was required to maintain contact with the pins during pull-back, (particularly for low angled trajectories), the path of the tow in the winding sequence was fully automated and designated by construction of custom G-code scripts.

Few significant manufacturing defects, such as tow puncturing, were observed. This held even for the maximum feasible pin density (as established in section 3.1.2), in which such defects were therefore most likely to occur due to inaccuracies with regards to tow placement during the filament winding process. This would support the hypothesis that a reduction in such manufacturing defects may be possible with a surface-structured joint created via filament winding, as opposed to one manufactured using braiding technologies.

Improvements to the manufacture process could be made through optimising machine movement speeds in order to minimise total fabrication time. Furthermore, the mechanism by which the fibre-tows are laid up onto the pin-structured end-fittings relied upon the tow slipping down the pin towards the end-fitting's surface. Reliability of tow placement in this region could be increased by developing a framework in which the tow delivery system can directly navigate the pin array, traversing the channels between the pins in order to place the tow directly onto the end-fitting's surface. This may require the use of a filament winding machine and tow delivery apparatus that are specifically designed and adapted in order to complete this specialist function. Further discussion is provided in section 7.3.

6.6.2 Validation of Multi-Filament (MF) method

Computed Tomography (μCT) scans were conducted to provide detailed imagery of the tow trajectory, position and shape, for the region of the joint at the strut ends. These were compared against those predicted using the Multi-Filament (MF) approach, as described in chapter 5.

Generally, the MF method was capable of capturing the variations in tow shape caused by inter-tows interactions and contacts with the pins. As seen in section 5.9.1, the inclusion of realistic tow geometries in the region of the joint, allowed for more accurate modelling of the joint's mechanical behaviour (in particular stress distribution in the metallic pins.

During pull-back, flattening and spreading of the tow onto the pin surfaces was observed both in the MF method and the physical reality. However, the degree of tow spreading was generally underestimated in the model, which may have been due to the fact that no attempt was made to simulate the actual filament winding process. The dynamic nature in which the fibre-tows are manipulated around the pin-structured end-fittings may lead to significant alterations to the tow position and shape that cannot be accounted for in the modelling framework.

Additionally, physical tow flexural rigidity and the non-uniformity of tow tension during the filament winding process, were not accounted for in the models, which led to discrepancies in

regards to tow path and shape between the MF simulation and the physical strut.

CHAPTER 7

CONCLUSIONS

In this thesis a novel hybrid composite-metal joining solution was proposed and assessed, for applications to tubular structures predominately loaded in axial tension and compression. The motivation for this research was provided by the project's industrial partners Airbus UK, with the intention of exploiting the high specific strength associated with composite materials in the development of weight optimised, high performance landing gear components.

To maximise structural integration, composite manufacture was considered simultaneously to initiation of the composite-metal joint. This allowed for direct manipulation of the (dry) fibre reinforcement, so that the high tensile stiffness and strength of the fibres could be utilised in the joint, offering the potential for increased joint efficiency and load carrying capability.

The main objectives of the research, (as outlined in chapter 1), are stated below, along with the thesis chapters in which they were addressed. Further details on the research outcomes are then given on a chapter-by-chapter basis, prior to an overall summary in section 7.2. Finally, recommendations for future development of the joining technology, modelling capabilities and manufacturing techniques established in this work, are then provided in 7.3.

Objectives and chapters in which they were addressed:

(1) Introduce the novel hybrid composite-metal strut and joining mechanism, and characterise the winding patterns necessary for its construction.
Chapter 3

(2) Explore the theoretical range of strut and joint designs.
Chapters 3, 4 and 5

(3) Develop efficient modelling tools that allow the mechanical performance potential of the hybrid composite-metal strut and joint to be assessed.
Chapters 3, 4 and 5

(4) Utilise the modelling tools to predict joint properties, such stiffness, strength and load transfer behaviour, and evaluate how this may vary between joint designs, and against alternate composite-metal joining solutions.
Chapters 4 and 5

(5) Examine the manufacturability of the proposed hybrid composite-metal joint and strut, and investigate limitations imposed by current technologies.
Chapter 6

7.1 Research outcomes by chapter

Chapter 3 - Joint and strut design

A novel composite-metal joining mechanism was proposed, in which carbon-fibre tows are integrated with a pin-structured metallic body using filament winding fabrication techniques. For the first time, tow pull-back was considered to occur directly around features (pins) structured on the metal's surface, in order to establish a robust connection between the composite-material's fibre reinforcement and the metal directly during composite manufacture, and thereby exploit the high tensile stiffness and strength of the fibres.

Unique winding patterns were theorised for the manufacture of the composite-metal strut and joint, in order to prevent the occurrence of manufacturing defects, such as tow puncturing, and fully utilise the pin array at the composite-metal interface. Joint and strut parameters were considered using analytical and numerical approaches, to develop understanding of the novel interaction between the filament wound tows and pins in the joint, and to assess the effect of variable tow coverage on the strut's central mandrel.

These analyses reduced the size of the design space prior to assessment of joint and strut properties using FEM in chapters 4 and 5, and also provided a preliminary performance ranking of the possible strut configurations A-E.

Chapter 4 - Meso-scale mechanical performance assessment of the hybrid composite-metal joint and strut

Joint and strut performance was assessed using Finite Element Analysis (FEA). For the first time, the Single-Filament (SF) Method, used for the modelling of yarn interactions in composite

fabrics, braids and preforms, was adapted to allow for prediction of the as-manufactured path of the tows on the strut, resulting from the filament winding process.

A novel method for providing a computationally efficient mechanical model of the strut was implemented through use of the LS-Dyna® function *CONSTRAINED_LAGRANGE_IN_SOLID (CLIS). This allowed for strut properties and behaviour to be representative of the final, consolidated strut component.

From virtual tests, strut and joint properties such as stiffness, strength and load transfer capability, were found to be highly dependant upon choice of configuration. Tow pull-back around the pins, resulted in high tensile stresses in the virtual tows, which fits the aims of the joining solution. It was concluded that further optimisation of the joint and strut configuration would be needed prior to offering strength, stiffness and weight-saving benefits against a fully metallic strut. Also, procedures must be undertaken to mitigate the strut's relatively poor properties in compression; although compressive response may have been understated as adhesion between the matrix and metallic end-fittings was not included in the models.

Chapter 5 - Meso-scale mechanical assessment of the hybrid composite-metal joint using a higher fidelity approach

Performance of the hybrid composite-metal joint at the strut ends was considered using a higher fidelity modelling framework, with more realistic tow geometries. This was motivated by limitations imposed by the use of virtual tows with constant, circular cross-section in the SF approach, which may not have characterised joint load transfer behaviour, and the stress distribution in the virtual tows and pins, with sufficient realism.

For the first time, the Multi-Filament (MF) method, used to obtain realistic yarn architectures in the woven fabric forming simulations, was adapted to provide realistic tow geometries and internal architectures for the region of the composite-metal joint. An innovative modelling approach in the Single-Filament Superposition (SFS) method, was then used to transfer this detailed description of the fibre-tows to a model capable of predicting the joints mechanical performance.

Joint properties, in particular load distribution across the metallic pins, was altered between the use of more realistic tow geometries, against the SF tow in chapter 4. This justified the efforts made to include more realistic tow geometries in the modelling framework. Moreover, the novel application of the MF method allowed for detailed understanding of the interactions occurring between the fibre-tows and the metal during the filament winding process.

Performance improvements in joint stiffness and strength were predicted against a reference joint using adhesive bonding, and a similar joining mechanism manufactured using braiding technologies. Against the braided joint, increased performance was determined to attributable to the manner of the tow-pin connection. Unlike the filament wound joint, the shear-locking

mechanism between the (non-axial) yarns and pins in the braided joint, did not exploiting the high strength and stiffness of the fibre reinforcement.

Chapter 6 - A manufacture concept for the novel, hybrid composite-metal joint

Manufacturability of the novel, composite-metal joint and strut was considered via the fabrication of an early-stage, conceptual, dry-fibre prototype. Modifications were made to a commercially available, 4-axis filament winding machine, in order to improve the manufacture process and prevent tow puncturing by the pins. Custom G-code scripts were constructed to produce the novel winding patterns necessary for strut fabrication, with limitations imposed by machine functionality taken into account.

It was found that manufacture of the hybrid composite-metal strut and joint is feasible using current technologies. Reversal of the tow direction around the pins during pull-back, was found to be achievable without inducing defects such as tow puncturing. This held even for high levels of pin density in the joint and therefore may offer advantages over similar braided joints, in which such defects have been found to be promoted frequently during the manufacture process.

However, a degree of manual manipulation of the fibre-tows was required to maintain contact between the fibre-tows and the "turn" pins during pull-back. As discussed in "Future Work", further efforts will be necessary to achieve full automation.

7.2 Overall research outcomes

The novel composite-metal joint proposed in this work aimed to utilise the high tensile stiffness and strength of the composite's materials fibre reinforcement. The modelling tools developed to study the mechanical properties of the hybrid composite-metal joint and strut, predicted this was achievable, and resulted from the composite-metal connection initiated via pull-back of the fibre-tows around the pins. Moreover, performance improvements were expected against alternative composite-metal joining techniques, due to the more robust tow-metal connection established in the novel joining solution.

Manufacturability of the composite-metal joint was also assessed, and determined to be feasible using current, commercially available technologies. This was an important step to verifying the composite-metal joining concept, if joint fabrication is infeasible, then it becomes non-viable regardless of the theoretical performance gains.

In order to justify the use of composite materials in the strut's design, significant work must first be invested to improve and optimise joint design. Analyses in section 4.7 found that a fully metallic strut is approximately 32% of the weight of the hybrid strut, and 6 times stronger. Model limitations with regards to possible under-prediction of the strength (adhesive properties of the matrix-metal interface not included in the modelling framework) and over-estimation

of the weight of the hybrid strut (an overly thick composite), and improved properties of the scaled, physical size strut; may not account for this considerable difference. Additionally, the poor properties observed in the joint and strut following compression loads, must be considered in more detail, in order for the composite-metal joint developed in this thesis to be suitable for applications such as aircraft landing gear strut components.

7.3 Future Work

Joint optimisation

A formal optimisation of the hybrid composite-metal joint and strut should be conducted using the modelling tools developed in this thesis. The joint is considered optimal if failure occurs in all its constituents simultaneously, and at their ultimate failure loads. Making use of the reserve factors (stated in chapters 4 and 5) R_t, R_m, and R_{ma}, for the fibre-tows, matrix and metallic pins, respectively, this is equivalent to a joint in which $R_t = R_m = R_{ma} = 1$.

As found in chapters 4 and 5, strut and joint failure was predicted occur via pin failure. The tows were generally loaded to less 40% of their maximum tensile strength. Joint efficiency could therefore be improved by designing configurations in which pin stress is reduced and loading of the virtual tows increased. For example, pins with larger diameters could be used. However, the effect of increased spacing between the tows and decreased fibre volume content in the strut should also be noted.

Alternatively, pin shape could be considered. In chapters 5 and 6, areas of the end-fitting's surface directly underneath the pins were not covered by the fibre-tows. Pin shape could be altered to a "spear-head" or "tear drop" shape, which may increase the pin's cross-sectional area (and consequently reduce pin stress) and fill the under utilised regions of the end-fitting (and prevent resin rich regions from forming in these locations), whilst maintaining a smoothed, curved surface at the top of the pin contacting the fibre tow (and reducing the likelihood of fibre-breakage and stress concentrations resulting from tow pull-back).

Additional joint and strut parameters (section 3.3, such as end-fitting shape and pin angle (inclination) could also be considered as part of an optimisation strategy. The end-fitting in this work was assumed to be cylindrical, but for example, truncated (part-)cone shaped end-fittings would also be feasible. The mechanical interaction between the fibre-tows and the pins in the joint may be effected by alteration of the end-fitting shape. The pins were assumed to project orthogonally from the end-fitting's surface. Angled pins may consolidate the tows closer to the end-fitting's surface, thereby reduce bending moments about the pin base and alter load distribution across the pins.

Further exploitation of the model tool-set

There is scope for further exploitation of the modelling tools developed in this thesis to study the hybrid composite-metal joint and strut. For example, realistic descriptions of the fibre-tow geometries and internal architectures in the joint region, were obtained in chapter 5 through use of the Multi-Filament (MF) method. This tow description was then transferred to a mechanical model via the Single Filament Superposition (SFS) method (to overcome difficulties apparent with direct meshing of the MF tow geometries).

However, verification of the MF model from the manufacturing trials in chapter 6, found that tow geometries were not perfectly represented. The modelling approach could not predict the effect of the dynamic nature of the filament winding process, and non-uniformity of tow tension, on the final tow geometries. The SFS method could be employed as a "stand-alone" modelling technique, in which more realistic tow geometric dimensions are extracted directly from the physical strut and joint, via post-processing of μCT scan images following manufacturing trials. Although, the increased time and monetary cost associated with having to conduct separate manufacturing trials for each joint configuration, in order to obtain the necessary geometric data to inform construction of the SFS model, should be noted.

Strut and joint manufacture

To fully exploit the potential for the hybrid composite-metal joint proposed in this work, its manufacture must be fully automated and replicable. The mechanism, described in chapter 6, whereby layup of the fibre-tows in the region of the pin-structured end-fittings relied upon the tows slipping down the pin length to consolidate at the end-fitting's surface, was the primary practice requiring additional manual manipulation of the tows and inhibiting full automation. Future efforts should focus on the development of a custom filament winding machine and tow delivery apparatus, which is able to navigate the pin array and deposit the tows directly at the end-fittings surface.

Furthermore, chapter 6 considered only the manufacture of a dry-fibre prototype strut. Methods for matrix infiltration, curing and consolidation need to be considered for the manufacture of the final strut component. Attention must also be given to how the mandrel would be removed post-manufacture, or alternatively, the mechanics by which this structure would improve strut properties in compression, if it is left as a permanent part.

Finally, although significant damage to the fibre-tows, due to puncturing by the pins, was not observed during the manufacturing trials, as this type of manufacturing defect was largely prevented in the filament wound joint (in comparison to similar braided joints); no attempt was made to characterise and quantify possible micro-scale damage to the fibre reinforcement due to its manipulation (and relatively small turning radius) around the pins during pull-back. Future work should seek to study this phenomenon (if it occurs), determine if its contributes to significant fibre damage/breakage, and how the level of fibre damage may vary between joint

configurations. For example, the winding pattern and tow trajectory through the pin array as it transitions to the point of pull-back around the pins, and the number of pins around which tow pull-back is enacted, will effect the tow's turning radius and its degree of manipulation.

Once quantified, further work could be conducted to developed modelling capabilities in which this fibre damage, resulting from manufacture of the hybrid composite-metal joint and strut, is included prior to assessing mechanical properties of the joint and strut, and optimisation of the their designs.

Combined braiding/filament winding approach

As opposed to considering braided and filament wound surface-structured joints as "rival" solutions to integrating composite and metal efficiently, the possibility of combining these approaches should also be considered. Filament winding may provide the potential for both, increased joint stiffness and strength, and reduce manufacturing defects such as tow puncturing. However, braided/surface-structured joints have been used previously (as reviewed in chapter 2), improving the reliability and automation of manufacture process. Also, braiding may provide more uniform coverage of the mandrel's surface.

Therefore, a joint could exploit the advantages offered by both technologies by alternating between filament-wound and braided layers of fibre-tows. For example, the robust connection between the tows and pins could be established using the first few layers, with the outer layers being braided to increase mandrel coverage and perhaps provide improved consolidation. However, the associated increase in fabrication time and cost through use of the combined braided/filament wound approach would have to be considered.

Torsion applications

Finally, the joining solution examined in this could also be considered for applications to components that are subjected to torsional loads, such as drive-shafts for industries including automotive and rail. The connection established via tow pull-back around the pins should be equally robust in such cases. For example, the layup sequence for the mandrel could be altered to $[\pm 45]_3$, in order to improve joint properties in torsion. Moreover, the relatively poor properties observed for the strut and joint in compression, would be less significant in such applications.

References

[1] M. Thomas, P. Weaver, and S.R. Hallett.
Variable stiffness composite laminates for rotating pre-twisted plates.
ECCM 2016 -Proceeding of the 17th European Conference on Composite Materials, Munich, Germany, 26-30th June 2016, 2016.

[2] O. Volkersen.
Die nietkraftverteilung in zugbeanspruchten nietverbindungen mit konstanten laschenquerschnitten.
Luftfahrtfor schung, 15:41–47, 1938.

[3] S. Misri, M. R. Ishak, S. M. Sapuan, and Z. Leman.
Filament Winding Process for Kenaf Fibre Reinforced Polymer Composites, pages 369–383.
Springer International Publishing, Cham, 2015.

[4] M. Munro.
Review of manufacturing of fiber composite components by filament winding.
Polymer Composites, 9(5):352–359, October 1988.

[5] M.S. Babu, G. Srikanth, and S. Biswas.
Composite fabrication by filament winding-an insight.
Technology Information, Forecasting, and Assessment Council, 2007.

[6] X. Sun, L.F. Kawashita, T. Wollmann, S. Spitzer, A. Langkamp, and M. Gude.
Experimental and numerical studies on the braiding of carbon fibres over structured end-fittings for the design and manufacture of high performance hybrid shafts.
Production Engineering, 12(2):215–228, Apr 2018.

[7] F. Bianchi.
Numerical modelling of through-thickness reinforced structural joints, phd thesis, cranfield university.
2012.

[8] P.P. Camanho and F.L. Matthews.
Bonded metallic inserts for bolted joints in composite laminates.

Proceedings of the Institution of Mechanical Engineers, Part L: Journal of Materials: Design and Applications, 214(1):33–40, 2000.

[9] B. Kolesnikov, L. Herbeck, and A. Fink.
CFRP/titanium hybrid material for improving composite bolted joints.
Composite Structures, 83(4):368–380, June 2008.

[10] R. Matsuzaki, M. Shibata, and A. Todoroki.
Improving performance of GFRP/aluminum single lap joints using bolted/co-cured hybrid method.
Composites Part A: Applied Science and Manufacturing, 39(2):154–163, February 2008.

[11] S. Ucsnik, M. Scheerer, S. Zaremba, and D.H. Pahr.
Experimental investigation of a novel hybrid metal,Äìcomposite joining technology.
Composites Part A: Applied Science and Manufacturing, 41(3):369–374, March 2010.

[12] W. Xiong, B. Blackman, J.P. Dear, and X. Wang.
The effect of composite orientation on the mechanical properties of hybrid joints strengthened by surfi-sculpt.
Composite Structures, 134:587–592, 2015.

[13] Y. Wang and X. Sun.
Digital-element simulation of textile processes.
Composites Science and Technology, 61(2):311–319, February 2001.

[14] A. Thompson, B. El Said, J.P.H. Belnoue, and S.R. Hallett.
High fidelity numerical simulations of textile preform deformation.
In *Design, Manufacturing and Applications of Composites Tenth Workshop 2014: Proceedings of the Tenth Joint Canada-Japan Workshop on Composites, August 2014, Vancouver, Canada*, page 155. DEStech Publications, Inc, 2015.

[15] G. Zhou, X. Sun, and Y. Wang.
Multi-chain digital element analysis in textile mechanics.
Composites Science and Technology, 64(2):239–244, February 2004.

[16] L. Huang, Y. Wang, Y. Miao, D. Swenson, Y. Ma, and C-f. Yen.
Dynamic relaxation approach with periodic boundary conditions in determining the 3-D woven textile micro-geometry.
Composite Structures, 106:417–425, 2013.

[17] A.J. Thompson, B.El. Said, D. Ivanov, J. P-h. Belnoue, and S.R. Hallett.
International Journal of Solids and Structures High fidelity modelling of the compression behaviour of 2D woven fabrics.

International Journal of Solids and Structures, 154:104–113, 2018.

[18] N. Naouar, E. Vidal-Salle, J. Schneider, E. Maire, and P. Boisse.
3d composite reinforcement meso fe analyses based on x-ray computed tomography.
Composite Structures, 132:1094–1104, 2015.

[19] Safran landing systems, https://www.safran-landing-systems.com.

[20] S.T. Peters, W.D. Humphrey, and R.F. Foral.
Filament winding-composite structure fabrication.
1991.

[21] P. Mertiny and F. Ellyin.
Influence of the filament winding tension on physical and mechanical properties of reinforced composites.
Composites Part A: Applied Science and Manufacturing, 33(12):1615–1622, 2002.

[22] F.H. Abdalla, S.A. Mutasher, Y.A. Khalid, S.M. Sapuan, A.M.S. Hamouda, B.B. Sahari, and M.M. Hamdan.
Design and fabrication of low cost filament winding machine.
Materials & design, 28(1):234–239, 2007.

[23] S. Koussios, O.K. Bergsma, and A. Beukers.
Filament winding. Part 1: determination of the wound body related parameters.
Composites Part A: Applied Science and Manufacturing, 35(2):181–195, February 2004.

[24] V.V. Vasiliev, A.A. Krikanov, and A.F. Razin.
New generation of filament-wound composite pressure vessels for commercial applications.
Composite structures, 62(3-4):449–459, 2003.

[25] C-C. Liang, H-W. Chen, and C-H. Wang.
Optimum design of dome contour for filament-wound composite pressure vessels based on a shape factor.
Composite structures, 58(4):469–482, 2002.

[26] K. Bilisik.
Three-dimensional braiding for composites: a review.
Textile Research Journal, 83(13):1414–1436, 2013.

[27] Y. Kyosev.
Braiding technology for textiles: Principles, design and processes.
Elsevier, 2014.

[28] M. Munro and A. Fahim.
A Comparison of Helical Filament Winding and 2D Braiding of Fiber Reinforced Polymeric Components.
6914(February), 1995.

[29] P. Potluri, A. Rawal, M. Rivaldi, and I. Porat.
Geometrical modelling and control of a triaxial braiding machine for producing 3d preforms.
Composites Part A: Applied Science and Manufacturing, 34(6):481–492, 2003.

[30] J Paulo Davim, Pedro Reis, and C Conceicao Antonio.
Experimental study of drilling glass fiber reinforced plastics (gfrp) manufactured by hand lay-up.
Composites Science and Technology, 64(2):289–297, 2004.

[31] G. Caprino and V. Tagliaferri.
Damage development in drilling glass fibre reinforced plastics.
International Journal of Machine Tools and Manufacture, 35(6):817–829, 1995.

[32] J. Babu, T. Sunny, N.A. Paul, K.P. Mohan, J. Philip, and J.P. Davim.
Assessment of delamination in composite materials: a review.
Proceedings of the Institution of Mechanical Engineers, Part B: Journal of Engineering Manufacture, 230(11):1990–2003, 2016.

[33] P.P. Camanho and F.L. Matthews.
Stress analysis and strength prediction of mechanically fastened joints in FRP: a review.
Composites Part A: Applied Science and Manufacturing, 28(6):529–547, January 1997.

[34] E. Persson.
Fatigue of multiple-row bolted joints in carbon/epoxy laminates: ranking of factors affecting strength and fatigue life.
International Journal of Fatigue, 21(4):337–353, April 1999.

[35] P.P. Camanho, S. Bowron, and F.L. Matthews.
Failure mechanisms in bolted cfrp.
Journal of Reinforced Plastics and Composites, 17(3):205–233, 1998.

[36] P.J. Herrera-franco and G.L. Cloud.
Strain-Relief Inserts for Composite Fasteners -An Experimental Study.
(5):751–768, 1991.

[37] P.P. Camanho, A. Fink, A. Obst, and S. Pimenta.
Hybrid titanium‚ÄìCFRP laminates for high-performance bolted joints.
Composites Part A: Applied Science and Manufacturing, 40(12):1826–1837, December 2009.

[38] L.J. Hart-Smith.
Joints, adhesive-bonded single-lap, douglas aircraft co.
NASA Langley Report CR, 112236, 1973.

[39] I.A. Ashcroft, M.M.A. Wahab, A.D. Crocomb, D.J. Hughes, and S.J. Shaw.
The effect of environment on the fatigue of bonded composite joints. Part 1: testing and fractography.
Composites Part A: Applied Science and Manufacturing, 32(1):45–58, January 2001.

[40] F.L. Matthews, P.F. Kilty, and E.W. Godwin.
A review of the strength of joints in fibre-reinforced plastics. part 2. adhesively bonded joints.
Composites, 13(1):29–37, 1982.

[41] M.D. Banea and L.F.M. da Silva.
Adhesively bonded joints in composite materials: an overview.
Proceedings of the Institution of Mechanical Engineers, Part L: Journal of Materials: Design and Applications, 223(1):1–18, January 2009.

[42] K.W. Allen.
"at forty cometh understanding": A review of some basics of adhesion over the past four decades.
International journal of adhesion and adhesives, 23(2):87–93, 2003.

[43] L.F.M. Da Silva and R.D. Adams.
Techniques to reduce the peel stresses in adhesive joints with composites.
International Journal of Adhesion and Adhesives, 27(3):227–235, 2007.

[44] A.P. Mouritz, M.K. Bannister, P.J. Falzon, and K.H. Leong.
Review of applications for advanced three-dimensional fibre textile composites.
Composites Part A: Applied Science and Manufacturing, 30(12):1445–1461, December 1999.

[45] A.P. Mouritz.
Review of z-pinned composite laminates.
Composites Part A: Applied Science and Manufacturing, 38(12):2383–2397, December 2007.

[46] D.D.R. Cartié, B.N. Cox, and N.A. Fleck.
Mechanisms of crack bridging by composite and metallic rods.
Composites Part A: Applied Science and Manufacturing, 35(11):1325–1336, 2004.

[47] L.J. Hart-Smith.
Bonded-bolted composite joints.
Journal of Aircraft, 22(11):993–1000, 1985.

[48] G. Kelly.
Load transfer in hybrid (bonded/bolted) composite single-lap joints.
Composite Structures, 69(1):35–43, June 2005.

[49] G. Kelly.
Quasi-static strength and fatigue life of hybrid (bonded/bolted) composite single-lap joints.
Composite Structures, 72(1):119–129, January 2006.

[50] R.W. Messler.
Joining Composite Materials and Structures: Some Thought-Provoking Possibilities.
Journal of Thermoplastic Composite Materials, 17(1):51–75, January 2004.

[51] W. Meiners, K. Wissenbach, and R. Poprawe.
Direct selective laser sintering of steel powder.
In *Proceedings of the LANE*, volume 97, pages 615–622, 1997.

[52] C. Over, W. Meiners, K. Wissenbach, M. Lindemann, and J. Hutfless.
Laser melting: a new approach for the direct manufacturing of metal parts and tools.
Proceedings of the Euro-uRapid, 2002.

[53] B.G.I. Dance and A.L. Buxton.
An introduction to surfi-sculpt technology–new opportunities, new challenges.
In *Proceedings of the 7th International Conference on Beam Technology*, pages 75–84, 2007.

[54] A. Schierl.
The cmt process a revolution in welding technology.
Welding in the world-London-, 49(I):38, 2005.

[55] A.T.T. Nguyen, M. Brandt, A.C. Orifici, and S. Feih.
Hierarchical surface features for improved bonding and fracture toughness of metal–metal and metal–composite bonded joints.
International Journal of Adhesion and Adhesives, 66:81–92, 2016.

[56] K. Cinar, N. Ersoy, and M.A. Unal.
Design of a real-sized composite drive shaft and critical points from beginning to end.
ECCM18 - 18th European Conference on Composite Materials Athens, Greece, 24-28th June 2018, Athens, Greece, 24-28 June 2018, 2018.

[57] M. Gude, F. Lenz, A. Gruhl, B. Witschel, A. Ulbricht, and W. Hufenbach.
Design and automated manufacturing of profiled composite driveshafts.
Science and engineering of composite materials, 22(2):187–197, 2015.

[58] H.S. Kim, J.W. Kim, and J.K. Kim.

Design and manufacture of an automotive hybrid aluminum/composite drive shaft. *Composite structures*, 63(1):87–99, 2004.

[59] Teufelberger composite ges.m.b.h. vogelweiderstr. 50, 4600 wels, austria.

[60] L.F.M. Da Silva, P.J.C. das Neves, R.D. Adams, and J.K. Spelt.
Analytical models of adhesively bonded joints‚Äîpart i: Literature survey.
International Journal of Adhesion and Adhesives, 29(3):319–330, 2009.

[61] L.F.M. Da Silva, P.J.C. das Neves, R.D. Adams, A. Wang, and J.K. Spelt.
Analytical models of adhesively bonded joints‚Äîpart ii: Comparative study.
International Journal of Adhesion and Adhesives, 29(3):331–341, 2009.

[62] Araldite.
Araldite 2015 technical datasheet, 2015.

[63] R. M. Jones and C. W. Bert.
Mechanics of Composite Materials.
Journal of Applied Mechanics, 42:748, 1975.

[64] A.W. Blom, B.F. Tatting, J.M.A.M. Hol, and Z. Gürdal.
Fiber path definitions for elastically tailored conical shells.
Composites Part B: Engineering, 40(1):77–84, January 2009.

[65] A. Mahmood, X. Wang, and C. Zhou.
Elastic analysis of 3d woven orthogonal composites.
Grey Systems: Theory and Application, 1(3):228–239, 2011.

[66] C.C. Chamis.
Mechanics of composite materials: past, present, and future.
Journal of Composites, Technology and Research, 11(1):3–14, 1989.

[67] M.H. Sadd.
Elasticity: theory, applications, and numerics.
Academic Press, 2009.

[68] Abaqus.
Abaqus 6.11.
Dassault Systemes Simulia Corp Providence, RI, USA, 2011.

[69] S.D. Green, M.Y. Matveev, A.C. Long, D. Ivanov, and S.R. Hallett.
Mechanical modelling of 3D woven composites considering realistic unit cell geometry.
Composite Structures, 118:284–293, December 2014.

[70] S. Palanivelu, W. Van Paepegem, J. Degrieck, J. Van Ackeren, D. Kakogiannis, D. Van Hemelrijck, J. Wastiels, and J. Vantomme.
Experimental study on the axial crushing behaviour of pultruded composite tubes.
Polymer testing, 29(2):224–234, 2010.

[71] S. Palanivelu, W. Van Paepegem, J. Degrieck, D. Kakogiannis, J. Van Ackeren, D. Van Hemelrijck, J. Wastiels, and J. Vantomme.
Parametric study of crushing parameters and failure patterns of pultruded composite tubes using cohesive elements and seam, part i: Central delamination and triggering modelling.
Polymer Testing, 29(6):729–741, 2010.

[72] A.W. Blom, P.B. Stickler, and Z. Gürdal.
Optimization of a composite cylinder under bending by tailoring stiffness properties in circumferential direction.
Composites Part B: Engineering, 41(2):157–165, March 2010.

[73] A.W. Blom, P. Stickler, M. Rassaian, and Z. Gürdal.
Bending test of a variable-stiffness fiber reinforced composite cylinder.
In *51st AIAA/ASME/ASCE/AHS/ASC Structures, Structural Dynamics, and Materials Conference 18th AIAA/ASME/AHS Adaptive Structures Conference 12th*, page 2600, 2010.

[74] E.J. Barbero.
Finite Element Analysis of Composite Materials Using Abaqus.
CRC press, 2013.

[75] Livermore Software Technology Corporation.
Ls-dyna keyword user's manual.
2015.

[76] G. Farin.
Curves and surfaces for computer-aided geometric design: a practical guide.
Elsevier, 2014.

[77] Y. Mahadik and S.R. Hallett.
Finite element modelling of tow geometry in 3D woven fabrics.
Composites Part A: Applied Science and Manufacturing, 41(9):1192–1200, September 2010.

[78] N. Isart, B. El Said, D.S. Ivanov, S.R. Hallett, J.A. Mayugo, and B.N.
Internal geometric modelling of 3d woven composites: A comparison between different approaches.
Composite Structures, 132:1219–1230, 2015.

[79] N. Naouar, E. Vidal-Sallé, J. Schneider, E. Maire, and P. Boisse.
Meso-scale fe analyses of textile composite reinforcement deformation based on x-ray computed tomography.
Composite structures, 116:165–176, 2014.

[80] P. Potluri and T.V. Sagar.
Compaction modelling of textile preforms for composite structures.
Composite structures, 86(1-3):177–185, 2008.

[81] S.V. Lomov, G. Huysmans, Y. Luo, R.S. Parnas, A. Prodromou, I. Verpoest, and F.R. Phelan.
Textile composites: modelling strategies.
Composites Part A: applied science and manufacturing, 32(10):1379–1394, 2001.

[82] M. Sherburn.
Geometric and mechanical modelling of textiles.
PhD thesis, University of Nottingham, 2007.

[83] J.J. Crookston, S. Kari, N.A. Warrior, I.A. Jones, and A.C. Long.
3d textile composite mechanical properties prediction using automated fea of the unit cell.
In *Proc. of the 16th Int. Conf. on Composite Materials*, pages 1–7, 2007.

[84] F. Stig and S. Hallström.
A modelling framework for composites containing 3d reinforcement.
Composite Structures, 94(9):2895–2901, 2012.

[85] H.J. Kim and C.C. Swan.
Voxel-based meshing and unit-cell analysis of textile composites.
International Journal for Numerical Methods in Engineering, 56(7):977–1006, February 2003.

[86] B. El Said, D. Ivanov, A.C. Long, and S.R. Hallett.
Multi-scale modelling of strongly heterogeneous 3d composite structures using spatial voronoi tessellation.
Journal of the Mechanics and Physics of Solids, 88:50–71, 2016.

[87] I. Verpoest and S.V. Lomov.
Virtual textile composites software wisetex: Integration with micro-mechanical, permeability and structural analysis.
Composites Science and Technology, 65(15-16):2563–2574, 2005.

[88] E. Potter, S.T. Pinho, P. Robinson, L. Iannucci, and A.J. McMillan.
Mesh generation and geometrical modelling of 3d woven composites with variable tow cross-sections.

Computational Materials Science, 51(1):103–111, 2012.

[89] W-G. Jiang, S.R. Hallett, and M.R. Wisnom.
Development of domain superposition technique for the modelling of woven fabric composites.
In *Mechanical response of composites*, pages 281–291. Springer, 2008.

[90] S.A. Tabatabaei, S.V. Lomov, and I. Verpoest.
Assessment of embedded element technique in meso-fe modelling of fibre reinforced composites.
Composite Structures, 107:436–446, 2014.

[91] D. Carlsson.
Arbitrary lagrangian-eulerian simulations of a pressure pulse inside a flexible porous fabric bag.
Chalmers university of technology, 2014.

[92] L. Moutoussamy, G. Herve, and F. Barbier.
Qualification of* constrained_lagrange_in_solid command for steel/concrete interface modeling.
In *Proceedings of the 8 th European LS-Dyna Conference, USA*, 2011.

[93] Z. Wu.
Three-dimensional exact modeling of geometric and mechanical properties of woven composites.
Acta Mechanica Solida Sinica, 22(5):479–486, 2009.

[94] S. Buchanan, A. Grigorash, J.P. Quinn, A.T. McIlhagger, and C. Young.
Modelling the geometry of the repeat unit cell of three-dimensional weave architectures.
The Journal of The Textile Institute, 101(7):679–685, 2010.

[95] J. Quinn, R. McIlhagger, and A.T. McIlhagger.
A modified system for design and analysis of 3d woven preforms.
Composites Part A: applied science and manufacturing, 34(6):503–509, 2003.

[96] MSC Patran.
User's guide-msc.
Software Corporation, 2013.

[97] J.H. Maker, R. Grimes, and J. Day.
Introduction to ls-dyna® implicit.
2007.

[98] J.W.G. Treiber.
Performance of tufted carbin fibre/epoxy composites.
2011.

[99] Y. Gofman.
Outline of a set of points.
Pattern recognition letters, 14(1):31–38, 1993.

[100] S.D. Green, A.C. Long, B.S.F. El Said, and S.R. Hallett.
Numerical modelling of 3D woven preform deformations.
Composite Structures, 108:747–756, February 2014.

[101] P. Sorbo, J. Girardot, F. Dau, and I. Iordanoff.
Numerical investigations on a yarn structure at the microscale towards scale transition.
Composite Structures, 183:489–498, 2018.

[102] A. Rawal, P. Potluri, and C. Steele.
Geometrical modeling of the yarn paths in three-dimensional braided structures.
Journal of Industrial Textiles, 35(2):115–135, 2005.

[103] Ultimaker.
Cura 3d printing slicing software.
2012.

[104] X-winder 4.0, ohio, usa.

[105] J-W. Kim, G. Sauti, R.J. Cano, R.A. Wincheski, J.G. Ratcliffe, M. Czabaj, N.W. Gardner, and E.J. Siochi.
Assessment of carbon nanotube yarns as reinforcement for composite overwrapped pressure vessels.
Composites Part A: Applied Science and Manufacturing, 84:256–265, 2016.

APPENDIX A

APPENDIX

A.1 Tow size

The cross-section dimensions of a physical carbon fibre tow can be approximated using the dimensions of its constituent fibres. The cross-sectional area of a single carbon fibre, A_f, is firstly found using the known fibre diameter, $D_f = 7e-3$mm. By considering the tow as a "perfect" bundle of aligned fibres, a theoretical tow cross-sectional area of (A_t) can be taken as the product of the individual fibre area, and the number of fibres in the tow (N_f), as shown in equation A.1.

$$\begin{aligned} A_f &= \pi(\frac{D_f}{2})^2 \\ A_t &= N_f A_f \\ D_t &= 2\sqrt{\frac{A_t}{\pi}} \end{aligned} \tag{A.1}$$

A.2 Tow cross-section (for layup thickness in chapter 3)

In chapter 3, appropriate values for the tow height (T_t) and width were required to determine an approximate thickness for each filament wound layer (which was then considered equivalent to lamina thickness in section 3.5), and to assess tow coverage of the mandrel's surface (section 3.6), respectively. These were determined by firstly adjusting the "perfect" tow cross-section area for the assumed intra-tow fibre volume fraction of 70%, to give an "actual" tow cross-section area, $\overline{A}_t$.

$$\begin{aligned} \overline{A}_t &= \frac{1}{V_f} A_t \\ T_t &= \frac{\overline{A}_t}{2\pi} \end{aligned} \tag{A.2}$$

The virtual tow was assumed to have an elliptical cross-section, and a nominal major-axis length was assigned for the tow width. For the 12k carbon fibre tow (i.e. $N_f = 12{,}000$) utilised in this work, a tow width of 2mm was used. The minor axis length (of 0.42mm) can then be calculated from $\overline{A}_t$, as shown in equation A.2.

A.3 Tow cross-section (for SF and MF joint model in chapter 5)

In chapter 5, the virtual tow was represented as a bundle of virtual fibres arrayed in an initial configuration of a circular-patterned cross-section. The cross-sectional area of each virtual fibre was calculated from the "perfect" tow cross-section area (A_t) divided by the number of virtual fibres (N_{vf}) used for virtual tow. The diameter of the virtual fibres (D_{vf}) could then be found accordingly.

The diameter of minimum bounding circle that enclosed the virtual fibre bundle, was then used for the cross-section of the Single-Filament (SF) tow in stage 1 of the full joint forming simulation in section 5.4.1. This minimised inter-penetrations between virtual tows once converted to a Multi-Filament (MF) representation in the second stage of the full-joint forming simulation 5.4.2.

$$\begin{aligned} A_{vf} &= \frac{A_t}{N_{vf}} \\ D_{vf} &= 2\sqrt{\frac{A_{vf}}{\pi}} \end{aligned} \tag{A.3}$$

A.4 Layup sequences 1-10

Table A.1: Unaltered layup sequences on the mandrel vs altered layup sequences (to prevent tow puncturing).

Layup No.	Unaltered sequence $[\theta_1/.../\theta_6]$	Altered sequence $[\theta_{1d}/\theta_{1u}/.../\theta_{6d}/\theta_{6u}]$	Relative imbalance
1	$[0]_6$	$[-3.55/0]_3$	1
2	$[\mp 5/0_2/\pm 5]$	$[-7.06/-3.55/0/3.55/-3.55/0]_s$	1.99
3	$[\mp 10/0_2/\pm 10]$	$[-13.92/-10.53/7.06/10.53/-3.55/0]_s$	1.95
4	$[\mp 15/0_2/\pm 15]$	$[-17.21/-13.92/10.53/13.92/-3.55/0]_s$	1.92
5	$[\mp 20/0_2/\pm 20]$	$[-23.45/-20.39/17.21/20.39/-3.55/0]_s$	1.84
6	$[\mp 25/0_2/\pm 25]$	$[-29.15/-26.37/23.45/26.37/-3.55/0]_s$	1.74
7	$[\mp 30/0_2/\pm 30]$	$[-31.78/-29.15/26.37/29.15/-3.55/0]_s$	1.68
8	$[\mp 35/0_2/\pm 35]$	$[-36.63/-34.28/31.78/34.28/-3.55/0]_s$	1.58
9	$[\mp 40/0_2/\pm 40]$	$[-42.91/-40.94/38.85/40.94/-3.55/0]_s$	1.43
10	$[\mp 45/0_2/\pm 45]$	$[-46.49/-44.75/42.91/44.75/-3.55/0]_s$	1.39

A.5 Accuracy of linear fit for extrapolation of strut and joint stiffness

Table A.2: Assessment of the accuracy of extrapolation provided by linear fitting of the Force vs Strain curve using the root-mean-square error. Lower values indicate improved reliability of the linear fit.

	Root-mean-square error
Strut Configuration (section 4.6.1)	
A	0.9892
B	0.9237
C	0.9220
D	0.9878
E	0.9885
Joint Type (section 5.9.3)	
A	0.9876
E	0.9790
Braid	0.9640

A.6 G-code for 2nd filament wound layer in manufacturing trials

[G-CODE GENERATED BY Jordan Jones on 27.Feb.2019]
[FileName Layer2.X2G]
[INITIALISE WINDING SESSION]
C C0
G20
G90
X X4.200 T4 Z0.79 Y5.04
[ENABLE STEP MOTORS AND HOME]
M17
G1 I10 J10 K10 N10 O10 T10
G28 E0.10 R4 F0.98 C-84.01
G4 P10000
G1 J1.250 K1.250 O1.250 T10
G4 Z P10000
G1 F0.98 Z3.78
G1 E0.20 Y1.30
G1 R3.00 B0.00
[BEGIN WINDING]
M0
M601
G1 F0.12 Z2.83 R-1.35 B-65.00 S0.63 C30.00 A30.00
G1 F0.12 Z2.36 S0.63 C15.00 A45.00
G1 F0.12 Z2.83 R5.42 B65.00 S0.63 C15.00 A60.00
G1 F0.12 Z3.78 S0.63 C30.00 A90.00
G1 F0.98 Z11.97 S3.00 C150.00 A240.00
G1 F0.12 Z12.91 S0.63 C30.00 A270.00
G1 F0.12 Z13.39 S0.63 C15.00 A285.00
G1 F0.12 Z12.91 R5.42 B-65.00 S0.63 C15.00 A300.00
G1 F0.12 Z11.97 S0.63 C30.00 A330.00
G1 F0.98 Z3.78 S3.00 C150.00 A480.00
M0
M601
G1 F0.12 Z2.83 R-1.35 B-65.00 S0.63 C30.00 A510.00
G1 F0.12 Z2.36 S0.63 C15.00 A525.00
G1 F0.12 Z2.83 R5.42 B65.00 S0.63 C15.00 A540.00

G1 F0.12 Z3.78 S0.63 C30.00 A570.00
G1 F0.98 Z11.97 S3.00 C150.00 A720.00
G1 F0.12 Z12.91 S0.63 C30.00 A750.00
G1 F0.12 Z13.39 S0.63 C15.00 A765.00
G1 F0.12 Z12.91 R5.42 B-65.00 S0.63 C15.00 A780.00
G1 F0.12 Z11.97 S0.63 C30.00 A810.00
G1 F0.98 Z3.78 S3.00 C150.00 A960.00
M0
M601
G1 F0.12 Z2.83 R-1.35 B-65.00 S0.63 C30.00 A990.00
G1 F0.12 Z2.36 S0.63 C15.00 A1005.00
G1 F0.12 Z2.83 R5.42 B65.00 S0.63 C15.00 A1020.00
G1 F0.12 Z3.78 S0.63 C30.00 A1050.00
G1 F0.98 Z11.97 S3.00 C150.00 A1200.00
G1 F0.12 Z12.91 S0.63 C30.00 A1230.00
G1 F0.12 Z13.39 S0.63 C15.00 A1245.00
G1 F0.12 Z12.91 R5.42 B-65.00 S0.63 C15.00 A1260.00
G1 F0.12 Z11.97 S0.63 C30.00 A1290.00
G1 F0.98 Z3.78 S3.00 C150.00 A1440.00
G1 S0.50 C15.00 A1455.00
M0
M601
G1 F0.12 Z2.83 R-1.35 B-65.00 S0.63 C30.00 A1485.00
G1 F0.12 Z2.36 S0.63 C15.00 A1500.00
G1 F0.12 Z2.83 R5.42 B65.00 S0.63 C15.00 A1515.00
G1 F0.12 Z3.78 S0.63 C30.00 A1545.00
G1 F0.98 Z11.97 S3.00 C150.00 A1695.00
G1 F0.12 Z12.91 S0.63 C30.00 A1725.00
G1 F0.12 Z13.39 S0.63 C15.00 A1740.00
G1 F0.12 Z12.91 R5.42 B-65.00 S0.63 C15.00 A1755.00
G1 F0.12 Z11.97 S0.63 C30.00 A1785.00
G1 F0.98 Z3.78 S3.00 C150.00 A1935.00
M0
M601
G1 F0.12 Z2.83 R-1.35 B-65.00 S0.63 C30.00 A1965.00
G1 F0.12 Z2.36 S0.63 C15.00 A1980.00
G1 F0.12 Z2.83 R5.42 B65.00 S0.63 C15.00 A1995.00
G1 F0.12 Z3.78 S0.63 C30.00 A2025.00

G1 F0.98 Z11.97 S3.00 C150.00 A2175.00
G1 F0.12 Z12.91 S0.63 C30.00 A2205.00
G1 F0.12 Z13.39 S0.63 C15.00 A2220.00
G1 F0.12 Z12.91 R5.42 B-65.00 S0.63 C15.00 A2235.00
G1 F0.12 Z11.97 S0.63 C30.00 A2265.00
G1 F0.98 Z3.78 S3.00 C150.00 A2415.00
M0
M601
G1 F0.12 Z2.83 R-1.35 B-65.00 S0.63 C30.00 A2445.00
G1 F0.12 Z2.36 S0.63 C15.00 A2460.00
G1 F0.12 Z2.83 R5.42 B65.00 S0.63 C15.00 A2475.00
G1 F0.12 Z3.78 S0.63 C30.00 A2505.00
G1 F0.98 Z11.97 S3.00 C150.00 A2655.00
G1 F0.12 Z12.91 S0.63 C30.00 A2685.00
G1 F0.12 Z13.39 S0.63 C15.00 A2700.00
G1 F0.12 Z12.91 R5.42 B-65.00 S0.63 C15.00 A2715.00
G1 F0.12 Z11.97 S0.63 C30.00 A2745.00
G1 F0.98 Z3.78 S3.00 C150.00 A2895.00
G1 S0.50 C15.00 A2910.00
M0
M601
G1 F0.12 Z2.83 R-1.35 B-65.00 S0.63 C30.00 A2940.00
G1 F0.12 Z2.36 S0.63 C15.00 A2955.00
G1 F0.12 Z2.83 R5.42 B65.00 S0.63 C15.00 A2970.00
G1 F0.12 Z3.78 S0.63 C30.00 A3000.00
G1 F0.98 Z11.97 S3.00 C150.00 A3150.00
G1 F0.12 Z12.91 S0.63 C30.00 A3180.00
G1 F0.12 Z13.39 S0.63 C15.00 A3195.00
G1 F0.12 Z12.91 R5.42 B-65.00 S0.63 C15.00 A3210.00
G1 F0.12 Z11.97 S0.63 C30.00 A3240.00
G1 F0.98 Z3.78 S3.00 C150.00 A3390.00
M0
M601
G1 F0.12 Z2.83 R-1.35 B-65.00 S0.63 C30.00 A3420.00
G1 F0.12 Z2.36 S0.63 C15.00 A3435.00
G1 F0.12 Z2.83 R5.42 B65.00 S0.63 C15.00 A3450.00
G1 F0.12 Z3.78 S0.63 C30.00 A3480.00
G1 F0.98 Z11.97 S3.00 C150.00 A3630.00

G1 F0.12 Z12.91 S0.63 C30.00 A3660.00
G1 F0.12 Z13.39 S0.63 C15.00 A3675.00
G1 F0.12 Z12.91 R5.42 B-65.00 S0.63 C15.00 A3690.00
G1 F0.12 Z11.97 S0.63 C30.00 A3720.00
G1 F0.98 Z3.78 S3.00 C150.00 A3870.00
M0
M601
G1 F0.12 Z2.83 R-1.35 B-65.00 S0.63 C30.00 A3900.00
G1 F0.12 Z2.36 S0.63 C15.00 A3915.00
G1 F0.12 Z2.83 R5.42 B65.00 S0.63 C15.00 A3930.00
G1 F0.12 Z3.78 S0.63 C30.00 A3960.00
G1 F0.98 Z11.97 S3.00 C150.00 A4110.00
G1 F0.12 Z12.91 S0.63 C30.00 A4140.00
G1 F0.12 Z13.39 S0.63 C15.00 A4155.00
G1 F0.12 Z12.91 R5.42 B-65.00 S0.63 C15.00 A4170.00
G1 F0.12 Z11.97 S0.63 C30.00 A4200.00
G1 F0.98 Z3.78 S3.00 C150.00 A4350.00
G1 S0.50 C15.00 A4365.00
M0
M601
G1 F0.12 Z2.83 R-1.35 B-65.00 S0.63 C30.00 A4395.00
G1 F0.12 Z2.36 S0.63 C15.00 A4410.00
G1 F0.12 Z2.83 R5.42 B65.00 S0.63 C15.00 A4425.00
G1 F0.12 Z3.78 S0.63 C30.00 A4455.00
G1 F0.98 Z11.97 S3.00 C150.00 A4605.00
G1 F0.12 Z12.91 S0.63 C30.00 A4635.00
G1 F0.12 Z13.39 S0.63 C15.00 A4650.00
G1 F0.12 Z12.91 R5.42 B-65.00 S0.63 C15.00 A4665.00
G1 F0.12 Z11.97 S0.63 C30.00 A4695.00
G1 F0.98 Z3.78 S3.00 C150.00 A4845.00
M0
M601
G1 F0.12 Z2.83 R-1.35 B-65.00 S0.63 C30.00 A4875.00
G1 F0.12 Z2.36 S0.63 C15.00 A4890.00
G1 F0.12 Z2.83 R5.42 B65.00 S0.63 C15.00 A4905.00
G1 F0.12 Z3.78 S0.63 C30.00 A4935.00
G1 F0.98 Z11.97 S3.00 C150.00 A5085.00
G1 F0.12 Z12.91 S0.63 C30.00 A5115.00

G1 F0.12 Z13.39 S0.63 C15.00 A5130.00
G1 F0.12 Z12.91 R5.42 B-65.00 S0.63 C15.00 A5145.00
G1 F0.12 Z11.97 S0.63 C30.00 A5175.00
G1 F0.98 Z3.78 S3.00 C150.00 A5325.00
M0
M601
G1 F0.12 Z2.83 R-1.35 B-65.00 S0.63 C30.00 A5355.00
G1 F0.12 Z2.36 S0.63 C15.00 A5370.00
G1 F0.12 Z2.83 R5.42 B65.00 S0.63 C15.00 A5385.00
G1 F0.12 Z3.78 S0.63 C30.00 A5415.00
G1 F0.98 Z11.97 S3.00 C150.00 A5565.00
G1 F0.12 Z12.91 S0.63 C30.00 A5595.00
G1 F0.12 Z13.39 S0.63 C15.00 A5610.00
G1 F0.12 Z12.91 R5.42 B-65.00 S0.63 C15.00 A5625.00
G1 F0.12 Z11.97 S0.63 C30.00 A5655.00
G1 F0.98 Z3.78 S3.00 C150.00 A5805.00
G1 S0.50 C15.00 A5820.00
M0
M601
G1 F0.12 Z2.83 R-1.35 B-65.00 S0.63 C30.00 A5850.00
G1 F0.12 Z2.36 S0.63 C15.00 A5865.00
G1 F0.12 Z2.83 R5.42 B65.00 S0.63 C15.00 A5880.00
G1 F0.12 Z3.78 S0.63 C30.00 A5910.00
G1 F0.98 Z11.97 S3.00 C150.00 A6060.00
G1 F0.12 Z12.91 S0.63 C30.00 A6090.00
G1 F0.12 Z13.39 S0.63 C15.00 A6105.00
G1 F0.12 Z12.91 R5.42 B-65.00 S0.63 C15.00 A6120.00
G1 F0.12 Z11.97 S0.63 C30.00 A6150.00
G1 F0.98 Z3.78 S3.00 C150.00 A6300.00
M0
M601
G1 F0.12 Z2.83 R-1.35 B-65.00 S0.63 C30.00 A6330.00
G1 F0.12 Z2.36 S0.63 C15.00 A6345.00
G1 F0.12 Z2.83 R5.42 B65.00 S0.63 C15.00 A6360.00
G1 F0.12 Z3.78 S0.63 C30.00 A6390.00
G1 F0.98 Z11.97 S3.00 C150.00 A6540.00
G1 F0.12 Z12.91 S0.63 C30.00 A6570.00
G1 F0.12 Z13.39 S0.63 C15.00 A6585.00

G1 F0.12 Z12.91 R5.42 B-65.00 S0.63 C15.00 A6600.00
G1 F0.12 Z11.97 S0.63 C30.00 A6630.00
G1 F0.98 Z3.78 S3.00 C150.00 A6780.00
M0
M601
G1 F0.12 Z2.83 R-1.35 B-65.00 S0.63 C30.00 A6810.00
G1 F0.12 Z2.36 S0.63 C15.00 A6825.00
G1 F0.12 Z2.83 R5.42 B65.00 S0.63 C15.00 A6840.00
G1 F0.12 Z3.78 S0.63 C30.00 A6870.00
G1 F0.98 Z11.97 S3.00 C150.00 A7020.00
G1 F0.12 Z12.91 S0.63 C30.00 A7050.00
G1 F0.12 Z13.39 S0.63 C15.00 A7065.00
G1 F0.12 Z12.91 R5.42 B-65.00 S0.63 C15.00 A7080.00
G1 F0.12 Z11.97 S0.63 C30.00 A7110.00
G1 F0.98 Z3.78 S3.00 C150.00 A7260.00
G1 S0.50 C15.00 A7275.00
M0
M601
G1 F0.12 Z2.83 R-1.35 B-65.00 S0.63 C30.00 A7305.00
G1 F0.12 Z2.36 S0.63 C15.00 A7320.00
G1 F0.12 Z2.83 R5.42 B65.00 S0.63 C15.00 A7335.00
G1 F0.12 Z3.78 S0.63 C30.00 A7365.00
G1 F0.98 Z11.97 S3.00 C150.00 A7515.00
G1 F0.12 Z12.91 S0.63 C30.00 A7545.00
G1 F0.12 Z13.39 S0.63 C15.00 A7560.00
G1 F0.12 Z12.91 R5.42 B-65.00 S0.63 C15.00 A7575.00
G1 F0.12 Z11.97 S0.63 C30.00 A7605.00
G1 F0.98 Z3.78 S3.00 C150.00 A7755.00
M0
M601
G1 F0.12 Z2.83 R-1.35 B-65.00 S0.63 C30.00 A7785.00
G1 F0.12 Z2.36 S0.63 C15.00 A7800.00
G1 F0.12 Z2.83 R5.42 B65.00 S0.63 C15.00 A7815.00
G1 F0.12 Z3.78 S0.63 C30.00 A7845.00
G1 F0.98 Z11.97 S3.00 C150.00 A7995.00
G1 F0.12 Z12.91 S0.63 C30.00 A8025.00
G1 F0.12 Z13.39 S0.63 C15.00 A8040.00
G1 F0.12 Z12.91 R5.42 B-65.00 S0.63 C15.00 A8055.00

G1 F0.12 Z11.97 S0.63 C30.00 A8085.00
G1 F0.98 Z3.78 S3.00 C150.00 A8235.00
M0
M601
G1 F0.12 Z2.83 R-1.35 B-65.00 S0.63 C30.00 A8265.00
G1 F0.12 Z2.36 S0.63 C15.00 A8280.00
G1 F0.12 Z2.83 R5.42 B65.00 S0.63 C15.00 A8295.00
G1 F0.12 Z3.78 S0.63 C30.00 A8325.00
G1 F0.98 Z11.97 S3.00 C150.00 A8475.00
G1 F0.12 Z12.91 S0.63 C30.00 A8505.00
G1 F0.12 Z13.39 S0.63 C15.00 A8520.00
G1 F0.12 Z12.91 R5.42 B-65.00 S0.63 C15.00 A8535.00
G1 F0.12 Z11.97 S0.63 C30.00 A8565.00
G1 F0.98 Z3.78 S3.00 C150.00 A8715.00
G1 S0.50 C15.00 A8730.00
M0
M601
G1 F0.12 Z2.83 R-1.35 B-65.00 S0.63 C30.00 A8760.00
G1 F0.12 Z2.36 S0.63 C15.00 A8775.00
G1 F0.12 Z2.83 R5.42 B65.00 S0.63 C15.00 A8790.00
G1 F0.12 Z3.78 S0.63 C30.00 A8820.00
G1 F0.98 Z11.97 S3.00 C150.00 A8970.00
G1 F0.12 Z12.91 S0.63 C30.00 A9000.00
G1 F0.12 Z13.39 S0.63 C15.00 A9015.00
G1 F0.12 Z12.91 R5.42 B-65.00 S0.63 C15.00 A9030.00
G1 F0.12 Z11.97 S0.63 C30.00 A9060.00
G1 F0.98 Z3.78 S3.00 C150.00 A9210.00
M0
M601
G1 F0.12 Z2.83 R-1.35 B-65.00 S0.63 C30.00 A9240.00
G1 F0.12 Z2.36 S0.63 C15.00 A9255.00
G1 F0.12 Z2.83 R5.42 B65.00 S0.63 C15.00 A9270.00
G1 F0.12 Z3.78 S0.63 C30.00 A9300.00
G1 F0.98 Z11.97 S3.00 C150.00 A9450.00
G1 F0.12 Z12.91 S0.63 C30.00 A9480.00
G1 F0.12 Z13.39 S0.63 C15.00 A9495.00
G1 F0.12 Z12.91 R5.42 B-65.00 S0.63 C15.00 A9510.00
G1 F0.12 Z11.97 S0.63 C30.00 A9540.00

G1 F0.98 Z3.78 S3.00 C150.00 A9690.00
M0
M601
G1 F0.12 Z2.83 R-1.35 B-65.00 S0.63 C30.00 A9720.00
G1 F0.12 Z2.36 S0.63 C15.00 A9735.00
G1 F0.12 Z2.83 R5.42 B65.00 S0.63 C15.00 A9750.00
G1 F0.12 Z3.78 S0.63 C30.00 A9780.00
G1 F0.98 Z11.97 S3.00 C150.00 A9930.00
G1 F0.12 Z12.91 S0.63 C30.00 A9960.00
G1 F0.12 Z13.39 S0.63 C15.00 A9975.00
G1 F0.12 Z12.91 R5.42 B-65.00 S0.63 C15.00 A9990.00
G1 F0.12 Z11.97 S0.63 C30.00 A10020.00
G1 F0.98 Z3.78 S3.00 C150.00 A10170.00
G1 S0.50 C15.00 A10185.00
M0
M601
G1 F0.12 Z2.83 R-1.35 B-65.00 S0.63 C30.00 A10215.00
G1 F0.12 Z2.36 S0.63 C15.00 A10230.00
G1 F0.12 Z2.83 R5.42 B65.00 S0.63 C15.00 A10245.00
G1 F0.12 Z3.78 S0.63 C30.00 A10275.00
G1 F0.98 Z11.97 S3.00 C150.00 A10425.00
G1 F0.12 Z12.91 S0.63 C30.00 A10455.00
G1 F0.12 Z13.39 S0.63 C15.00 A10470.00
G1 F0.12 Z12.91 R5.42 B-65.00 S0.63 C15.00 A10485.00
G1 F0.12 Z11.97 S0.63 C30.00 A10515.00
G1 F0.98 Z3.78 S3.00 C150.00 A10665.00
M0
M601
G1 F0.12 Z2.83 R-1.35 B-65.00 S0.63 C30.00 A10695.00
G1 F0.12 Z2.36 S0.63 C15.00 A10710.00
G1 F0.12 Z2.83 R5.42 B65.00 S0.63 C15.00 A10725.00
G1 F0.12 Z3.78 S0.63 C30.00 A10755.00
G1 F0.98 Z11.97 S3.00 C150.00 A10905.00
G1 F0.12 Z12.91 S0.63 C30.00 A10935.00
G1 F0.12 Z13.39 S0.63 C15.00 A10950.00
G1 F0.12 Z12.91 R5.42 B-65.00 S0.63 C15.00 A10965.00
G1 F0.12 Z11.97 S0.63 C30.00 A10995.00
G1 F0.98 Z3.78 S3.00 C150.00 A11145.00

M0
M601
G1 F0.12 Z2.83 R-1.35 B-65.00 S0.63 C30.00 A11175.00
G1 F0.12 Z2.36 S0.63 C15.00 A11190.00
G1 F0.12 Z2.83 R5.42 B65.00 S0.63 C15.00 A11205.00
G1 F0.12 Z3.78 S0.63 C30.00 A11235.00
G1 F0.98 Z11.97 S3.00 C150.00 A11385.00
G1 F0.12 Z12.91 S0.63 C30.00 A11415.00
G1 F0.12 Z13.39 S0.63 C15.00 A11430.00
G1 F0.12 Z12.91 R5.42 B-65.00 S0.63 C15.00 A11445.00
G1 F0.12 Z11.97 S0.63 C30.00 A11475.00
G1 F0.98 Z3.78 S3.00 C150.00 A11625.00
G1 S0.50 C15.00 A11640.00
M0
M601
M5